Influence of Horizontal Inhomogeneity of Refractivity Vertical Profiles on Electromagnetic Measurements in Application to Refractivity Inversions

Erin E. Hackett, Ph.D.
Coastal Carolina University
Department of Marine Science
P.O. Box 261954, Conway, SC, 29528
843.349.4087 Office
443.677.6964 Cell
ehackett@coastal.edu

Final Performance Report: N00014-19-1-2350 (331 [Russell, Steven])

1.0 Major Goals

The environment impacts system performance predictions and evaluation of ship communication and sensing technologies that involve transmission and receipt of electromagnetic (EM) waves. The complex fluid dynamics of the marine atmospheric surface layer (MASL) and its interaction with the ocean surface layer cause changes in temperature and humidity over a wide range of scales. These changes result in variability of radio refractivity that in extreme cases causes ducting layers to form that can change, for example, the effective range of radar or create "holes" in radar coverage (Skolnik, 2001; Zhao et al., 2017). In particular, evaporation ducts are extremely prevalent over marine surfaces (Hitney and Vieth, 1990; Babin 1997; Yang et al., 2015). Direct measurement of humidity and temperature at all the relevant scales in the MASL is difficult and costly; thus, inversion methods that infer the refractive environment based on EM measurements have gained favor as a means to retrieve environmental information *in-situ*. There are numerous considerations for optimizing an inversion approach beyond the inversion methodology itself, including, treatment of the sea surface (or other non-refractive environmental effects), amount and location of data, data quality, sufficiency of the refractivity model, and inclusion of secondary effects such as horizontal inhomogeneity, the rough ocean surface, and atmospheric turbulence. The influence of horizontal inhomogeneity has been relatively sparsely examined over the last several decades and few inversion approaches have attempted to account for it.

Effect and significance of horizontal inhomogeneity of the refractivity vertical profile on EM propagation was investigated using both numerical and experimental data. This combination of data is useful because each type of data has its unique limitations. Trends in range of the refractivity data were characterized including categorization into typical types of range variations and their correlation to prevailing meteorological conditions. Considering these results, a parametric range-dependent refractivity model was suggested that extends the model discussed in Saeger et al. (2015), Penton and Hackett (2018), and Matsko and Hackett (2019). This range-dependent refractivity model can be utilized in inversion approaches, and more generally, for propagation predictions in heterogenous refractivity conditions. The effect of the refractivity range variations on propagation loss was evaluated using a propagation model, the Variable Terrain Radio Wave Parabolic Equation (VTRPE) simulation (Ryan, 1991). One of the major aspects of this study is to evaluate the relative importance of these inhomogeneity variations relative to other secondary sources of propagation loss variation such as rough surface effects and refractive index turbulence. To evaluate the relative importance of these phenomena, a refractive index turbulence model was assembled based-on current literature and verified with measured meteorological data. This turbulence model, an inhomogeneity model, and mean refractivity model were merged to generate a comprehensive refractive environment. The sensitivity of VTRPE to the model parameters for each of these phenomena were computed using the extended Fourier Amplitude Sensitivity Test, which is a variance-based global sensitivity method used in previous propagation studies (Lentini and Hackett, 2015). The eFAST results enable one to decipher which of these phenomena dominate propagation loss variability beyond the geometric horizon under different atmospheric stability regimes (unstable, neutral, stable). This information is invaluable because it provides insight into which aspects of the environment are most important to capture when modeling a particular refractive and sea state environment for the purposes of propagation predictions, which also has implications for refractivity inversion problems.

The results show that duct height variations in range are most commonly linear with variation of only a few meters over ~60 km. While these range variations can cause non-negligible changes in propagation loss, especially in localized regions in certain circumstances, such as when conditions change between trapping and non-trapping over range; but more typically, inhomogeneity is insignificant relative to variability introduced by the rough ocean surface and atmospheric turbulence. Only under near-neutral atmospheric conditions does horizontal inhomogeneity play a role comparable to some of the other parameters examined. Overall, the results suggest that horizontal inhomogeneity is not likely to be a significant factor for accurate propagation predictions in most scenarios; however, there will always be outlying cases where this assumption is not valid especially near boundaries like the land-sea interface (i.e., the coast) or in unique propagation conditions. This knowledge concerning the relative importance of these various environmental components informs, and therefore can help improve, assessments of system performance and susceptibility.

2.0 Accomplished

The research results are comprised of several components. First, the mean refractivity was investigated by comparing estimates of mean refractivity from several different methods (i.e., direct measurement, numerical weather prediction, boundary layer theory, and RF inversions) at nearly synchronous times, while approximately co-located. The differences in the mean refractivity between the methods are related to both prevailing meteorological conditions as well as to their impact on propagation predictions at X-band. This research is further discussed in subsection 2.1. In subsection 2.2, results of a characterization study on horizontal inhomogeneity are discussed, where horizontal inhomogeneity was categorized into different functional forms and frequency of occurrence and its relationship to prevailing meteorological conditions were analyzed. Verified numerical weather predictions for two different field campaigns in different hemispheres, different seasons, and different latitudes were used to help verify the generality of the results. Following the results of the characterization study, a range-dependent mean refractivity model is introduced that can be used in refractivity inversion problems involving evaporation duct range heterogeneity. The subsection concludes with exploring the impact of commonly occurring horizontal evaporation duct variations on X-band propagation predictions. With mean horizontally-varying refractivity studied and parameterized, in subsection 2.3, a refractive index turbulence model is introduced and verified with unique high-resolution meteorological measurements. The study also corroborates that the observed scatter in direct measurements of meteorological parameters (i.e., temperature and humidity) are primarily driven by turbulence rather than other sources of uncertainty or spatiotemporal variability. Finally, in subsection 2.4, the parameters describing these various components of the refractivity (mean, turbulent, horizontal variations) along with a few parameters describing the sea state were utilized in a global sensitivity analysis, which provides a ranking of the relative influence of the included parameters on X-band propagation predictions. Specifically, three sensitivity analyses were conducted for atmospheric stability regimes of unstable, neutral, and stable as the relative importance of these parameters can vary with conditions.

2.1 Mean Refractivity

Environmental predictions in the marine atmospheric surface layer are imperative to optimize X-band radar system performance in marine environments. Evaporation ducts (ED) lead to anomalous propagation where characterization of EDs in the MASL occurs primarily through two methods: *in-situ* measurements and numerical modeling. This study investigates the differences in co-located and synchronous refractivity estimations from the CASPER-East field campaign. Propagation predictions are generated for refractive profiles from *in-situ* measurements, Monin-Obukov boundary layer similarity theory, and numerical weather prediction forecasts. Variations in evaporation duct height (EDH) are found to be a primary driver of differences in propagation predictions between the estimated refractivity profiles, where location of the EDH relative to the transmitter changes the sensitivity of propagation predictions to EDH estimates. Differences in propagation are large when EDH estimates span the transmitter height and the lowest EDH across the methods is small, regardless of how much variation there is in EDH estimates. When the lowest EDH is small and EDH estimates span the transmitter height there are differences in physical regimes causing large propagation discrepancies – e.g., leakage into versus trapping within the duct. Variation in EDH between the methods is greatest in stable atmospheric conditions. M-deficit and curvature of the refractive profiles also influence propagation specifically in scenarios when EDHs span the transmitter height. When all EDHs are below the transmitter, EDH variance is the primary contributor to propagation variance, but M-deficit and profile curvature variance play a secondary role. M-deficits and curvature between the methods agree most often during periods of atmospheric stability. All the details regarding this study can be found in Appendix A, which is a copy of Pastore et al. (2021).

Following this characterization of mean refractivity based on three different forward methods, we also implement a similar study using these three forward methods and compare it with an inversion method. This study utilizes a unique dataset collected during the CASPER-East field campaign, including multiple refractivity estimation methods and twelve point-to-point (PTP) electromagnetic datasets, to assess the efficacy of PTP inversion techniques for remote sensing of mean atmospheric refractivity within the MASL. Comparison of mean refractivity between the inverse and other refractivity methods show reasonable evaporation duct height estimates by the inversion, and inverse-based propagation predictions are also shown to be more accurate than propagation based on other refractivity prediction methods – numerical weather prediction, theory, and *in-situ* atmospheric measurements. These results propose the effectiveness of a PTP metaheuristic radar inversion to remotely sense mean refractive environments from radar propagation measurements in stable and unstable atmospheric conditions. All the details regarding this study can be found in Appendix B, which is a copy of Pastore et al. (2022).

2.2 Characterize and Parameterize Radio Refractivity Horizontal Inhomogeneity for Evaporation Ducts

To evaluate range heterogeneity of modified refractivity in the marine atmospheric surface layer – three subobjectives are achieved: (i) characterize typical range variations of evaporation ducts and explore their potential causes, (ii) develop a parametric model reflecting those typical variations to implement in inversion problems and for propagation predictions, and (iii) perform a cursory evaluation of whether these typically observed refractivity range variations can impact propagation predictions.

First, we discuss results from the characterization of horizontal variations in evaporation duct characteristics. The evolution of the evaporation duct over range has been reported to cause adverse effects on X-band sensing technologies in some circumstances. However, in terms of the predictability of these effects, more research is still needed. This research explores evaporation duct variations over range and characterizes them based-on two verified numerical datasets from different latitudes, different hemispheres, and during different seasons as well as correlating their range distributions to distributions of other atmospheric variables. It is found, for both datasets, that most often a linear function accurately represents variations in evaporation duct characteristics over ~60 km in range, but higher-order functional distributions of evaporation duct characteristics with range do occur albeit less frequently. Furthermore, range distributions of mean wind speed and mean specific humidity within the evaporation layer are strongly correlated to the range distributions of duct height; while range distributions of duct shape are driven mainly by the specific humidity gradient in the evaporation layer. The mid-latitude dataset exhibits more complex range distributions during frontal events; while the equatorial dataset shows the most complex range distributions near sunrise. All the details regarding this study can be found in Appendix C, which is a full draft of a manuscript intended to be submitted for publication within the next few months (Greenway et al., 2024).

Based on the results from the characterization study, a novel refractivity parametric model for heterogenous evaporation ducts was developed: a range-dependent stacked (or layered) model (RaDS). The RaDS model extends the Penton and Hackett (2018) model to capture heterogeneities in duct height and curvature with range:

$$M(z,r) = M_0 + \begin{cases} c_0(r)\left(z - z_d(r)\ln\left(\frac{z + z_0}{z_0}\right)\right), & z_L \leq z \\ m_1 z - M_1, & z > z_L \end{cases} \quad (1)$$

$$z_d(r) = z_{d_0} + \xi r \quad (2)$$

$$c_0(r) = c_{0_0} + \gamma r \quad (3)$$

where M_0 is surface modified refractivity, z is altitude, r is range, z_d is duct height, c_0 is the potential refractivity gradient or duct shape parameter, z_0 is the aerodynamic roughness factor, z_L is the height of the evaporation layer ($z_L = 2z_d$), m_1 is the mixed layer slope above the duct, M_1 ensures continuity between the two layers and is a function of the other parameters, z_{d_0} is the duct height at the location of the radar transmitter, ξ is the slope of duct height over range, c_{0_0} is the potential refractivity gradient at the location of the radar transmitter, and γ is the slope of the potential refractivity gradient over range. This model can be utilized in inversion problems or in parabolic wave equation propagation simulations that need to account for horizontal inhomogeneity of duct height and shape over range.

For examining the influence of these horizontal variations on propagation predictions, we chose to focus on linear variations of duct height over range because it was shown in section 2.1 that duct height is a leading order effect on propagation, as has also been shown by many other studies, and the characterization results showed linear variations are much more common than other types

of range variations. Thus, it seems most imperative to investigate the effect of linear duct height changes over range before studying secondary effects (like range variations of duct shape) on propagation. Duct shape has been studied rather sparsely even under range homogeneous refractivity conditions.

Propagation simulations were performed for a range of z_{d_0} and ξ – performing a classic one-at-a-time sensitivity study where one parameter is varied while all others are held at fixed values. All combinations of z_{d_0} and ξ are included while parameters not investigated in this classic sensitivity study (γ, c_{0_0}, M_0, m_1, and z_0) are fixed. These parameters are fixed to values of 0 M-units/m^2, 0.125 M-units/m, 333 M-units, 0.12 M-units/m, and 0.00015 m, respectively. These are all parameter values that reflect either an average, typical, or neutral condition aside from γ, which was chosen so that duct shape does not vary in range. ξ is varied from -0.1 to 0.17 m/km in increments of 0.005 m/km. This slope range results in z_d changes between 0.3 m to 10.2 m over a 60 km transect (increasing or decreasing over range). z_{d_0} is varied from 1-19 m in increments of 2 m, plus a value of z_{d_0} at the transmitter height (Tx; 10.4 m). These search spaces are chosen to encompass z_d both above and below the transmitter and also ensures that the largest duct height slope combined with the largest initial duct height keeps the range-dependent duct heights below ~30 m. Evaporation ducts do not frequently exhibit duct heights above 30 m. Combinations of ξ and z_{d_0} that produce negative estimates of z_d are discarded because negative duct heights are not physically possible. Performing propagation simulations for all of these initial duct height and slope combinations results in 574 simulation runs after removing the aforementioned unphysical profile transects. It is also noteworthy that these search space parameter ranges for z_{d_0} and ξ encompass all values of these parameters found within the numerical weather prediction forecasts explored in the characterization study described in Appendix C. The antenna properties for the simulations were a transmitter at a height of 10.4 m emitting horizontally polarized EM waves at 9 GHz with a Gaussian antenna pattern with two side lobes and beamwidth of 15 degrees. The output grid from the simulation covers 0-100 m in altitude and 0-60 km in range with a spacing of 1 m and 50 m, respectively. All simulations were performed over a smooth sea surface.

To explore how common large differences in propagation predictions are due to assuming a homogenous atmosphere, we quantify the amount of simulation runs where the assumption of homogeneity leads to significant propagation prediction errors (> 5 dB) for several different trapping scenarios. All the simulation runs are first divided into several categories depending on the trapping condition for that simulation:

i. Trapping could occur along the entire transect (~72% of simulation runs)
ii. Trapping could not occur along the entire transect (~9%)
iii. Trapping could occur at the Tx but changes to non-trapping somewhere along the transect (~5%)
iv. Trapping could not occur at the Tx but changes to trapping somewhere along the transect (~14%)

For this categorization, trapping is defined according to the criteria originally derived by Kerr (1951) and later referenced in Turton et al. (1988) and Cherret (2015):

$$\lambda_{max} = \frac{2}{3} C z_d \Delta M^{\frac{1}{2}} \quad (4)$$

where λ_{max} is the maximum EM wavelength (m) that is trapped, ΔM is the difference between the modified refractivity at the surface and at the duct height-commonly referred to as the *M*-deficit, and C = 3.77 x 10^{-3}. A refractivity vertical profile along a transect is considered to be "trapping" if the maximum trapping wavelength (Eq. (4)) is greater than or equal to ~0.03331 m. Thus, importantly, this criterion does not determine whether trapping actually occurred or not, but whether the environment enables trapping at this particular radar frequency if EM energy enters the duct. Figure 1 shows example modified refractivity profile range transects that exemplify the four categories mentioned above.

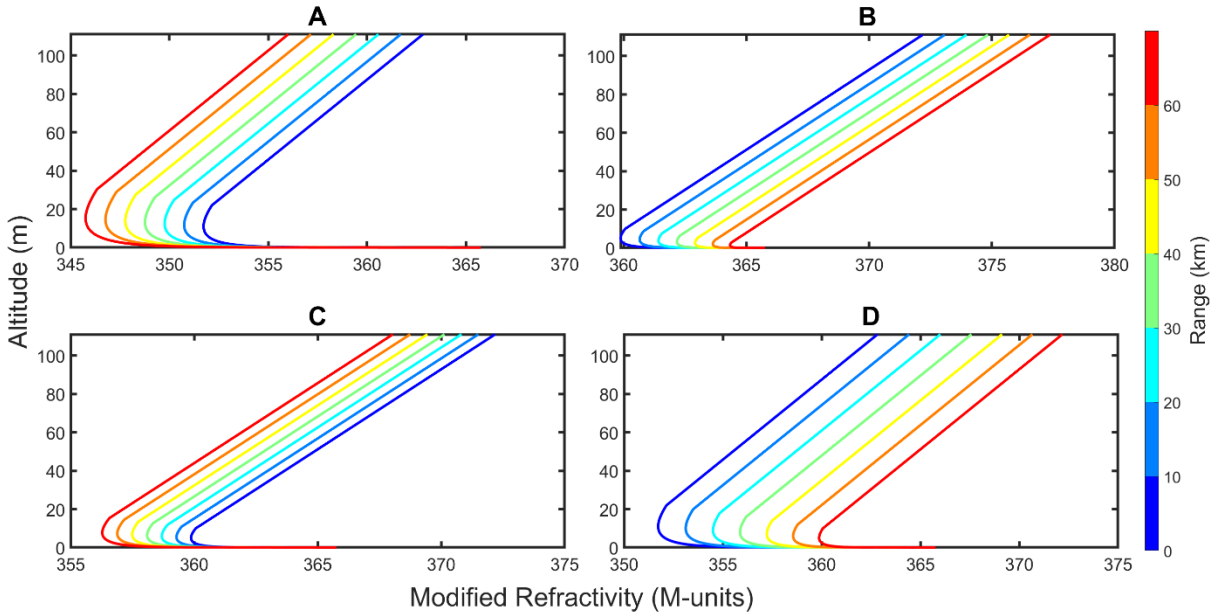


Figure 1. Example modified refractivity vertical profiles in heterogeneous conditions for the various trapping classifications: (A) X-band trapping along the entire transect, (B) no trapping along the entire transect, (C) no trapping at the transmitter but changes to trapping along the transect, and (D) trapping at the transmitter but changes to no trapping along the transect. The dark blue M-profiles, corresponding to r = 0 km, are used as the refractivity profiles for the homogeneous conditions, used for PL comparisons.

For each propagation simulation within each category, all locations within the propagation domain in which there is more than a 5 dB difference resulting from using the range heterogenous refractivity environment relative to using the refractivity profile at the transmitter and assuming it is homogenous in range are identified. After identifying these locations in all propagation patterns for a given category, the percentage of simulations runs (for that category and location within the domain) that have greater than 5 dB differences are computed. The 5 dB threshold is based-off Goldhirsh and Dockery (1998) defining a "baseline" propagation measurement error as 5 dB. The results are shown in Figure 2. In cases where there is trapping, or non-trapping, along the entire transect, significant differences in the propagation predictions due to assumption of refractivity homogeneity are rather infrequent and exclusively localized to long range (i.e., beyond geometric

horizon) (Figures 2A and 2B). In contrast, when the there is a change in the trapping condition along the transect due to duct height horizontal inhomogeneity, significant differences in propagation predictions occur when assuming homogenous conditions. This observation is especially true when trapping is assumed to occur over the entire transect (due to homogeneity assumption) but it actually switches to a non-trapping condition along the transect due to heterogeneity (Figure 2D). This scenario results in frequent significant discrepancies (> 5dB) in propagation predictions at altitudes below ~40 m and ranges beyond 35 km (~100% of the time). These results suggest that while inhomogeneity may not frequently cause significant changes in propagation, there are scenarios where it does make a significant difference routinely. The relative importance of these propagation differences stemming from inhomogeneity in comparison to differences in propagation predictions due to, for example, neglecting turbulence or inaccurate representation of the sea surface are further explored in section 2.4.

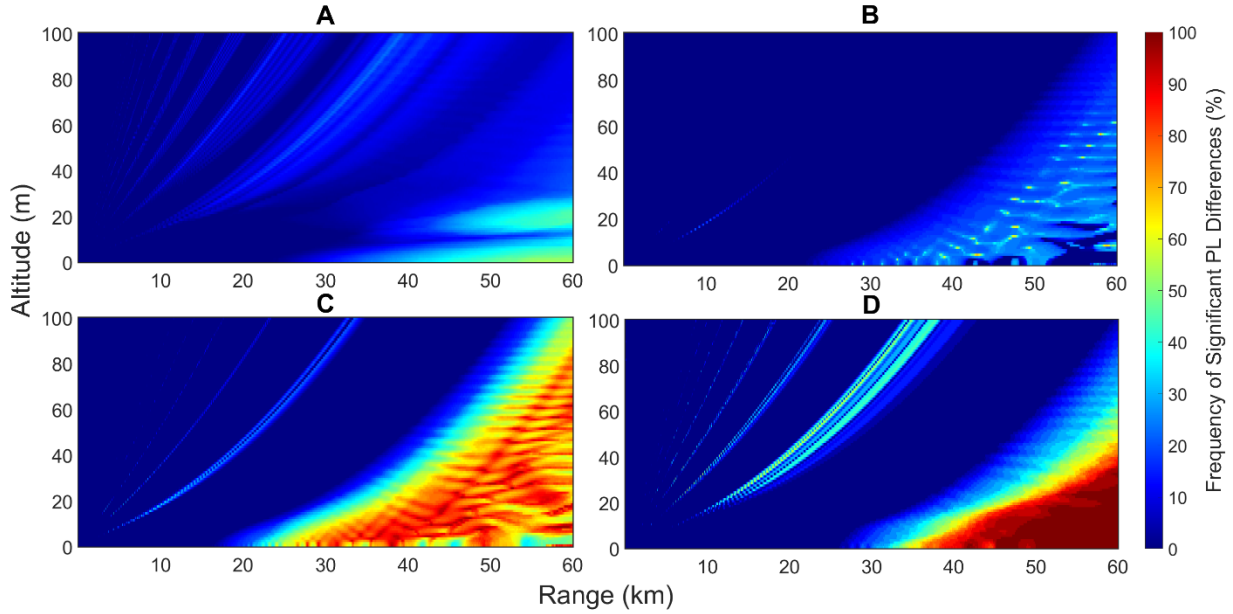


Figure 2. Frequency (shown as percent of simulations – see colorbar) of significant PL differences (> 5 dB) between PL predictions for a homogeneous refractivity profile and that of a heterogeneous refractivity environment for each trapping classification at all locations within the propagation simulation domain. Panel A is for trapping is possible over the entire range transect, Panel B is for when trapping is not possible over the entire range transect, Panel C is for environments that switch from non-trapping conditions at the transmitter to trapping conditions along the transect, and Panel D shows results for environments that switch from trapping at the transmitter to non-trapping environments along the transect.

2.3 Refractive Index Turbulence Modeling

In order to model refractive index turbulence and determine its relative importance with respect to horizontal inhomogeneity, a refractive index turbulence model was implemented and verified with *in-situ* measurements. Direct measurement of profiles of atmospheric properties near the ocean surface and within the marine atmospheric surface layer often and inevitably contain a large degree of variability. The variability observed can be explained through numerous technical and natural

reasons – such as temporal variability over the time span a profile is measured (unsteadiness in the mean), spatial variations (inhomogeneity), turbulent fluctuations, and measurement uncertainty. In this study, we seek to explore the observed variability in vertical distributions of refractive index measured with a tethered-balloon-based marine atmospheric profiling system (MAPS). MAPS profiles the atmosphere from approximately 0.5-50 m, with instantaneous (order 1 s) measurements performed at each profiled altitude. To explore whether the observed scatter can be largely explained by (inertial-scale) turbulent fluctuations, we simulate refractive index fluctuations with a spectral-based turbulent refractive index fluctuation (TRIF) model. TRIF is optimized based on the MAPS measurements to determine a vertical length scale of the turbulence because this length scale cannot be computed directly from the measurements. Scales computed in the optimization are reasonable based-on other estimates in the literature under similar atmospheric conditions. However, finer-scale trends of the length scale with atmospheric stability do not match expectations and thus, estimated length scales may be considered more as an order of magnitude estimate rather than an exact measurement of this scale. The ability to match the observed variability in the MAPS data using a turbulence model with a reasonable choice of vertical length scale suggests the MAPS variability is dominated by physical processes like turbulence rather than being primarily driven by measurement uncertainty; and, simultaneously verifies the TRIF model. All the details regarding this study can be found in Appendix D, which is a copy of Pastore et al. (2023).

2.4 Evaluate Relative Influence of Mean Refractivity, Horizontal Inhomogeneity, Refractive Index Turbulence, and Sea State

This subsection represents the culmination of all work performed in the prior subsections. The mean, turbulent, and horizontal variability investigated and modeled in subsections 2.1-2.3 were used along with a sea state model to evaluate the relative influence of these phenomena on X-band propagation predictions.

In predicting electromagnetic wave propagation within the marine atmospheric surface layer, it is common to assume steady homogenous conditions. However, discrepancies between predicted and measured propagation remain, which could be due in-part to turbulent fluctuations of the refractive index, spatially heterogenous evaporative ducting environments, and mischaracterization of the rough ocean bottom boundary. To better understand the relative importance of these contributors, this study explores the sensitivity of X-band propagation to parameters describing sea-state conditions and refractive environments, including turbulent fluctuations and spatially heterogenous conditions. This study employs the extended Fourier Amplitude Sensitivity Test to compute sensitivity indices that evaluate the leading-order effects and effects due to non-linear interactions between these refractive and sea state parameters on a parabolic wave equation electromagnetic wave propagation simulation. The parameters are delineated and evaluated in three atmospheric stability regime experiments: stable, neutral, and unstable, and also consider both trapping and non-trapping propagation conditions. Parameter sensitivity indices are ranked for each experiment to examine the relative effects of the parameters on X-band propagation predictions. The results show that in neutral and stable regimes, mean evaporation duct characteristics have the greatest impact on propagation beyond the geometric horizon, while in unstable conditions, turbulence also plays a significant role. Additionally, in the lowest 10 m of the atmosphere, forward scattering from the rough sea-surface has the greatest effect on

propagation predictions regardless of atmospheric stability. Generally, horizontal inhomogeneity is a negligible factor relative to the other parameters investigated except in near-neutral conditions, where it can play a secondary role similar to some of the other parameters. However, as discussed in subsection 2.2, there can be some unique conditions in which its effects on propagation are more significant. All the details regarding this study can be found in Appendix E, which is a copy of Pastore and Hackett (2024), an in-preparation manuscript that is planned for submission before September 2023.

3.0 Training

Four students were trained during the course of this research effort – half of which were from underrepresented groups in physical science (women). One was exclusively an undergraduate student, one started as an undergraduate student and transitioned to a Master's student during the award period, one started as a Master's student and transitioned to a Ph.D. student during the award period, and one was exclusively a Ph.D. student during the award period. All of the students working on the project have either transitioned to positions relevant to the U.S. Navy or are pursuing relevant further advanced degrees. The exclusively undergraduate student will be starting her Master's degree studies under my advisement with a thesis on a related topic starting Fall 2023 and is participating in a Naval Research Enterprise Internship Program (NREIP) this summer at the Naval Research Laboratory. The second student whom transitioned to the M.S. degree, completed an NREIP, completed an M.S. thesis involving related research, and is currently working part-time for the Naval Research Laboratory while completing a Ph.D. in Atmospheric Science at Texas A&M. The Master's student whom transitioned to a Ph.D. student also completed an NREIP, and is continuing to work on his dissertation research that is related to these topics of study. Finally, the Ph.D. student completed their dissertation, and accepted a job at the Naval Surface Warfare Center, Dahlgren Division, to start in September 2023. All of these students gained experience in data analysis and interpretation of both simulation and *in-situ* data, as well as presented their results at conferences and contributed to peer-reviewed journal publications. Ph.D. students were also mentored in leading small teams of researchers and integrating their results into a larger body of work as well as leading publication efforts. A list of associated theses and dissertations are provided below, and conference presentations and peer-reviewed journal publications coauthored by these students are highlighted in the next section (4.0).

Theses and Dissertations

Greenway, D.P., 2020, Parametric model development for heterogeneous atmospheric conditions, *M.S. Thesis*, Coastal Carolina University.

Wessinger, S.E., 2022, Improving near-surface refractivity estimates in marine environments, *M.S. Thesis*, Coastal Carolina University.

Pastore, D.M., 2023, Characteristics of refractivity and sea state in the marine atmospheric surface layer and their influence on X-band propagation, *Doctoral Dissertation*, Coastal Carolina University.

4.0 Dissemination

Several publications and presentations were generated as a result of this research effort. In addition, the PI worked closely with scientists at the Naval Research Laboratory in Monterey, CA (Tracy Haack, Andrew Kammerer) and at the Naval Surface Warfare Center, Carderock Division (Anne Fullerton) to keep them apprised of the findings and results of this research. Annual briefings at the ONR Code 331 Topside Signatures Review Meeting were also given. A listing of associated publications and conference presentations is provided below for reference.

4.1 Publications

Published (* denotes student author):

Pastore*, D. M., Greenway*, D. P., Stanek*, M. J., Wessinger*, S. E., Haack, T., Wang, Q., and E.E. Hackett (2021). Comparison of atmospheric refractivity estimation methods and their influence on radar propagation predictions. Radio Science, 56, e2020RS007244. https://doi.org/10.1029/2020RS007244 (*herein Appendix A*)

Pastore*, D.M., Wessinger*, S.E., Greenway,* D.P., Stanek*, M.J., Burkholder, R.J., Haack, T., Wang, Q., and E.E. Hackett (2022). Refractivity inversions from point-to-point X-band radar measurements, Radio Science, 57, e2021RS007345. https://doi.org/10.1029/2021RS007345 (*herein Appendix B*)

Pastore*, D.M., Yamaguchi, R.T, Wang, Q., and E.E. Hackett (2023). On the variability of *in situ* surface layer refractivity measurements, Atmosphere, 14, 1085. https://doi.org/10.3390/atmos14071085 (*herein Appendix D*)

In-preparation, fully drafted, with submission planned within the next few months:

Pastore*, D.M., and E.E. Hackett (2024). Relative influence of sea state and mean, turbulent, and heterogenous refractivity on X-band propagation, *in-preparation* for submission to IEEE Transactions on Geoscience and Remote Sensing. (*herein Appendix E*)

Greenway*, D.P., Vaughan*, A.E., Kammerer, A.J., and E.E. Hackett, Range-dependent variations of the evaporation duct, *in-preparation* for submission to IEEE Transactions on Antennas and Propagation. (*herein Appendix C*)

4.2 Presentations

Conference presentations (* denotes student author).

Pastore*, D.M., M.J. Stanek*, D.P. Greenway*, Q. Wang, R. Burkholder, T. Haack, Q. Wang and E.E. Hackett, 2019, Comparison of Measured and Predicted Propagation during CASPER East Field Campaign using Different Methods of Environmental Estimation, 2019, *IEEE International Symposium on Antennas and Propagation and U.S. National Committee URSI Radio Science Meeting*, Atlanta, GA, July.

Pastore*, D.M., D.P. Greenway*, M.J. Stanek*, S.E. Wessinger*, T. Haack, Q. Wang, and E.E. Hackett, 2020, Comparison of Atmospheric Refractivity Methods and their Influence on Radar Propagation Predictions, *IEEE International Symposium on Antennas and Propagation and North American Radio Science Meeting*, virtual, July.

Pastore*, D.M., and E.E. Hackett, 2021, Numerical Modeling of Turbulent Refractive Index Fluctuations in the Coastal Marine Atmospheric Surface Layer, *7th Young Coastal Scientists and Engineers Conference – Americas*, Myrtle Beach, SC, October.

Greenway*, D.P., Haack, T., and E.E. Hackett, 2021, Characterizing the Coastal Evaporation Duct and its Effects on X-band Radar Propagation, *7th Young Coastal Scientists and Engineers Conference – Americas*, Myrtle Beach, SC, October.

Pastore*, D.M. and E.E. Hackett, 2022, Global Sensitivity of X-band Propagation to Environmental Parameters during Evaporative Ducting Conditions, *URSI National Radio Science Meeting*, Boulder, CO, January.

Pastore*, D.M. and E.E. Hackett, 2023, Global Sensitivity of X-Band Propagation to Refractivity and Sea State in a Turbulent Heterogenous Marine Atmospheric Surface Layer, *URSI National Radio Science Meeting,* Boulder, CO, January.

Vaughan*, A.E., D.P. Greenway*, A.J. Kammerer, and E.E. Hackett, 2023, Exploring Relationships of Evaporation Duct Height with Wind Speed and Humidity, *American Meteorological Society Annual Meeting 2023,* Denver, CO, January.

Bruno*, M.T., D.M. Pastore*, D.P. Greenway*, and E.E. Hackett, 2023, Optimization of an Ocean Wave Model using *In-situ* Buoy Wave Spectral Measurements, *American Meteorological Society Annual Meeting 2023,* Denver, CO, January.

Pastore*, D.M., D.P. Greenway*, M.T. Bruno*, and E.E. Hackett, 2023, Radar Remote Sensing of Vertical Refractivity in the Marine Atmospheric Surface Layer, *American Meteorological Society Annual Meeting 2023,* Denver, CO, January.

Greenway*, D.P., A.E. Vaughan*, A.J. Kammerer, and E.E. Hackett, 2023, Characterizing Range Heterogenous Evaporation Ducts, *American Meteorological Society Annual Meeting 2023,* Denver, CO, January.

5.0 References

Babin, S. M., Young, G. S., and J. A. Carton (1997). A new model of the oceanic evaporation duct, *Journal of Applied Meteorology*, 36, 3, 193-204.

Cherrett, R. C. (2015). Capturing characteristics of atmospheric refractivity using observations and modeling approaches, Doctoral dissertation, Naval Postgraduate School.

Greenway, D.P., Vaughan, A.E., Kammerer, A.J., and E.E. Hackett (2024). Range-dependent variations of the evaporation duct, *in-preparation*.

Goldhirsh, J. and D. Dockery (1998). Propagation factor errors due to the assumption of lateral homogeneity, *Radio Science*, 33, 2, 239-249.

Hitney, H.V. and R. Vieth (1990). Statistical assessment of evaporation duct propagation, *IEEE Transactions on antennas and propagation*, 38,6, 794-799.

Kerr, D.E. (1951). Propagation of short radio waves. New York, McGraw-Hill Book Co.

Lentini, N.E., and E.E. Hackett (2015). Global sensitivity of parabolic equation radar wave propagation simulation to sea state and atmospheric refractivity structure, *Radio Science*, 50(10), 1027-1049. doi:10.1002/2015RS005742

Matsko, I.J., and E.E. Hackett (2019). Impact of radar data sampling on the accuracy of atmospheric refractivity inversions over marine surfaces, *Radio Science*, 54(7), 704-714. doi: 10.1029/2018RS006757

Pastore, D.M., and E.E. Hackett (2024). Relative influence of sea state and mean, turbulent, and heterogenous refractivity on X-band propagation, *in-preparation*.

Pastore, D. M., Greenway, D. P., Stanek, M. J., Wessinger, S. E., Haack, T., Wang, Q., and E.E. Hackett (2021). Comparison of atmospheric refractivity estimation methods and their influence on radar propagation predictions. *Radio Science*, 56, e2020RS007244. https://doi.org/10.1029/2020RS007244

Pastore, D.M., Wessinger, S.E., Greenway, D.P., Stanek, M.J., Burkholder, R.J., Haack, T., Wang, Q., and E.E. Hackett (2022). Refractivity inversions from point-to-point X-band radar measurements, *Radio Science*, 57, e2021RS007345. https://doi.org/10.1029/2021RS007345

Pastore, D.M., Yamaguchi, R.T, Wang, Q., and E.E. Hackett (2023). On the variability of *in situ* surface layer refractivity measurements, *Atmosphere*, 14, 1085. https://doi.org/10.3390/atmos14071085

Penton, S.E., and E.E. Hackett (2018). Rough ocean surface effects on evaporative duct atmospheric refractivity inversions using genetic algorithms, *Radio Science*, 53(6), 804-819. doi: 10.1029/2017RS006440

Ryan, F.J. (1991). User's guide for the VTRPE (Variable Terrain Radio Parabolic Equation) computer model, *Naval Ocean Systems Center*, San Diego, CA, No. NOSC/TR-1456.

Saeger, J.T., Grimes, N.G., Rickard, H.E., and E.E. Hackett (2015). Evaluation of simplified evaporation duct refractivity models for inversion problems, *Radio Science*, 50, 10, 1110-1130.

Skolnik, M. I. (2001). *Introduction to Radar Systems*, 3rd ed., McGraw-Hill, Boston, MA.

Turton, J.D., Bennetts, D.A., and S.G. Farmer (1988). An introduction to radio ducting, *Meteorological Magazine*, 117(1393), 245-254.

Yang, S., Kun-De, Y., Yi-Xin, Y., and M. Yuan-Liang (2015). Experimental verification of effect of horizontal inhomogeneity of evaporation duct on electromagnetic wave propagation, *Chin. Phys.* B, 24, 4, 044102, pp. 9.

Zhao, X., Yardim, C., Wang, D., and B. Howe (2017). Estimating range-dependent evaporation duct height, *Journal of Atmospheric and Oceanic Technology,* 34, 1113-1123.

Appendix A: Published Manuscript

Pastore, D. M., Greenway, D. P., Stanek, M. J., Wessinger, S. E., Haack, T., Wang, Q., and E.E. Hackett (2021). Comparison of atmospheric refractivity estimation methods and their influence on radar propagation predictions. Radio Science, 56, e2020RS007244. https://doi.org/10.1029/2020RS007244

Radio Science®

RESEARCH ARTICLE
10.1029/2020RS007244

Special Section:
Air-Sea Coupling and its Effect on Electromagnetic Propagation in the Marine Atmospheric Boundary Layer

Comparison of Atmospheric Refractivity Estimation Methods and Their Influence on Radar Propagation Predictions

Douglas M. Pastore[1], Daniel P. Greenway[1], Mathew J. Stanek[1], Sarah E. Wessinger[1], Tracy Haack[2], Qing Wang[3], and Erin E. Hackett[1]

[1]Department of Marine Science, Coastal Carolina University, Conway, SC, USA, [2]Marine Meteorology Division, Naval Research Laboratory, Monterey, CA, USA, [3]Graduate School of Engineering and Applied Sciences, Naval Postgraduate School, Monterey, CA, USA

Key Points:

- Refractivity generated from models and measured data are compared to explore influences on radar wave propagation
- Proximity of duct height to transmitter and its variance have large effects on propagation; typically occurring during stable conditions
- M-deficit and profile curvature affect propagation when duct heights span the transmitter; largest variations occur in unstable conditions

Correspondence to:
E. E. Hackett,
ehackett@coastal.edu

Citation:
Pastore, D. M., Greenway, D. P., Stanek, M. J., Wessinger, S. E., Haack, T., Wang, Q., & Hackett, E. E. (2021). Comparison of atmospheric refractivity estimation methods and their influence on radar propagation predictions. *Radio Science*, *56*, e2020RS007244. https://doi.org/10.1029/2020RS007244

Received 20 NOV 2020
Accepted 31 AUG 2021

© 2021. American Geophysical Union. All Rights Reserved.

Abstract Environmental predictions in the marine atmospheric surface layer (MASL) are imperative to optimize X-band radar system performance in marine environments. Evaporation ducts (ED) lead to anomalous propagation where characterization of EDs in the MASL occurs primarily through two methods: *in-situ* measurements and numerical modeling. This study investigates the differences in co-located and synchronous refractivity estimations from the CASPER-East campaign. Propagation predictions are generated for refractive profiles from *in-situ* measurements, Monin-Obukov boundary layer similarity theory, and numerical weather prediction forecasts. Variations in evaporation duct height (EDH) are found to be a primary driver of differences in propagation between the estimated refractivity profiles, where location of the EDH relative to the transmitter changes the sensitivity of propagation predictions to EDH estimates. Differences in propagation are large when EDH estimates span the transmitter height and the lowest EDH across the methods is small, regardless of how much variation there is in EDH estimates. When the lowest EDH is small and EDH estimates span the transmitter height there are differences in physical regimes causing large propagation discrepancies–for example, leakage into versus trapping within the duct. Variation in EDH between the methods is greatest in stable environments. M-deficit and curvature of the refractive profiles also influence propagation specifically in scenarios when EDH spans the transmitter. When all EDHs are below the transmitter, EDH variance is the primary contributor to propagation variance, but M-deficit and profile curvature variance play a secondary role. M-deficits and curvature between the methods agree most often during periods of atmospheric stability.

1. Introduction

Accurate prediction of the environment within the marine atmospheric surface layer (MASL) is an essential part of optimizing X-band radar system performance in marine environments. The MASL is a dynamic region dominated by temporally and spatially varying momentum, heat, and water vapor exchange between the ocean and atmosphere, making it difficult to accurately predict or model surface layer processes. Vertical variations in temperature (T), pressure (p), wind (U), and specific humidity (q) in the marine environment are commonly studied due to their importance in ocean-atmosphere exchange as well as their strong influence on electromagnetic (EM) wave propagation (Fairall et al., 1996; Hitney et al., 1985; Wang et al., 2018). Anomalous propagation in the MASL is commonly caused by refraction of EM waves due to the rapid decrease in humidity over the ocean causing evaporation ducts. Generally, EDs are common in marine environments due to increased water vapor in the near surface air where evaporation duct height and M-deficit (sometimes referred to as evaporation duct strength) are commonly used to characterize the duct (Cherrett, 2015).

Previous research has explored *in-situ* measurement techniques to estimate p, T, and q in the MASL where most often radiosondes are deployed into the atmosphere via rockets, tethered or untethered weather balloons or kites, or ship- or buoy-based mast towers (Edson et al., 2004; Kang & Wang, 2016; Wang et al., 2018). These platforms directly measure the environment often at high sampling rates but have spatial coverage limitations. Limitations in measured data are also observed close to the sea surface, where they lack fidelity due to contamination of the measurements from the observation platform and increased turbulence near

1944799x, 2021, 56, Downloaded from https://agupubs.onlinelibrary.wiley.com. By Coastal Carolina University - on [28/09/2021]. Re-use and distribution is strictly not permitted, except for Open Access articles

1944799x, 2021, 56, Downloaded from https://agupubs.onlinelibrary.wiley.com. By Coastal Carolina University - on [28/09/2021]. Re-use and distribution is strictly not permitted, except for Open Access articles

the ocean surface. The Marine Atmospheric Profiling System (MAPS; Kang & Wang, 2016) utilized in the Coupled Air Sea Processes and Electromagnetic Ducting (CASPER; Wang et al., 2018) East campaign is an example of a radiosonde tethered balloon system. Sea spray and wave interactions with MAPS instruments at the air-sea interface cause errors and gaps in the data close to the sea surface. These limitations as well as measurement uncertainties and limited temporal and spatial coverage make it difficult to collect large comprehensive datasets of *in-situ* measurements, especially close to the sea surface where EDs typically reside.

Semi-empirical surface layer models have been developed to represent the mean state of vertical variations of wind, humidity, and temperature within the lowest ~50 m of the atmosphere. These models utilize Monin Obukhov similarity theory (MOST) to estimate surface fluxes using universal, non-dimensional functions based-on bulk environmental parameters, including near surface estimates of T, q, p, and U along with surface properties: wavefield characteristics and sea surface temperature (SST). Algorithms such as the Coupled Ocean Atmosphere Response Experiment (COARE) use MOST to model fluxes in the MASL and estimate these vertical profiles of T, U, and q (Fairall et al., 1996, 2003). Numerical weather prediction models such as the Coupled Ocean Atmosphere Mesoscale Prediction System (COAMPS®; Hodur, 1997) are often augmented with MOST profiles by implementing the Naval Atmospheric Vertical Surface Layer Model (NAVSLaM; Frederickson, 2016; Karimian et al., 2013) to "blend" vertical atmospheric profiles in the lowest layers. In that case, COAMPS® forecasts provide the inputs to NAVSLaM allowing for wide spatial coverage with horizontal resolutions generally spanning 1–4 km; however, forecasts are generated hourly due to computational load which may yield poorer temporal resolution than *in-situ* measurements (Haack et al., 2010).

Parabolic equation (PE) methods are used to model EM propagation in the troposphere due to the inclusion of environmental factors (i.e., refraction, reflection, attenuation, etc.; Craig & Levy, 1991; Skolnik, 2001; Sirkova, 2012; Wagner et al., 2016). The included physical phenomena allow for accurate predictions of the propagation; thus, limitations of the simulations are driven by the environmental characterization (Sirkova, 2012). Previous studies have included measured and modeled data in PE propagation predictions but more comparisons of multiple methods of refractivity estimation at similar times and locations is needed to better understand discrepancies between derived propagation predictions.

This study investigates the variations in refractivity estimated by MAPS measurements (Wang et al., 2018), COAMPS®-NAVSLaM blended numerical weather prediction forecasts (Hodur, 1997), and the COARE algorithm (v3.0; Fairall et al., 2003) at similar times and locations based on data collected during the CASPER-East field campaign. Variations in propagation generated by refractivity profiles from each method are linked to changes in the environment and characteristics of the corresponding refractive profiles in order to highlight variations that impact propagation most significantly. It is important to note that this study does not consider any estimation method as representative of the "true" environment, but rather focuses on comparisons of approximately synchronous co-located estimated refractivity and associated propagation from these common refractivity estimation methods. The following section describes the methods of refractivity generation as well as the propagation simulation. Results are then presented and discussed in the subsequent section followed by conclusions.

2. Methods

2.1. MAPS Measurements

During the CASPER-East campaign, meteorological measurements within the marine atmospheric boundary layer (MABL) were performed offshore Duck, NC over 25 days in 2015, October 12 to November 6 (Wang et al., 2018). The goal of the CASPER-East campaign was to perform electromagnetic (EM), oceanographic, and meteorological measurements aiding in the representation and understanding of the environment within the MABL as well as explore novel techniques for modeling EM wave propagation through the observed environments. This paper focuses on meteorological and sea-surface measurements made within the MASL from a small workboat and the vessel from which it was deployed, the research vessel (R/V) Sharp. Sea surface temperature (SST) observations from the R/V Sharp are averaged on 5-min intervals consisting of bulk SST measurements corrected to skin temperature measurements (Wang et al., 2018). The meteorological measurements during CAPSER-East occurred aperiodically over 12 days during CASPER-East

1944799x, 2021, 56, Downloaded from https://agupubs.onlinelibrary.wiley.com. By Coastal Carolina University - on [28/09/2021]. Re-use and distribution is strictly not permitted, except for Open Access articles

Table 1
Summary of Vertical Refractivity Profiles Computed From the MAPS Measurements, COARE Algorithm, and COAMPS-NAVSLaM Numerical Weather Predictions

Day	Profile set number	Start time (ET)	Range (km)
October 13, 2015	1	12:49	4
October 14, 2015	2[a]	9:06	28
	3[a]	12:42	4
	4	15:32	28
October 15, 2015	5[a]	8:22	28
	6[a]	11:03	3
October 16, 2015	7	9:12	28
	8	12:16	3
	9	14:38	30
October 17, 2015	10	8:07	28
	11[a]	11:04	4
	12[a]	14:06	20
	13	18:25	28
October 20, 2015	14[a]	9:41	29
	15[a]	12:57	4
	16[a]	15:29	30
October 21, 2015	17[a]	7:01	44
	18[a]	8:57	28
	19[a]	10:29	16
	20[a]	12:10	3
October 23, 2015	21	8:43	60
	22[a]	11:44	78
October 24, 2015	23	8:05	60
October 25, 2015	24[a]	11:25	28
	25	14:11	16
	26	15:58	4
	27[a]	18:28	28

Note. Time corresponds to the first measurement made by the MAPS system and range is the offshore distance of the workboat (MAPS) from Duck pier. COAMPS-NAVSLaM times and locations are the closest possible time and location (within the temporal and spatial resolution of the numerical forecasts) to the start time and location of the MAPS data (see Section 2.2). COARE estimates are generated for each MAPS profile. COAMPS, Coupled Ocean Atmosphere Mesoscale Prediction System; COARE, Coupled Ocean Atmosphere Response Experiment; MAPS, Marine Atmospheric Profiling System; NAVSLaM, Naval Atmospheric Vertical Surface Layer Model.

[a]denoted a profile time in which all refractive estimates possess duct heights below the transmitter height.

resulting in 36 mean estimates of modified refractivity (M) vertical profiles of which, 27 showed evaporation ducts and are therefore used in this study.

Deployed from a small workboat, MAPS was composed of a radiosonde attached to a balloon tethered to and controlled by an electronic winch allowing for measurement profiles within the MASL ranging from ~0.5–50 m in altitude above the sea surface. Due to the small size of the workboat and implementation of MAPS, it is assumed that effects from the sampling equipment on the environment are minimal; further detail of the MAPS system can be found in Wang et al. (2018). Each MAPS data set includes pressure, relative humidity (RH), and temperature over approximately seven repeated ascents and descents of the system (~150–450 samples), where T is subsequently converted to potential temperature (θ) and RH is converted to specific humidity. Vertical profiles of p, θ, and q were generated by fitting a seventh order polynomial model to each respective MAPS data set as described in detail by Wang et al., (2018). M is then computed using (Bean & Dutton, 1968):

$$M = \frac{77.6}{T}\left[p + \frac{4810e}{T}\right] + \left(\frac{z}{a}\right) \times 10^6, \quad (1)$$

where, e is partial water vapor pressure (millibars) that is computed using q and T to estimate the saturation vapor pressure (Buck, 1981), p is the pressure profile in hPa, z is the height above the earth's surface, and a is the radius of the earth. Note that the surface values of q and T profiles were obtained by extrapolation to the surface, which determines surface refractivity, M_0 (Wang et al., 2018).

An overview of the resulting vertical refractivity profiles used for the analysis presented in this paper is located in Table 1. The resulting 27 vertical evaporative duct M-profiles contain modified refractivity estimated every 0.1 m from the surface up to 50 m.

2.2. COAMPS® Forecasts

COAMPS® (Hodur, 1997) is used to produce refractive environment forecasts for this study. COAMPS is two-way coupled with the Navy Coupled Ocean Model (NCOM) with a horizontal grid spacing of 2 km and 70 terrain following levels averaging ~32 m vertical grid spacing in the lowest 1 km of the atmosphere. COAMPS is initialized and fed with boundary conditions from the Navy Global Environmental Model (NAVGEM) for the atmosphere (Hogan et al., 2014) and the Global Hybrid Coordinate Ocean Model (HYCOM) for the ocean (Halliwell et al., 1998). COAMPS forecasts have been validated extensively for the CASPER-East campaign by Ulate et al. (2019) and previously over the eastern seaboard during the Wallops-2000 experiment (Haack et al., 2010). Forecasts were generated hourly using a 6-h update cycle throughout the duration of the CASPER-East campaign. COAMPS forecasts are merged with an atmospheric surface layer model to increase the resolution in the lowest 100 m (Karimian et al., 2013). Specifically, the Navy Atmospheric Vertical Surface Layer Model (NAVSLaM; Frederickson, 2016) is blended with COAMPS forecasts near the surface in order to resolve evaporation ducts. NAVSLaM is based-off MOST, and seeded with COAMPS forecasts of q, p, and U near the surface and NCOM forecasts of bulk SST; it simulates near-surface profiles of refractivity, temperature, winds, and humidity (Frederickson, 2016). Forecasts used in this study consist of (hourly) vertical profiles of modified refractivity along a transect from Duck Pier (North

1944799x, 2021, 56, Downloaded from https://agupubs.onlinelibrary.wiley.com. By Coastal Carolina University - on [28/09/2021]. Re-use and distribution is strictly not permitted, except for Open Access articles

Carolina; 36.18°N, 284.27°E) to 60 km offshore with ~2 km horizontal resolution. The COAMPS-NAVSLaM blended forecasts have decimeter vertical resolution in the lowest 100 m of altitude above the sea surface. COAMPS-NAVSLaM blended refractivity forecasts are used in this study for the same locations and times as the MAPS-based refractivity data (see Table 1), within the limits of the horizontal spatial resolution (2 km) and temporal resolution (hourly). In order to compare MAPS and COAMPS-NAVSLaM profiles on equal footing, the blended COAMPS T, q, and p profiles for the times and locations outlined in Table 1 are extrapolated from 0.5 m in altitude to the sea-surface, and modified refractivity is subsequently calculated using Equation 1.

2.3. COARE Algorithm

The Coupled Ocean Atmosphere Response Experiment algorithm (COARE; version 3.0) is a bulk parametrization algorithm used to estimate near-surface air properties based on MOST (Fairall et al., 1996, 2003; Garratt, 1994). For this study, COARE is used to estimate temperature, humidity, and wind profiles from bulk measurements collected during the CASPER-East field campaign (Wang et al., 2018). COARE requires the following parameters to estimate these profiles: sea-surface temperature (SST) and wind speed, specific humidity, and temperature at a reference height. These parameters are obtained from instruments located on two platforms: the R/V Sharp and the small workboat. Temperature and specific humidity at a height of 10 meters are extracted from the seventh order polynomial fits of measurements from the MAPS data set (Wang et al., 2018) in order to match the *in-situ* data. SST is required, and here to keep the comparisons on equal footing, we utilize the surface layer temperature (SLT; temperature at $z \sim 0$ m) from the MAPS profile extrapolation. Specific humidity at the surface is estimated assuming 98% relative humidity and using a saturation value based on the SLT (Buck, 1981). Wind speed was not measured by the MAPS system; thus, it is obtained from an anemometer located on the R/V Sharp bow mast at an altitude of 12 meters representing wind speed averaged over 30-min intervals. Wind speed averages are all within 15 min of the start of the MAPS measurements. The distance between the R/V Sharp and the location of any given MAPS-based data set is between 0.038 and 4.83 km with an average distance of 0.6 km; thus, the use of the mean wind speed data from the R/V Sharp seems reasonable.

Again, for the purposes of maintaining equivalency between the methods, the COARE generated humidity and temperature profiles are extrapolated to the surface from 0.5 m in altitude. These profiles in conjunction with the MAPS-based seventh order polynomial pressure profiles are used to calculate modified refractivity using Equation 1. A COARE-based M-profile is computed for each of the 27 MAPS-based M-profiles in Table 1.

2.4. Propagation Simulations

Propagation loss (PL) corresponding to the refractivity profiles outlined in Table 1 are estimated using the Variable Terrain Radio-wave Parabolic Equation (VTRPE) simulation (Ryan, 1991). VTRPE simulates radar wave propagation in a variety of environmental conditions. The full-wave solution of electromagnetic fields using a split-step rotated Green's function parabolic wave equation derived from Maxwell's equations is implemented in VTRPE (Ryan, 1991). VTRPE minimizes error within the solution of the PE via a relative error tolerance parameter that varies the step size of the simulation to meet this relative error tolerance, which was set to 10^{-6} in this study (Ryan, 1991; Sirkova, 2012). With such a low relative error tolerance, we assume all the variations/discrepancies observed between PL distributions are associated with the modified refractivity profiles (i.e., we assume negligible error build-up in the PE simulation). PL simulations are performed at 10.7 GHz (X-band frequency) transmitted at a height of 10.4 m with vertical polarization and a Gaussian antenna pattern containing two side-lobes. Dielectric boundary conditions are used in the model, where salinity and temperature are 35 ppt and 21°C, respectively. A smooth sea surface is employed as a bottom boundary condition to ensure differences in propagation between refractive estimation methods are primarily driven by refractivity. Refractivity profiles from Table 1 are simulated in VTRPE as vertical profiles that are homogenous in range. At the top of the simulation domain is an absorption layer to prevent reflections from the upper boundary into the usable portion of the domain. The resulting output simulation grid covers 60 km in range and 50 m in altitude with a resolution of 2 and 1 m, respectively.

1944799x, 2021, 56, Downloaded from https://agupubs.onlinelibrary.wiley.com. By Coastal Carolina University- on [28/09/2021]. Re-use and distribution is strictly not permitted, except for Open Access articles

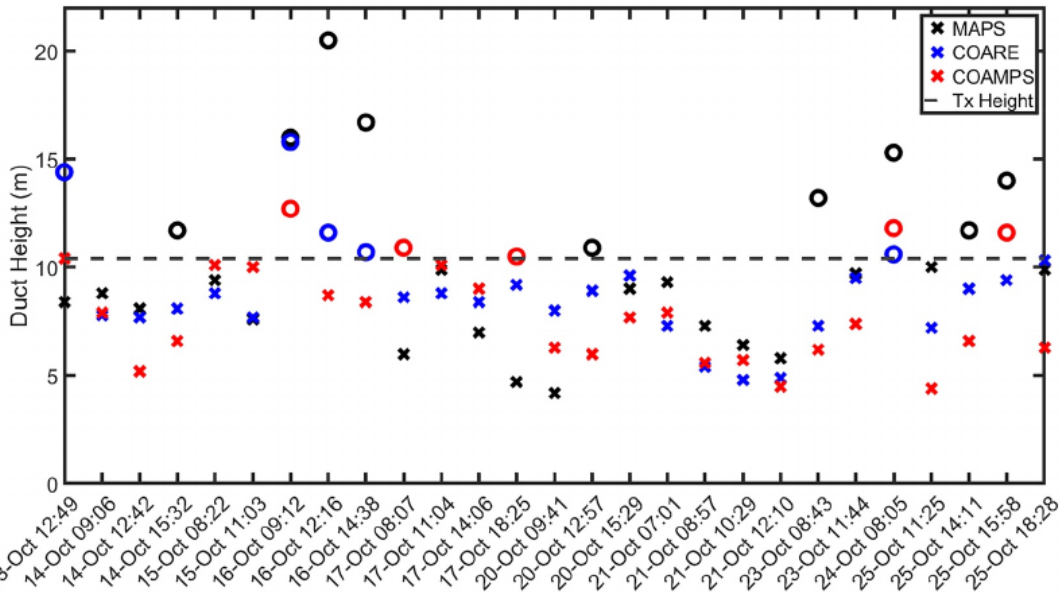


Figure 1. Time series of duct heights corresponding to Marine Atmospheric Profiling System (MAPS), Coupled Ocean Atmosphere Response Experiment (COARE), and Coupled Ocean Atmosphere Mesoscale Prediction System (COAMPS)-Naval Atmospheric Vertical Surface Layer Model (NAVSLaM) refractivity profile estimations (see legend for colors). Radar transmitter (Tx) height (10.4 m) is illustrated by the gray dashed line and duct heights are marked by O and × denoting duct heights above and below the transmitter, respectively.

3. Results and Discussion

This study focuses on comparing approximately co-located synchronous modified refractivity profiles estimated through multiple methods (MAPS, COARE, and COAMPS-NAVSLaM) and examining the impact of their differences on X-band propagation. Refractive profile parameters such as M-deficit, curvature or "shape" (analogous to the potential refractivity gradient; Paulus, 1990; Saeger et al., 2015), and evaporation duct height are used to compare profile estimation methods due to their leading order effects on propagation (Lentini & Hackett, 2015; Turton et al., 1988; Whalen, 1998; Yue & Yuanliang, 2006). Evaporation ducts are commonly described by the M-deficit (also known as evaporation duct strength; EDS) and the evaporation duct height; both parameters affect the surface refractivity gradients (Cherrett, 2015; Saeger et al., 2015; Zhang et al., 2011). To understand the effects of the environment on variations in these estimated refractive properties, M-deficit and EDH are examined with respect to thermal stability using the air-sea temperature difference (ASTD).

Although EDH and M-deficit commonly characterize refractivity profiles in evaporative ducting environments, there is dependence of propagation on the second derivative of the M-profile with altitude (Craig & Levy, 1991); thus, mean curvature ($<d^2M/dz^2>$) of the refractive profiles, where $<>$ denotes a mean over altitude within the trapping layer, is also used for refractivity profile characterization. The results include the following key components: (a) compare and discuss the propagation predictions generated by the estimated refractivity profiles, (b) characterize and compare the refractive profiles from MAPS, COAMPS-NAVSLaM, and COARE estimation methods using the properties discussed above, and (c) relate the observed environment to variations in the refractive parameter's PL predictions to aid in understanding how changes in the environment affect propagation predictions based on these methods of refractivity estimation.

3.1. Duct Height

The largest differences in PL are driven by variations in duct heights between the methods of refractivity estimation. The time series (in local time; ET) of duct height estimations for MAPS, COAMPS-NAVSLaM, and COARE are illustrated in Figure 1; EDH exceeding the transmitter height are represented by O and EDH below the transmitter are presented by ×. A similar subset of the MAPS evaporation duct heights from

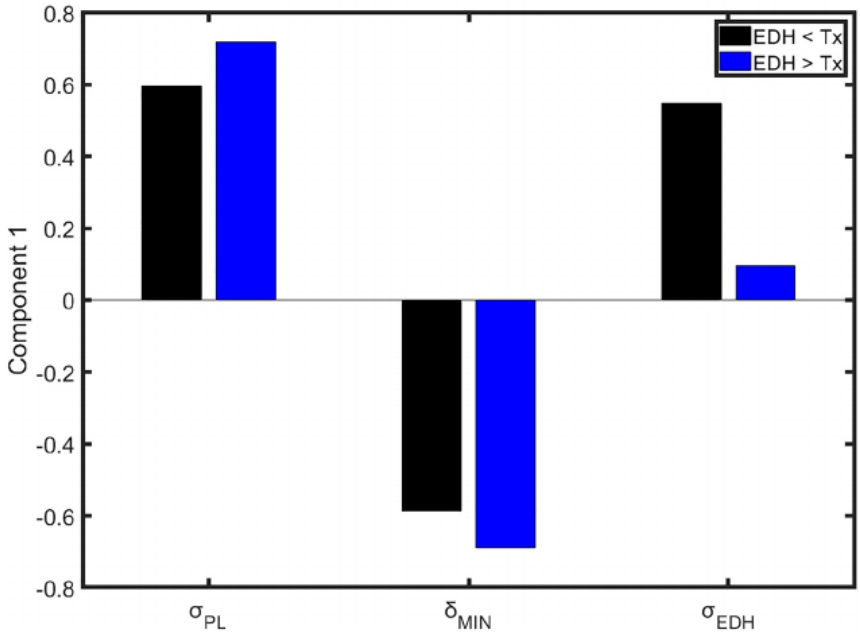


Figure 2. Principal component one loadings from a principal component analysis (PCA) for scenarios where all evaporation duct height (EDHs) within a profile set are less than the transmitter (Tx) height (black) and where at least one EDH from within a profile set is greater than the Tx height (blue) (see legend). Component 1 accounts for 71% of the PCA data set variance for scenarios where all EDHs are less than the Tx height and 59% of the variance for scenarios where at least one estimate of EDH is greater than the Tx height. Variables included in the PCA are standard deviations of mean propagation loss across the methods where propagation loss (PL) is averaged from 45 to 60 km in range and 2–20m in altitude (σ_{PL}), minimum duct height (δ_{MIN}) across the estimation methods, and standard deviation of EDHs across the estimation methods for each profile set (σ_{EDH}).

CASPER-East can also be found in Ulate et al. (2019). It should be noted that there are scenarios where all the duct height estimates are below the transmitter height and also scenarios where the duct height estimates span the transmitter height; there are only two times in which all duct heights are above the transmitter height. The sets of evaporation duct heights are compared in terms of propagation predictions. Differences in propagation related to the differences in EDH are examined with respect to effects of the environment on EDH estimation. This analysis enables discussion of how changes in the environment are reflected in PL predictions.

The relationships between variations (across the methods) in propagation loss and EDH are explored using the multivariate technique, principal component analysis (PCA), where PL is averaged over 45–60 km in range and over 2–20 m in altitude (number of PL points included in the average [N_p] is 5.4×10^6). The PL is averaged over this area because variations in PL due to duct height frequently occur at long range and within a region encapsulating the duct height (Lentini & Hackett, 2015); 2–20 m includes all duct heights in this study, which range 4–18 m. Furthermore, PL along a single height transect can be misleading as PL variations at a single altitude may miss a region of significant discrepancy (or cause overinterpretation of an isolated localized discrepancy); thus, averaging the PL enables a more comprehensive area to be evaluated including regions influenced by duct trapping and leakage. The multivariate statistical technique used here, PCA, reduces dimensionality of a problem by introducing new variables that are orthonormal to each other referred to as components. By examining how the original variables combine to create the new variables (components)–referred to as loadings (e.g., shown as bars in Figure 2), one can gain insight into the relationships between the original variables. The components describe variations in the entire data set optimally, where the first component captures the majority of the data set variance so that the data can be largely explained by only one component. By examining what parameters (original variables) contribute to the same component, linear relationships between parameters are revealed. The data set used for the PCA includes: the standard deviations in average PL between the estimation methods (σ_{PL}), standard deviations in duct height between the estimation methods (σ_{EDH}), and the minimum duct height across the estimation

1944799x, 2021, 56, Downloaded from https://agupubs.onlinelibrary.wiley.com. By Coastal Carolina University- on [28/09/2021]. Re-use and distribution is strictly not permitted, except for Open Access articles

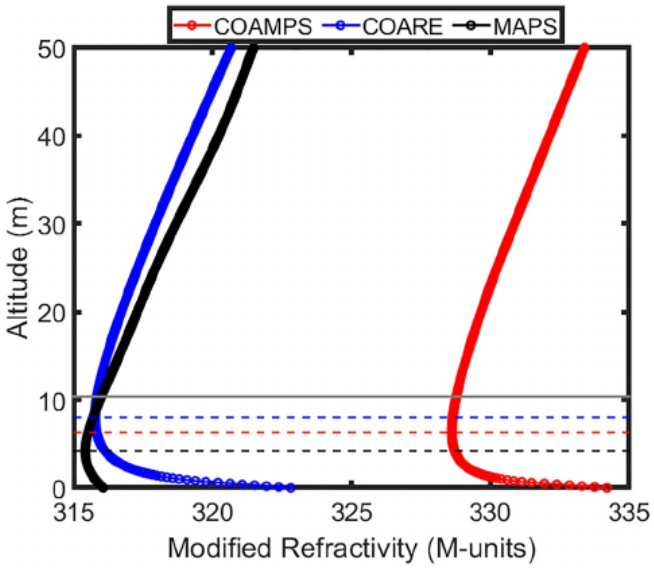


Figure 3. Marine Atmospheric Profiling System (MAPS), Coupled Ocean Atmosphere Response Experiment (COARE), and Coupled Ocean Atmosphere Mesoscale Prediction System (COAMPS)-Naval Atmospheric Vertical Surface Layer Model (NAVSLaM) modified refractivity profiles for profile set 14, on October 20 at 09:41 local time (see legend). M-deficits in the figure are 5.59, 7.05, and 0.64 M-units for COAMPS-NAVSLaM, COARE, and MAPS, respectively. Evaporation duct heights are denoted with the corresponding horizontal dashed lines, and the transmitter height is marked by the gray line.

methods (δ_{MIN}) for times where: (a) EDH estimates are all below the transmitter height (10.4 m), and (b) EDH estimates span the transmitter height. Because there are only two datasets where all duct height estimates are above the transmitter, this scenario is not independently considered in this study. PL variance (across methods) is used rather than PL itself because the goal of this analysis is to link variations in refractivity profile parameters (e.g., EDH estimates) to variations (across methods) in PL. The results of the PCA are shown in Figure 2. Component one accounts for 71% and 59% of the variance in the PCA data set for times when EDH heights are below and span the transmitter, respectively. Component one loadings are only shown due to the majority of (PCA data set) variance being associated with component one. As expected, deviations in EDH vary directly with deviations in PL (Figure 2). Minimum duct height varies inversely with deviations in PL and EDH. This result suggests that as the duct height decreases the methods tend to have more discrepancies between them, both in terms of EDH and PL. This result is valid for duct heights of both scenarios but the relationship between PL and EDH standard deviations is much stronger when all duct heights are below the Tx, suggesting that when all EDH estimates are below the Tx, discrepancies in PL directly and strongly correlate to discrepancies in EDH estimation. The relationship between minimum duct height and duct height standard deviation is weaker when the duct heights span the Tx height. When EDH estimates span the transmitter height, the height of the minimum EDH is shown to be significantly more related to deviations in PL than deviations in EDH. This result suggests that small differences in duct height that span the transmitter height can generate large differences in PL. Not surprisingly, this means PL predictions are more sensitive to EDH discrepancies when duct height estimates are near the transmitter height. The reduced correlation between standard deviations of duct height and PL when the EDHs span the transmitter is therefore due to both small and large discrepancies in duct heights influencing PL variations. Furthermore, in these scenarios, as the minimum duct height increases, the propagation regimes are likely to be more similar, which yields the strong (inverse) correlation between minimum duct height and PL variations.

An example of these trends can be seen from the duct heights and refractive estimates on October 20, 09:41 ET (profile set 14), illustrated in Figure 3. This example shows duct height estimates that all occur below the transmitter, have a relatively high EDH standard deviation (2.15 m), and have the lowest minimum duct height observed over the study. PL predictions for this profile set can be seen in Figure 4. The duct heights in these profiles are 4.2, 6.4, and 8.5 m for MAPS, COAMPS-NAVSLaM, and COARE, respectively. Figure 4a shows a steeper slope in PL at long range at 9 m altitude as duct height decreases. The lower the duct height below the transmitter the more the propagation behaves like a normal atmosphere in the region over which the average is taken–refracting away from the surface and increasing PL at long range. Figure 4 demonstrates that large differences (>20 dB) in PL are possible due to deviations in EDH estimates when EDH estimates are all below the transmitter.

The location of the largest differences between PL predictions are observed at long ranges (~45–60 km). Discrepancies in long range propagation between MAPS and the other propagation predictions for October 20, 09:41 are likely due to the relatively low MAPS EDH. Cherrett (2015) showed similar PL (>200 dB) from refractive profiles with EDHs less than 5 m at X-band frequencies, transmitting at a height of 20 m with a receiver height of 15 m. These results suggest that duct height can significantly influence the differences between propagation predictions particularly if one EDH is low enough to drastically reduce leakage into the duct. Consistent with this trend, the second lowest duct height from COAMPS-NAVSLaM is associated with higher PL at long range than COARE PL, which has the highest duct height. Presumably similar signal leakage into the duct exists for these two methods due to the more similar duct heights, but, the duct height closer to the transmitter (COARE) shows some evidence of trapping. This discussion supports the

1944799x, 2021, 56, Downloaded from https://agupubs.onlinelibrary.wiley.com. By Coastal Carolina University- on [28/09/2021]. Re-use and distribution is strictly not permitted, except for Open Access articles

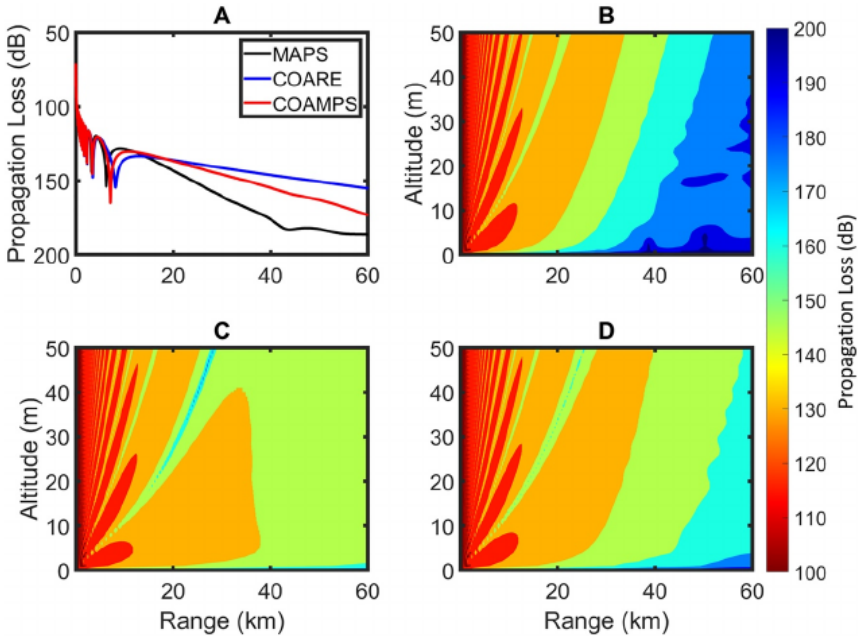


Figure 4. Propagation loss predictions for refractivity profiles shown in Figure 3. Propagation loss is shown in dB at a (a) receiver height of 9 m, and for the entire prediction domain for (b) Marine Atmospheric Profiling System (MAPS), (c) Coupled Ocean Atmosphere Response Experiment (COARE), and (d) Coupled Ocean Atmosphere Mesoscale Prediction System (COAMPS)-Naval Atmospheric Vertical Surface Layer Model (NAVSLaM). Colorbar shows propagation loss (PL) in dB for (b–d).

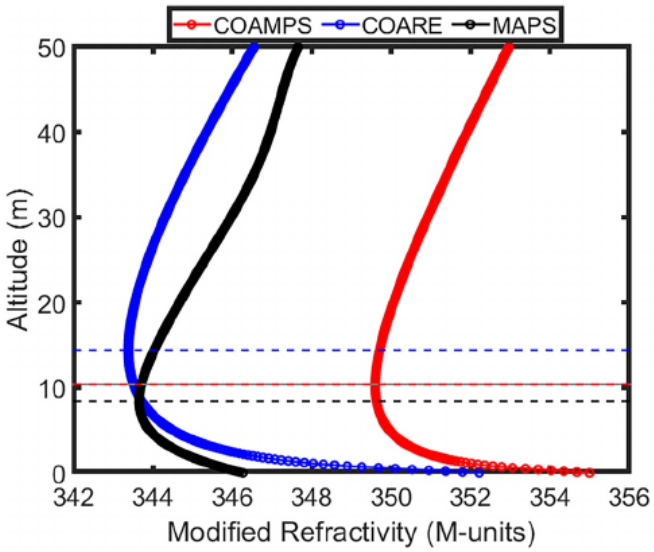


Figure 5. Marine Atmospheric Profiling System (MAPS), Coupled Ocean Atmosphere Response Experiment (COARE), and Coupled Ocean Atmosphere Mesoscale Prediction System (COAMPS)-Naval Atmospheric Vertical Surface Layer Model (NAVSLaM) modified refractivity profiles for profile set 1, October 13 at 12:49 local time. M-deficits in the figure are 5.40, 8.84, and 2.62 M-units for COAMPS-NAVSLaM, COARE, and MAPS, respectively. Evaporation duct heights are denoted with the corresponding horizontal dashed lines and the transmitter height is marked by the gray line.

results shown in Figure 2 that PL standard deviations (or discrepancies) are influenced by both the minimum EDH across methods and variations in EDH estimates. PL differences associated with discrepancies in the shapes of the profiles are discussed in the next subsection.

Significant differences in PL also occur when EDH estimates differ such that some are above and below the transmitter height. An example of this scenario is observed in Figure 5 occurring on October 13, 12:49 ET (profile set 1). Duct heights for MAPS, COARE, and COAMPS-NAVSLaM are 8.4, 14.5, and 10.4 m, respectively, and Tx is at 10.4 m. Propagation loss for the refractive profiles are illustrated in Figure 6. PL variations between methods are mainly due to the COARE EDH location being above the transmitter, while the others are at or below the transmitter. COAMPS-NAVSLaM does not show significant trapping but shows enhanced signal carry within the duct presumably due to EM signal leakage into the duct from the EDH's close proximity to the Tx height. MAPS PL shows much less trapping relative to the modeled data due to the EDH falling below the transmitter height resulting in propagation more similar to a normal atmosphere, including multipath null positioning. Specifically, the different duct heights cause different interactions with the lowest altitude null (above the surface) depending on whether the duct height is above or below the transmitter (Skolnik, 1990). COAMPS-NAVSLaM's and MAPS' (EDHs at or below the transmitter) lowest null is only slightly deflected downward (toward lower altitudes; Figures 6b and 6d), whereas PL prediction for the COARE profile (Figure 6c) shows this null significantly deflected downward and washed out–it is no longer present at 9 m altitude (Figure 6a). Observations from Figures 5 and 6 exemplify the results shown in Figure 2, that differences in propagation loss generated

1944799x, 2021, 56, Downloaded from https://agupubs.onlinelibrary.wiley.com. By Coastal Carolina University- on [28/09/2021]. Re-use and distribution is strictly not permitted, except for Open Access articles

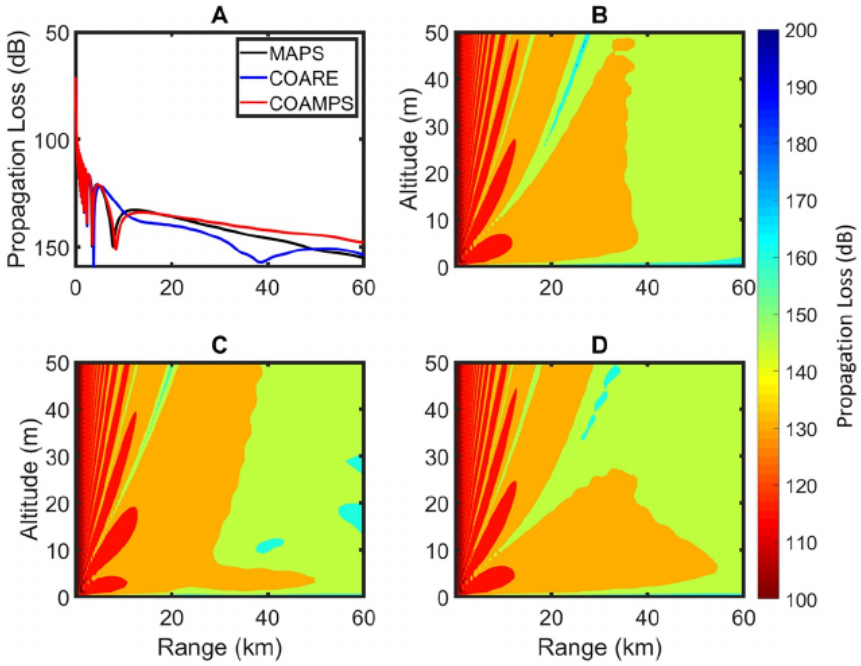


Figure 6. Propagation predictions from refractivity profiles shown in Figure 5, with a transmitter height of 10.4 m. Propagation loss is shown in dB (colorbar) for all refractive estimation methods at a (a) receiver height of 9 m, and for the entire prediction domain for (b) Marine Atmospheric Profiling System (MAPS; evaporation duct height [EDH] of 8.4 m), (c) Coupled Ocean Atmosphere Response Experiment (COARE; EDH of 14.5 m), and (d) Coupled Ocean Atmosphere Mesoscale Prediction System (COAMPS)-Naval Atmospheric Vertical Surface Layer Model (NAVSLaM; EDH of 10.2 m). Colorbar shows propagation loss in dB for (b–d).

from profile sets with at least one EDH estimated above the transmitter are more influenced by the minimum duct height than the standard deviation of EDH between the methods. In this case, the duct height standard deviation is relatively large (3.1 m), and the minimum duct height is relatively high (8.4 m); here, Figure 6, the PL comparisons are more similar to each other even though the duct height standard deviation is higher than the prior case shown (Figure 4) demonstrating that the high minimum duct height is more influential on the PL variations than the duct height standard deviation. When duct heights span the transmitter, one duct height may invoke very different physics than another estimate because one may be influenced more by leakage into the duct while another by trapping inside the duct regardless of how close the duct heights are to each other. Thus, a small or large standard deviation between the duct height estimates can result in large propagation differences, which weakens the correlation between standard deviation of duct height and standard deviation of PL.

Differences in EDH estimates are often largest during times when R/V Sharp ASTD estimations suggest stable conditions, and sometimes when they suggest relatively large thermodynamic instabilities; these conditions can be seen in Figure 7. Increases in EDH variation at times of thermodynamic stability is expected due to the documented limitations of MOST in stable environments, which is used in the COAMPS-NAVSLaM and COARE models. NAVSLaM surface layer predictions, which are blended with COAMPS, have been shown to sometimes construct inaccurate meteorological profiles in stable thermodynamic regimes (Babin et al., 1997; Karimian et al., 2013). Karimian et al. (2013) shows that during times of increased stability, duct height estimates diverge significantly for varying humidity at constant wind speeds resulting in large uncertainty during periods of stability. Similar limitations are found in the COARE algorithm, which uses empirical stability functions generated for highly unstable conditions (Fairall et al., 1996) and for stable conditions (Beljaars & Holtslag, 1991). The main limitation of the MAPS profile is the use of the seventh order model fit to the measured data (Wang et al., 2018), and the extrapolation of variables T and q to represent surface temperature and surface specific humidity (q_0). The fit profile does not capture all of the variability in the measured data, likely due to essentially time averaging the data, impacting the meteorological profiles generated. Furthermore, the seventh order polynomial fit is not guaranteed to work outside the range of the

1944799x, 2021, 56, Downloaded from https://agupubs.onlinelibrary.wiley.com. By Coastal Carolina University- on [28/09/2021]. Re-use and distribution is strictly not permitted, except for Open Access articles

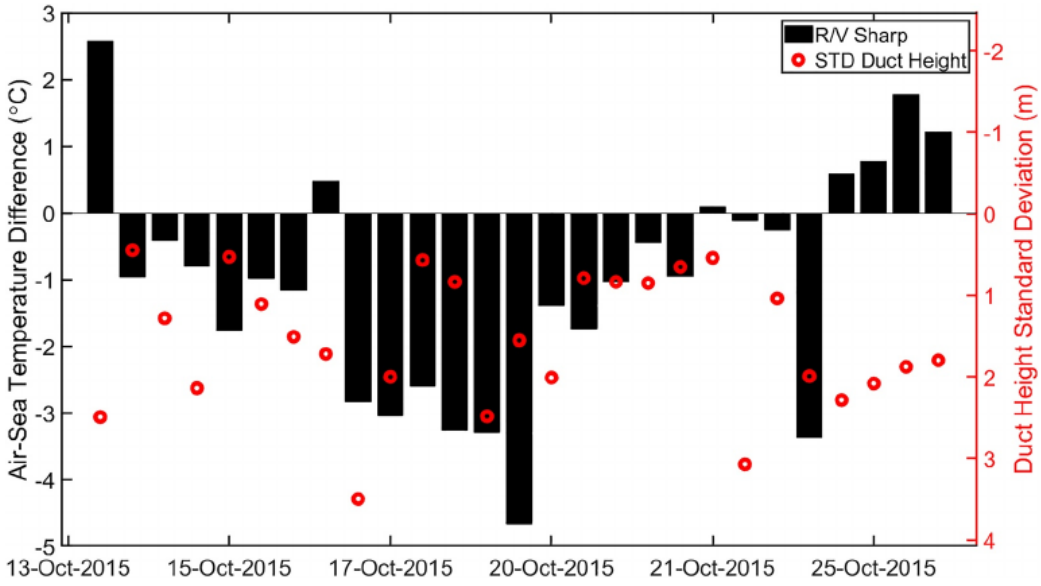


Figure 7. The air-sea temperature difference from the R/V Sharp (black) and standard deviation of the duct heights between Marine Atmospheric Profiling System (MAPS), Coupled Ocean Atmosphere Response Experiment (COARE), and Coupled Ocean Atmosphere Mesoscale Prediction System (COAMPS)-Naval Atmospheric Vertical Surface Layer Model (NAVSLaM) for each profile set, which is indicated by the red circles and the right-hand axis.

data, including the surface; thus, estimates of surface refractivity from extrapolation are very different from those obtained by use of bulk or skin SST and q_0 obtained assuming 98% humidity, as is typical for water surfaces. The limitations described above likely lead to the differences in duct height estimates (Figure 1) suggesting that during periods of surface layer stability, EDH and, therefore, propagation predictions may vary most significantly between the methods.

3.2. Profile Shape and Duct Strength

Differences in propagation loss are not only driven by duct height but by the refractivity profile shape, which is reflected in changes to M-deficit and mean curvature of the M-profile. M-deficit is the difference in the surface refractivity and the refractivity at the EDH, where changes in M-deficit can shift the location of multipath nulls in propagation, presumably through ED trapping (Turton et al., 1988; Anderson, 1995; Cherett, 2015). Mean curvature $(<d^2M/dz^2>)$ is used to represent the shape of the refractive profile from 0.5 m to the EDH; EDH shape has been shown to affect long range propagation in a similar manner, including shifting multipath null locations (Lentini & Hackett, 2015; Saeger et al., 2015). Time series of M-deficit and mean curvature are shown in Figure 8 for MAPS, COARE, and COAMPS-NAVSLaM. M-deficits of the COARE and COAMPS-NAVSLaM profiles vary similarly with an increase from October 13 to 17 and a decrease from October 20 to 25 (Figures 8a and 8b). Average M-deficits over the study are 6.77 and 6.73 M-units for COARE and COAMPS-NAVSLaM, respectively. This commonality is not too surprising given that both COARE and NAVSLaM rely on Monin-Obukhov boundary layer similarity theory. MAPS M-deficits are smaller in magnitude and show no discernable pattern over time, fluctuating between 0.4 and 6.24 M-units with an average of 2.87 M-units. Mean curvature of the refractive profiles exhibit a similar trend in time as the M-deficits (Figure 8b). Average mean curvature over the time series are 4.6×10^{-3} and 5.9×10^{-3} M-units/m^2 for COARE and COAMPS-NAVSLaM, respectively. Like the M-deficits, the MAPS mean curvatures are smaller than the COARE and COAMPS curvatures with an average mean curvature of 8.3×10^{-4} M-units/m^2. A direct linear relationship between M-deficit and curvature is present within the MAPS (linear correlation coefficient, $R = 0.73$, p-value $<<0.05$) and COAMPS data ($R = 0.52$, $p<<0.05$) suggesting an increase in M-deficit leads to an increase in curvature of the profile. A statistically significant relationship could not be determined for the COARE data.

1944799x, 2021, 56, Downloaded from https://agupubs.onlinelibrary.wiley.com. By Coastal Carolina University - on [28/09/2021]. Re-use and distribution is strictly not permitted, except for Open Access articles

1944799x, 2021, 56, Downloaded from https://agupubs.onlinelibrary.wiley.com. By Coastal Carolina University - on [28/09/2021]. Re-use and distribution is strictly not permitted, except for Open Access articles

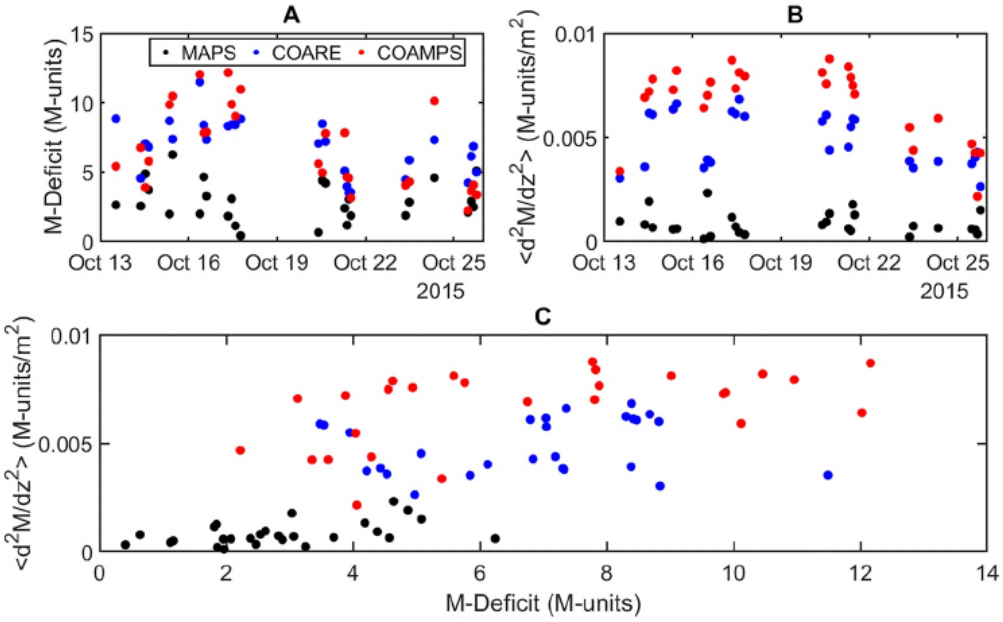


Figure 8. Time series of the (a) M-deficit and (b) mean curvature calculated from refractivity profile estimations generated from Marine Atmospheric Profiling System (MAPS), Coupled Ocean Atmosphere Response Experiment (COARE), and Coupled Ocean Atmosphere Mesoscale Prediction System (COAMPS®; see legend); (c) M-deficit shown in (a) versus mean curvature ($<d^2M/dz^2>$) shown in (b). Linear relationships between M-deficit and curvature observed in (c) correspond to correlation coefficients of 0.75 and 0.52 for MAPS and COAMPS-NAVSLaM, respectively (no statistically significant relationship is observed for COARE.).

To understand how the shape of the refractive profiles affects PL, PCA is used to explore the relationships between variations in M-deficit, mean curvature, EDH, and PL between the methods. PL is averaged over 45–60 km in range and over 2–30 m in altitude (N_p =8.4 × 10⁶) based on the region of largest PL variations due to changes in the M-deficit from propagation simulations. Similar to Section 3.1, PCA is performed for scenarios where at least one EDH > Tx and where all EDH < Tx; results for each case are shown in Figures 9a and 9b, respectively. Two PCAs are performed: (a) using standard deviations of PL (σ_{PL}), EDH (σ_{EDH}), and M-deficit (σ_{MD}; blue), and (b) using σ_{PL}, σ_{EDH}, and standard deviation of mean curvature (σ_{CV}; red). Separate PCA results for curvature and M-deficit are presented for each EDH scenario to ensure variations in refractive parameters' loading on the components are not attributed to the strong relationships between M-deficit and curvature previously demonstrated in Figure 8c. EDH variation, a primary driver of PL variation (Section 3.1), is included to provide insight into the relative importance variations in M-deficit and mean curvature have on variations in PL relative to variation in EDH between the methods.

Figure 9a illustrates how variations in refractive parameters influence variations in PL when EDH spans the transmitter. In the M-deficit PCA (Figure 9a-blue), loadings of σ_{MD} and σ_{PL} are primarily on component one (52.5% of the PCA data set variability) indicating a direct relationship between variations in M-deficit and PL. The same relationship is observed for variations in mean curvature and PL (Figure 9A-red) where component one accounts for 52.2% of variability in the PCA data set. These similar loadings of mean curvature and M-deficit variations relative to variations in PL are expected due to the direct relationships between M-deficit and mean curvature previously described. The common PCA loadings between σ_{MD}, σ_{CV}, and σ_{PL} suggest that as M-deficit and curvature between the methods become more similar so do PL predictions. Variations in EDH load mainly on component two for both PCAs, accounting for ~33% of variability in each PCA data set. These results suggest that variations in M-deficit and mean curvature are most tightly coupled to variations in PL when EDHs span the transmitter (because they primarily load on component one), accounting for the majority of variability in the (PCA) data set. Thus, although EDH is important to propagation, when EDHs span the transmitter, the shape of the profile dominates the variations observed in PL between MAPS, COARE, and COAMPS-NAVSLaM relative to the variations in EDH. This result is also consistent with the low loading of σ_{EDH} on component one (relative to σ_{PL}) in the previous PCA from

1944799x, 2021, 56, Downloaded from https://agupubs.onlinelibrary.wiley.com. By Coastal Carolina University - on [28/09/2021]. Re-use and distribution is strictly not permitted, except for Open Access articles

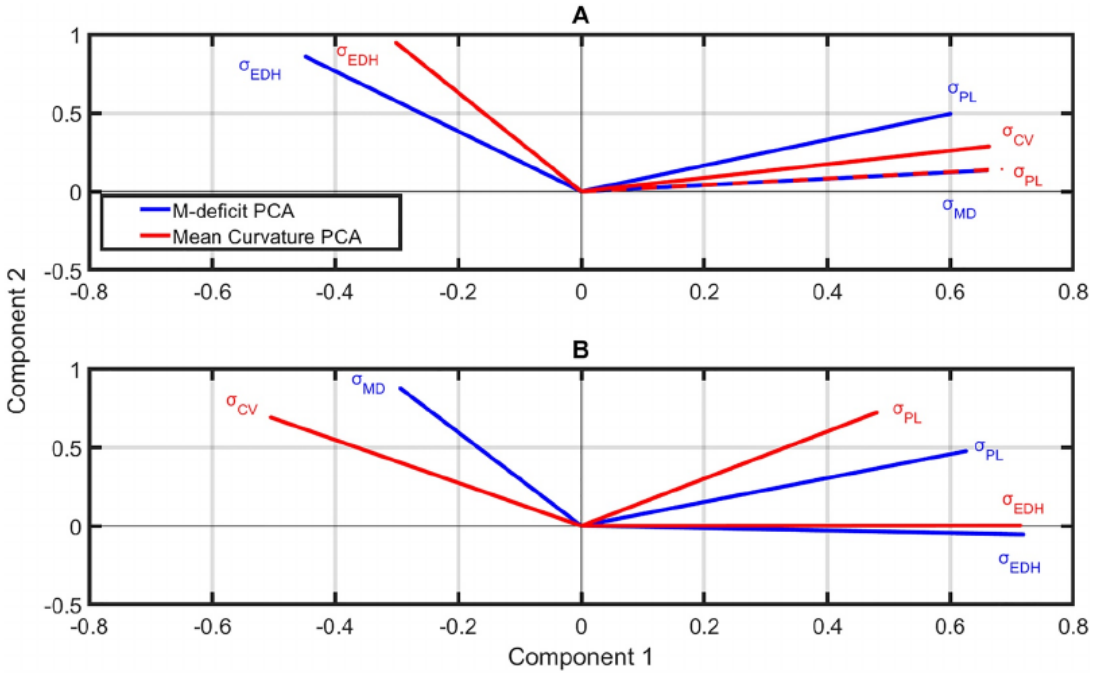


Figure 9. Principal component one and two loadings from a principal component analysis (PCA) on standard deviations of Marine Atmospheric Profiling System (MAPS), Coupled Ocean Atmosphere Mesoscale Prediction System (COAMPS)-Naval Atmospheric Vertical Surface Layer Model (NAVSLaM), and Coupled Ocean Atmosphere Response Experiment (COARE) refractivity parameters and propagation loss (PL) for scenarios where (a) at least one of the evaporation duct height (EDH) from within a profile set is greater than the transmitter height and (b) where all EDHs within a profile set are less than the transmitter height. Component one in (a) accounts for 52% and 52% of the data set variance for standard deviation of M-deficit (σ_{MD}) and mean curvature (σ_{CV}) PCAs, respectively. Component one in (b) accounts for 58% and 52% of the data set variance for σ_{MD} and mean curvature (σ_{CV}) PCAs, respectively. Component two in both (a) and (b) (for both PCAs) accounts for ~33% of the data set variance. Variables included are: standard deviation of PL between MAPS, COARE, and COAMPS-NAVSLaM (σ_{PL}), where propagation loss is averaged over 45–60 km in range and 2–30 m in altitude, standard deviation of evaporation duct height (σ_{EDH}), and either σ_{MD} or σ_{CV} for each method of refractivity estimation.

Section 3.1. The relationship between σ_{PL} and σ_{MD} or σ_{CV} is expected due to their connection to the M-gradient below the duct height. Both curvature and M-deficit are simplified parameters ultimately describing the M-gradient (or how it varies with altitude), which is a primary physical driver of propagation patterns, most notably when trapping occurs. Increases in the magnitude of the M-gradient below the duct increases the refraction angle at which EM waves are bent toward the surface of the earth, which can increase coverage of EM signal within a duct. Thus, variations in M-deficit and mean curvature between the methods suggest differing low altitude M-gradients cause different refraction of EM waves ultimately resulting in differences in propagation between the methods.

Figure 9b illustrates similar PCAs to Figure 9a except it shows results for times where EDHs are all below the transmitter. These PCAs illustrate that variations in EDH load primarily on component one accounting for 58.6% and 52.9% of the variability for M-deficit and mean curvature PCAs, respectively. The loading of σ_{EDH} and σ_{PL} on component one indicates a direct relationship between the two parameters consistent with results in Figure 2. In this case, variations in EDH are primarily related to variations in PL due to EDH influence on the magnitude of signal leakage into the duct; divergence of EDH from the transmitter toward the Earth's surface restricts leakage into the duct creating PL patterns more similar to a normal atmosphere. Although σ_{EDH} loads primarily on component one, there are also differences in the loading of σ_{PL} between the two scenarios for the duct curvature PCA (Figure 9a vs. 9b, red), where σ_{PL} loads more evenly onto the two components when all the EDHs are below the duct height. This result suggests that variations in mean curvature are also significantly related to variations in PL because they both load heavily onto the same component (two). The direct relationship between σ_{MD} or σ_{CV} and σ_{PL} on component two accounts for ~33% of variability in the data for both PCAs. This direct relationship suggests that, although increased

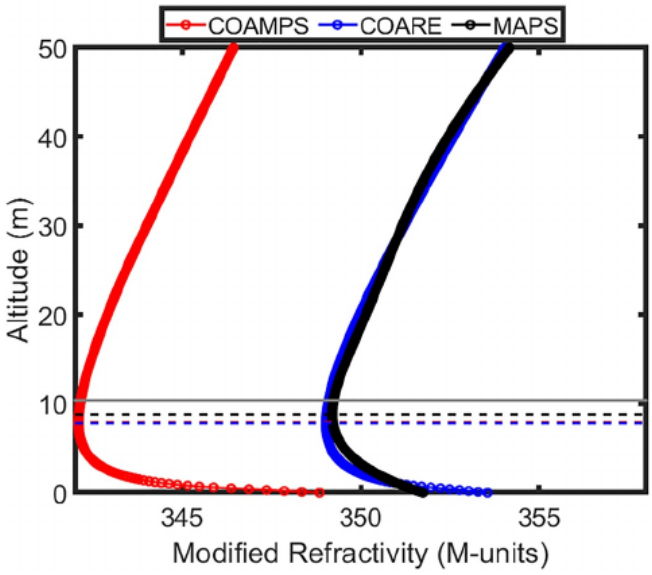


Figure 10. Marine Atmospheric Profiling System (MAPS), Coupled Ocean Atmosphere Response Experiment (COARE), and Coupled Ocean Atmosphere Mesoscale Prediction System (COAMPS)-Naval Atmospheric Vertical Surface Layer Model (NAVSLaM) modified refractivity profiles for profile set 2, October 14 at 09:06 local time. The COAMPS-NAVSLaM profile has an M-deficit of 6.74 M-units and a mean curvature of 0.007 M-units/m^2. The COARE profile has an M-deficit of 4.53 M-units, and a mean curvature of 0.004 M-units/m^2. The MAPS profile has an M-deficit of 2.54 M-units and a mean curvature of 8.04×10^{-4} M-units/m^2. Evaporation duct heights are denoted with the corresponding horizontal dashed lines and the transmitter height is marked by the gray line.

variability in EDH is the primary cause of PL differences between the methods, an increase in variability of the profile shape can also increase variability in PL (i.e., it is a secondary effect). As previously discussed, variability in PL due to profile shape can be attributed to the relationship between M-deficit, mean curvature, and M-gradient, where increases in M-deficit and mean curvature likely increase EM signal leakage into the duct, leading to the direct relationship on component two (Figure 9b). In summary, when duct heights are all below the Tx height, both the variation in EDH as well as M-deficit and/or curvature influence variations in PL with EDH variation exhibiting a stronger relationship.

It is also noteworthy that the relative influence of curvature on PL is slightly greater than that of M-deficit. σ_{PL} loads evenly on both components in both scenarios for the M-deficit PCA (blue) whereas in the curvature PCA (red) σ_{PL} loads onto component one strongly in the case where the EDHs span the transmitter height but in the other case it loads more evenly on both components. This higher loading of σ_{PL} on component one for the case where the EDHs' span the transmitter (Figure 9a) implies that curvature variations are more closely coupled to PL variations in these cases than are variations in M-deficit. The shift of the loading of σ_{PL} onto component two in the case where all the EDHs are below the duct height (Figure 9b) implies that curvature plays a larger secondary role in PL variations compared to M-deficit. Consequently, albeit slight, both cases suggest that curvature variations are more closely linked to variations in PL than variations in M-deficit.

Figure 10 illustrates an example profile set of refractivity estimates for MAPS, COARE, and COAMPS-NAVSLaM where all EDHs are similar (profile set 2); the associated propagation predictions are illustrated in Figure 11. The MAPS profile in Figure 10 has an EDH of 8.8, an M-deficit of 2.54 M-units, and a mean curvature of 8.04×10^{-4} M-units/m^2. The COAMPS-NAVSLaM profile has an EDH of 7.9 m, an M-deficit of 6.74 M-units, and a mean curvature of 0.007 M-units/m^2. The COARE profile has an EDH of 7.8 m, an M-deficit of 4.53 M-units, and a mean curvature of 0.004 M-units/m^2. As expected, MAPS propagation (Figure 12b) reveals less PL at long range relative to the other propagation predictions (see $r \sim$ 50–60 km and $z <$ 5 m). This result is likely due to increased leakage of the EM signal into the duct for MAPS, which has an EDH located closest to the Tx for this profile set. Similar EDHs (~0.1 m difference) are observed between COARE and COAMPS-NAVSLaM, which are therefore expected to produce very similar PL predictions, but some discrepancies can be observed in PL between the two methods. This result is likely due to the relatively large difference in M-deficit and mean curvature between COARE and COAMPS-NAVSLaM (COAMPS curvature/M-deficit ~1.5 times greater than COARE curvature/M-deficit). Comparison of refractivity profiles with similar EDHs highlights the differences in PL for variations in M-deficit and curvature. The profile exhibiting larger M-deficit should be associated with lower PL in long range due to increased duct strength. Mean curvature is also expected to introduce similar effects on propagation. This result can be seen between COARE (Figures 11c) and COAMPS-NAVSLaM (Figures 11d) PL, where the variation in PL (~10 dB) between the propagation predictions occurs beyond 40 km in range and beneath ~8 m in altitude. These results exemplify PCA results (Figure 9) previously discussed for EDH < Tx, where larger variations in propagation are observed for differences in duct heights and for similar EDHs discrepancies can be explained by differences in M-deficit and mean curvature. These results further demonstrate that evaporation duct shape influences low altitude long range propagation significantly.

The differences observed in refractive profiles that result in propagation loss discrepancies are examined to shed light on environmental factors that might cause such discrepancies. Thermodynamic regime changes influence temperature and humidity profiles that change modified refractivity, thus observations of air-sea

1944799x, 2021, 56, Downloaded from https://agupubs.onlinelibrary.wiley.com. By Coastal Carolina University- on [28/09/2021]. Re-use and distribution is strictly not permitted, except for Open Access articles

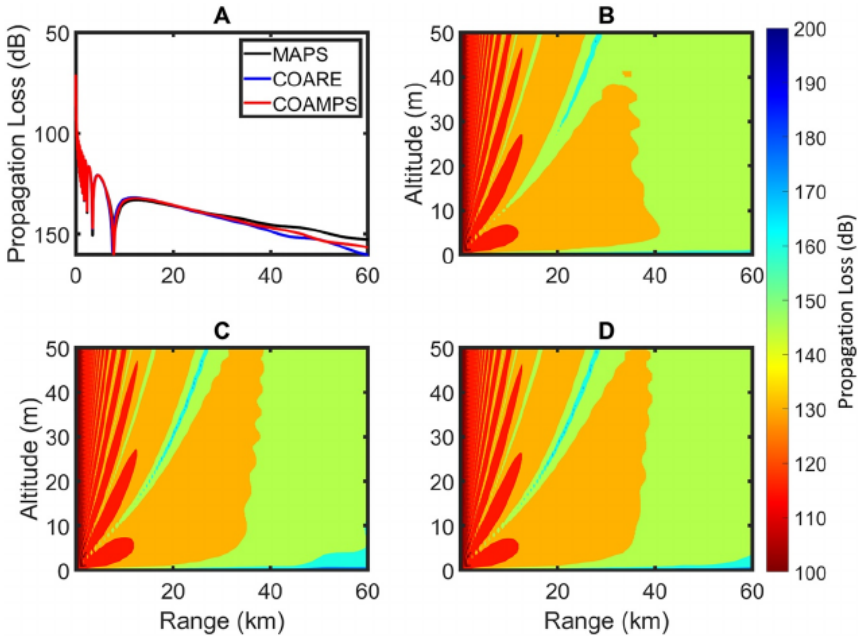


Figure 11. Propagation predictions for refractivity profiles shown in Figure 10. Propagation loss is shown for: (a) receiver height of 9m, and for the entire prediction domain for (b) Marine Atmospheric Profiling System (MAPS), (c) Coupled Ocean Atmosphere Response Experiment (COARE), and (d) Coupled Ocean Atmosphere Mesoscale Prediction System (COAMPS)-Naval Atmospheric Vertical Surface Layer Model (NAVSLaM). Colorbar denotes propagation loss (PL) in dB for (b–d).

temperature difference and mixing ratio are included in the following discussion. Figure 12 shows σ_{MD} (Figure 12a) and σ_{CV} (Figure 12b) and how these statistics vary with air-sea temperature difference and mixing ratio (colorbar) at 12 m based on measurements from the R/V Sharp.

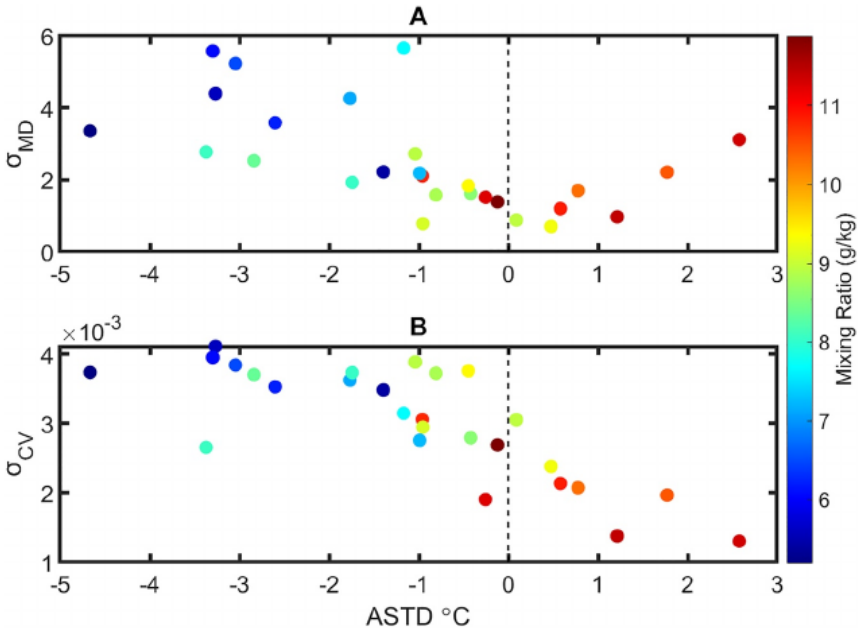


Figure 12. Air-sea temperature differences (ASTD) from the R/V Sharp plotted against (a) standard deviation of M-deficit (σ_{MD}) and (b) standard deviation of mean curvature (σ_{CV}) between the profile estimation methods. Mixing ratio at 12 m represented by colors (see colorbar) and thermodynamic neutrality (ASTD = 0°) is denoted by the vertical dashed line.

1944799x, 2021, 56, Downloaded from https://agupubs.onlinelibrary.wiley.com. By Coastal Carolina University- on [28/09/2021]. Re-use and distribution is strictly not permitted, except for Open Access articles

1944799x, 2021, 56, Downloaded from https://agupubs.onlinelibrary.wiley.com. By Coastal Carolina University - on [28/09/2021]. Re-use and distribution is strictly not permitted, except for Open Access articles

Thermodynamic conditions during the CAPSER-East study range from unstable to stable where most environmental observations from the R/V Sharp reveal unstable thermodynamic conditions, and these unstable conditions typically coincided with lower mixing ratios. Variations in M-deficit are shown to be inversely related to ASTD ($R = -0.56$, $p<<0.05$) and mixing ratio ($R = -0.62$, $p<<0.05$) at 12 m (Figure 12a), as ASTD approaches neutral conditions, variations in M-deficit between the estimation methods become smaller. This result suggests that as the surface layer (between 0 and 12 m) becomes more neutral and humid the M-deficits between the methods become more similar. A similar inverse relationship is observed between σ_{CV} and ASTD ($R = -0.79$, $p<<0.05$) or mixing ratio ($R = -0.75$, $p<<0.05$; Figure 12b). The stronger relationship between σ_{CV} and ASTD is presumably due to a consistent relationship between these variables across all stabilities (ASTD ≤ 0 and ASTD > 0) in comparison to σ_{MD}, where the nature of the relationship (direct or inverse) changes depending on stability, as shown in Figure 12. Results suggest as environmental conditions become more humid and approach neutral conditions, σ_{MD} and σ_{CV} decrease, thus profile shapes between the refractive estimation methods become more similar.

Differences in the M-deficit and curvature are likely driven by the different surface characterization by each estimation method where variations in surface characterization can be attributed to the estimated humidity and temperature at the surface. Despite aligning the surface conditions to be as similar as possible by extrapolating all the profiles (MAPS, COARE, and COAMPS) from 0.5 m to the surface to determine the surface refractivity, the conditions at the surface appear to influence the overall profile shape. The MAPS profile is generated from a seventh order polynomial model that does not necessarily capture the expected exponential increases in humidity at the surface. In contrast, the COARE and COAMPS-NAVSLaM use an assumption of 98% relative humidity at the surface. The COARE used the same approximation for SST as the MAPS data but COAMPS-NAVSLaM uses NCOM forecasted SST. Although each of these surface conditions are not explicitly included due to modifying the profiles such that they are extrapolated from 0.5 m to the surface, the influence of these surface conditions on the overall profile shape is evidenced by the different curvatures and M-deficits. In short, the stability functions implemented in MOST create much larger increases in T and q near the surface, thus M-deficits and curvatures are greater than they are for MAPS data for both COARE and COAMPS-NAVSLaM. In addition, COARE and NAVSLaM humidity profiles rely on empirical stability functions that may not be ideal for the present experiment–for example, in some cases, they are based on measurements performed over land surfaces (Beljaars & Holtslag, 1991; Fairall et al., 2003; Frederickson, 2016; Grachev et al., 2007).

4. Conclusions

This study explores the differences in approximately co-located and synchronous refractivity estimates between the COARE algorithm, COAMPS numerical weather prediction model, and MAPS measurements as they relate to propagation. The CASPER-East data set (Wang et al., 2018) is unique in that the refractive environment is estimated via multiple methods at approximately the same times and locations enabling a direct comparison between the methods with little to no assumptions. Variations in the environment and resulting refractivity are linked to differences in propagation predictions to improve understanding of environmental variations that impact propagation most significantly. Study data includes tethered balloon measurements, shipboard measurements, NWP forecasts, and semi-empirical model estimates. This study parameterizes the refractive environment using not only EDH and M-deficit, but also introduces mean curvature of the profile beneath the duct height as a factor affecting PL; analogous to the critical potential refractivity gradient (c_0) parameter discussed in simplified refractivity models (Matsko & Hackett, 2019; Paulus, 1990; Penton & Hackett, 2018; Saeger et al., 2015; Zhang et al., 2011).

Variations in duct height between COAMPS-NAVSLaM, COARE, and MAPS cause significant variations (>10 dB) between propagation predictions. For scenarios where all methods estimate EDH below the transmitter height (10.4 m), discrepancies in PL predictions (σ_{PL}) are influenced by the minimum duct height across the methods (δ_{MIN}) affecting the amount of signal leaked into the duct depending on proximity to the transmitter height, and expectedly variations in duct height between the methods (σ_{EDH}). In contrast, for times where EDH estimates span the transmitter height, there is less correlation between σ_{EDH} and σ_{PL}, indicating that even small discrepancies in duct height relate to large differences in PL. In cases where at least one EDH is above the transmitter height, the minimum duct height between the estimates is a good

1944799x, 2021, 56, Downloaded from https://agupubs.onlinelibrary.wiley.com. By Coastal Carolina University - on [28/09/2021]. Re-use and distribution is strictly not permitted, except for Open Access articles

indicator of the magnitude of differences in PL because the further a duct height is below the transmitter height, the more likely large discrepancies will occur with another prediction based on an EDH above the Tx. Discrepancies between duct height estimates occur primarily during periods of stability and can likely be attributed to the documented limitations of COAMPS-NAVSLaM and COARE during these stable thermodynamic conditions (Fairall et al., 1996; Karimian et al., 2013). Results also suggest that periods of strong thermal instabilities may also result in large discrepancies between EDH estimates.

Discrepancies in PL between the measured and modeled data, specifically at long range beneath the transmitter, are also caused by differences in M-deficit and mean curvature of the refractive profiles. For scenarios where EDH span the transmitter height, variations in M-deficit and mean curvature correspond more strongly to increased variations in PL than do variations in duct height (Figure 9a). Conversely, it is shown for scenarios where all EDHs are below the transmitter, variations in EDH are the primary driver of PL differences but variations in M-deficit and mean curvature are secondary drivers of differences in PL, which also align with results shown in Figure 2.

Differences in the measured and modeled M-deficits and mean curvature are likely due to differences introduced by the treatment of the surface despite efforts to make surface conditions similar by extrapolating all the data (MAPS, COARE, and COAMPS) from 0.5 m to the surface. The influence of the surface conditions in combination with MOST generates different profile shapes than that fit from the MAPS data. MOST uses empirical models for the stability functions, which may not always be representative of the environment, and the fit MAPS data also likely does not accurately capture the rapid increases in surface humidity, resulting in skewed profile shapes.

All these findings are based on the unique data set acquired during the CASPER-East experiment (Wang et al., 2018), future studies of similar scope should examine whether they are valid in other locations. Future research should also explore methods for accurate near surface (<50 cm) humidity measurements to enable improved estimation of surface refractivity (and therefore near surface refractive gradients and profile shape).

Data Availability Statement

Access to the refractivity and propagation loss data is available at the DRYAD data repository at: https://doi.org/10.5061/dryad.sbcc2fr58.

Acknowledgments
The authors would like to thank Frank Ryan (Applied Technology Inc.) for his assistance with the VTRPE simulation. We would also like to thank the Office of Naval Research and Program Officer Dr. Steven Russell for their support of this research (grants: N00014-16-1-2075, N00014-19-1-2350).

References

Anderson, D. L. (1995). The tropical ocean global atmosphere program. *Contemporary Physics*, *36*(4), 245–265. https://doi.org/10.1080/00107519508230334

Babin, S. M., Young, G. S., & Carton, J. A. (1997). A new model of the oceanic evaporation duct. *Journal of Applied Meteorology*, *36*(3), 193–204. https://doi.org/10.1175/1520-0450(1997)036<0193:anmoto>2.0.co;2

Bean, B. R., & Dutton, E. J. (1968). *Radio meteorology* (1st ed.). College Entrance Book Company, Dover.

Beljaars, A. C. M., & Holtslag, A. A. M. (1991). Flux parameterization over land surfaces for atmospheric models. *Journal of Applied Meteorology*, *30*(3), 327–341. https://doi.org/10.1175/1520-0450(1991)030<0327:fpolsf>2.0.co;2

Buck, A. L. (1981). New equations for computing vapor pressure and enhancement factor. *Journal of Applied Meteorology*, *20*(12), 1527–1532. https://doi.org/10.1175/1520-0450(1981)020<1527:nefcvp>2.0.co;2

Cherrett, R. C. (2015). *Capturing characteristics of atmospheric refractivity using observations and modeling approaches* [Dissertation]. Naval Postgraduate School.

Craig, K. H.-, & Levy, M. F. (1991). Parabolic equation modelling of the effects of multipath and ducting on radar systems. In IEE Proceedings F (Radar and Signal Processing), (Vol. 38, No. 2, pp. 153–162). IET Digital Library. https://doi.org/10.1049/ip-f-2.1991.0021

Edson, J. B., Zappa, C. J., Ware, J. A., McGillis, W. R., & Hare, J. E. (2004). Scalar flux profile relationships over the open ocean. *Journal of Geophysical Research*, *109*(C8). https://doi.org/10.1029/2003jc001960

Fairall, C. W., Bradley, E. F., Hare, J. E., Grachev, A. A., & Edson, J. B. (2003). Bulk parameterization of air–sea fluxes: Updates and verification for the COARE algorithm. *Journal of Climate*, *16*(4), 571–591. https://doi.org/10.1175/1520-0442(2003)016<0571:bpoasf>2.0.co;2

Fairall, C. W., Bradley, E. F., Rogers, D. P., Edson, J. B., & Young, G. S. (1996). Bulk parameterization of air-sea fluxes for tropical ocean-global atmosphere coupled-ocean atmosphere response experiment. *Journal of Geophysical Research*, *101*(C2), 3747–3764. https://doi.org/10.1029/95jc03205

Frederickson, P. (2016). *Navy atmospheric measurements for EM propagation modeling. [Executive summary]*. Naval Postgraduate School.

Garratt, J. R. (1994). The atmospheric boundary layer. *Earth-Science Reviews*, *37*(1–2), 89–134. https://doi.org/10.1016/0012-8252(94)90026-4

Grachev, A. A., Andreas, E. L., Fairall, C. W., Guest, P. S., & Persson, P. O. G. (2007). SHEBA flux–profile relationships in the stable atmospheric boundary layer. *Boundary-Layer Meteorology*, *124*(3), 315–333. https://doi.org/10.1007/s10546-007-9177-6

Haack, T., Wang, C., Garrett, S., Glazer, A., Mailhot, J., & Marshall, R. (2010). Mesoscale modeling of boundary layer refractivity and atmospheric ducting. *Journal of Applied Meteorology and Climatology*, *49*(12), 2437–2457. https://doi.org/10.1175/2010jamc2415.1

Halliwell, G., Bleck, R., & Chassignet, E. (1998). Atlantic Ocean simulations performed using a new hybrid-coordinate ocean model. EOS, Transactions AGU meeting.

Hitney, H. V., Richter, J. H., Pappert, R. A., Anderson, K. D., & Baumgartner, G. B. (1985). Tropospheric radio propagation assessment. *Proceedings of the IEEE*, *73*(2), 265–283. https://doi.org/10.1109/proc.1985.13138

Hodur, R. M. (1997). The Naval Research Laboratory's coupled ocean/atmosphere mesoscale prediction system (COAMPS). *Monthly Weather Review*, *125*(7), 1414–1430. https://doi.org/10.1175/1520-0493(1997)125<1414:tnrlsc>2.0.co;2

Hogan, T. F., Liu, M., Ridout, J. A., Peng, M. S., Whitcomb, T. R., Ruston, B. C., et al. (2014). The navy global environmental model. *Oceanography*, *27*(3), 116–125. https://doi.org/10.5670/oceanog.2014.73

Kang, D., & Wang, Q. (2016). Optimized estimation of surface layer characteristics from profiling measurements. *Atmosphere*, *7*(2), 14. https://doi.org/10.3390/atmos7020014

Karimian, A., Yardim, C., Haack, T., Gerstoft, P., Hodgkiss, W. S., & Rogers, T. (2013). Toward the assimilation of the atmospheric surface layer using numerical weather prediction and radar clutter observations. *Journal of Applied Meteorology and Climatology*, *52*(10), 2345–2355. https://doi.org/10.1175/jamc-d-12-0320.1

Lentini, N. E., & Hackett, E. E. (2015). Global sensitivity of parabolic equation radar wave propagation simulation to sea state and atmospheric refractivity structure. *Radio Science*, *50*(10), 1027–1049. https://doi.org/10.1002/2015rs005742

Matsko, I. J., & Hackett, E. E. (2019). Impact of radar data sampling on the accuracy of atmospheric refractivity inversions over marine surfaces. *Radio Science*, *54*(7), 704–714. https://doi.org/10.1029/2018rs006757

Paulus, R. A. (1990). Evaporation duct effects on sea clutter. *IEEE Transactions on Antennas and Propagation*, *38*(11), 1765–1771. https://doi.org/10.1109/8.102737

Penton, S. E., & Hackett, E. E. (2018). Rough ocean surface effects on evaporative duct atmospheric refractivity inversions using genetic algorithms. *Radio Science*, *53*(6), 804–819. https://doi.org/10.1029/2017rs006440

Ryan, F. J. (1991). *Analysis of electromagnetic propagation over variable terrain using the parabolic wave equation (No. NOSC/TR-1453)*. Naval Ocean Systems Center.

Saeger, J. T., Grimes, N. G., Rickard, H. E., & Hackett, E. E. (2015). Evaluation of simplified evaporation duct refractivity models for inversion problems. *Radio Science*, *50*(10), 1110–1130. https://doi.org/10.1002/2014rs005642

Sirkova, I. (2012). Brief review on PE method application to propagation channel modeling in sea environment. *Open Engineering*, *2*(1), 19–38. https://doi.org/10.2478/s13531-011-0049-y

Skolnik, M. I. (1990). *Radar handbook* (2nd ed.). McGraw-Hill.

Skolnik, M. I. (2001). *RADAR systems*. McGraw-Hill.

Turton, J. D., Bennetts, D. A., & Farmer, S. G. (1988). An introduction to radio ducting. *The Meteorological Magazine*, *117*(1393), 245–254.

Ulate, M., Wang, Q., Haack, T., Holt, T., & Alappattu, D. P. (2019). Mean offshore refractive conditions during the CASPER east field campaign. *Journal of Applied Meteorology and Climatology*, *58*(4), 853–874. https://doi.org/10.1175/jamc-d-18-0029.1

Wagner, M., Gerstoft, P., & Rogers, T. (2016). Estimating refractivity from propagation loss in turbulent media. *Radio Science*, *51*(12), 1876–1894. https://doi.org/10.1002/2016rs006061

Wang, Q., Alappattu, D. P., Billingsley, S., Blomquist, B., Burkholder, R. J., Christman, A. J., et al. (2018). CASPER: Coupled air–sea processes and electromagnetic ducting research. *Bulletin of the American Meteorological Society*, *99*(7), 1449–1471. https://doi.org/10.1175/bams-d-16-0046.1

Whalen, J. D. (1998). *Comparison of evaporation duct height measurement methods and their impact on radar propagation estimates*. Naval Postgraduate School.

Yue, P., & Yuanliang, M. (2006). Modelling evaporation duct effects on microwave propagation with experiment validation. In: *IEEE 7th International Symposium on Antennas, Propagation and EM Theory* (pp. 1–4). https://doi.org/10.1109/isape.2006.353492

Zhang, J. P., Wu, Z. S., Zhu, Q. L., & Wang, B. (2011). A four-parameter M-profile model for the evaporation duct estimation from radar clutter. *Progress in Electromagnetics Research*, *114*, 353–368. https://doi.org/10.2528/pier11012204

1944799x, 2021, 56, Downloaded from https://agupubs.onlinelibrary.wiley.com. By Coastal Carolina University- on [28/09/2021]. Re-use and distribution is strictly not permitted, except for Open Access articles

Appendix B: Published Manuscript

Pastore, D.M., Wessinger, S.E., Greenway, D.P., Stanek, M.J., Burkholder, R.J., Haack, T., Wang, Q., and E.E. Hackett (2022). Refractivity inversions from point-to-point X-band radar measurements, Radio Science, 57, e2021RS007345. https://doi.org/10.1029/2021RS007345

Check for updates

Radio Science

RESEARCH ARTICLE
10.1029/2021RS007345

Special Section:
Air-Sea Coupling and its Effect on Electromagnetic Propagation in the Marine Atmospheric Boundary Layer

Refractivity Inversions From Point-To-Point X-Band Radar Propagation Measurements

Douglas M. Pastore[1], Sarah E. Wessinger[1], Daniel P. Greenway[1], Mathew J. Stanek[1], Robert J. Burkholder[2], Tracy Haack[3], Qing Wang[4], and Erin E. Hackett[1]

[1]Department of Marine Science, Coastal Carolina University, Conway, SC, USA, [2]Department of Electrical and Computer Engineering, Columbus, OH, USA, [3]Marine Meteorology Division, Naval Research Laboratory, Monterey, CA, USA, [4]Graduate School of Engineering and Applied Sciences, Naval Postgraduate School, Monterey, CA, USA

Key Points:

- Inversion employing a genetic algorithm solves for refractivity from point-to-point radar propagation measurements in a marine environment
- Inversion results scrutinized by comparison with other refractivity sources: numerical weather prediction, theory, and in situ measurements
- Inversion solutions adequately remotely sense atmospheric refractivity in unstable and stable atmospheric regimes

Correspondence to:
E. E. Hackett,
ehackett@coastal.edu

Citation:
Pastore, D. M., Wessinger, S. E., Greenway, D. P., Stanek, M. J., Burkholder, R. J., Haack, T., et al. (2022). Refractivity inversions from point-to-point X-band radar propagation measurements. *Radio Science*, *57*, e2021RS007345. https://doi.org/10.1029/2021RS007345

Received 9 AUG 2021
Accepted 30 JAN 2022

Author Contributions:
Conceptualization: Erin E. Hackett
Data curation: Robert J. Burkholder, Tracy Haack, Qing Wang
Formal analysis: Douglas M. Pastore, Sarah E. Wessinger, Daniel P. Greenway, Mathew J. Stanek
Funding acquisition: Erin E. Hackett
Investigation: Douglas M. Pastore, Erin E. Hackett

© 2022. The Authors.
This is an open access article under the terms of the Creative Commons Attribution-NonCommercial-NoDerivs License, which permits use and distribution in any medium, provided the original work is properly cited, the use is non-commercial and no modifications or adaptations are made.

Abstract Dynamic refractive environments within the marine atmospheric boundary layer (MABL) pose difficulties in the prediction of X-band radar wave propagation due to natural phenomena such as evaporation ducts (ED). This study utilizes a unique data set collected during the Coupled Air-Sea Processes and Electromagnetic Ducting Research (CASPER)-East field campaign, including multiple refractivity estimation methods and twelve point-to-point (PTP) electromagnetic datasets, to assess the efficacy of PTP inversion techniques for remote sensing of atmospheric refractivity within the MABL. Comparison of refractivity between the inverse and other refractivity methods show reasonable evaporation duct height estimates by the inversion, and inverse-based propagation predictions are also shown to be more accurate than propagation based on other refractivity prediction methods: numerical weather prediction, theory, and in situ atmospheric measurements. These results propose the effectiveness of a PTP metaheuristic radar inversion to remotely sense refractive environments from radar propagation measurements in stable and unstable atmospheric conditions.

Plain Language Summary Continually varying atmospheric properties in the marine environment, especially at altitudes within 100 m of the surface, cause radar waves to deviate from expected patterns resulting in positioning uncertainties and other adverse effects. Measurements and mathematical models are commonly implemented to understand atmospheric structure, where data from these models or measurements are used within radar simulations to evaluate the impact of such conditions on radar. This study demonstrates the application of a technique that models the atmosphere in a reverse manner-determining the atmospheric structure based on radar wave propagation measurements that are impacted by this structure. The radar measurements used in this study were collected in conjunction with measured and modeled atmospheric data, which are used to verify the results of the reverse methodology, a unique data set for this application. We find that remote sensing of the atmosphere based on propagation measurements generates adequate representation of the atmospheric structure. The highlighted technique also most accurately predicts the propagation measurements as compared to more common atmospheric measurement and modeling techniques. Thus, this method of determining atmospheric conditions shows merit for sensing of the environment in order to enable corrections of a radar system, paving the way for improvements in associated technologies.

1. Introduction

Over the last couple decades, inversion methods of estimating refractivity from radar measurements have become increasingly prominent (Karimian et al., 2011). Inversion methods using measured sea clutter data (referred to as RFC approaches) have been examined extensively (Compaleo et al., 2018; Gerstoft et al., 2003; Karimian et al., 2013; Rogers et al., 2000, 2005; Tepecik & Navruz, 2018; Yardim et al., 2009; Zhao & Huang, 2012; Zhao et al., 2017), but few studies demonstrate inversion methods using point-to-point (PTP) radar wave propagation data. Of those studies, most have demonstrated the validity of inverse approaches using synthetic propagation loss (PL) data (Fountoulakis & Earls, 2016; Gersoft et al., 2000; Gingras et al., 1997; Matsko & Hackett, 2019; Penton & Hackett, 2018; Tabrikian & Krolik, 1999; Wagner et al., 2016; Zhang & Yang, 2018; Zhang et al., 2016; Zhao, 2012; Zhao et al., 2011). The PTP approach has a major advantage over RFC methods in that no sea surface scattering coefficient needs to be estimated, which is a major element of uncertainty in such approaches (Plant & Irisov, 2017). Measured PTP PL has been implemented in inversions studies to estimate duct heights via comparison with an a priori library of simulated PL based on refractivity profiles with differing duct heights (Pozderac et al., 2018; Wang et al., 2019).

Methodology: Douglas M. Pastore, Erin E. Hackett
Project Administration: Erin E. Hackett
Supervision: Erin E. Hackett
Visualization: Douglas M. Pastore, Sarah E. Wessinger
Writing – original draft: Douglas M. Pastore
Writing – review & editing: Douglas M. Pastore, Sarah E. Wessinger, Daniel P. Greenway, Mathew J. Stanek, Robert J. Burkholder, Erin E. Hackett

This study expands investigation of such PTP inversion approaches by evaluating refractivity profiles for evaporation ducts using multiple parameters that include duct height but also parameters characterizing near-surface refractive gradients (or duct "curvature") and mixed layer slope. This study also implements the PTP inversions using a metaheuristic algorithm rather than look-up libraries. Finally, and importantly, it utilizes a comprehensive and unique data set for assessment of inversion results collected during the Coupled Air-Sea Processes and Electromagnetic Ducting Research (CASPER) East field campaign (Wang et al., 2018). CASPER-East involved extensive in situ atmospheric measurements and numerical weather prediction models that are used to evaluate results of the inversions and also scrutinizes results as a function of atmospheric stability regimes. Metaheuristic PTP inverse approaches are promising for remote sensing of the atmosphere as PTP propagation measurements are easily obtained relative to rigorous atmospheric in situ measurements, for example, propagation between two ships, or between a ship and another platform such as a pier, tower, buoy, or even an autonomous ariel vehicle. This paper demonstrates its feasibility with a robust data set.

2. CASPER-East Data

The CASPER-East field campaign occurred offshore Duck, NC from 12 October – 6 November 2015 (Wang et al., 2018). The goal of the CASPER-East campaign was to perform concurrent electromagnetic (EM), oceanographic, and meteorological measurements aiding in the representation and understanding of the environment within the MABL as well as explore novel techniques for modeling EM wave propagation through the observed environments (Wang et al., 2018). This study looks to incorporate all aspects of the CASPER-East data set to verify the remote sensing method proposed, the following paragraphs describe data incorporated from CASPER-East: (a) EM propagation measurements, (b) wave buoy sea surface spectra, and (c) meteorological estimates (i.e., in situ measurements, semiempirical models, and numerical weather prediction).

RF measurements during the CASPER-East campaign were comprised of both ship transmitted and ship received (ship-to-ship) as well as shore transmitted and ship received (shore-to-ship) datasets. Due to the longer propagation path of the shore-to-ship measurements along with the fixed (non-moving) transmitter, the current study focuses on 12 shore-to-ship X-band wave propagation datasets acquired aperiodically over 9 days during CASPER-East. These datasets were sub-selected after quality control ensuring that the measurements span ranges greater than 30 km (∼over the horizon) and that measurements were relatively continuous (i.e., do not exhibit frequent signal dropouts), which reduced the useable measurements to 12 datasets from an available 14 shore-to-ship datasets collected during CASPER-East. Shore-to-ship datasets utilized vertically polarized 10.7 GHz radio frequency (RF) signals transmitted from a radio tower located on Duck pier which were received aboard the research vessel (R/V) Atlantic Explorer (AE) as the vessel transited offshore. The transmitter was located between 10.3 and 11.1 m above mean sea level depending on tidal phase, and receivers were located on the aft A-frame of the R/V AE at heights of 4.0, 6.0, 9.2, and 12.3 m (Wang et al., 2018, 2019). Each data set was collected over ∼1–3.5 hr while the R/V AE traversed 3–60 km offshore; exact times and locations of datasets are illustrated in Figure 1 and outlined in Table 1. Comprehensive information on collection and post-processing of the RF data can be found in Wang et al. (2019).

Sea surface conditions during CASPER-East were measured via five moored wave buoys deployed along the research vessel excursion tracks (Figure 1). These mini-wave buoys sampled at a frequency of 2 Hz over ∼40 s periods measuring sea surface wave spectra throughout CASPER-East every 30 min. To mitigate the fact that RF and meteorological measurements are taken over a range of offshore positions at various times throughout each day, wave spectra are averaged over each day and over all buoys to generate a single daily sea state spectrum for the study area (Figure 1) for each day (Table 1). More information about the buoys deployed and the resulting time series can be found in Wang et al. (2018). The sea surface conditions are statistically matched in the propagation simulations as described in Section 3.

Meteorological measurements from CASPER-East are utilized for comparison of refractivity generated by the inversion. Meteorological measurements and resulting refractivity within the marine atmospheric surface layer (MASL) were obtained with the marine atmospheric profiling system (MAPS; Alappattu et al., 2016; Rainer, 2016; Wang et al., 2018). MAPS was deployed from a small workboat, composed of a radiosonde attached to a tethered balloon raised and lowered through the MASL via electronic winch, allowing for measurement profiles spanning ∼0.5–50 m in altitude. Effects from the deployment vessel are considered negligible due

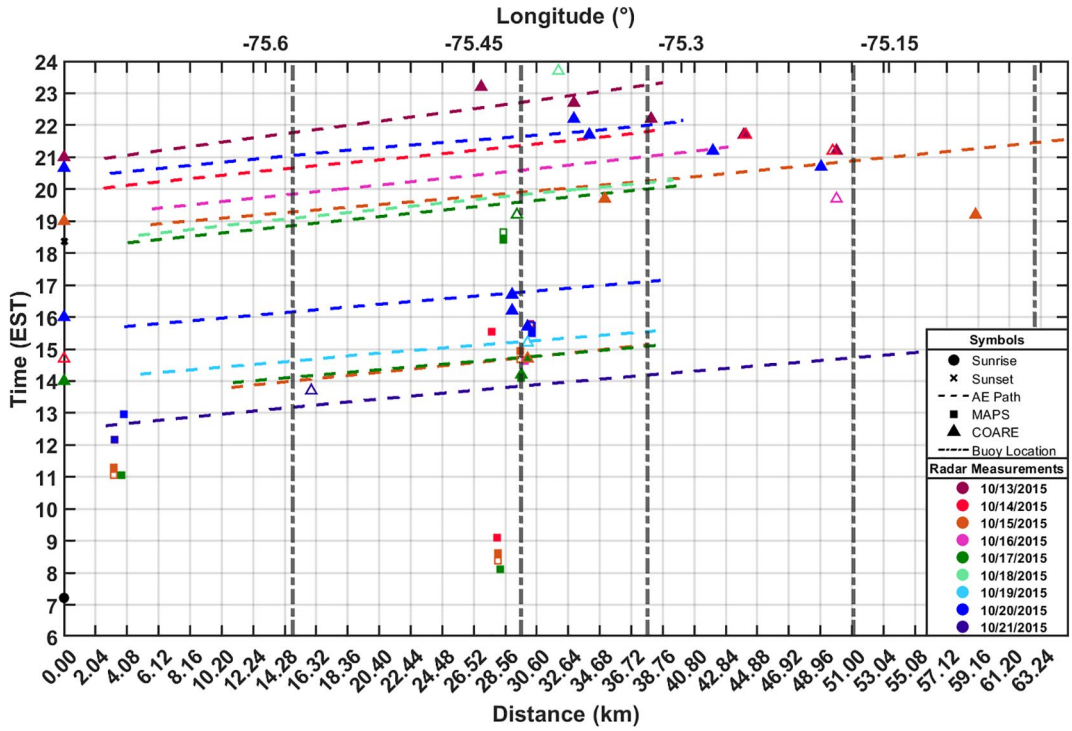


Figure 1. Temporal and spatial coverage of the R/V Atlantic Explorer (AE) radio frequency (RF) measurement tracks, marine atmospheric profiling system (MAPS), Coupled Ocean-Atmosphere Response Experiment algorithm (COARE), and COAMPS®/NAVSLaM refractivity profiles, and moored wave buoys. The *y*-axis represents hours that span measurements performed throughout Coupled Air-Sea Processes and Electromagnetic Ducting Research (CASPER)-East, and the *x*-axis represents the offshore distance or range from Duck pier which is located at the origin. Distance from the pier is shown in both km (bottom *x*-axis) and longitudinal position (top *x*-axis); resolution of the *x*- and *y*-axis corresponds to the Coupled Ocean Atmosphere Mesoscale Prediction System (COAMPS) spatial and temporal resolution, respectively, where intersection of the temporal and spatial lines indicates a COAMPS prediction/forecast. Colors correspond to the day on which measurements occurred for each RF data set. Filled markers represent refractivity profiles that contribute to a mean profile where hollow markers indicate singular profiles, which are incorporated in either range dependent or range independent refractivity forward models. This figure shows data outlined in Table 1.

to the small size of the boat and MAPS system. MAPS datasets are collected over several repeated ascents and descents of the balloon (~150–450 samples) each including, temperature (T), converted to potential temperature (θ), relative humidity (RH), converted to specific humidity (q), and pressure (p). Vertical profiles of p, θ, and q are estimated by fitting a seventh order polynomial model to these measurements for each respective MAPS data set as described in Alappattu et al. (2016), Rainer (2016), and Wang et al. (2018). M-profiles are then computed using (Bean & Dutton, 1968):

$$M = \frac{77.6}{T}\left[p + \frac{4810e}{T}\right] + \left(\frac{z}{a}\right) \times 10^6 \quad (1)$$

where, a is the radius of the earth, z is height above sea level, e is partial water vapor pressure (millibars) that is computed from q as well as T for estimating the saturation vapor pressure (Buck, 1981), and p is pressure in hPa. Surface refractivity (M_0) is determined by the surface values of q and T profiles after extrapolation to the sea surface (Pastore et al., 2021; Wang et al., 2018). MAPS refractivity profiles are measured within ±12 hr of RF measurements. Variations in location and time of the MAPS data relative to the RF measurements is due to poor weather/sea state conditions and limited to daylight hours (Wang et al., 2018); MAPS profile times and locations can be seen in Figure 1 and Table 1. Further details on the deployment of MAPS and justification for the seventh order polynomial fit can be found in Alappattu et al. (2016), Rainer (2016), Wang et al. (2018), and Pastore et al. (2021).

Table 1
Time and Transmitter Height of Radio Frequency (RF) Measurements, Forward Modeling Option (e.g., CR1, MP1, CP1) That Generated The Lowest Propagation Loss (PL) Mean Square Error (MSE) for Each Method (COARE, MAPS, COAMPS) Along With Times and Locations Associated With Those Options (§3), the MSE Between Each Method and the RF Measurements, and Duct Height for Each Method

Experiment	Radar time (EST)	Tx height (m)	Forward modeling option	Profile Time (EST)	Profile distance from pier (km)	MSE (dB^2) all Rx	Duct height (m)
A	10/13/2015 20:57–23:20	10.5	CR1	21:00–23:12	0, 27, 33, 38, 44, 50	27.7	8.1*
			MP1	15:47	30	48.58	44.7
			CP1	20:00–23:00	0–60	33.14	8.1*
			Inversion			7.14	9.15
B	10/14/2015 20:01–21:53	10.3	CR4	14:42–21:42	0,44,50	34.62	13.9
			MP4	09:06–15:32	4, 28	26.3	8.4*
			CP4	21:00	0–60	29.37	9.4
			Inversion			25.18	12.93
C	10/15/2015 13:48–15:09	10.9	CR2	14:42	30	14.38	7.9
			MP2	08:22–14:42	3, 28, 30	20.13	7.1*
			CP1	13:00–15:00	0–60	14.38	8.0*
			Inversion			6.89	5.33
D	10/15/2015 18:53–22:07	10.5	CR1	19:00–19:42	0, 35, 59	79.8	7.1*
			MP4	08:22–14:42	3, 30, 28	53.17	7.1*
			CP1	18:00–22:00	0–60	49.56	8.7*
			Inverson			8.09	19.19
E	10/16/2015 19:23–21:19	10.6	CR2	19:42	50	57.29	8.8
			MP1	14:38	30	35.54	10.3
			CP1	19:00–21:00	0–60	162.1	11.9*
			Inversion			10.62	16.7
F	10/17/2015 13:57–15:09	10.7	CR1	14:00–14:42	0, 29, 30	18.2	9*
			MP1	18:25	28	14.28	7.8
			CP4	13:00	0–60	22.54	9
			Inversion			5.35	6.22
G	10/17/2015 18:19–20:08	10.8	CR3	19:12	29	62.44	9.3
			MP2	08:07–18:25	4, 28, 29, 30	25.55	8.5*
			CP2	19:00	0–60	371.55	11.5*
			Inversion			9.06	14.99
H	10/18/2015 18:33–20:19	10.8	CR2	23:42	32	33.04	13.9
			MP			N/A	N/A
			CP4	22:00–00:00(ND)	0–60	46.75	14.4*
			Inversion			12.81	19.98
I	10/19/2015 14:13–15:35	10.4	CR2	15:12	30	22.13	9.8
			MP			N/A	N/A
			CP4	15:00	0–60	41.51	10
			Inversion			9.96	8.45
J	10/20/2015 15:42–17:09	10.7	CR4	16:00–16:42	0, 29, 29, 30	271.6	8.5*
			MP1	15:29	30	160.99	9.9
			CP4	16:00	0–60	146.6	6.4*
			Inversion			18.78	18.83

Table 1
Continued

Experiment	Radar time (EST)	Tx height (m)	Forward modeling option	Profile Time (EST)	Profile distance from pier (km)	MSE (dB^2) all Rx	Duct height (m)
K	10/20/2015 20:29–22:09	11.1	CR4	20:40–22:12	0, 33, 34, 42, 49	30.91	5.2*
			MP2	12:57–15:35	4, 30	38.26	10.8*
			CP3	20:00–22:00	0–60	70.68	9.1*
			Inversion			8.68	16.34
L	10/21/2015 12:34–14:54	10.4	CR3	13:42	16	10.53	5.8
			MP1	12:57	4	13.22	6.4
			CP1	12:00–14:00	0–60	29.9	5.3*
			Inversion			3.16	6.6

Note. * Denotes a mean. Note in some cases, there was no MAPS measurement within a ±12 hr window of the RF.

Modified refractivity is also estimated using the Coupled Ocean-Atmosphere Response Experiment algorithm (COARE; version 3.0); a bulk parameterization algorithm used to estimate near-surface air properties based on Monin-Obukhov similarity theory (MOST; Garratt, 1994; Fairall et al., 1996; Fairall et al., 2003). Vertical profiles of modified refractivity are computed from COARE generated meteorological profiles via Equation 1. Meteorological and sea surface parameters required for the COARE algorithm include the following: sea surface temperature (SST), significant wave height, peak wavenumber, and wind speed, humidity, and temperature at a reference height. In this study, COARE profiles are generated using data from two measurement platforms: Duck Pier and the R/V Sharp. Data from Duck Pier used for the COARE profiles include: wind speed, T, and q, measured on 10 s intervals, and averaged over 20-min intervals, from one of the seven fixed sensors mounted to the handrail of the pier (1.1 m above and 5.2, 4.3, 3.4, 2.4, 1.5, and 0.6 m below; Wang et al., 2018). Sensor heights relative to the sea-surface fluctuated corresponding to tidal phase; meteorological parameters used for COARE are from the sensor nearest to 10 m above the sea-surface. Meteorological measurements from the R/V Sharp are also used to generate COARE profiles where wind speed, T, and q were measured on a bow-mast on the R/V Sharp, sampled at 1 Hz and averaged over 30-min intervals, at ∼12 m above the sea-surface. Time series of the thermodynamic variables measured during the CASPER-East campaign used for COARE in this study are illustrated in Figure 2. SST for COARE is measured at Duck Pier and aboard the R/V Sharp consisting of the skin temperature corrected from the 5-min bulk SST (Wang et al., 2018). Specific humidity at the sea-surface is estimated assuming 98% relative humidity and using a saturation value based on the SST (Buck, 1981). It is important to note, the R/V AE (RF receivers) and R/V Sharp are located 0–58 km apart during the RF measurements as ship tracks converge or diverge over the course of the day (Wang et al., 2018). Significant wave height and peak wavenumber parameters for COARE were retrieved from the daily averaged wave buoy spectra from the associated day.

To compliment the in situ (MAPS) and semiempirical (COARE) estimations of refractivity, this study utilizes a numerical weather prediction model, specifically, the Coupled Ocean Atmosphere Mesoscale Prediction System (COAMPS®; Hodur, 1997). COAMPS is initialized with boundary conditions from the Navy Global Environment Models (NAVGEM) for the atmosphere (Hogan et al., 2014) and the Global Hybrid Ocean Coordinate Model (HYCOM) for ocean conditions (Halliwell et al., 1998). Meteorological forecasts were generated hourly from a 6-hr initialization cycle throughout the duration of CASPER-East (Pastore et al., 2021; Ulate et al., 2019). In the lowest kilometer of the atmosphere, the average vertical resolution of the model is ∼32 m with 70 terrain following levels; this resolution is unsatisfactory for resolving evaporation ducts thus, COAMPS is blended with the Navy Atmospheric Surface Layer Model (NAVSLaM; Frederickson, 2016) increasing resolution to a decimeter in the lowest 100 m enabling resolution of evaporation ducts (Pastore et al., 2021). NAVSLaM is based-off MOST, and seeded with COAMPS forecasts of q, p, and U near the surface and the Navy Coastal Ocean Model (NCOM) forecasts of bulk SST (Frederickson, 2016). COAMPS-NAVSLaM derived vertical refractivity profiles have hourly temporal resolution every ∼2 km along a transect from Duck Pier (North Carolina; 36.18°N, 284.27°E) to 60 km offshore (Pastore et al., 2021).

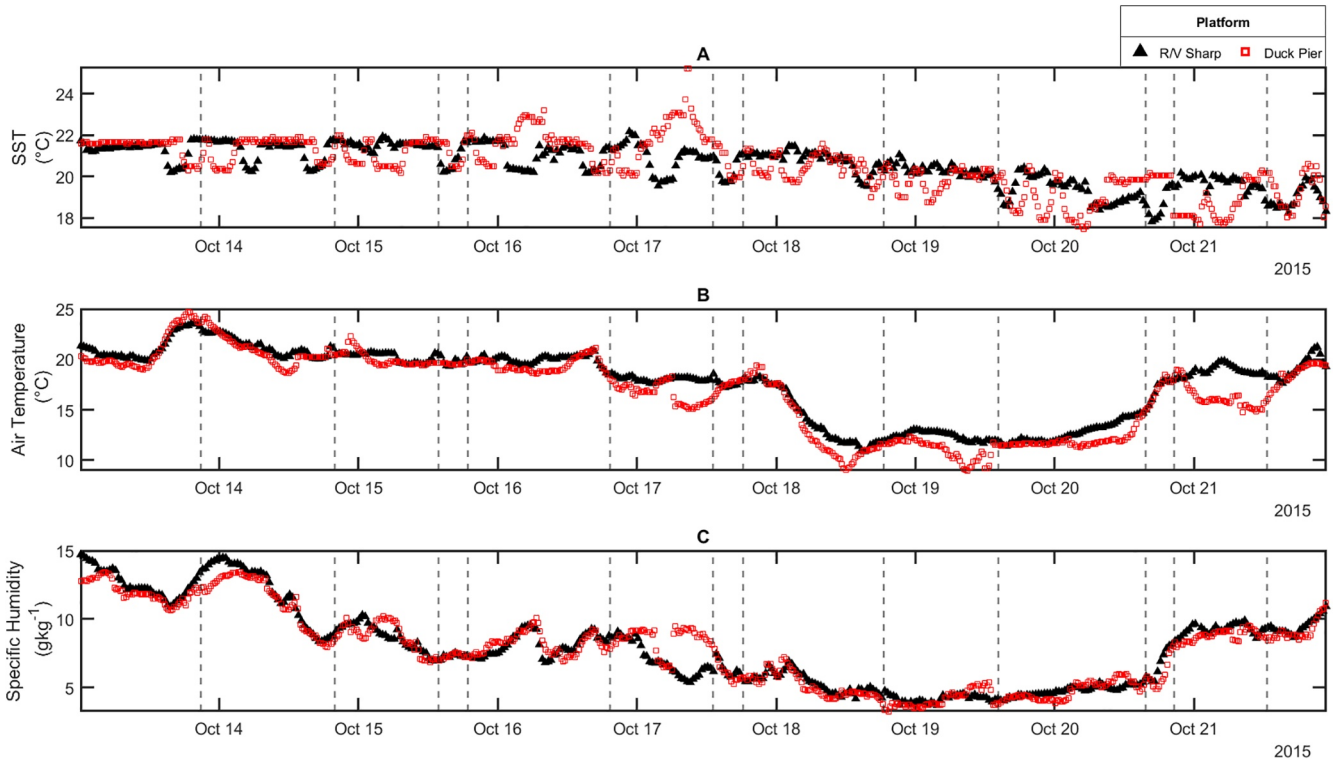


Figure 2. Time series of thermodynamic variables, (a) sea surface temperature (SST), (b) air temperature, and (c) specific humidity, measured at Duck Pier and aboard the R/V Sharp during Coupled Air-Sea Processes and Electromagnetic Ducting Research (CASPER)-East associated with the time periods of the radar measurements, see Table 1. The vertical black dashed lines denote start times of the radio frequency (RF) measurements used in the inversions.

3. Forward Propagation Modeling

Propagation predictions are generated by the Variable Terrain Radio-Wave Parabolic Equation (VTRPE) simulation; VTRPE simulates radio wave propagation in a variety of environmental conditions (Ryan, 1991). The full-wave solution of the EM field is computed via a split step rotated Green's function parabolic equation (Matsko & Hackett, 2019; Pastore et al., 2021; Penton & Hackett, 2018; Ryan, 1991; Saeger et al., 2015; Sirkova, 2012). PL data are simulated matching the antenna characteristics of the measured RF data (Table 1), including the Gaussian antenna pattern with two side lobes emulating the horn antennae. The simulation domain is 60 km in range and 50 m in altitude with an output grid resolution of 2 and 1 m, respectively.

Dielectric boundary conditions are prescribed in the simulation using the skin SST (Wang et al., 2018) measured aboard the R/V AE and assumes a salinity of 35 ppt. Rough surface bottom boundary conditions for PL simulations are generated within VTRPE as sea surface realizations. Sea surface elevation transects are extracted from a two-dimensional surface generated from an inverse transform of the convolution of a two-dimensional zero-mean Gaussian process and a two-dimensional ocean wavenumber spectrum (Penton & Hackett, 2018). The ocean wavenumber spectrum is produced from a modified Donelan-Pierson-Banner wave spectral model (Banner et al., 1989; Donelan et al., 1985; Pierson & Moskowitz, 1964) for the wind seas, and is appended with a Gaussian narrow-band swell spectrum. The daily average wave spectrum obtained from the buoy measurements (§2) is matched to the wave model spectrum via adjustment of the wave model parameters in VTRPE to generate a statistically similar sea surface. Specifically, significant wave height was matched within 15%, where significant wave height was estimated as $H_s = 4\sqrt{m_0}$, where m_0 is the zeroth-order moment of the 1D wave spectrum. The peak wavelength of the average buoy and VTRPE sea state spectra were also matched via adjustment of the VTRPE wave model parameters. An example illustrating a comparison of the spectrum from the VTRPE wave model, and the averaged buoy wave spectrum is illustrated in Figure 3.

Forward modeled propagation is included in this study to evaluate the efficacy of the proposed inversion method. The following paragraphs describe CASPER-East refractivity datasets available for forward propagation modeling

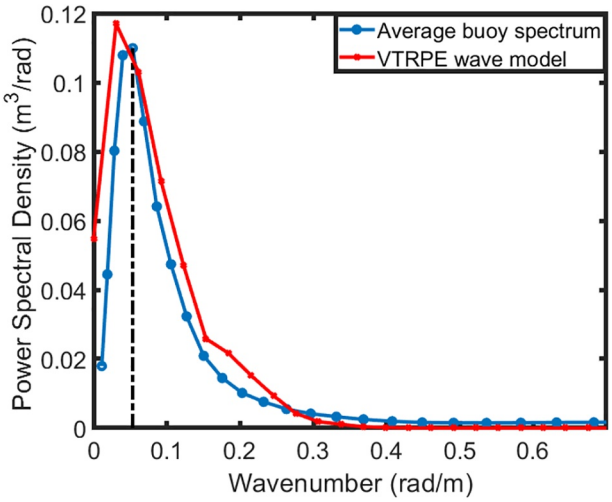


Figure 3. Example sea state spectra from the wave buoys and the Variable Terrain Radio-Wave Parabolic Equation (VTRPE) wave model for 21 October 2015. Peak wavelength from the average wave buoy spectrum is ~117 m (vertical black dashed line) and the significant wave height is 0.43 m. The VTRPE wave model has a peak wavelength of 150 m with a significant wave height of 0.43 m.

as well as several possible options for each refractivity estimation method (COAMPS, COARE, and MAPS) that can be used to describe RF measurement environments (i.e., due to the temporal and spatial variability of the meteorological and RF measurements multiple options exist). No option discussed below can be considered the "true" environment due to the temporal and spatial discrepancies between the refractivity estimates and RF measurements thus, propagation comparisons based-on refractivity for the forward modeled refractivity estimation methods are performed to determine the option that best matches each RF measurement data set. Discussion of the mean square error (MSE) used to determine the "best" forward model option with respect to the RF measurements (Table 1) is described at the end of this subsection.

Several possible options exist for comparisons of refractivity estimated by MAPS to that estimated by the inversion. The RF data was collected over several hours while the ship traversed ~60 km in range; MAPS data are collected at discrete ranges at discrete times. In other words, there exist multiple ways in which the MAPS data could be used to generate a propagation prediction for a (single) corresponding RF data set. In order to select the most accurate MAPS-based representation of the environment for each RF data set, several options were compared and the option/refractivity estimate that produced the best match to the measured RF data are used for comparisons. The following options were evaluated for forward modeling associated with each inversion/RF data set: (MP1) the (range independent) refractivity profile closest in time (during if possible), regardless of the range at which it was acquired, (MP2) a (range independent) mean profile averaging all profiles measured within a ±~12 hr window surrounding the RF measurements (which span several ranges), (MP3) a (range-independent) refractivity profile closest to the mid-range of the RF collection track, regardless of time (within the ±12 hr window), and (MP4) a range-dependent profile set that consists of single profiles within the ±12 hr window at their associated ranges.

Similar spatiotemporal matching issues occur for COARE estimates of refractivity. In this case, multiple COARE estimates can be associated with a single RF data set because the COARE data are from the R/V Sharp or Duck Pier, which collected thermodynamic data at ~30 min intervals, so the temporal resolution is better than MAPS, but the R/V Sharp samples are taken at various discrete ranges over the RF data collection time period. For COARE, the following options were considered: (CR1) a (range independent) mean refractive profile inclusive of both Duck Pier and R/V Sharp based refractivity profiles over the duration of the RF measurements (that occur

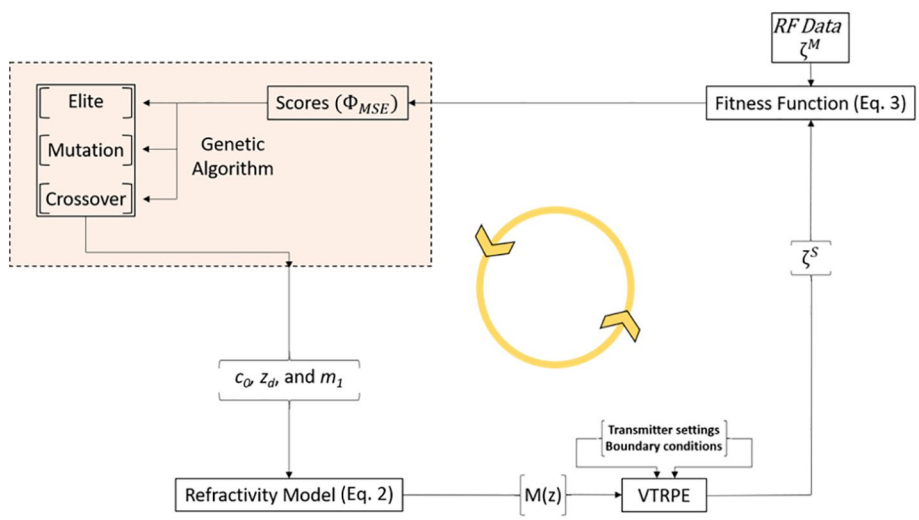


Figure 4. Depiction of the inversion procedure illustrating the iterative genetic algorithms (GA) process.

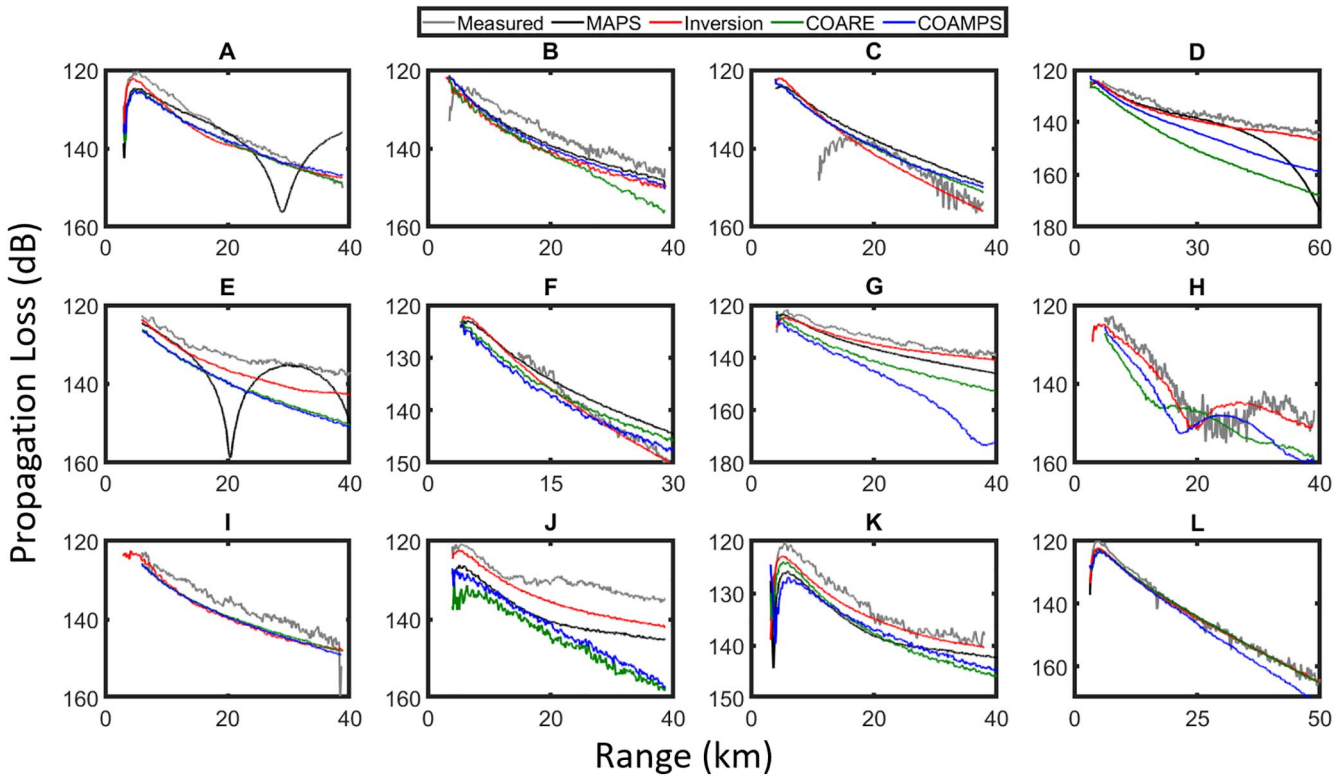


Figure 5. ζ^S at 4 m for the forward model option with the lowest mean square error (MSE) for each method, and the inversion-based propagation loss along with measured radio frequency (RF) data (4 m receiver height). ζ^S predictions shown here are considered to be the "best" representation of measured propagation from each method (§3). A-L follow in order of the experiments outlined in Table 1.

at various ranges), (CR2) the (range independent) refractivity profile closest to the mid-range of the RF collection track, regardless of time (within a ±6 hr window), (CR3) the (range independent) midtime profile relative to the RF measurements, regardless of the range at which it was acquired, and (CR4) a range dependent profile set comprised of a pier-based refractive profile closest in time to the RF measurements and R/V Sharp-based profiles in range that occur during the RF measurement data collection time period.

Similar to the other environmental sources, radar measurements span multiple COAMPS/NAVSLaM forecast periods (see Figure 1) so several options were examined for forward modeling of the propagation: (CP1) a range-dependent refractivity profile set from the time average of all forecasts during the RF measurements, (CP2) range-dependent refractivity profile set estimated from the forecast closest to the mid-time of the RF measurements, (CP3) range-independent refractivity estimated from the time and range average of all forecasts during RF measurements, and (CP4) range-independent refractivity estimated from the range average of the forecast closest to the midtime of the RF measurements.

PL is simulated for each refractivity source (and associated configurations) delineated above and comparisons are made between measured and simulated PL; receiver heights for the latter correspond to RF receiver height rounded to the nearest meter. The comparison is computed as a MSE summed over all the receiver heights (and ranges). MSE over all receiver heights and ranges is used to provide an overall evaluation of the match to the RF propagation data (rather than at one specific height or range). Before computing the MSE, both the simulated and measured RF data are smoothed with a running average filter of length equal to the peak wavelength of the sea surface. This technique minimizes the influence of slight differences in the multipath null/peak locations on the MSE statistic due to the sea surface (Penton & Hackett, 2018). For each environmental source, the option (e.g., CP1, CP2, or CP3) that produced the smallest MSE is used for comparison to the inversion results (Table 1). It is assumed that the environmental configuration/option that produced the lowest PL MSE relative to the RF measurements is the optimal representation of the environment for each respective forward modeling method. The inclusion of range dependent refractivity forward modeling options potentially allows for more accurate

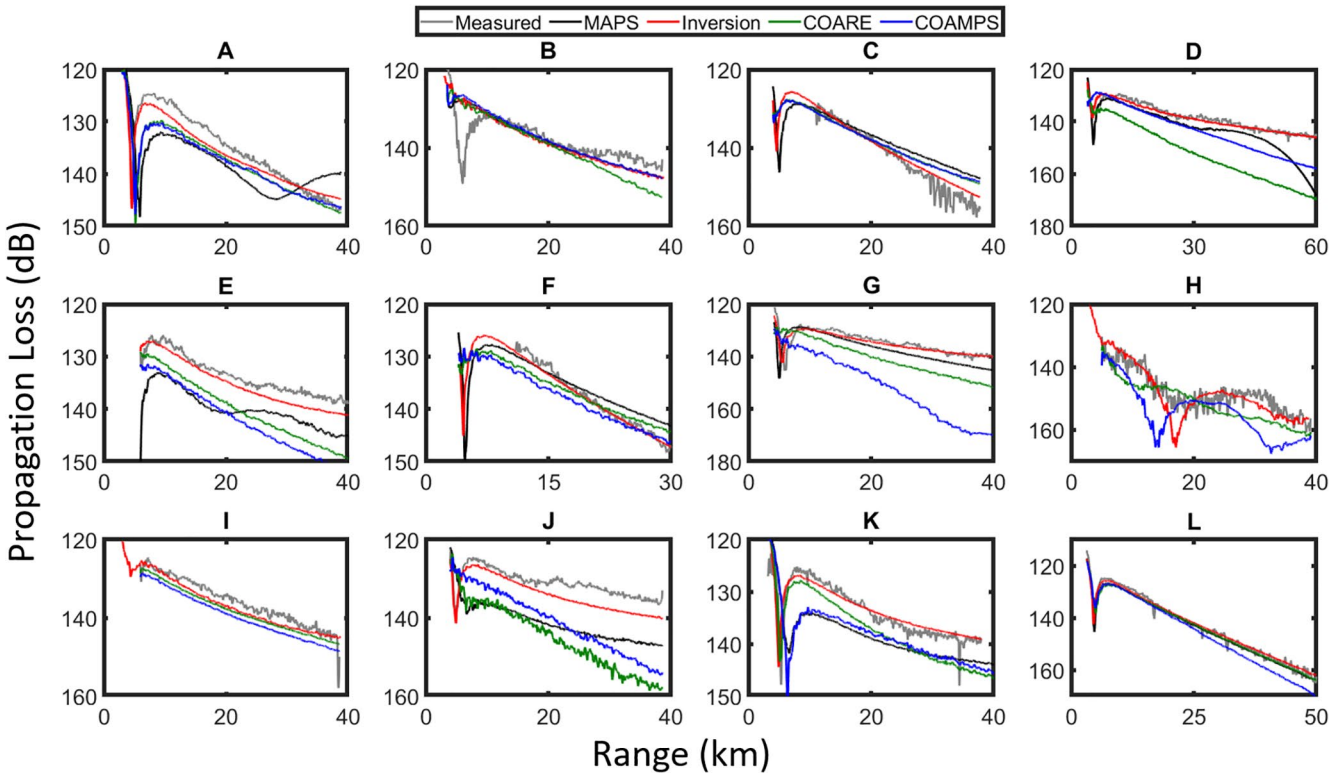


Figure 6. ζ^S at 6 m for the forward model option with the lowest mean square error (MSE) for each method, and the inversion-based propagation loss along with measured radio frequency (RF) data (6 m receiver height). All other aspects of the data shown here are the same as that described in Figure 5 caption.

propagation predictions in cases where the influence of horizontal inhomogeneity on the propagation may be significant, which is an aspect that the inversion process cannot account for (§4), and therefore, this approach also enables insight into how that assumption might impact the accuracy of inversion results. Times and locations of measurements associated with the optimal options are shown in Figure 1 and described in Table 1 (including the MSEs).

4. PTP Inversion Modeling

An overview of the inversion algorithm is outlined in Figure 4. Genetic algorithms are used to generate refractivity parameter sets that construct a refractivity vertical profile using a parametric refractivity model that is homogenous in range. Propagation loss is then simulated for the refractive profile using transmitter and sea state conditions that match those associated with the RF data, as described in §3.0 for the forward modeling. Simulated propagation loss is subsequently compared to the RF data via a fitness (or objective) function. This process is iterated until an optimal solution is reached by achieving a specified threshold for the objective function or a specific number of iterations have been completed. More information about the genetic algorithms, parametric refractivity model, and the fitness function are described in the subsequent paragraphs.

Genetic algorithms (GA), the chosen optimization method in this research, have been effective in deriving refractivity from sea surface clutter (Gerstoft et al., 2003; Rogers et al., 2000, 2005) and synthetic PTP propagation data (Fountoulakis & Earls, 2016; Matsko & Hackett, 2019; Penton & Hackett, 2018; Wagner et al., 2016; Zhang & Yang, 2018; Zhang et al., 2016). In addition to GAs, prior inversion studies have also used other optimization methods such as adjoint models (Zhao et al., 2017), Markov chain marching algorithms (Anderson et al., 2001), maximum likelihood estimation (Wagner et al., 2016), particle swarm optimization (Zhang & Yang, 2018), iterative local search (Wang et al., 2019), and simulated annealing (Xiao-Feng et al., 2011) all of which could be feasible for this application as well. Nevertheless, GAs optimize a set of parameters through Darwin's theory of natural evolution, where individuals in a population influence future individuals through natural selection and

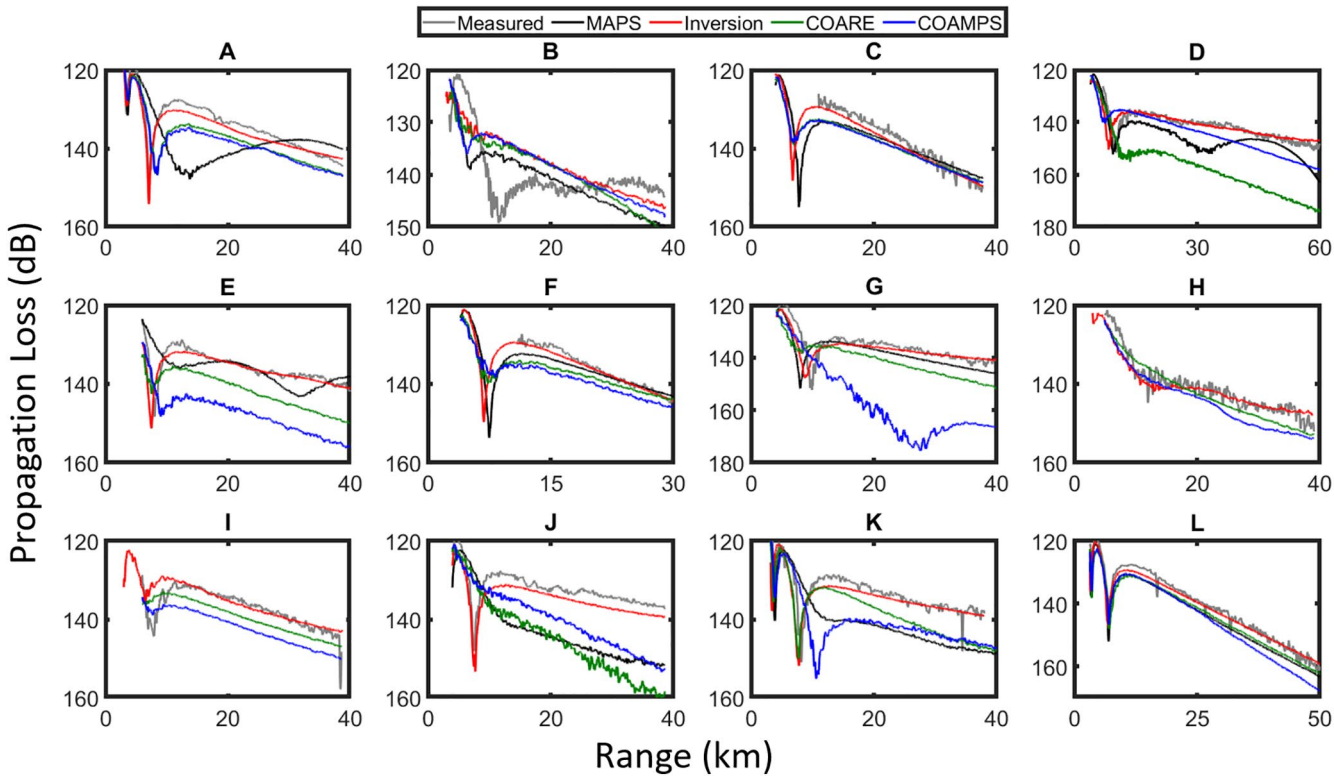


Figure 7. ζ^Sat 9 m for the forward model option with the lowest mean square error (MSE) for each method, and the inversion-based propagation loss along with measured radio frequency (RF) data (9.2 m receiver height). All other aspects of the data shown here are the same as that described in Figure 5 caption.

genetic mutation (Goldberg, 1989; Johnson & Rahmat-Samii, 1997; Penton & Hackett, 2018). In this study we apply a GA to optimize parameters of a refractivity model that best represent the atmospheric conditions in which the RF data were collected. The parametric model is a piecewise modified refractivity model consisting of two layers, an evaporation layer and a mixed layer (Gerstoft, 2003; Matsko & Hackett, 2019; Penton & Hackett, 2018; Saeger et al., 2015):

$$M(z) = M_0 + \begin{cases} c_0\left(z - z_d \ \ln\left(\frac{z + 0.00015}{0.00015}\right)\right), & z \le z_L \\ m_1 z - M_1, & z > z_L \end{cases} \tag{2}$$

where M is modified refractivity, the surface refractivity is $M_0 = 333$ M-units, z_d is evaporation duct height (EDH), m_1 is mixed layer slope, and M_1 is a term defined by other parameters (c_0, z_d, and m_1) ensuring a continuous profile between layers. The potential refractivity gradient (Paulus, 1990), c_0, allows adjustment of evaporation layer "curvature" for a given duct height (Saeger et al., 2015). The evaporation layer extends from the surface to $z_L \equiv 2z_d$. A fixed value is used for M_0 because it is the gradient of the M-profile that affects propagation, not the specific values (Wang et al., 2018).

Refractivity parameters are randomly assigned to the 25-member initial population, which has a restricted search space of $0.03 < c_0 < 0.47$ M-units/m, $0.03 < m_1 < 0.18$ M-units/m, and $1 < z_d < 20$ m. The search space of c_0 is relatively large compared to the value for a neutral atmosphere (0.125 M-units/m; Paulus, 1989), which is necessary to ensure c_0 is properly explored by the GA due to the unknown distribution of c_0 for nonneutral atmospheres. The range selected for m_1, similar to c_0, is selected to cover a wide range of mixed layer slopes due to the unknown distribution of m_1 for differing environments but is inclusive of the global average value of 0.118 M-units/m (Gossard & Strauch, 1983; Penton & Hackett, 2018). The range of z_d is determined from MAPS, COARE, and

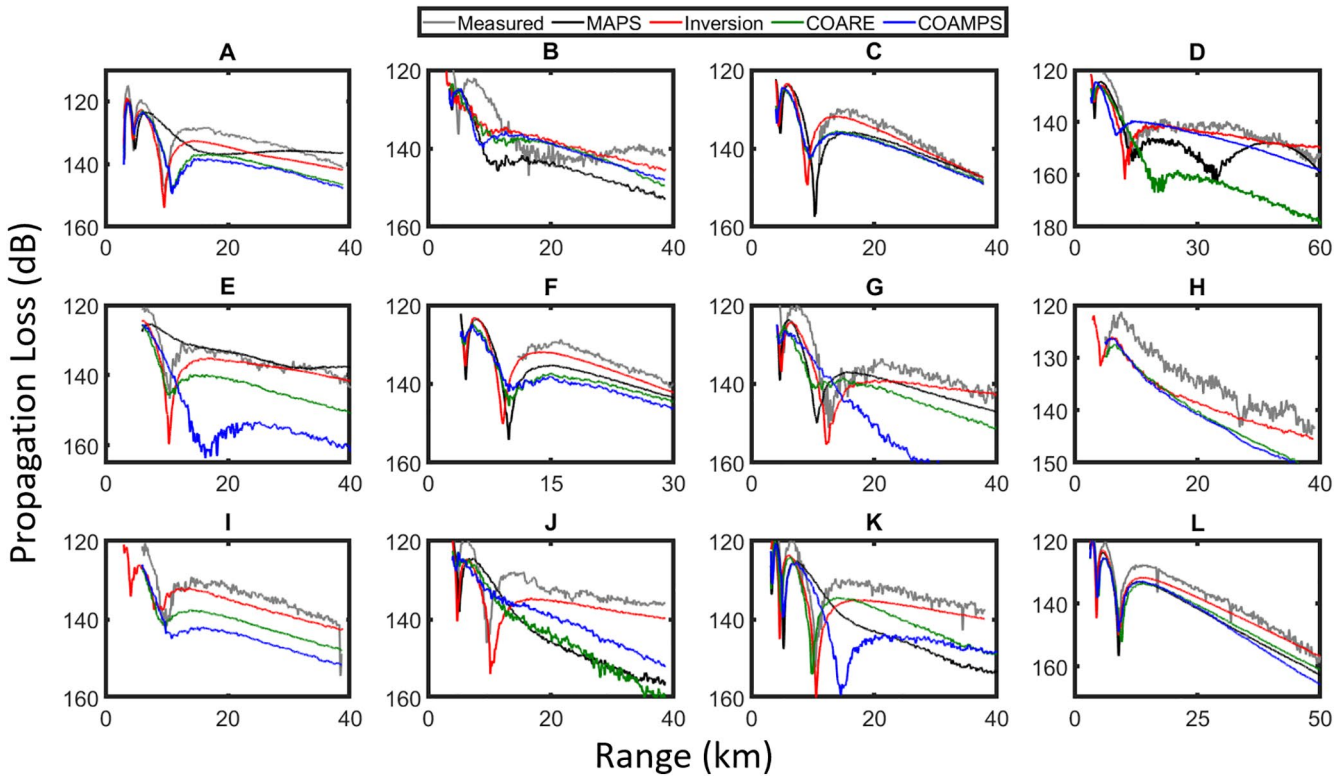


Figure 8. ζ^S at 12 m for the forward model option with the lowest mean square error (MSE) for each method, and the inversion-based propagation loss along with measured radio frequency (RF) data (12.3 m receiver height). All other aspects of the data shown here are the same as that described in Figure 5 caption.

COAMPS EDH estimates during CASPER-East. Ulate et al. (2019) and Pastore et al. (2021) show that during CASPER-East duct heights from the three methods generally occur below 20m in altitude.

Populates, comprised of refractivity model parameters (i.e., c_0, z_d, and m_1), generate refractivity profiles that are then used to generate PL predictions, which are directly compared to the measured RF data, generating a fitness score for each populate:

$$\Phi_{MSE} = \frac{1}{N}\sum_{i=1}^{N}\left(\zeta_i^M - \zeta_i^S\right)^2 \tag{3}$$

where ζ^M is the measured PL in dB, ζ^S is simulated PL in dB corresponding to modified refractivity generated by the GA, and N represents the number of PL data – all the points in range for all four receiver heights. ζ^S and ζ^M are averaged over the peak wavelength as previously described in the forward modeling section prior to computing Φ_{MSE}. Measured RF data are not always continuous in range due to post-processing procedures and signal dropouts, thus only points of co-located PL between measured and simulated data at all receiver heights are included for N. RF receiver heights are compared to the nearest simulation altitude (e.g., ζ^M at $z = 9.3$ m is compared to ζ^S at $z = 9.0$ m).

Once each populate is evaluated, a new generation is produced where cross-over between and mutation of populates occurs creating the new population that can scrutinize the entire parameter search space with varying individuals. Individuals with the two best fitness scores are passed down to the next generation, this process is known as elitism. The algorithm continues to optimize the populations until one of the following is achieved: (a) 60 generations have been realized, (b) an ideal fitness score is achieved ($\leq$0.2 dB^2), or (c) over 25 generations, the average relative change in fitness scores is below 0.002 dB^2. All inversions in this study were terminated via criterion (c) except for inversion *E* (Table 1), which terminated satisfying criterion (a). More information on the GA configuration can be found in Penton and Hackett (2018) and Matsko and Hackett (2019).

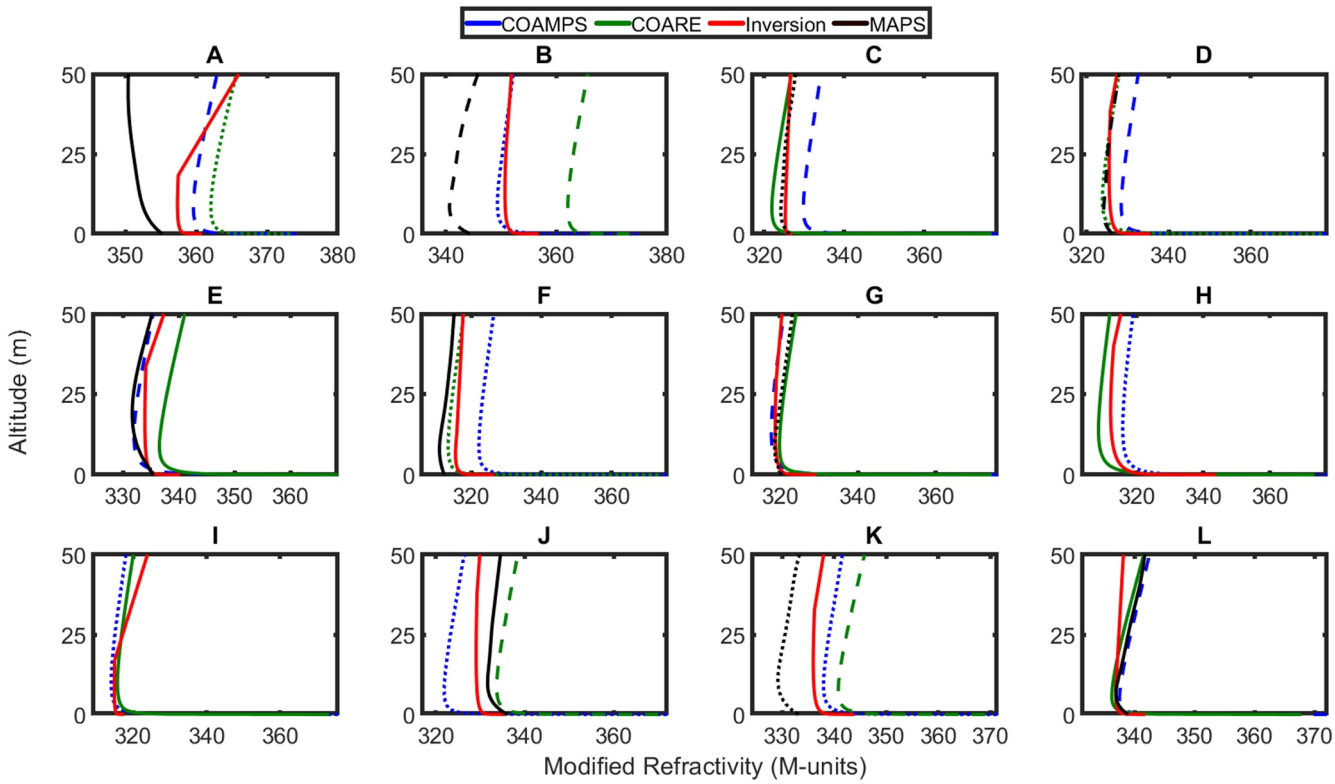


Figure 9. Modified refractivity profiles for the forward model with the lowest propagation loss (PL) mean square error (MSE) for each method and inversion result for each experiment. Range-dependent profiles are not shown for clarity, instead, solid lines denote range-independent (singular) refractivity profiles, dotted lines denote one range-independent mean profile, and dashed lines denote range-dependent (multiple) refractive profiles averaged over range for illustrative purposes. Surface refractivities for inversion profiles are shifted such that modified refractivity at the evaporation duct height (EDH) is the mean refractivity of the other environmental estimates at the EDH. A-L correspond to experiments outlined in Table 1.

5. Results and Discussion

Figures 5–8 show forward modeled PL (for the option with the lowest MSE), RF measurements, and the inversion-based PL for each receiver height, respectively. As expected, given that this is the basis for the optimization, overall, the inversion method produces the most accurate match to the propagation. In most cases, null position and PL at ranges beyond the multipath nulls are more similar to the measured data for the inversion solution than the forward model predictions, including those that describe the environment with range dependent refractivity. Furthermore, the inversion is significantly more successful at predicting propagation relative to the forward models as is statistically evident by comparison of the average MSEs: 9.94, 54.05, 76.15, and 45.36 dB^2 for the inversion, COARE, COAMPS, and MAPS, respectively. Although the lower average Φ_{MSE} for inversion PL confirms more accurate PL predictions, the better propagation predictions do not necessarily imply improved environmental predictions. The inversion approach may converge on an environment that only predicts the propagation accurately at the receiver heights and not necessarily everywhere, in other words, there can be nonunique solutions with a limited RF data set (Matsko & Hackett, 2019; Wang et al., 2019).

To evaluate the inversion-based environment, refractivity for the forward models that resulted in lowest PL MSE are compared to the (refractivity) inverse solutions in Figure 9, where it should be noted that forward model cases with range dependent refractivity are averaged over range to improve legibility of the figure (e.g., COAMPS refractivity profile in Figure 9a). The most striking differences occur with respect to the mixed layer slope (e.g., Figures 9A, 9I or 9L); however, it has been shown that differences in the mixed layer slope do not affect propagation as significantly as other refractive parameters in the near surface (Lentini & Hackett, 2015; Matsko & Hackett, 2019; Pastore et al., 2021; Penton & Hackett, 2018), resulting in a relative insensitivity of the GA optimization to this parameter. Much more important is the duct height and the shape below the duct height (Cherrett, 2015; Pastore et al., 2021). In many cases, EDHs from the inversions are similar to other estimates

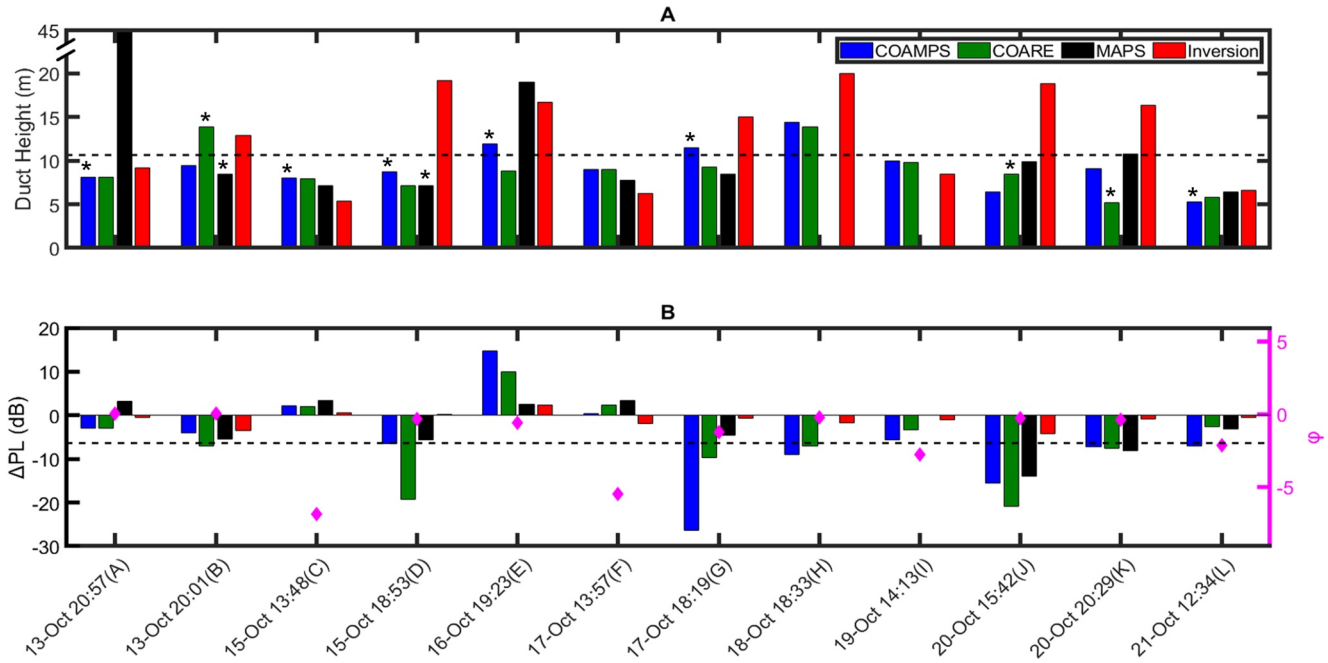


Figure 10. (a) Duct heights for each forward method and the inverse solution for all experiments where the horizontal dashed line represents average EM transmitter height. Evaporation duct height (EDH) in (a) for range dependent refractivity is a mean EDH over range, denoted with an asterisk. (b) Difference between measured and modeled propagation loss averaged over all receiver heights and ranges greater than 30 km on the left *y*-axis and average atmospheric stability (φ) on the right *y*-axis. $\varphi = -2$ is marked by the horizontal dashed line in (b). Experiment label corresponding to Table 1 precedes the radar start time on the *x*-axis.

(see Table 1). Disagreements in EDH could be caused by temporal and spatial evolution of the environment during RF measurements (collected over ∼1.5–3 hr and over ∼50 km) as also mentioned in Wang et al. (2019). Consequently, none of the predictions are likely to represent the "true" environment that the EM waves traversed; thus, discrepancies between the refractivity estimates are expected.

To scrutinize the comparisons of EDH specifically, Figure 10a shows EDH comparisons between the forward methods determined to be the "best" estimate of the environment (determined by the lowest propagation loss MSE for each refractive estimation method) for each RF data set and EDH derived from the inverse solutions; note that EDH for range-dependent refractivity is represented by an average EDH over range. Figure 10b shows average stability over the radar data acquisition time, $\varphi = z/L$, where $z = 12$ m and L is the Monin-Obukhov length based on R/V Sharp measurements. For bulk meteorological measurements, L is defined in Fairall et al. (1996):

$$L^{-1} = \frac{\frac{\kappa g}{T}\left(T_* + 0.61 T q_*\right)}{u_*^2} \tag{4}$$

where T_*, q_*, and u_* are scaled temperature, humidity, and wind speed respectively (Fairall et al., 1996), g is gravitational acceleration, and κ the von Karman constant. When $\varphi < -2$ (denoted by the horizontal black dashed line in Figure 10b), which is indicative of highly unstable environments, EDH across all methods is in relatively good agreement, and all PL estimates show good agreement with RF measurements at long range. This result is shown in Figure 10b, where the bars show ΔPL, which is average propagation loss difference between each respective method and the measured RF over all receiver heights at ranges greater than 30 km. Ranges greater than 30 km are used for comparison because this region is most influenced by trapping of EM waves; furthermore, this region is mostly devoid of multipath peaks/nulls that can have large impacts on the MSE statistic. Thus, this region is expected to most accurately capture variations in propagation due to differences in the ducting phenomenon. Under such unstable environmental conditions, the inversion solution predicts the environment as well as the other methods. COARE and COAMPS/NAVSLaM are also known to perform best during unstable conditions (Fairall et al., 1996; Frederickson, 2016). Conversely, when $-2 < \varphi < 0.05$, EDH varies more substantially between the methods. Corresponding variations in Φ_{MSE} are at least partly due to these variations in EDH,

which are known to have significant effects on PL (Cherrett, 2015; Hitney & Vieth, 1990; Pastore et al., 2021). Neutral/stable regimes generally correspond to higher duct heights from the inversion solution, which is consistent with previous studies showing EDH increases in stable environments (Cherrett, 2015; Zhang et al., 2017). Higher EDH during near-neutral or stable conditions predicted by the inversion coupled with the more similar propagation (Figure 10b) suggests that the deviation of the inversion solutions from the other methods does not necessarily indicate that it is an inaccurate representation of the environment. The possibility exists that the spatiotemporal variability during RF data collection results in nonideal environmental estimates from the other methods presumably causing the discrepancies relative to the measured RF. Although other environmental characterizations beyond the stability parameter could be considered, these results still suggest that the inversion method employed in this study is a viable technique for obtaining estimates of atmospheric refractivity in all included stability regimes.

6. Summary and Conclusions

This study utilizes a unique data set to verify a PTP radar inversion approach that utilizes a metaheuristic algorithm and inverts for three parameters associated with evaporation ducts. 12 RF measurement sets from the CASPER-East campaign are compared to PL generated from several different forward models of refractivity and the inverse refractivity model. Due to finite time periods over which the propagation measurements are acquired, multiple options for environmental characterization exist for these forward methods. Several options were examined and the forward method that generated PL closest to that of the RF measurements were used for comparisons of both refractivity and PL from inverse solutions. All methods, inverse and forward, were in relative agreement during periods of large instability ($\varphi < -2$) in terms of propagation and EDH. However, when conditions were stable or near neutral more discrepancies between the methods were observed. In these cases, the inversion often predicted a higher EDH than other methods and also showed more accurate PL relative to the RF measurements suggesting that this inverse-based environment might be a better representation of the environment than other estimates because high EDH is consistent with stable regimes. In general, inversion solutions provide reasonable predictions of the environment under a range of conditions relative to the other methods examined and resulted in more accurate PL predictions at the locations of the receivers. Future research should involve inverting for range inhomogeneous refractive features to investigate the effect spatial variability of the environment can have on refractivity inversions.

Data Availability Statement

Access to the refractivity, propagation loss, and measured RF data are available at the DRYAD data repository at https://doi.org/10.5061/dryad.sbcc2fr61.

Acknowledgments
The authors would like to thank Frank Ryan (Applied Technology Inc.) for his assistance with the VTRPE simulation. They would also like to thank the Office of Naval Research and Program Officer Dr. Steven Russell for their support of this research (grants: N00014-16-1-2075, N00014-19-1-2350).

References

Alappattu, D. P., Wang, Q., Rainer, R., Yamaguchi, R., & Lind, R. J. (2016). *Characteristics of surface layer scalar profiles using the in-situ measurements from an undisturbed marine environment. 22nd conference on air-sea interaction*. American Meteorological Society. Retrieved from https://ams.confex.com/ams/21SATMET20ASI/webprogram/Paper297336.html

Anderson, R., Vasudevan, S., Krolik, J. L., & Rogers, L. T. (2001). Maximum a posteriori refractivity estimation from radar clutter using a Markov model for microwave propagation. In *IGARSS 2001. Scanning the present and resolving the future. Proceedings. IEEE 2001 international geoscience and remote sensing symposium (Cat. No. 01CH37217)* (pp. 906–909). IEEE.

Banner, M. L., Jones, I. S., & Trinder, J. C. (1989). Wavenumber spectra of short gravity waves. *Journal of Fluid Mechanics*, *198*, 321–344. https://doi.org/10.1017/s0022112089000157

Bean, B. R., & Dutton, E. J. (1968). *Radio meteorology* (1st ed.). College Entrance Book Company.

Buck, A. L. (1981). New equations for computing vapor pressure and enhancement factor. *Journal of Applied Meteorology and Climatology*, *20*(12), 1527–1532. https://doi.org/10.1175/1520-0450(1981)020<1527:nefcvp>2.0.co;2

Cherrett, R. C. (2015). *Capturing characteristics of atmospheric refractivity using observations and modeling approaches. (Dissertation)*. Naval Postgraduate School.

Compaleo, J., Yardim, C., Xu, L., Wijesundara, S., Johnson, J., & Burkholder, B. (2018). *Preliminary refractivity from clutter (RFC) evaporation duct inversion results from CASPER west experiment*. Proceedings of the 2018 IEEE radar conference. https://doi.org/10.1109/radar.2018.8378791

Donelan, M. A., Hamilton, J., & Hui, W. (1985). Directional spectra of wind-generated ocean waves. *Philosophical Transactions of the Royal Society of London - Series A: Mathematical and Physical Sciences*, *315*(1534), 509–562.

Fairall, C. W., Bradley, E. F., Hare, J. E., Grachev, A. A., & Edson, J. B. (2003). Bulk parameterization of air-sea fluxes: Updates and verification for the COARE algorithm. *Journal of Climate*, *16*(4), 571–591. https://doi.org/10.1175/1520-0442(2003)016<0571:bpoasf>2.0.co;2

Fairall, C. W., Bradley, E. F., Rogers, D. P., Edson, J. B., & Young, G. S. (1996). Bulk parameterization of air-sea fluxes for tropical ocean-global atmosphere coupled-ocean atmosphere response experiment. *Journal of Geophysical Research: Oceans*, *101*(C2), 3747–3764. https://doi.org/10.1029/95jc03205

Fountoulakis, V., & Earls, C. (2016). Inverting for maritime environments using proper orthogonal bases from sparsely sampled electromagnetic propagation data. *IEEE Transactions on Geoscience and Remote Sensing*, *54*(12), 7166–7176. https://doi.org/10.1109/tgrs.2016.2597138

Frederickson, P. (2016). *Navy atmospheric measurements for EM propagation modeling. (Executive summary)*. Naval Postgraduate School.

Garratt, J. R. (1994). The atmospheric boundary layer. *Earth-Science Reviews*, *37*(1–2), 89–134. https://doi.org/10.1016/0012-8252(94)90026-4

Gerstoft, P., Rogers, L. T., Krolik, J. L., & Hodgkiss, W. S. (2003). Inversion for refractivity parameters from radar sea clutter. *Radio Science*, *38*(3). https://doi.org/10.1029/2002rs002640

Gingras, D. F., Gerstoft, P., & Gerr, N. L. (1997). Electromagnetic matched-field processing: Basic concepts and tropospheric simulations. *IEEE Transactions on Antennas and Propagation*, *45*(10), 1536–1545. https://doi.org/10.1109/8.633863

Goldberg, D. E. (1989). Genetic algorithms and Walsh functions: Part II, deception and its analysis. *Complex Systems*, *3*, 153–171.

Gossard, E. E., & Strauch, R. G. (1983). *Radar observation of clear air and clouds (Book)* (p. 14). Elsevier Developments in Atmospheric Science.

Halliwell, G., Bleck, R., & Chassignet, E. (1998). Atlantic Ocean simulations performed using a new hybrid-coordinate ocean model. In *EOS, transactions AGU, fall 1998 AGU meeting*.

Hitney, H. V., & Vieth, R. (1990). Statistical assessment of evaporation duct propagation. *IEEE Transactions on Antennas and Propagation*, *38*(6), 794–799. https://doi.org/10.1109/8.55574

Hodur, R. M. (1997). The Naval Research Laboratory's coupled ocean/atmosphere mesoscale prediction system (COAMPS). *Monthly Weather Review*, *125*(7), 1414–1430. https://doi.org/10.1175/1520-0493(1997)125<1414:tnrlsc>2.0.co;2

Hogan, T. F., Liu, M., Ridout, J. A., Peng, M. S., Whitcomb, T. R., Ruston, B. C., et al. (2014). The navy global environmental model. *Oceanography*, *27*(3), 116–125. https://doi.org/10.5670/oceanog.2014.73

Johnson, J. M., & Rahmat-Samii, V. (1997). Genetic algorithms in engineering electromagnetics. *IEEE Antennas and Propagation Magazine*, *39*(4), 7–21. https://doi.org/10.1109/74.632992

Karimian, A., Yardim, C., Gerstoft, P., Hodgkiss, W. S., & Barrios, A. E. (2011). Refractivity estimation from sea clutter: An invited review. *Radio Science*, *46*(06), 1–16. https://doi.org/10.1029/2011rs004818

Karimian, A., Yardim, C., Haack, T., Gerstoft, P., Hodgkiss, W. S., & Rogers, T. (2013). Toward the assimilation of the atmospheric surface layer using numerical weather prediction and radar clutter observations. *Journal of Applied Meteorology and Climatology*, *52*(10), 2345–2355. https://doi.org/10.1175/jamc-d-12-0320.1

Lentini, N. E., & Hackett, E. E. (2015). Global sensitivity of parabolic equation radar wave propagation simulation to sea state and atmospheric refractivity structure. *Radio Science*, *50*(10), 1027–1049. https://doi.org/10.1002/2015rs005742

Matsko, I. J., & Hackett, E. E. (2019). Impact of radar data sampling on the accuracy of atmospheric refractivity inversions over marine surfaces. *Radio Science*, *54*(7), 704–714. https://doi.org/10.1029/2018rs006757

Pastore, D. M., Greenway, D. P., Stanek, M. J., Wessinger, S. E., Haack, T., Wang, Q., & Hackett, E. E. (2021). Comparison of atmospheric refractivity estimation methods and their influence on radar propagation predictions. *Radio Science*, *56*(9), 1–17. https://doi.org/10.1029/2020rs007244

Paulus, R. A. (1989). *Specification for environmental measurements to assess radar sensors*. Naval Ocean Systems Center.

Paulus, R. A. (1990). Evaporation duct effects on sea clutter. *IEEE Transactions on Antennas and Propagation*, *38*(11), 1765–1771. https://doi.org/10.1109/8.102737

Penton, S. E., & Hackett, E. E. (2018). Rough ocean surface effects on evaporative duct atmospheric refractivity inversions using genetic algorithms. *Radio Science*, *53*(6), 804–819. https://doi.org/10.1029/2017rs006440

Pierson, W. J., Jr, & Moskowitz, L. (1964). A proposed spectral form for fully developed wind seas based on the similarity theory of SA Kitaigorodskii. *Journal of Geophysical Research*, *69*(24), 5181–5190. https://doi.org/10.1029/jz069i024p05181

Plant, W. J., & Irisov, V. (2017). A joint active/passive physical model of the sea surface microwave signatures. *Journal of Geophysical Research: Oceans*, *122*, 3219–3239. https://doi.org/10.1002/2017jc012749

Pozderac, J., Johnson, J., Yardim, C., Merrill, C., de Paolo, T., Terrill, E., et al. (2018). X -band beacon-receiver array evaporation duct height estimation. *IEEE Transactions on Antennas and Propagation*, *66*(5), 2545–2556. https://doi.org/10.1109/tap.2018.2814060

Rainer, R. B. (2016). *In-situ observation of undisturbed surface layer scaler profiles for characterizing evaporative duct properties (M.S. Thesis)*. Naval Postgraduate School Monterey United States.

Rogers, L. T., Hattan, C. P., & Stapleton, J. K. (2000). Estimating evaporation duct heights from radar sea echo. *Radio Science*, *35*(4), 955–966. https://doi.org/10.1029/1999rs002275

Rogers, L. T., Jablecki, M., & Gerstoft, P. (2005). Posterior distributions of a statistic of propagation loss inferred from radar sea clutter. *Radio Science*, *40*(6). https://doi.org/10.1029/2004rs003112

Ryan, F. J. (1991). *Analysis of electromagnetic propagation over variable terrain using the parabolic wave equation (No. NOSC/TR-1453)*. Naval Ocean Systems Center.

Saeger, J. T., Grimes, N. G., Rickard, H. E., & Hackett, E. E. (2015). Evaluation of simplified evaporation duct refractivity models for inversion problems. *Radio Science*, *50*(10), 1110–1130. https://doi.org/10.1002/2014rs005642

Sirkova, I. (2012). Brief review on PE method application to propagation channel modeling in sea environment. *Open Engineering*, *2*(1), 19–38. https://doi.org/10.2478/s13531-011-0049-y

Tabrikian, J., & Krolik, J. L. (1999). Theoretical performance limits on tropospheric refractivity estimation using point-to-point microwave measurements. *IEEE Transactions on Antennas and Propagation*, *47*(11), 1727–1734. https://doi.org/10.1109/8.814953

Tepecik, C., & Navruz, I. (2018). A novel hybrid model for inversion problem of atmospheric refractivity estimation. *International Journal of Electronics and Communications*, *84*, 258–264. https://doi.org/10.1016/j.aeue.2017.12.009

Ulate, M., Wang, Q., Haack, T., Holt, T., & Alappattu, D. P. (2019). Mean offshore refractive conditions during the CASPER East field campaign. *Journal of Applied Meteorology and Climatology*, *58*(4), 853–874. https://doi.org/10.1175/jamc-d-18-0029.1

Wagner, M., Gerstoft, P., & Rogers, T. (2016). Estimating refractivity from propagation loss in turbulent media. *Radio Science*, *51*(12), 1876–1894. https://doi.org/10.1002/2016rs006061

Wang, Q., Alappattu, D. P., Billingsley, S., Blomquist, B., Burkholder, R. J., Christman, A. J., & Franklin, K. B. (2018). CASPER: Coupled air-Sea Processes and electromagnetic ducting research. *Bulletin of the American Meteorological Society*, *99*(7), 1449–1471. https://doi.org/10.1175/bams-d-16-0046.1

Wang, Q., Burkholder, R. J., Yardim, C., Xu, L., Pozderac, J., Christman, A., et al. (2019). Range and height measurement of X-band EM propagation in the marine atmospheric boundary layer. *IEEE Transactions on Antennas and Propagation*, *67*(4), 2063–2073. https://doi.org/10.1109/tap.2019.2894269

Xiao-Feng, Z., Si-Xun, H., Jie, X., & Wei-Lai, S. (2011). Remote sensing of atmospheric duct parameters using simulated annealing. *Chinese Physics B*, *20*(9), 099201.

Yardim, C., Gerstoft, P., & Hodgkiss, W. S. (2009). Sensitivity analysis and performance estimation of refractivity from clutter techniques. *Radio Science*, *44*(1). https://doi.org/10.1029/2008rs003897

Zhang, Q., & Yang, K. (2018). Study on evaporation duct estimation from point-to-point propagation measurements. *IET Science, Measurement & Technology*, *12*(4), 456–460. https://doi.org/10.1049/iet-smt.2017.0342

Zhang, Q., Yang, K., & Yang, Q. (2017). Statistical analysis of the quantified relationship between evaporation duct and oceanic evaporation for unstable conditions. *Journal of Atmospheric and Oceanic Technology*, *34*(11), 2489–2497. https://doi.org/10.1175/jtech-d-17-0156.1

Zhang, Z., Sheng, Z., Shi, H., & Fan, Z. (2016). Inversion for refractivity parameters using a dynamic adaptive cuckoo search with crossover operator algorithm. *Computational Intelligence and Neuroscience*, *2016*(10), 2016. https://doi.org/10.1155/2016/3208724

Zhao, X. (2012). Evaporation duct height estimation and source localization from field measurements at an array of radio receivers. *IEEE Transactions on Antennas and Propagation*, *60*(2), 1020–1025. https://doi.org/10.1109/tap.2011.2173115

Zhao, X., & Huang, S. (2012). Estimation of atmospheric duct structure using radar sea clutter. *Journal of the Atmospheric Sciences*, *69*(9), 2808–2818. https://doi.org/10.1175/jas-d-12-073.1

Zhao, X., Huang, S., & Du, H. (2011). Theoretical analysis and numerical experiments of variational adjoint approach for refractivity estimation. *Radio Science*, *46*, RS1006. https://doi.org/10.1029/2010rs004417

Zhao, X., Yardim, C., Wang, D., & Howe, B. M. (2017). Estimating range-dependent evaporation duct height. *Journal of Atmospheric and Oceanic Technology*, *34*(5), 1113–1123. https://doi.org/10.1175/jtech-d-16-0125.1

Appendix C: Prepared Manuscript

Greenway, D.P., Vaughan, A.E., Kammerer, A.J., and E.E. Hackett (2024). Range-dependent variations of the evaporation duct, *in-preparation*.

Range-Dependent Variations of the Evaporation Duct

Daniel P. Greenway, Alexis E. Vaughan, Andrew J. Kammerer, and Erin E. Hackett

***Abstract*—Evaporation ducts are an observed electromagnetic phenomenon caused by rapid decreases of humidity with altitude. Sensing technologies that operate at X-band frequencies (8-12 GHz) exhibit extension of radar signals beyond the radar horizon and holes in coverage at high altitudes during evaporative ducting conditions. In addition, the evolution of the evaporation duct over range has been reported to cause further adverse effects on these technologies in some circumstances. However, in terms of the predictability of these effects, more research is still needed. This research explores evaporation duct variations over range and characterizes them based-on two numerical datasets from different latitudes, different hemispheres, and during different seasons as well as correlating their range distributions to distributions of other atmospheric variables. It is found, for both datasets, that most often a linear function accurately represents variations of evaporation duct characteristics over ~60 km in range, but higher-order functional distributions of evaporation duct characteristics with range do occur albeit less frequently. Furthermore, range distributions of mean wind speed and mean specific humidity within the evaporation layer are strongly correlated to the range distributions of duct height; while range distributions of duct shape are driven mainly by the specific humidity gradient in the evaporation layer. The mid-latitude dataset exhibits more complex range distributions during frontal events; while the equatorial dataset shows the most complex range distributions near sunrise.**

***Index Terms*— dimensionality reduction, evaporation duct, meteorological properties, radio wave propagation, evaporation duct height, inhomogeneity**

I. Introduction

Evaporation ducts are an atmospheric phenomenon that cause X-band electromagnetic (EM) waves to bend their trajectory towards the earth's surface. This downward bending can cause EM waves to be trapped near the earth's surface extending the radar's range of detection at low altitudes and this trapping, along with subrefraction above the duct, leads to "holes" in radar coverage at higher altitudes. These EDs are created by rapid decreases in humidity with height, making them a nearly permanent worldwide feature in marine and coastal environments ([1]). Vertical profiles of the index of refraction (*n*), atmospheric refractivity (*N*), or modified refractivity (*M*) are used to explore radar wave propagation in evaporative ducting conditions.

Atmospheric refractivity (*N*) is calculated using an empirical relationship described by [2]:

$$N = \frac{77.6}{T}p + \frac{373256e}{T^2} \tag{1}$$

where *T* is temperature (K), *p* is pressure (mb), and *e* is partial water vapor pressure (mb). Modified refractivity is considered, in lieu of atmospheric refractivity because it makes evaporative ducting conditions easy to detect as it accounts for earth's curvature:

$$\begin{aligned} \mathrm{M} &= (\mathrm{n}-1)\times 10^6 + \left(\frac{z}{R_e}\right)\times 10^6 \\ &= \mathrm{N} + \left(\frac{z}{R_e}\right)\times 10^6 \end{aligned} \tag{2}$$

where R_e is the radius of the earth (m) and *z* is altitude (m). Any negative vertical gradient of modified refractivity ($\frac{\partial \mathrm{M}}{\partial z} < 0$) indicates the presence of ducting conditions.

Fig. 1 shows an example of a typical *M*-profile in evaporation ducting conditions and a few of its primary characteristics known to cause changes in radar wave propagation in the lowest 100 meters ([3]). These primary characteristics are the duct height, which is the critical point within a modified refractivity profile (i.e., when $\frac{\partial \mathrm{M}}{\partial z} = 0$), and the duct shape previously quantified by the altitudinal-mean second derivative of modified refractivity within the evaporation layer ($\overline{\frac{\partial^2 M}{\partial z^2}}$; [4]).

M-profiles depend on temperature, pressure, and humidity (Eqns. 1 & 2) but prediction of the distribution of these thermodynamic properties based on atmospheric dynamics in the near surface region is complex and an active area of research; consequently, the linkages between EDs and atmospheric conditions are not fully understood. It is known EDs are mainly affected by near surface wind speed, air temperature, sea surface temperature (SST), and relative humidity ([1], [5]). However, reference [6] reports that the response of duct height to these variables is dependent on atmospheric stability (e.g., air-sea temperature difference

Manuscript received INSERT DATE HERE; revised INSERT DATE HERE; accepted INSERT DATE HERE. This work was supported by the Office of Naval Research (grant: N00014-19-1-2340).

Daniel P. Greenway is with the Department of Marine Science at Coastal Carolina University Conway, SC 29572 USA (email: dpgreenwa@coastal.edu)

Alexis E. Vaughan is with the Department of Marine Science at Coastal Carolina University Conway, SC 29572 USA (email: aevaugh1@coastal.edu)

Andrew J. Kammerer is with the Marine Meteorology Division at the Naval Research Laboratory Monterey, CA 93943 USA (email: Andrew.kammerer@nrlmry.navy.mil)

Erin E. Hackett is with the Department of Marine Science at Coastal Carolina University Conway, SC 29572 USA (email: ehackett@coastal.edu)

(ASTD)). More recent studies have revealed strong mathematical relationships between regional

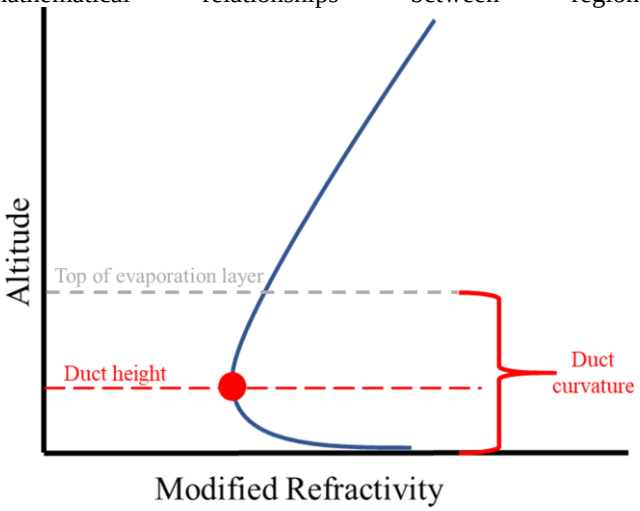


Fig. 1. Primary characteristics (in red) of an M-profile in evaporation ducting conditions that primarily impact X-band radar propagation within the lowest 100 meters of the atmosphere. The evaporation layer is also defined as twice the duct height.

evaporation and evaporation duct height ([7]) and have used this relationship to predict evaporation duct height ([6]).

Contrarily, few have investigated atmospheric linkages to duct shape although duct shape has been reported to affect the propagation of X-band radar signals ([3], [8]). Reference [4] suggests variations of estimates of duct shape between different prediction techniques correlate to differences in ASTD, suggesting dependence on atmospheric stability. Furthermore, [9] finds that near-surface specific humidity gradients are strongly related to duct shape. In EM propagation studies, horizontal homogeneity is commonly assumed despite the occurrence of heterogeneous environments in locations such as coastal zones.

Horizontal variations in EDs have been shown to cause significant effects on radar wave propagation, and thus radar system performance. Reference [10] was the first to report that rays emitted at low elevation angles are sensitive to extreme horizontal variations of the atmosphere near the surface. Reference [11] further found that radar propagation differences between homogeneous and heterogeneous environments were large at ranges greater than 30 kilometers from the radar, suggesting that one needs to account for heterogeneous environments to accurately predict long range propagation. Other studies have reached similar conclusions ([12], [13], [14], [15], [16]). However, these studies mainly focus on heterogeneous variations of refractivity and their impacts on propagation, but don't investigate the likelihood of different heterogeneous distributions of refractivity and how they connect to prevailing meteorological conditions. Thus, it is imperative to continue investigating typical horizontal distributions of duct height and duct shape in marine environments, understand how radar systems are being affected, and deepen our understanding of the interplay between horizontal variations of these evaporation duct characteristics and the atmospheric state.

The horizontal distribution of evaporation duct height has been most commonly studied. Reference [12] revealed that evaporation duct heights typically vary by just a few meters over ranges of up to 200 km. Reference [14] showed that drastic decreases in evaporation duct height of 5 meters over less than 10 km can occur around a coastal headland, which is subject to large horizontal changes in wind speed depending on the wind direction. Reference [17] found that evaporation duct heights typically increased from a height of 7 meters near California to 15 m near Hawaii. Most recently, reference [16] has reported that the evaporation duct height increases offshore of Duck, North Carolina during autumn. More research is needed investigating the probabilities of occurrence and meteorological causes of certain horizontal duct height distributions. Such trends could be seasonally dependent at certain latitudes or modified during certain synoptic-scale events such as weather fronts. Lastly, to the authors' knowledge, horizontal variations of evaporation duct shape, independent of shape changes due to duct height variations, have yet to be studied.

This research aims to address some of these knowledge gaps by exploring the interplay of atmospheric variables well known to affect EDs (wind speed, humidity, temperature, and ASTD), along with variables less explored (humidity gradient, wind shear, gradient Richardson number, and sea level pressure), with ED characteristics (duct height and shape) using two verified numerical weather prediction model forecasts in coastal environments, where heterogeneous environments have been observed. These numerical weather prediction (NWP) forecasts were generated as part of large field campaigns, located in different hemispheres in different seasons and at different latitudes, and have been verified against direct meteorological measurements ([16], [18]). The NWP forecasts must be used in this study rather than direct measurements because they contain sufficient range resolution to carry out the analyses. Typical distributions of duct height and duct shape over range are classified and probabilities of occurrence are investigated. These distribution types are correlated to the aforementioned range distributions of atmospheric variables to determine linear relationships, while principal component analysis is used to decipher multivariate relationships.

II. Data

The Coupled/Ocean Atmosphere Mesoscale Prediction System (COAMPS®; [19]) is used to generate weather forecasts to explore heterogeneous variabilities in evaporation ducts. COAMPS® is a high-resolution, nonhydrostatic mesoscale model based upon the Navier-Stokes equations that describe temporal changes in atmospheric variables such as pressure (p), temperature (T), and humidity (q), which can be used to estimate modified refractivity (M) ([19]) as discussed in Section I. COAMPS® has been used to provide operational forecasts for the U.S. Naval Fleet as well as used in historical case studies to validate and advance forecast skill ([18]; [20]; [21]; [22]; [23]).

More specifically, simulated vertical profiles of modified refractivity, wind speed, specific humidity, and air temperature along with bulk sea-surface temperatures along cross-shore transects predicted by COAMPS® verified for two separate field campaigns are utilized for analysis. The two field campaigns include the Coupled Air-Sea Processes and

Electromagnetic Ducting Research East field campaign (CASPER-East; [24]) and the Tropical Air Propagation Study (TAPS; [18]). Each numerical dataset consists of predictions for these field campaigns occurring in different hemispheres at different latitudes, and during different seasons, offering insight into whether phenomenon examined herein are strongly location or seasonally dependent. Other *in-situ* meteorological datasets measured during both field campaigns, but not used extensively here, are measurements from repeated winched tethered balloons, research vessels (R/V), and on piers. See [24] and [18] for further information on CASPER-East and TAPS field campaigns, respectfully.

COAMPS forecasts are two-way coupled with NCOM and use initial boundary conditions estimated from the Navy Global Environmental Model (NAVGEM; [25]) for the atmosphere and the Global Hybrid Coordinate Ocean Model (HYCOM; [26]) for the ocean. Forecasts are hourly using a 6-hour update cycle during both field campaigns. To enable resolution of evaporation ducts near the ocean surface, COAMPS® is blended with a surface layer model – the Navy Atmospheric Vertical Surface Layer Model (NAVSLaM; [27]). The blending process, similar to that discussed by [28], [29], and [4], results in cross-shore transects of meteorological vertical profiles for both field campaigns examined in this study. The blended method uses COAMPS® specific humidity, atmospheric pressure (p), and wind speed near the surface along with bulk sea surface temperatures (SSTs) from the Navy Coupled Ocean Model (NCOM) for NAVSLaM estimates of vertical profiles of specific humidity, wind speed, air temperature, and modified refractivity. These blended forecasts are referred to as COAMPS hereafter for simplicity.

CASPER-East transects are forecasted from Duck Pier in North Carolina to ~62 km offshore with ~2 km horizontal spacing and decimeter vertical spacing and are estimated hourly between October 12 and November 6, 2015. Cross shore transects from TAPS occur from a jetty offshore of Ingham, Queensland to ~86 km offshore with ~1.5 km horizontal spacing and decimeter vertical spacing hourly between November 24 and December 5, 2013. Both transects are shown in Fig. 2. TAPS forecasts are linearly interpolated over range at each altitude to the same horizontal spacing as CASPER-East forecasts for ease of analysis. If a forecast contains an elevated duct within the first 100 meters of altitude at any range along a transect, then the entire transect is removed to focus exclusively on evaporation ducts. This filtering results in a total of 460 cross-shore transects (each with 31 vertical profiles for a total of 14260 M-profiles) for CASPER-East and 216 cross-shore transects (31 vertical profiles per transect for a total of 6696 M-profiles) for TAPS. Examples of modified refractivity profiles used in this study from both the CASPER-East and

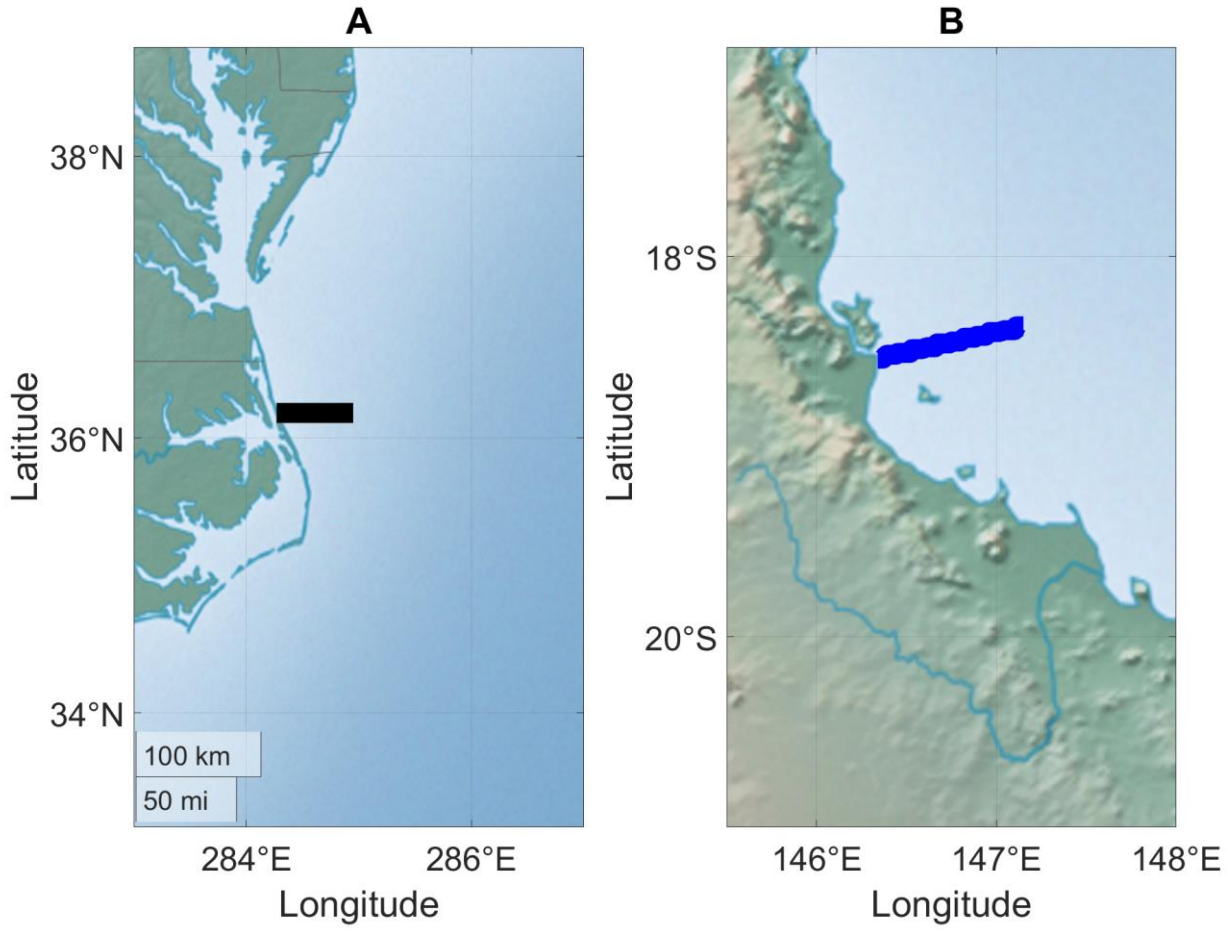


Fig. 2. COAMPS® transect locations from CASPER-East (A - black line) and TAPS (B- blue line).

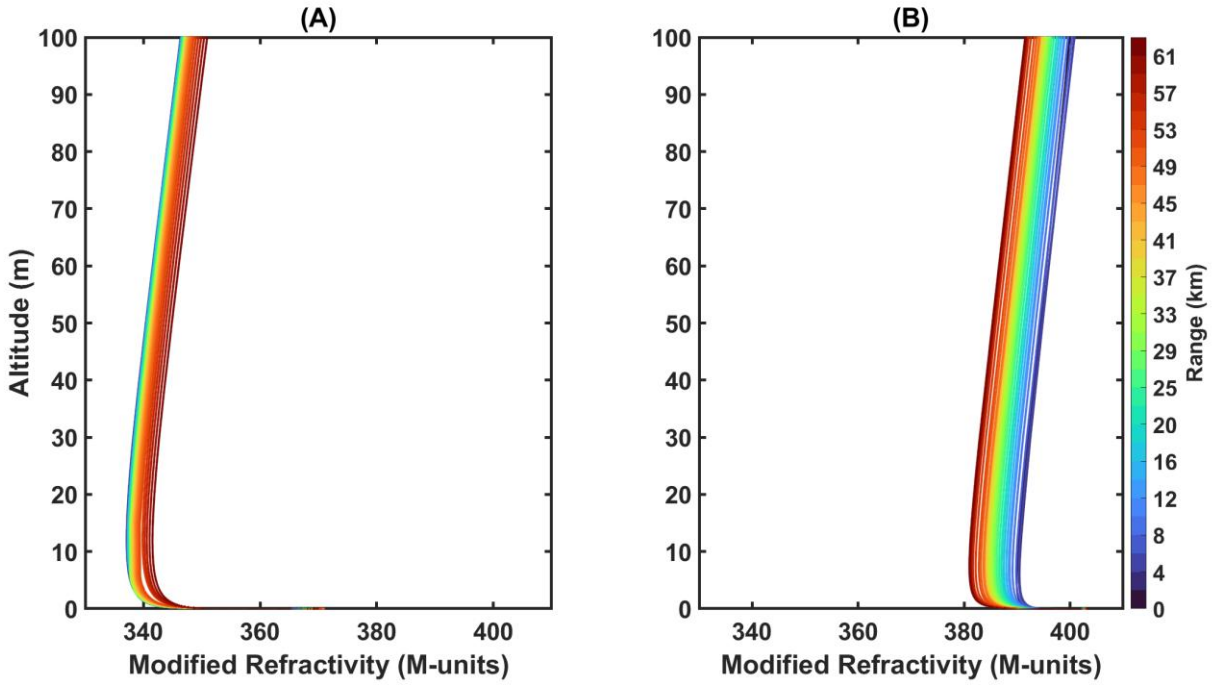


Fig. 3. Example vertical profiles of modified refractivity at various ranges for a COAMPS-NAVSLaM blended forecast during CASPER-East (A) and TAPS (B) field campaigns. Note that the TAPS forecast shown is linearly interpolated over range to the same horizontal resolution as the CASPER-East (A) forecast.

(interpolated) TAPS datasets are illustrated in Fig. 3.

III. Methods

The purpose of this study is to examine typical distributions of heterogeneous evaporation ducts in coastal regions and generally explore the relationships between horizontal variations of evaporation duct characteristics and the horizontal variations of other atmospheric variables. These explorations shed light on which atmospheric parameters may be driving changes in the evaporation duct over cross-shore transects.

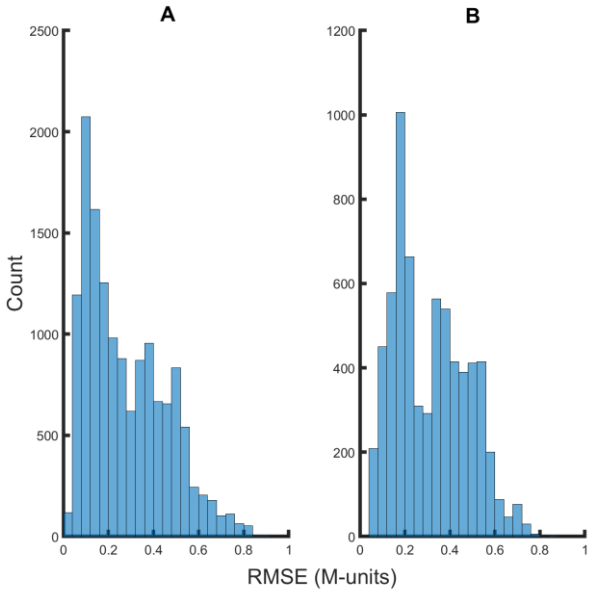


Fig. 4. RMSEs between each NWP M-profile and the M-profile for the corresponding parametric model fit (Eqn. 3) for both CASPER-East (A) and TAPS (B) field campaigns.

Each *M*-profile within each transect (described in Section II) is fit using a weighted iterative non-linear least squares regression to an evaporation duct parametric refractivity model described by [30]:

$$M(z) = M_0 + \begin{cases} c_0\left(z - z_d \ln\left(\frac{z + z_0}{z_0}\right)\right), & z_L \le z \\ m_1 z - M_1, & z > z_L \end{cases} \quad (3)$$

where z is altitude, M_0 is surface modified refractivity, c_0 is the potential refractivity gradient - a parameter shown to be directly related to duct curvature or shape ([9]), m_1 is the modified refractivity slope of the mixed layer, z_d is the evaporation duct height, M_1 is a parameter ensuring continuity between the two layers (and is defined by the other parameters), z_0 is the aerodynamic roughness factor, and z_L is the altitude of the top of the evaporation layer, where $z_L \equiv 2z_d$. $z_0 = 0.0015$ m, which is the average value for oceanic conditions ([31]) and remaining parameters (M_0, c_0, m_1, and z_d) are estimated in the regression. Initial guesses for each parameter are estimated using the surface modified refractivity (M_0) of the COAMPS *M*-profile, the commonly assumed neutral stability value for c_0 (0.125 M-units/m) ([32]; [33]; [34]; [35]; [36]; [37]), the altitude of the minimum modified refractivity for z_d, and the slope of modified refractivity ($\frac{\Delta M}{\Delta z}$) between the highest altitude (z = 100 m) and z_L (where z_d defining z_L uses the z_d initial guess). The weights of the regression technique are distributed such that data at altitudes $\pm$1.5 m closest to the initial guess of z_d are weighted twenty-five times more than that of other altitudes. Because the duct height influences propagation most significantly ([3], [4])

greater emphasis is placed on its accurate prediction in the regression. A histogram of root-mean-square errors (RMSEs) calculated between each COAMPS *M*-profile and its corresponding parametric model fit for all transects are illustrated in Fig. 4. This weighting scheme and regression technique results in all fits having an RMSE of less than 1 *M*-unit, making the parametric model an ideal representation of the modified refractivity vertical profiles. These regressions, performed for vertical refractivity profiles at each range and for each forecast time, result in a single range distribution of these fit evaporation duct characteristics (M_0, c_0, m_1, and z_d) for every forecast during both field campaigns. Range-distributions of duct height (z_d) and duct shape (via the c_0 parameter) for each forecast are used to categorize the various range-dependent variations of the evaporation duct for both datasets. These distributions are further utilized to compute Pearson's correlation coefficient with various atmospheric properties as well as principal components analyses (PCA) to characterize which atmospheric properties may be driving range-variations of the evaporation duct.

Distributions of z_d and c_0 over range are categorized into one of six categories for each forecast: linear, quadratic, cubic, 4th-degree, oscillatory, or step. Categorizations are determined by fitting z_d or c_0 over range for each forecast to a polynomial function using linear least squares regression.

Range-distributions of z_d are categorized using an ordered operation of linear least squares regression polynomial fits. Polynomials from linear up to 4th degree are fit to range-distributions of z_d for each forecast until a polynomial fit produces an RMSE of less than 0.60 m and contains an absolute bias at all ranges that is less than 2 m. These thresholds followed guidelines found in reference [38], which states that range variations of z_d as small as 1 m over range cause differences in propagation loss of at least 10 dB at ranges far from the transmitter (> 45 km). The order of polynomial fits applied over range to each forecast is from lowest-degree (linear) to highest degree (4th degree) to avoid unneeded model complexity when multiple models meet the accuracy requirements. The lowest degree which fulfills the above conditions (RMSE < 0.6 m and max bias < 2 m) is the classification of the z_d distribution for that forecast. If none of these polynomials fulfill the criteria, then a 7th degree polynomial is fit to the distribution of z_d over range. If the RMSE for the 7th degree polynomial fit is < 1 m, the forecast is categorized as oscillatory, otherwise, it is categorized as a step function. These categorizing criteria (i.e., RMSE < 0.6 m and max bias < 2 m) are chosen because visual inspection of fits and range distribution patterns showed most distinct variations between each category with these criteria. The authors found that stricter conditions would lead to too many seemingly unnecessary higher-order categorizations, while more lenient conditions would lead to too many linear categorizations that were poor-fits visually. Fig. 5 shows examples of each z_d range-distribution category.

Range-distributions of c_0 are categorized similarly to z_d distributions but instead utilize criteria of an RMSE < 0.03 M-units/m and an absolute bias at every range that is less than 0.12 M-units/m. These criteria were chosen by cursory findings that suggested variations of c_0, which were as small as 0.03 M-units/m over range, could cause nonnegligible effects on X-band radar wave propagation. These thresholds should be further verified, but they were found to best represent the different types of range distributions visually as well. A c_0

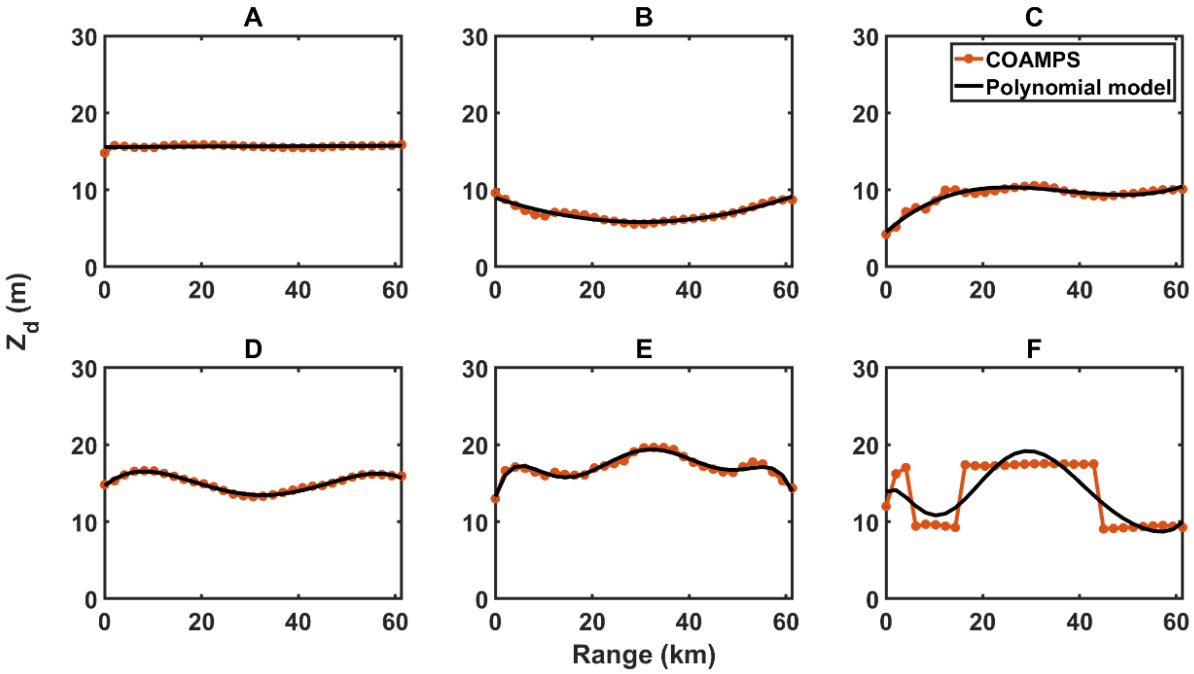


Fig. 5. Examples of linear (A), quadratic (B), cubic (C), 4th degree polynomial (D), oscillatory (E), and step-like distributions (F) of z_d over range found throughout this study. Corresponding polynomial fits are shown in black on each plot. Note that the black lines in E and F show the fit of a seventh-degree polynomial to z_d over range.

distribution is categorized as oscillatory if a 7th order polynomial fit produces an RMSE < 0.03 M-units/m, otherwise it is categorized as a step function. Fig. 6 shows examples of each c_0 range-distribution category.

Potential atmospheric causes of the different categories of z_d and c_0 range-distributions are investigated using range-distributions of atmospheric variables. Atmospheric variables include sea level pressure (SLP), mean gradient Richardson number ($\overline{Ri}$), mean temperature ($\bar{T}$), air-sea temperature difference (ASTD), mean specific humidity ($\bar{q}$), specific humidity gradient ($\frac{dq}{dz}$), mean wind speed ($\bar{U}$), wind shear ($\frac{dU}{dz}$), and bulk sea surface temperature (SST).

Ri is calculated:

$$Ri(z,r) = \frac{\frac{g}{T_v}\frac{\partial \theta_v(z,r)}{\partial z}}{\left(\frac{\partial U(z,r)}{\partial z}\right)^2 + \left(\frac{\partial V(z,r)}{\partial z}\right)^2} \quad (4)$$

where g is gravitational acceleration (9.81 m/s^2), θ_V is the virtual potential temperature, T_v is the average virtual temperature over all altitudes between the surface (z = 0 m) and $z = z_{ref}$ where z_{ref} is a reference altitude. U and V are the real wind components towards the east and north, respectively. Ri is calculated at each altitude and range, the altitudinal average between the surface and $z = z_{ref}$ at each range is used to calculate $\overline{Ri}$ transects for this study. The mean temperature, specific humidity, and wind speed are calculated by taking the mean of each variable over all altitudes from the surface to $z = z_{ref}$. ASTD is calculated by subtracting the bulk SST from the air temperature at $z = z_{ref}$. Gradients of specific humidity and wind speed (i.e., wind shear) are calculated by subtracting the respective variable at $z = z_{ref}$ from that at z = 0 m and dividing by z_{ref}. For z_d transect analyses, $z_{ref} = z_d$, while for c_0 transects $z_{ref} = 2z_d$. Thus, range-distributions of atmospheric variables for each duct characteristic analysis (z_d and c_0) are not the same, as each are averaged over altitudes that presumably most influence each duct characteristic respectively (Fig. 1).

For each hourly forecast, the forecasted range-distributions of each atmospheric variable previously described (i.e., SLP, $\bar{T}$, $\overline{Ri}$, ASTD, $\bar{q}$, $\frac{dq}{dz}$, $\bar{U}$, $\frac{dU}{dz}$, and SST) are correlated over range to both evaporation duct parameters (z_d and c_0) range distributions estimated from the nonlinear regressions. Thus, for each forecast from both CASPER-East and TAPS, 18 correlation coefficients are calculated for all combinations between each atmospheric variable, and each evaporation duct parameter.

Multivariate relationships are also investigated using principal component analysis (PCA). In this study, PCA utilizes a 10-dimensional dataset that includes range-distributions at one hourly forecast of each atmospheric parameter (i.e., SLP, $\overline{Ri}$, $\bar{T}$, ASTD, etc.) and a range-distribution of either z_d or c_0 as the 10th dimension during the same hourly forecast. Thus, PCA will be applied to each forecast twice, once using a transect of z_d, and once using a transect of c_0. A line is fit through each 10-dimensional space referred to as the first principal component, which generally describes the mean variation within the dataset. Further components are derived by creating lines of best fit orthonormal to the previous component. By projecting each of the 10 variables (i.e., SLP, $\overline{Ri}$, z_d, etc.) onto each component one

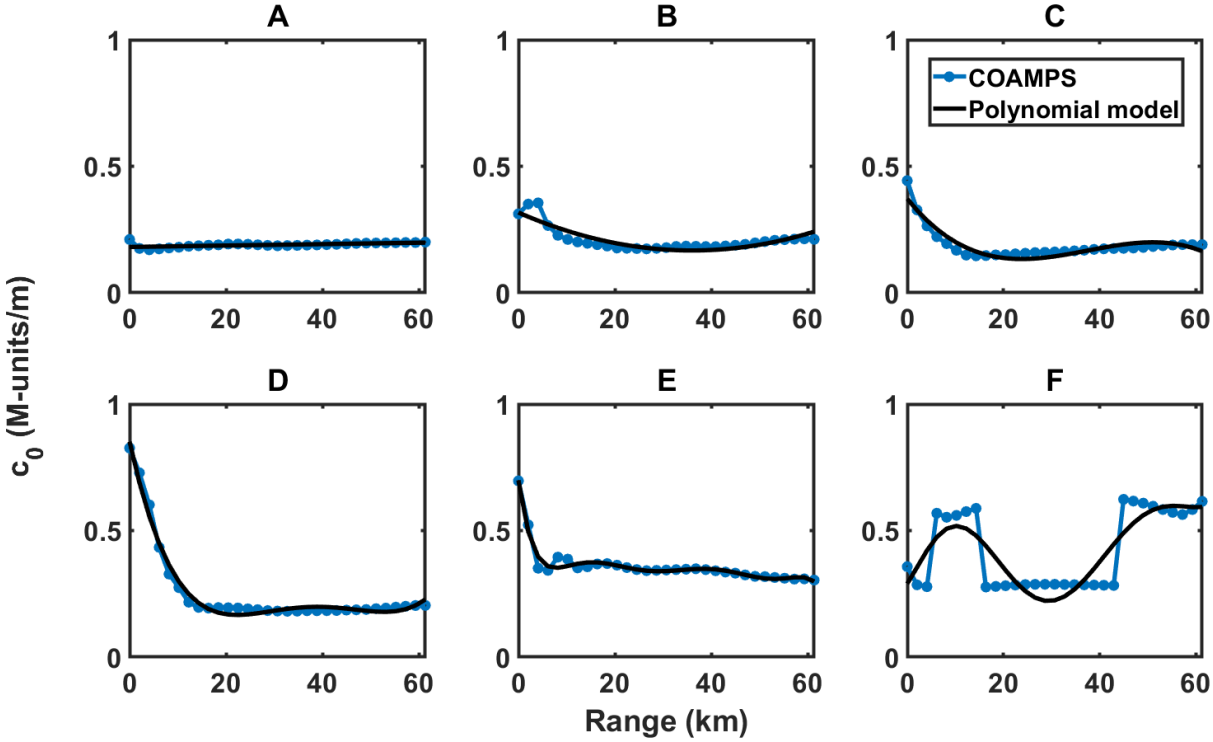


Fig. 6. Examples of linear (A), quadratic (B), cubic (C), 4th degree polynomial (D), oscillatory (E), and step-like distributions (F) of c_0 over range found throughout this study. Corresponding polynomial fits are shown in black on each plot. Note that the black lines in (E) and (F) show the fit of a 7th degree polynomial to c_0 over range.

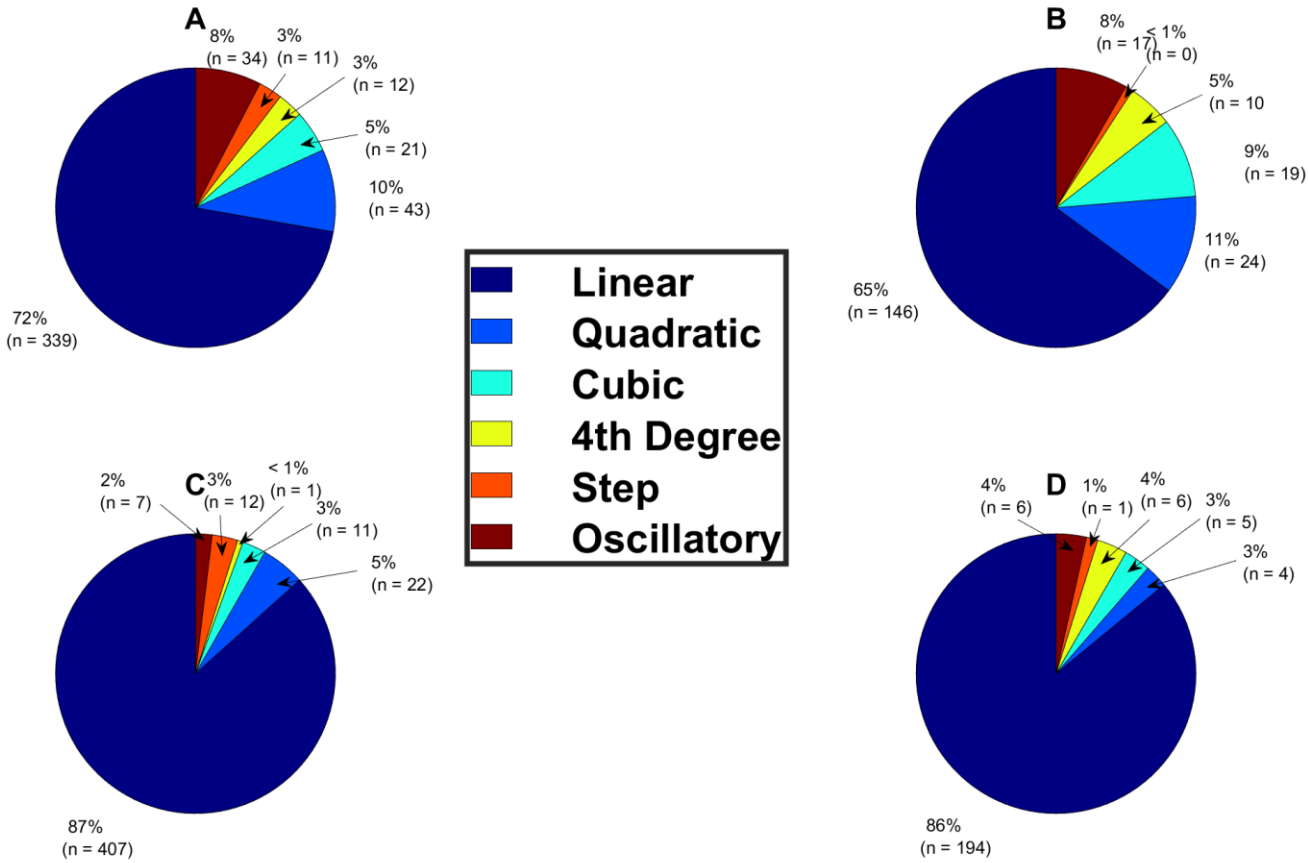


Fig. 7. Pie charts for frequency of occurrence for each type of evaporation duct parameter distribution examined in both CASPER-East (A and C) and TAPS (B and D). (A) and (B) show occurrence frequencies for z_d distributions, while (C) and (D) show occurrence frequencies for c_0 distributions.

can glean potential relationships between parameters, providing insight as to which variables vary together. This projection of a variable onto a component is commonly referred to as a loading. Atmospheric variable loadings onto the component where the highest loading of either z_d or c_0 occurs are determined for all forecasts.

Lastly, occurrence frequency of categorically sorted z_d and c_0 range-distributions and their variation over the diurnal cycle during both field campaigns allows discussion about common heterogeneous distributions, how often they occur, and when each distribution type might be expected. Results from linear correlations and PCA loadings offer fresh insights about which atmospheric conditions lead to heterogeneous evaporation ducting scenarios. Comparisons between both field campaigns can provide insight into which atmospheric variables, if any, can be used to parameterize heterogeneous evaporation ducts in a variety of locations and seasons.

IV. Results And Discussion

Pie charts showing the frequency of occurrence of each range-distribution category are shown in Fig. 7. From this figure, it is clearly evident that linear z_d and c_0 range-distributions occur most often for both datasets (>60% and >80% of the time, respectively). These results suggest that further work investigating heterogeneous effects on electromagnetic propagation should first focus on effects caused by linear distributions of both z_d and c_0. It is also clear that z_d range-distributions are more frequently higher-order than c_0 distributions. Although generally similar, TAPS forecasts illustrate fewer z_d or c_0 step-like range-distributions compared to CASPER-East. These differences between CASPER and TAPS may be due to differences between the diurnal cycles of both locations, or the presence of different mesoscale atmospheric phenomena. Following these hypotheses, the next subsections explore the frequency of occurrence between range-distributions with respect to the diurnal cycle (Section 4A), as well as linear (Section 4B) and multivariate (Section 4B) correlations of z_d and c_0 range-distributions to range-distributions of atmospheric variables previously mentioned.

A. *Diurnal Cycle*

Patterns of both z_d and c_0 range-distribution categories with the diurnal cycle are explored in Fig. 8. Fig. 8A shows that linear distributions over range may be more common throughout the hottest part of the day (i.e., between 12:00-18:00 EDT) as evidenced by the brighter blue colors during this time period for CASPER-East. Furthermore, higher-order range-distributions of z_d (cubic and above) occur least frequently during this hottest part of the day, where linear distributions dominate. TAPS results show that linear distributions of z_d peak a little later in the day comparatively, and are infrequent near sunrise and early morning (Fig. 8B). Linear range-distributions

of c_0 tend to follow the same trends as z_d for each respective field campaign but in a manner that is slightly less coherent than the z_d trends. Trends for the higher order distributions of c_0 are inconsistent, especially for CASPER-East, and are based-on only a few cases, but typically occur during nighttime for CASPER-East and during sunrise to late morning for TAPS. These differences might suggest temporary dominance of more

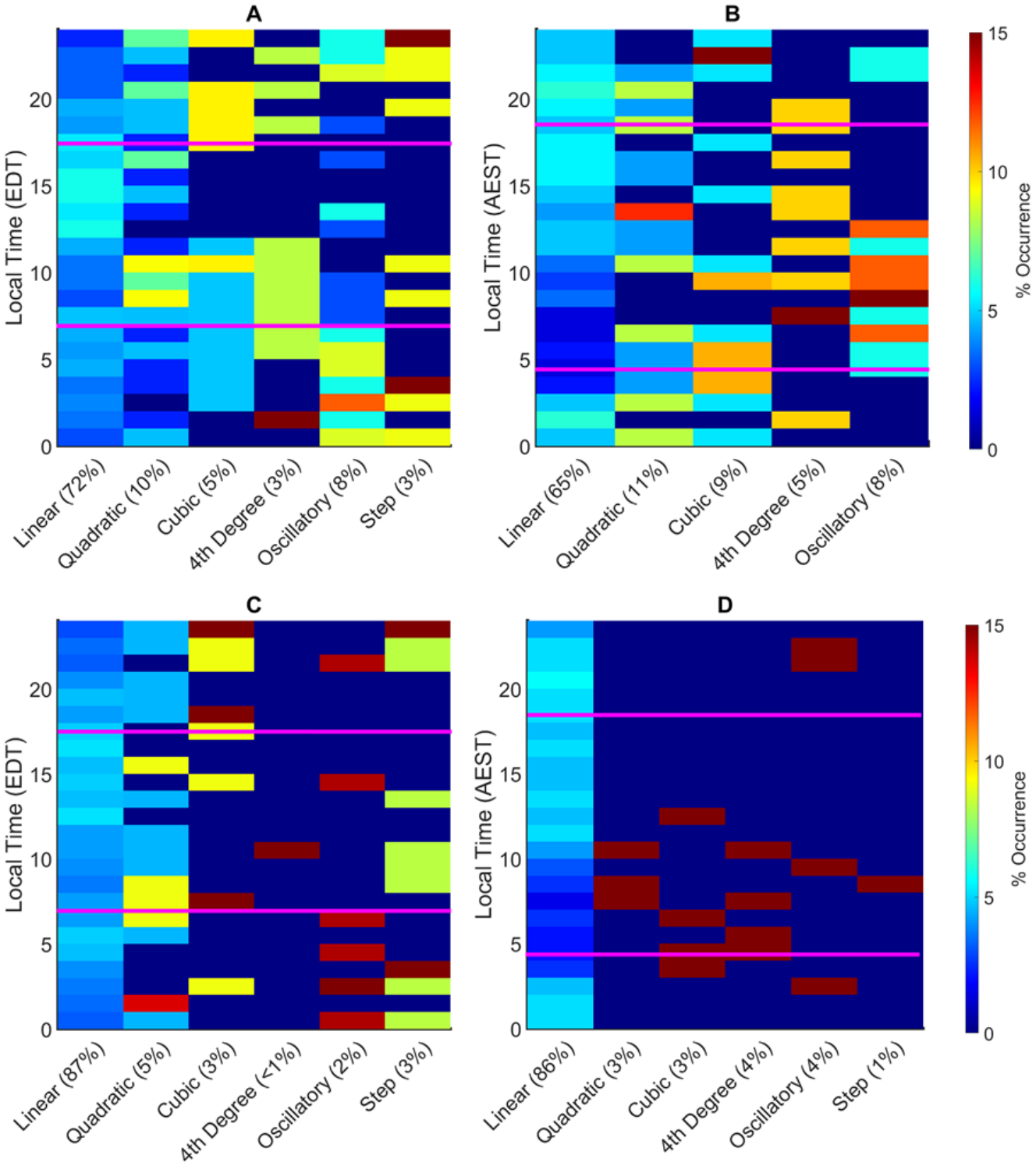


Fig. 8. Frequency of occurrence of z_d (A and B) and c_0 (C and D) range-distribution categories binned by local time during both CASPER-East (A and C) and TAPS (B and D) field campaigns. Occurrence is represented as a percentage of the number of z_d or c_0 distributions occurring at a specific local time divided by the total number of distributions in its range-distribution category. Only percentages between 0-15% are shown to improve visibility of variations for the linear category (which is the most common category within TAPS and CASPER-East). Magenta lines illustrate sunrise and sunset. Lastly, percentages on the x-axis are the percentages of occurrence for each distribution type within each dataset.

localized weather patterns are associated with the higher order distributions, which is why they are also uncommon.

In general, linear variations of z_d are relatively similar with slight offset in timing between the two field campaigns suggesting that the diurnal cycle may play a part in the commonly occurring linear variation with range. This connection might be expected as the influence of the land-sea boundary diminishes moving seaward along the cross-shore transect. During the daytime, differential heating between the land and sea can drive development of internal boundary layers near the coast influencing duct height distributions cross-shore.

B. Atmospheric Conditions

Fig. 9 shows the forecast-averaged Pearson's correlation coefficients calculated between range-distributions of many atmospheric variables and range-distributions of either z_d or c_0 to further investigate the physical properties associated with horizontal variations of evaporation duct characteristics. Dominant trends across both field campaigns reveal strong relationships both between mean wind speed or mean specific humidity and z_d along range. Mean temperature also varies strongly with duct height along range in TAPS but this relationship is not as influential or consistent in CASPER-East.

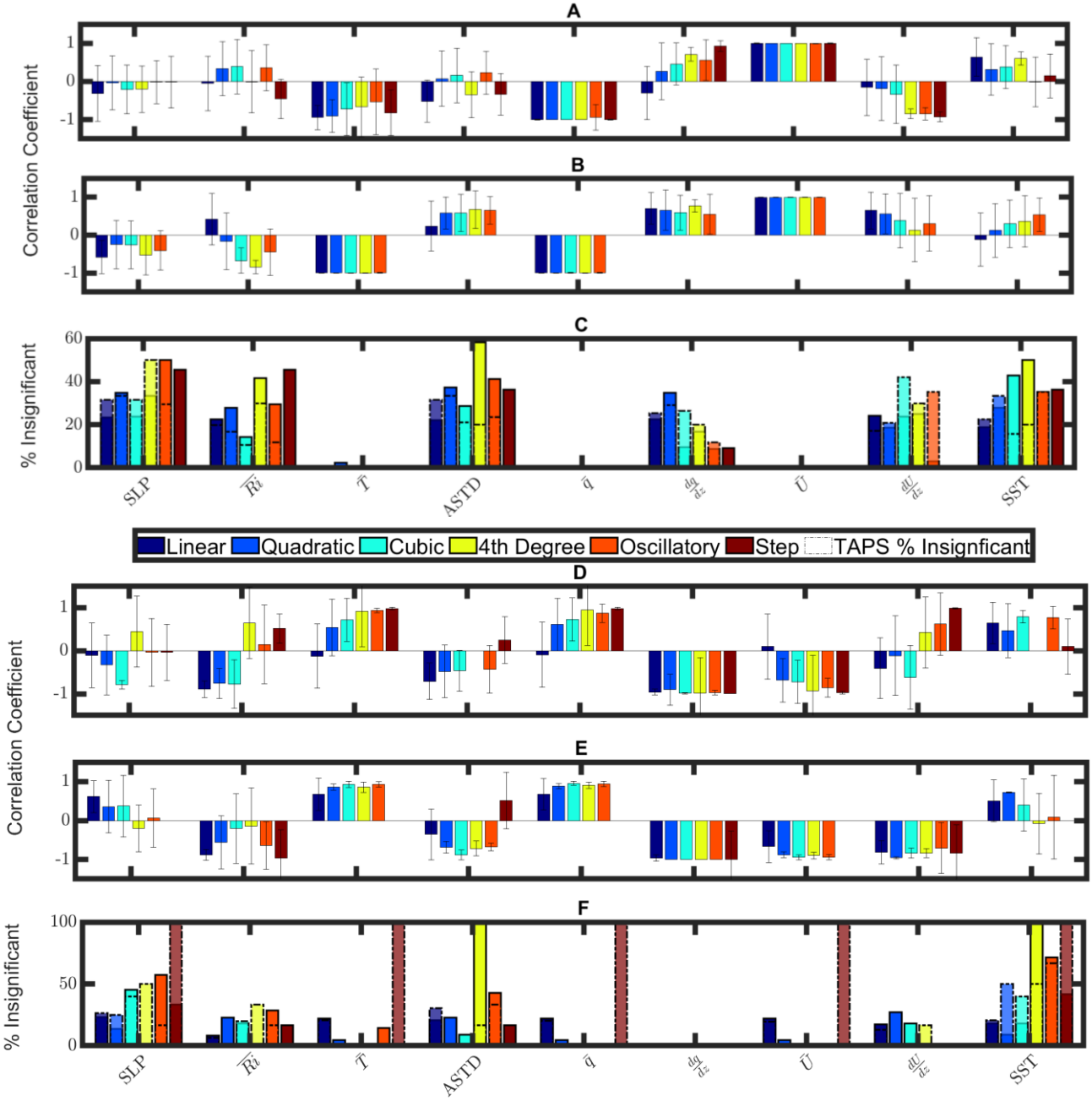


Fig. 9. Forecast-averaged correlation coefficients calculated between range-dependent distributions of different atmospheric parameters (see x-axis) and either z_d (A and B) or c_0 (D and E) range distributions during both CASPER-East (A and D) and TAPS (B and E) field campaigns. Error bars represent two standard deviations of correlation coefficients. C and F indicate the percentage of correlations which were insignificant in both field campaigns, where dashed bars represent the percentage during the TAPS field campaign.

For both field campaigns, specific humidity gradient is most strongly (inversely) correlated to c_0 along range; although mean wind speed, mean specific humidity, and mean temperature also show relatively strong significant correlations, with these relationships in TAPS being more consistent than those in CASPER-East. Range-correlations of other atmospheric variables to z_d or c_0 differ based-on field campaign or range-distribution type, or contain large fractions of insignificant results (Fig. 9C and 9F).

The direct relationship with wind speed indicates that as the average wind speed beneath the duct increases/decreases offshore, z_d typically increases/decreases and alternatively, the indirect relationship with mean specific humidity, indicates that as mean specific humidity increases/decreases below the duct height offshore, duct height decreases/increases. These results support statements from [1], [18], and [7] whom also noted similar relationships between the variation of z_d with wind speed or humidity. Physically, these results imply that more mechanical mixing near the surface is associated with increasing duct heights while more humid air at low altitudes can be associated with lower duct heights. Thus, for example, an increasing wind offshore may indicate a linear duct height trend in range with higher duct heights offshore.

Another clear finding from Fig. 9 is that c_0 distributions are inversely correlated to distributions of humidity gradient. However, large variance of the correlation coefficients occurs for CASPER-East, and in TAPS, no significant results are found for c_0 step distributions. Nevertheless, the inverse correlation suggests that as the humidity gradient decreases (becomes more negative) or increases (approaches zero) the duct curvature, c_0, increases or decreases, respectively, supporting results reported by [9], which found a strong inverse correlation between the humidity gradient and duct curvature/shape.

Although the above correlations are evident in both campaigns, some strong relationships appear during only one. TAPS forecasts indicate a strong correlation between z_d and mean temperature along range, but such a strong consistent correlation is not observed in the CASPER-East forecasts. Furthermore, during TAPS, mean wind speed and mean temperature are inversely correlated with c_0 more consistently; and while these correlations exist for CASPER-East, they are more variable and weaker.

The lack of a consistent relationship between z_d or c_0 with atmospheric stability metrics (i.e., ASTD and $\overline{Ri}$) is somewhat surprising but may be reflective of the relatively restricted stability regimes within each field campaign. During TAPS, the atmosphere was almost always unstable due to the low latitude (warm surface water temperatures) and the season (late spring/early summer), whereas more complex stability regimes are found along cross-shore transects during CASPER-East due to SST influences from the Gulf Stream and the fall season. Frequently, CASPER-East regimes include environments that switch from stable to unstable along a transect. The possibility that a lack of data is influencing these results is partly reflected in the large percentages of insignificant results for these atmospheric variables. ASTD doesn't correlate well to range-distributions of c_0 for all distribution types during CASPER-East, but shows moderate to strong inverse correlations during TAPS for higher-order polynomial distribution types. Furthermore, it was found that during all linear distributions of c_0, $\overline{Ri} < 0$ at all ranges. This observation suggests that linear distributions of c_0 along a transect tend to occur when the environment is unstable across the entire transect and conversely that higher-order distributions of c_0 are likely if the stability regime over range changes from unstable to free convective, or unstable to stable.

Although based-on limited statistics, for CASPER-East, frontal systems may explain the somewhat consistent stronger correlations between mean wind shear or mean temperature and z_d or c_0 for higher-order range-distribution types. In contrast, the absence of higher-order distributions of z_d correlating to wind shear during TAPS, as well as the low occurrence of step functions in general, further suggests frontogenesis as the cause of some of the higher-order distributions for CASPER-East since Queensland's latitude makes it insusceptible to frontogenesis. Also, all CASPER-East step distributions of c_0 occur during periods where mean wind speeds > 8 ms^{-1}, and when frontal effects from a cold front or a warm front were reported to occur during CASPER-East ([24]). Further work should investigate correlations between air temperature and wind shear variations with z_d or c_0 distributions during atmospheric phenomena such as thunderstorms or synoptic systems to further evaluate the hypotheses above.

The distributions of z_d and c_0 over range are related to complex nonlinear processes occurring at and above the air-sea interface, as such, although some consistent linear correlations were found, a multi-variate approach provides insight into coupled effects. The PCA method outlined in Section III is used to ascertain potential multivariate relationships between variables, where the results are illustrated in Fig. 10. Recall, PCA analysis is performed for a set of atmospheric variable transects and either z_d or c_0 transects for each forecast within a range-distribution category. The component on which either z_d or c_0 loads most strongly is identified and other variables that load onto that same component are identified and quantified by their loading. These loadings are averaged over all forecasts within a distribution category, and are shown as the bars in Fig.10.

In general, z_d tends to on-average load most heavily with both SST and ASTD rather than wind speed and specific humidity found previously. However, it is important to note that although the SST and ASTD loadings are large, they are also highly variable noted by the large error bars. In contrast, mean temperature and mean wind speed show small but consistent loadings illustrated by the very small error bars. Thus, these findings do not necessarily contradict those found in the linear correlation analysis. Instead, it illuminates the expected relationship of z_d with atmospheric stability that was seemingly absent in the linear correlation analysis. The high PCA loadings of SST and ASTD reflect sentiments made by [5], which states that the ASTD has a characterizing effect on the relationship of z_d with its environment. Furthermore, SST is a primary variable used to calculate evaporation rates, which have been reported to be directly related to the evaporation duct height ([39], [6]). These results further suggest that important non-linear relationships between stability (associated with SST and ASTD) and z_d exist.

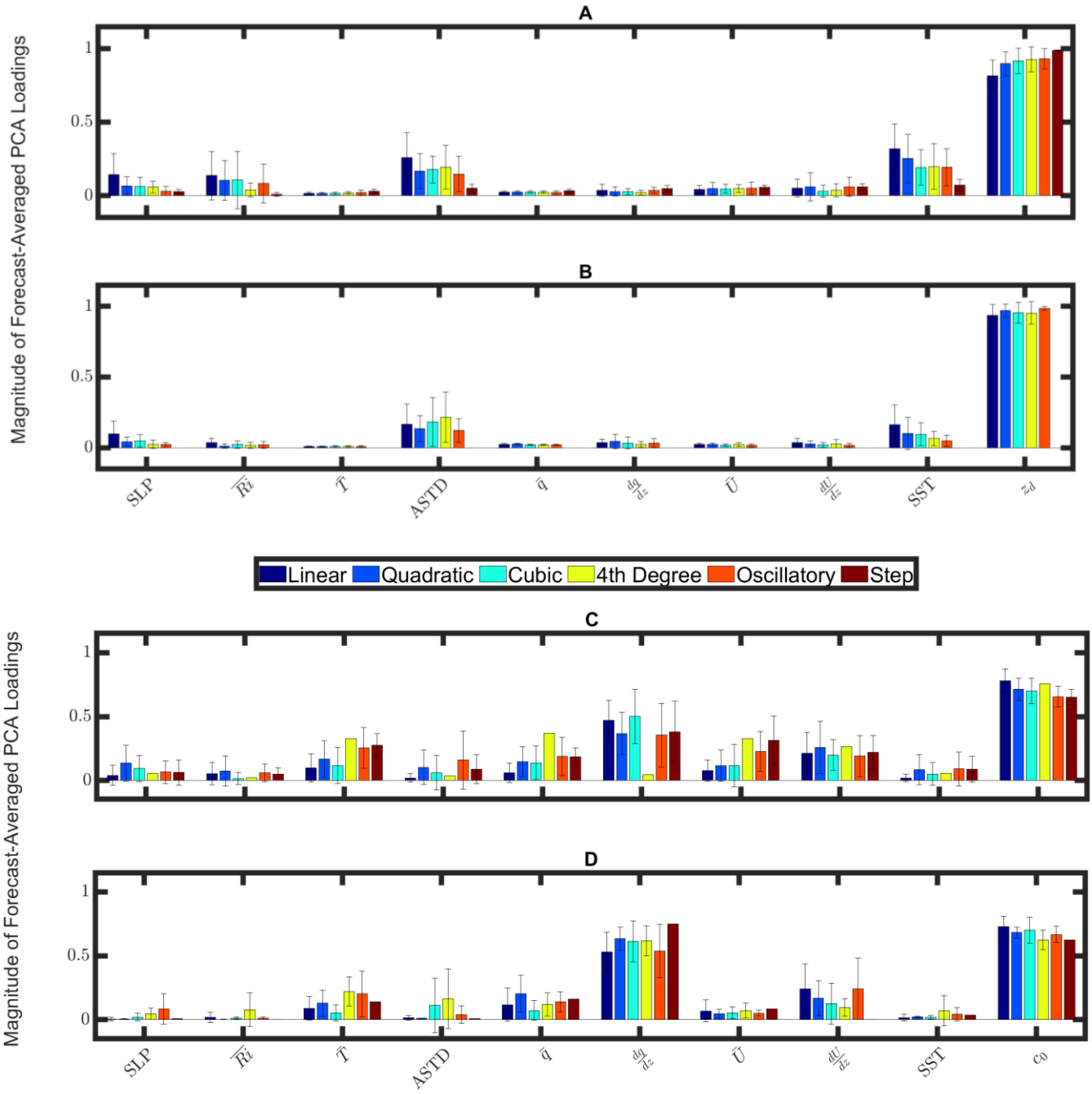


Fig. 10. Distribution type-averaged magnitudes of principal component loadings for range-distributions of atmospheric data (x-axis) and z_d (A and B) or c_0 (C and D). Loadings are those associated with the same component on-which z_d or c_0 loaded most heavily for CASPER-East (A and C) and TAPS (B and D) field campaigns. Note that the error bars represent two standard deviations of loadings for each distribution type.

In contrast, the PCA results for c_0 show obvious consistent results with those from the direct linear correlations that the strongest relationship across most range-distribution categories is with the specific humidity gradient, especially for TAPS. Relative to z_d, the number of variables with high loading onto the same component as c_0 is much larger – potentially suggesting a more complex relationship between duct shape and atmospheric conditions than that between those conditions and duct height. The (c_0) loadings of mean wind speed, mean temperature, and wind shear being slightly higher for CASPER-East than TAPS, especially for higher-order distribution types, further supports the notion of fronts playing a role in the higher-order distribution types for CASPER-East.

V. Conclusions

This research examined range-dependent distributions of the evaporation duct, characterized using two parameters known to greatly affect radar wave propagation in the marine atmospheric surface layer: the duct height and the duct curvature, using verified numerical weather prediction forecasts from two separate field campaigns. It is found that a majority of range-dependent distributions of duct height and duct curvature are

linearly distributed along coastal cross-shore transects. Linear duct height range-dependent distributions most commonly occurred during the warmest portions of the day and were strongly related to variations in mean wind speed (direct) and mean specific humidity (indirect) within the duct. Range-dependent distributions of duct curvature are associated most closely to horizontal changes in the humidity gradient within the evaporation layer ($z < 2z_d$).

It is found that relationships between higher-order range-distribution patterns of duct height and duct curvature with mean temperature, wind shear, and mean wind speed differ between CASPER-East and TAPS. The comparison between relationships suggests that fronts may play a role in these sparsely sampled events for CASPER-East, and their timing coincides with the arrival of reported fronts during CASPER-East. In contrast, for TAPS, relationships of duct height with wind shear were weaker or nonexistent, and therefore mean temperature range variations dominated as a secondary influence on z_d. TAPS occurred at a latitude where frontogenesis is unlikely.

Although these results are informative, it should be emphasized that the data used in this study are from blended NWP models due to current limitations in measurement technology (and/or dataset availability/existence). NWP models incorporate assumptions and simplifications that can cause the (prediction) forecasts to deviate from observations; however, the NWP model used in this study has been extensively validated ([28], [40], [18], [16]). Research efforts to obtain vertical profiles of direct atmospheric measurements simultaneously along horizontal transects with high vertical resolution over long horizontal scales in coastal regions should continue to be a goal to enable validation of the trends observed based-on these NWP forecasts.

REFERENCES

[1] M.I. Skolnik, "Radar Handbook," McGraw-Hill, 2017, New York, NY.

[2] B.R. Bean, and E.J. Dutton *Radio Meteorology* (1st ed.). College Entrance Book Company, 1968, Dover.

[3] N.E. Lentini, and E.E. Hackett (2015, Oct.). Global sensitivity of parabolic equation radar wave propagation simulation to sea state and atmospheric refractivity structure. *Radio Science*, *50*(10), pp. 1027–1049. https://doi.org/10.1002/2015RS005742.

[4] D.M. Pastore, D.P. Greenway, M. J. Stanek, S.E. Wessinger, T. Haack, Q. Wang, and E. E. Hackett (2021, Aug.). Comparison of Atmospheric Refractivity Estimation Methods and Their Influence on Radar Propagation Predictions. *Radio Science*, *56*(9). https://doi.org/10.1029/2020RS007244.

[5] B.D. McKeon, "Climate Analysis of Evaporation Ducts in the South China Sea," M.S. thesis, Naval Postgraduate School, Monterey, CA, 2013.

[6] Q. Zhang, K. Yang., and Q. Yang, (2017, Nov.). Statistical analysis of the quantified relationship between evaporation duct and oceanic evaporation for unstable conditions. *Journal of Atmospheric and Oceanic Technology*, *34*(11), pp. 2489–2497. https://doi.org/10.1175/JTECH-D-17-0156.1.

[7] K. Yang, Q. Zhang, and Y. Shi. (2017, Aug.). Interannual variability of the evaporation duct over the South China Sea and its relations with regional evaporation. *Journal of Geophysical Research: Oceans*, *122*(8), 6698–6713. https://doi.org/10.1002/2017JC012683.

[8] R.C. Cherrett. "Capturing Characteristics of Atmospheric Refractivity Using Observations and Modeling Approaches," Ph.D Dissertation, Naval Postgraduate School, Monterey, CA, 2015.

[9] S.E. Wessinger, (2022). Improving near-Surface Refractivity Estimates in Marine Environments. *Master's Thesis, Coastal Carolina University.*

[10] B. R Bean., and B. A. Cahoon. (1959, May). Effect of Atmospheric Horizontal Inhomogeneity Upon Ray Tracing 1. *Journal of Research of the National Bureau of Standards-D. Radio Propagation*, *63*(3).

[11] J. Goldhirsh, and D. Dockery. (1998, Mar.). Propagation factor errors due to the assumption of lateral homogeneity. *Radio Science*, *33*(2), pp. 239–249. https://doi.org/10.1029/97RS03321.

[12] I. M Brooks, A. K. Goroch, & D. P. Rogers. (1999, Sep.). Observations of Strong Surface Radar Ducts over the Persian Gulf. *Journal of Applied Meteorology and Climatology*, *38*(9), pp. 1293-1310.

[13] B.W. Atkinson, J.G. Li, and R.S. Plant. (2001, July). Numerical modeling of the propagation environment in the atmospheric boundary layer over the Persian Gulf. *Journal of applied meteorology*, *40*(3), pp. 586-603.

[14] I. M. Brooks. (2001, May). Air-sea interaction and spatial variability of the surface evaporation duct in a coastal environment. *Geophysical Research Letters*, *28*(10), 2009–2012. https://doi.org/10.1029/2000GL012751

[15] Y. Shi, K. de Yang, Y. X. Yang, and Y. L. Ma (2015, Feb.). Experimental verification of effect of horizontal inhomogeneity of evaporation duct on electromagnetic wave propagation. *Chinese Physics B*, *24*(4). https://doi.org/10.1088/1674-1056/24/4/044102.

[16] M. Ulate, Q. Wang, T. Haack, T. Holt, and D. P. Alappattu. (2019, Dec.). Mean offshore refractive conditions during the CASPER east field campaign. *Journal of Applied Meteorology and Climatology*, *58*(4), pp. 853–874. https://doi.org/10.1175/JAMC-D-18-0029.1.

[17] D. P Alappattu, Q. Wang, and J. Kalogiros, (2016, July). Anomalous propagation conditions over eastern Pacific Ocean derived from MAGIC data. *Radio Science*, *51*(7), pp. 1142–1156. https://doi.org/10.1002/2016RS005994.

[18] A. S. Kulessa, A. Barrios, J. Claverie, S. Garrett, T. Haack, J. M. Hacker, H. J. Hansen, K. Horgan, Y. Hurtaud, C. Lemon, R. Marshall, J. McGregor, M. McMillan, C. Périard, V. Pourret, J. Price, L. T. Rogers, C. Short, M. Veasey, and V. R. Wiss. (2017, Mar.). The tropical air-sea propagation study (taps). *Bulletin of the American Meteorological Society*, 98(3), 517–537. https://doi.org/10.1175/BAMS-D-14-00284.1.

[19] R. M. Hodur, (1997, Oct.). The Naval Research Laboratory's Coupled Ocean/Atmosphere Mesoscale Prediction System (COAMPS). *Monthly Weather Review*, *125*, pp. 1414–1430.

[20] T. Haack, & S.D. Burk, (2001, Apr.). Summertime marine refractivity conditions along coastal California. *Journal of Applied Meteorology and Climatology*, *40(4)*, pp. 673-687.

[21] W.T. Thompson, & T. Haack, (2011, Nov.). An investigation of sea surface temperature influence on microwave refractivity: The WALLOPS-2000 experiment. *Journal of applied meteorology and climatology*, *50(11)*, pp. 2319-2337.

[22] D.P. Alappattu, Q. Wang, R.T. Yamaguchi, T. Haack, M. Ulate, H.J. Fernando, and P. Frederickson, (2002, Nov.). Electromagnetic Ducting in the Near-Shore Marine Environment: Results from the CASPER-East Field Experiment. *Journal of Geophysical Research: Atmospheres*, *127(22)*: e20002JD037423.

[23] L. Xu, C. Yardim, and T. Haack, (2022, Jun.). Evaluation of COAMPS boundary layer refractivity forecast accuracy for 2-40 GHz electromagnetic wave propagation. *Radio Science*, *57(6)*: e2021RS007404.

[24] Q. Wang, D.P. Alappattu, S. Billingsley, B. Blomquist, R.J. Burkholder, A.J. Christman, E.D. Creegan, T. De Paolo, D.P. Eleuterio, H.J.S. Fernando, and K.B. Franklin. (2018, July). CASPER: Coupled air–sea processes and electromagnetic ducting research. *Bulletin of the American Meteorological Society*, *99*(7), pp.1449-1471.

[25] T. F. Hogan, M. Liu, J. A. Ridout, M. S. Peng, T. R. Whitcomb, B. C. Ruston, C. A. Reynolds, S. D. Eckermann, J. R. Moskaitis, N. L. Baker, J. P. McCormack, K. C. Viner, J. G. McLay, M. K. Flatau, and C. Chen, (2014, Sep.). The Navy Global Environmental Model. *Oceanography*, *27*(3), 116–125. https://doi.org/10.2307/24862194

[26] Halliwell, G. R. (2004, Dec.). Evaluation of vertical coordinate and vertical mixing algorithms in the Hybrid-Coordinate Ocean Model (HYCOM). *Ocean Modeling*, *7*(3–4), pp. 285–322. https://doi.org/10.1016/j.ocemod.2003.10.002

[27] Frederickson, P. (2016). *Navy atmospheric measurements for EM propagation modeling. [Executive summary]*. Naval Postgraduate School.

[28] T. Haack, C. Wang, S. Garrett, A. Glazer, J. Mailhot, and R. Marshall, (2010, Dec.). Mesoscale modeling of boundary layer refractivity and atmospheric ducting. *Journal of Applied Meteorology and Climatology*, *49*(12), pp. 2437–2457. https://doi.org/10.1175/2010JAMC2415.1

[29] A. J. Kammerer, and E. E. Hackett (2017, Aug.). Use of proper orthogonal decomposition for extraction of ocean surface wave fields from X-Band radar measurements of the sea surface. *Remote Sensing*, *9*(9). https://doi.org/10.3390/rs9090881

[30] S. E. Penton, and E. E. Hackett. (2018, May). Rough Ocean Surface Effects on Evaporative Duct Atmospheric Refractivity Inversions Using Genetic Algorithms. *Radio Science*, *53*(6), pp. 804–819. https://doi.org/10.1029/2017RS006440.

[31] J. Wu. (1980, Jan.). Wind-stress coefficients over sea surface near neutral conditions—A revisit. *Journal of Physical Oceanography*, *10*(5), pp.727-740.

[32] R. Paulus. (1990, Nov.). Evaporation duct effects on sea clutter. *IEEE transactions on antennas and propagation*, *38*(11), pp.1765-1771.

[33] S.M. Babin, G.S. Young, and J.A. Carton. (1997, Mar.). A new model of the oceanic evaporation duct. *Journal of applied meteorology*, *36*(3), pp.193-204.

[34] L.T. Rogers, C.P. Hattan, and J.K. Stapleton. (2000, Jul.). Estimating evaporation duct heights from radar sea echo. *Radio Science*, *35*(4), pp.955-966.

[35] P. Gerstoft, L. T. Rogers, J. L. Krolik, and W. S. Hodgkiss, (2003, Apr.). Inversion for refractivity parameters from radar sea clutter. *Radio Science*, *38*(3). https://doi.org/10.1029/2002rs002640

[36] Q. Zhang, K. Yang, and Q. Yang (2017, Mar.). Statistical analysis of the quantified relationship between evaporation duct and oceanic evaporation for unstable conditions. *Journal of Atmospheric and Oceanic Technology*, *34*(11), 2489–2497. https://doi.org/10.1175/JTECH-D-17-0156.1

[37] Q. Wang, R. J. Burkholder, C. Yardim, L. Xu, J. Pozderac, A. Christman, H. J. S. Fernando, D. P. Alappattu, and Q. Wang, (2019, Apr.). Range and Height Measurement of X-Band em Propagation in the Marine Atmospheric Boundary Layer. *IEEE Transactions on Antennas and Propagation*, *67*(4), pp. 2063–2073. https://doi.org/10.1109/TAP.2019.2894269.

[38] D.P. Greenway. "Parametric Model Development for Heterogeneous Atmospheric Conditions," M.S. Thesis, Coastal Carolina University, Conway, SC, 2020.

[39] J. Ding, J. Fei, X. Huang, X. Cheng, H. He, B. Yuan, and Z. Liang. (2020, Jan.). Validation of Evaporation Duct Model in Coastal Regions with ASIT Data. *Journal of Coastal Research*, *99*(sp1), pp. 270–281. https://doi.org/10.2112/SI99-039.1

[40] Q. Zhao, T. Haack, J. McLay, C. Reynolds. (2016, Jul.). Ensemble prediction of atmospheric refractivity conditions for EM propagation. *Journal of Applied Meteorology and Climatology*, *55*(10), pp. 2113–2130. https://doi.org/10.1175/JAMC-D-16-0033.1.



Daniel P. Greenway was born in Indianapolis, Indiana, 1994. He received a B.S. in meteorology and computer science from Ball State University in Muncie, Indiana. He earned his M.S. in coastal marine and wetland studies from Coastal Carolina University in Conway, South Carolina where his thesis developed a parametric heterogeneous refractivity model and explored the effects of heterogeneous media on X-band radio wave propagation.

Currently, he is pursuing his Ph.D. at Coastal Carolina University. His current research aims at advancing point-to-point microwave radar inversion problems. He's specifically interested in exploring radar inversion problems in heterogeneous media, as well as utilizing inversion problems to remotely sense the gradient of humidity and other atmospheric properties in the marine atmospheric surface layer.



Alexis E. Vaughan was born in Virginia Beach, Virginia. She received a B.S. in marine science in 2023 from Coastal Carolina University in Conway, South Carolina. She is currently continuing her education at Coastal Carolina University pursuing her M.S. in the Coastal Marine and Wetland Studies program.

Since 2022, she has been a student researcher in the Environmental Fluids Laboratory at Coastal Carolina University where her research focuses on evaporation ducts and their impact on radar system performance. In the summer of 2023, she participated in the Naval Research Enterprise Internship Program (NREIP) at the Marine Meteorology Division at the Naval Research Laboratory in Monterey, California.



Erin E. Hackett received the B.S. degree in physics from Roanoke College, Salem, VA, USA, and the Master's degree in civil engineering and the Ph.D. degree in earth and planetary sciences from The Johns Hopkins University, Baltimore, MD, USA. She is currently a Professor at the Department of Marine Science, and co-director of the Environmental Fluids Laboratory, at Coastal Carolina University, Conway, SC, USA. Previously, she held positions as a Research Scientist with the Carderock Division, Naval Surface Warfare Center, Bethesda, MD, and as a Systems Engineer with The Johns Hopkins University Applied Physics Laboratory, Columbia, MD. Her research focuses on experimental fluid mechanics as applied to coastal ocean and atmospheric dynamics, including boundary layers, surface waves, and turbulence, as well as electromagnetic wave propagation in the marine environment and radar remote sensing.

Appendix D: Published Manuscript

Pastore, D.M., Yamaguchi, R.T, Wang, Q., and E.E. Hackett (2023). On the variability of *in situ* surface layer refractivity measurements, Atmosphere, 14, 1085. https://doi.org/10.3390/atmos14071085

atmosphere

MDPI

Article

On the Variability of In Situ Surface Layer Refractivity Measurements

Douglas M. Pastore [1], Ryan T. Yamaguchi [2], Qing Wang [2] and Erin E. Hackett [1,*]

[1] Department of Marine Science, Coastal Carolina University, Conway, SC 29528, USA; dmpastore@coastal.edu
[2] Naval Postgraduate School, Monterey, CA 93943, USA; ryamaguc@nps.edu (R.T.Y.); qwang@nps.edu (Q.W.)
* Correspondence: ehackett@coastal.edu

Abstract: Direct measurements of profiles of atmospheric properties near the ocean surface and within the marine atmospheric surface layer often contain a large degree of variability. The variability observed can be explained by numerous technical and natural reasons such as the temporal variability over the time span a profile is measured (unsteadiness in the mean), spatial variations (inhomogeneity), turbulent fluctuations, and measurement uncertainty. In this study, we explored the observed variability in vertical distributions of refractive index measured with a tethered-balloon-based marine atmospheric profiling system (MAPS). MAPS profiled the atmosphere from approximately 0.5 to 50 m, with instantaneous (order 1 s) measurements performed at each profiled altitude. To explore whether the observed scatter could be largely explained by (inertial-scale) turbulent fluctuations, we simulated refractive index fluctuations with a spectral-based turbulent refractive index fluctuation (TRIF) model. TRIF was optimized based on the MAPS measurements to determine a vertical length scale of the turbulence. The scales computed in the optimization were reasonable based on other estimates in the literature under similar conditions. However, finer-scale trends of the length scale with atmospheric stability did not match expectations, and thus the estimated length scales may be considered more as an order-of-magnitude estimate rather than an exact measurement of this scale. The ability to match the observed variability in the MAPS data using a turbulence model with a reasonable choice of vertical length scale suggests that the MAPS variability is dominated by physical processes such as turbulence rather than being primarily driven by measurement uncertainty.

Keywords: marine atmospheric surface layer; particle swarm optimization; refractive index turbulence; marine atmospheric profiling system; CASPER-East; turbulence modeling

check for updates

Citation: Pastore, D.M.; Yamaguchi, R.T.; Wang, Q.; Hackett, E.E. On the Variability of In Situ Surface Layer Refractivity Measurements. *Atmosphere* **2023**, *14*, 1085. https://doi.org/10.3390/atmos14071085

Academic Editors: Yubin Li and Jie Tang

Received: 28 April 2023
Revised: 14 June 2023
Accepted: 16 June 2023
Published: 28 June 2023

Copyright: © 2023 by the authors. Licensee MDPI, Basel, Switzerland. This article is an open access article distributed under the terms and conditions of the Creative Commons Attribution (CC BY) license (https://creativecommons.org/licenses/by/4.0/).

1. Introduction

Exchanges of momentum, heat, and water vapor between the ocean and atmosphere have been the focal point of extensive research. Air–sea interaction, partly described by turbulent exchanges, plays a significant role in the forecasting of not only maritime weather but also global climate. The study of these exchanges is generally located within the first 100 m, a region known as the marine atmospheric surface layer (MASL). Turbulent exchanges, measured as fluxes of momentum, heat, and water vapor, have been the focus of multiple major field campaigns in recent decades. Specifically, the notorious Kansas experiments [1,2], which were performed over land, have been the foundation of statistical relationships relating surface fluxes to the mean vertical distributions of wind, temperature, and humidity within the atmospheric surface layer.

Experiments analogous to the Kansas experiments have been performed in the MASL, where one of the most prominent is the tropical ocean–global atmosphere (TOGA) campaign [3,4]. The goal of TOGA was to identify and understand the physical processes coupling the ocean and atmosphere and describe how the coupled effects of buoyancy and wind forcing drive variations in distributions of meteorological parameters (i.e., temperature, wind, and humidity). These field experiments inspired the coupled ocean–atmosphere

response experiment (COARE) [4,5], which estimated air–sea fluxes from bulk variables employing Monin–Obukhov (MO) similarity theory (MOST). COARE continues to be one of the most popular surface layer estimation algorithms, and [5] discusses updates to the algorithm, specifically the universal stability functions.

Similar to COARE, the Navy Atmospheric Vertical Surface Layer Model (NAVSLaM) estimates surface layer fluxes and related vertical distributions of meteorological parameters [6]. NAVSLaM is blended with a numerical weather prediction (NWP) model, the Coupled Ocean–Atmosphere Mesoscale Prediction System (COAMPS®) [7], to comprehensively forecast the MASL. The novelty of NAVSLaM, relative to COARE, is the dynamic application of stability functions, where unstable regimes employ Businger–Dyer stability functions [1], and stable regimes employ modified Grachev functions [8]. This dynamic use of stability functions presumably leads to a more accurate estimation of surface layer fluxes and, thus, more accurate estimates of vertical distributions of meteorological parameters [6]. While these models strive to capture the impact of turbulent fluctuations on the time-averaged vertical profiles of wind, temperature, and humidity, they are unable to predict instantaneous realizations of turbulent fields. Such realizations from first physical principles require complex numerical frameworks such as large eddy simulation (LES) of the air–sea interface [9].

To measure turbulent fluctuations directly requires high temporal and spatial resolution. An example of such a measurement system is the marine atmospheric profiling system (MAPS), pioneered by [10], which was designed to obtain independent measurements of temperature and humidity at multiple vertical levels within the first 50 m of the MASL. Each measurement, sampled at 1 Hz, as a tethered radiosonde is rapidly winched up and down over the lower 50 m of altitude, captures the instantaneous air property at each time and location. MAPS was extensively deployed during the Coupled Air–Sea Processes and Electromagnetic Ducting Research (CASPER) East and West campaigns [11,12], and multiple studies have incorporated this data, demonstrating its exceptional quality [13–17]. The MAPS measurements show a high degree of variability in space and time [10,16], which could be explained by, for example, turbulent fluctuations and/or measurement uncertainty. The latter would be random while the former only pseudo-random.

To model refractive index fluctuations, spectral modeling has been employed within the MASL. Prior studies have utilized statistical methods to describe turbulent fluctuations of refractivity where the most common approach is the use of the Kolmogorov spectrum [18–22]. This spectrum is a function of the refractive index structure constant (C_n^2) and the outer length scale (L_o) of turbulence, where C_n^2 is a parameter relating to the magnitude of turbulent fluctuations, and L_o delineates the length scale of the energy containing or "mixing" threshold of the inertial subrange.

The current study aimed to explore the MAPS measurements, specifically the variations captured by the system, over the course of the CASPER-East campaign. To investigate whether measurement variations can be explained by turbulent fluctuations, turbulent refractive index fluctuations were simulated using a 1-D anisotropic Kolmogorov spectral model, referred to as the TRIF model. Particle swarm optimization (PSO) was utilized to optimize the TRIF model to the measurements, specifically the outer vertical length scale, L_z, was derived via PSO for C_n^2 estimated from CASPER-East data via NAVSLaM. Comparisons of (i) MAPS and TRIF model fluctuations and (ii) derived L_z and previously reported estimations of surface layer L_z give insight into whether refractive index variability observed in MAPS refractivity could be physically explained by turbulent fluctuations. Furthermore, an ability to replicate the MAPS data variability also partly validates the TRIF modeling approach.

The following sections are organized as follows: Section 2 discusses the CASPER-East meteorological data, highlighting the MAPS dataset, Section 3 describes the TRIF model, and Section 4 discusses the optimization method. Section 5 presents the results of the optimization experiment and associated discussion of the results, followed by a concluding Section 6.

2. CASPER-East Measurements

The CASPER-East field campaign occurred over 25 days in 2015 between 12 October and 6 November [11]. The following paragraphs describe the measurements made within the MASL by MAPS and aboard the Research Vessel (R/V) Sharp. Comprehensive discussion of the CASPER-East campaign can be found in [11].

The MAPS system was constructed of an iMET rawinsonde attached to a balloon tethered to a small workboat, using a winch to control the ascent and decent of the system from ~0.5 m to ~50 m in altitude. The workboat used to deploy MAPS was small enough that its effects on the measured environment are considered minimal [10]. Pressure, temperature, and relative humidity accuracies were 0.5 hPa, 0.2 °C, and 5%, respectively, with resolutions of approximately one-tenth of their accuracy for each. Response times for all sensors were below 2 s. MAPS datasets were composed of pressure (p), temperature (T), and relative humidity (RH), where T and RH were converted to potential temperature (θ) and specific humidity (q), respectively. In [10], T, q, and p data were fit with a 7th-order polynomial for each MAPS dataset; the instantaneous measurements along with these fits were used in this study. Time series of meteorological variables at 12 m altitude are illustrated in Figure 1 along with bulk meteorological measurements (30 min averages) made aboard the R/V Sharp (note that the time series gap is due to a port call mid-cruise). Vertical profiles of modified refractivity (M) were computed from the mean meteorological profiles via [23]:

$$M = \frac{77.6}{T}\left[p + \frac{4810e}{T}\right] + \left(\frac{z}{a}\right) \times 10^6, \quad (1)$$

where z is the height above the earth's surface, a is the radius of the earth, and e is the partial water vapor pressure (millibars) computed with q and T to estimate the saturation vapor pressure [24]. The polynomial fits of mean p, T, and RH were based on data measured down to ~0.5 m; thus, the polynomial fit was also used to extrapolate M to the surface to obtain surface refractivity (M_0). Previous studies found that this 7th-order polynomial represents near-surface variations that are more consistent with MOST surface layer model predictions than lower-order polynomial fits, and it also results in a smoother vertical refractivity profile than using a method such as bin-averaging the data over altitude (Figure 2). A more extensive discussion of this methodology can be found in [13,14].

Table 1. Overview of MAPS datasets. Dataset number, deployment time, deployment duration, number of launches, number of samples, and root mean squared (RMS) fluctuation of the MAPS measurements over each deployment are shown. Also included are the NAVSLaM estimated refractive index structure constant (C_n^2), optimized vertical outer length scale (L_z), and corresponding fitness score (Ω_{Fit}), defined in (10), evaluated for each optimization.

MAPS Dataset	Deployment Time (EST)	Duration (min.)	Launches	Samples	M' RMS (M-Units)	NAVSLaM C_n^2 ($m^{-2/3}$)	Derived L_z (m)	Ω_{FIT} (M-Units^2)
1	13-Oct 12:49	22	7	1572	1.092	4.75×10^{-13}	4.69	0.010
2	13-Oct 15:47	25	7	1264	1.021	4.96×10^{-13}	4.24	0.001
3	14-Oct 09:06	19	5	698	1.471	4.66×10^{-13}	5.89	0.035
4	14-Oct 12:42	38	7	867	1.742	3.22×10^{-13}	8.09	0.022
5	14-Oct 15:32	17	6	684	1.442	8.34×10^{-13}	4.51	0.022
6	15-Oct 08:22	9	7	936	1.799	1.35×10^{-12}	4.58	0.095
7	15-Oct 11:03	54	6	981	1.835	1.17×10^{-12}	4.74	0.081

Table 1. *Cont.*

MAPS Dataset	Deployment Time (EST)	Duration (min.)	Launches	Samples	M' RMS (M-Units)	NAVSLaM C_n^2 ($m^{-2/3}$)	Derived L_z (m)	Ω_{FIT} (M-Units^2)
8	15-Oct 14:41	30	6	737	1.350	1.01×10^{-12}	4.08	0.019
9	16-Oct 09:12	44	2	364	1.580	1.73×10^{-12}	3.81	0.009
10	16-Oct 12:16	20	6	1077	1.664	1.79×10^{-12}	3.70	0.024
11	16-Oct 14:38	32	7	1134	2.186	1.27×10^{-12}	5.51	0.036
12	17-Oct 08:07	22	9	945	1.216	1.48×10^{-12}	3.19	0.035
13	17-Oct 11:04	14	7	1250	1.837	1.09×10^{-12}	5.01	0.091
14	17-Oct 14:06	16	7	873	1.481	1.23×10^{-12}	3.91	0.034
15	17-Oct 18:25	35	3	295	1.164	9.47×10^{-13}	3.58	0.092
16	20-Oct 09:41	32	20	2643	1.427	7.06×10^{-13}	4.93	0.016
17	20-Oct 12:57	23	10	1585	1.968	7.56×10^{-13}	5.87	0.060
18	20-Oct 15:29	45	15	2287	1.749	6.74×10^{-13}	5.70	0.020
19	21-Oct 07:01	41	7	969	1.605	1.95×10^{-13}	9.42	0.125
20	21-Oct 08:57	34	8	859	1.116	2.20×10^{-13}	6.42	0.059
21	21-Oct 10:29	17	7	619	1.094	5.30×10^{-13}	4.73	0.010
22	21-Oct 12:10	42	7	695	1.252	3.09×10^{-13}	5.85	0.030
23	23-Oct 08:43	22	14	1837	1.991	1.67×10^{-13}	11.80	0.021
24	23-Oct 11:44	18	9	1457	2.253	1.66×10^{-13}	13.57	0.061
25	24-Oct 08:05	31	6	920	2.290	1.81×10^{-12}	4.85	0.086
26	25-Oct 11:25	30	16	2072	1.870	4.43×10^{-13}	7.59	0.011
27	25-Oct 14:11	25	14	1892	1.190	2.98×10^{-14}	17.02	0.002
28	25-Oct 15:58	24	8	1187	0.955	3.44×10^{-13}	4.68	0.005
29	25-Oct 18:28	37	6	748	0.749	3.99×10^{-13}	3.98	0.010
30	31-Oct 17:19	25	8	799	0.958	9.96×10^{-13}	2.96	0.007
31	31-Oct 18:15	30	7	850	1.838	1.09×10^{-12}	4.85	0.072
32	01-Oct 08:31	21	10	1533	2.770	1.98×10^{-12}	5.38	0.127
33	01-Oct 10:57	19	10	1570	3.076	1.36×10^{-12}	7.07	0.260
34	01-Oct 13:30	28	8	1306	2.601	2.52×10^{-12}	4.75	0.065
35	01-Oct 15:39	19	7	1226	2.390	2.16×10^{-12}	4.78	0.019
36	01-Oct 17:32	11	12	967	1.183	1.64×10^{-12}	3.02	0.002

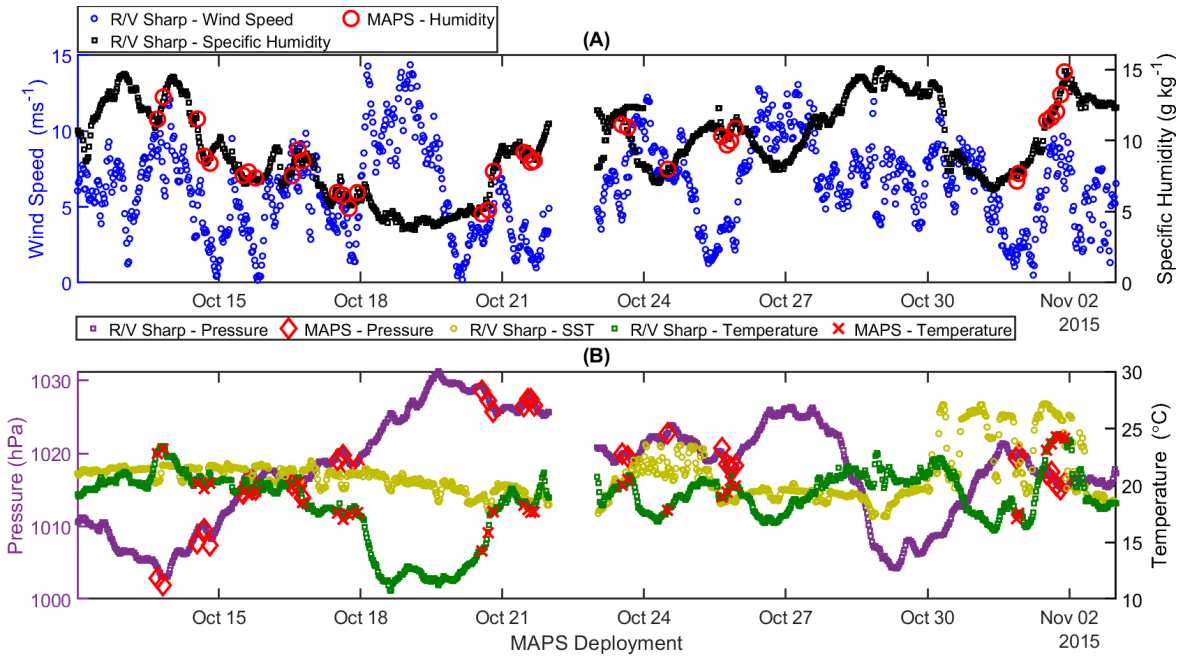


Figure 1. Time series of meteorological variables measured aboard the R/V Sharp and based-on the 7th-order polynomial fit of the MAPS data. (**A**) Shows wind speed and specific humidity and (**B**) shows air temperature, sea-surface temperature, and air pressure (see legends). All meteorological parameters were measured at an altitude of 12 m above mean sea level and are displayed for all MAPS deployment times during the CASPER-East field campaign (Table 1).

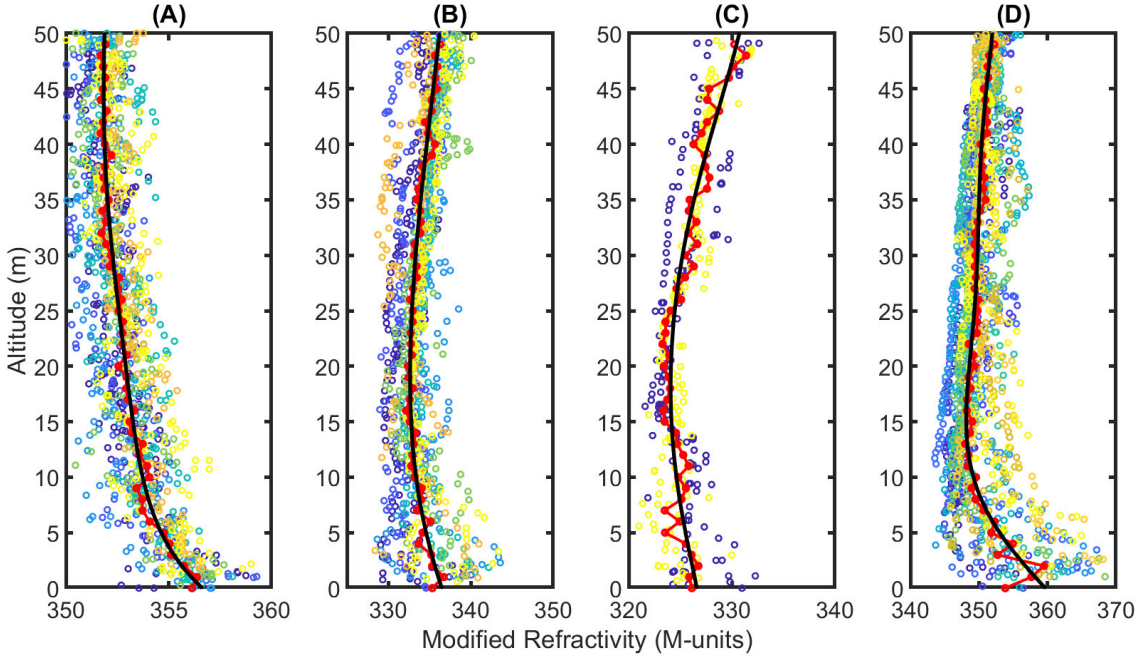


Figure 2. Example MAPS datasets corresponding to datasets 2 (**A**), 11 (**B**), 9 (**C**), and 33 (**D**) (Table 1). Circles represent the modified refractivity computed via (1) from the instantaneous measurements obtained from MAPS, where the black line is the 7th-order polynomial fit representing the mean refractivity profile, and the red line represents a 1 m bin-averaged profile. Colors included for the instantaneous refractivity measurements correspond to different launches (single ascent and descent) of MAPS.

MAPS measurements of p, T, and RH have been thoroughly verified [10,12–14]. This paper focuses on the modified refractivity estimated from these measurements. MAPS datasets used in this study are displayed in Table 1, showing that 36 deployments of the system were performed over the course of CASPER-East, and on average each deployment lasted 26 min and contained ~1158 samples. Numerous ascents and subsequent descents of MAPS occurred during each deployment, where the following use of the term "launch" will describe one ascent/descent of the system, each lasting on average ~3.5 min. For each MAPS deployment, multiple launches occurred. For this study, MAPS refractivity estimates were truncated above 50 m to remove measurement uncertainties occurring due to reorientation of the system from ascent to descent [13,14]. In Figure 2, 4 example deployments of MAPS from CASPER-East are illustrated, where the different marker colors indicate different launches of MAPS; the 7th-order polynomial fit represents the mean; and, for comparison, a 1 m altitudinally binned mean profile is shown for each dataset, with the former utilized as the mean profile in this study. MAPS measurements, and subsequent estimates of refractivity, individually can be considered instantaneous (within the longest response time of the sensors of <2 s) and can thus be decomposed as

$$M(z) = \bar{M}(z) + M'(z), \tag{2}$$

where the overbar and prime denote a mean and fluctuation, respectively. In Figure 2, instantaneous MAPS-based M are shown as markers, and the 7th-order polynomial fits, representing the mean of the markers, is shown as a black line ($\bar{M}$). Refractive index fluctuations (M') computed from (2) are illustrated in Figure 3. The mean M' for each MAPS dataset is approximately zero, as exemplified in Figure 3 for the same datasets shown in Figure 2. The zero means of M' confirm that the polynomial fits are reasonable estimates of $\bar{M}$.

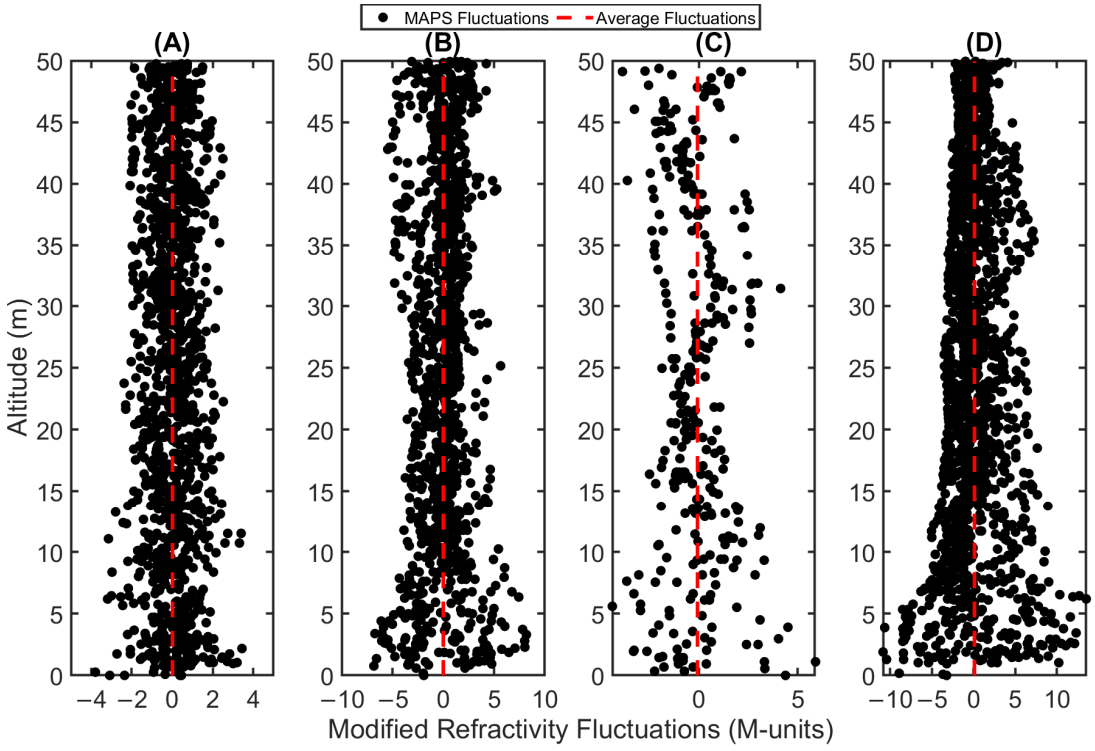


Figure 3. Fluctuations ($M'(z)$) computed via (2) corresponding to the MAPS datasets in Figure 2 (**A**) (dataset) 2, (**B**) 11, (**C**) 9, (**D**) 33. The red dashed line shows the mean of the fluctuations verifying the 7th-order polynomial fit as a good measure of the mean.

In conjunction with the MAPS deployments, meteorological and sea surface measurements were conducted aboard the R/V Sharp. Wind speed was not measured by MAPS and is needed for estimation of C_n^2, discussed in Section 3.2; thus, wind speed was obtained from an anemometer aboard the R/V Sharp bow mast (z = 12 m) averaged over 30 min intervals. Skin sea surface temperature (SST) was also measured aboard the R/V Sharp, corrected from the 5 min bulk SST [11,16]. Time series of R/V Sharp SST and wind speed are displayed in Figure 1.

3. Turbulent Refractive Index Fluctuations Model (TRIF)

Previous studies have modeled turbulent refractive index fluctuations using a variety of models for representing turbulence—such as Gaussian, von Karman, and Kolmogorov-based spectral models [18–22]. Because a Kolmogorov-based spectral model only emulates turbulence in the inertial subrange, it is easier to incorporate anisotropy into the model, which is a key characteristic of turbulence in the MASL. Therefore, an anisotropic Kolmogorov-based turbulent refractive index fluctuation model (TRIF) was implemented in this study [19]. Details of the implementation of this Kolmogorov model are discussed in Section 3.1, where it is revealed that a refractive index structure constant is needed for the model. The method for estimating this structure constant is described in Section 3.2.

3.1. Spectral Modeling of Tubulent Refractive Index Fluctuations

Refractivity was assumed to be constantly perturbed by continuous fluctuations due to atmospheric turbulence. Random fluctuations, as defined in (2), were modeled stochastically. The stochastic fluctuating component of the index of refraction (IOR) is described by the Kolmogorov spectrum derived by [25]:

$$\varnothing(\boldsymbol{k}) = \frac{0.033C_n^2}{\left(L_0^{-2} + \boldsymbol{k}^2\right)^{\frac{11}{6}}}, \tag{3}$$

where C_n^2 is in units of $\mathrm{m}^{-2/3}$, L_0 has units of meters, and $\boldsymbol{k}$ is the 3-dimensional wavenumber vector. The anisotropic MASL can be introduced into (3) via α, a parameter describing the relationship between horizontal (L_x) and vertical (L_z) outer length scales, where $L_z = \alpha L_x$ [18,20,22]; thus:

$$\varnothing\left(\kappa_x, \kappa_y, \kappa_z\right) = \frac{0.033C_n^2}{\left(L_x^{-2} + \kappa_x^2 + \kappa_y^2 + \alpha^2\kappa_z^2\right)^{\frac{11}{6}}} \tag{4}$$

For this study, α = 0.27 [26]. To collapse the three-dimensional spectrum in (4) into one-dimensional space, the transverse vertical spectrum was adopted as derived in [18,20]:

$$S_n(\kappa_z) = (2\pi)^2\delta x \int_{-\infty}^{+\infty} \varnothing\left(\kappa_x = 0, \kappa_y, \kappa_z\right) d\kappa_y, \tag{5}$$

where δx is a scaling factor that would account for the distance between realizations of vertical turbulent profiles in a numerical model. In the present study, we were not generating realizations within a numerical model but rather comparing a single vertical refractive index fluctuation realization to each MAPS dataset, so no scaling was required; thus, we simplify $\delta x = 1$ in (5). Substituting (5) into (4) results in the one-dimensional transverse spectrum:

$$S_n(\kappa_z) = (2\pi)^2 \frac{\Gamma\left(\frac{1}{2}\right)\Gamma\left(\frac{4}{3}\right)}{\Gamma\left(\frac{11}{6}\right)} \alpha^{-\frac{8}{3}} \frac{0.033C_n^2}{\left(L_z^{-2} + \kappa_z^2\right)^{\frac{4}{3}}}, \tag{6}$$

where Γ is a gamma function. The full derivation of (6) can be found in [18,20,22]. Realizations of refractive index fluctuations from $S_n(\kappa_z)$ are found using the approximate frequency domain method proposed in [27] and similarly implemented in [22]. Realized refractive index fluctuations are related to modified refractivity by

$$M = \left(n - 1 + \left(\frac{z}{a}\right)\right) \times 10^6, \tag{7}$$

where n is the IOR.

3.2. NAVSLaM Estimates of C_n^2

The estimation of C_n^2 was performed via NAVSLaM Version 1.2 [6], which is based on MO similarity theory and estimates near-surface profiles of thermodynamic properties and wind as well as related scaling parameters of the air–sea fluxes of momentum, sensible heat, and latent heat [6]. NAVSLaM employs similar parameterizations as COARE [4,5] and is only valid within the surface layer where turbulent fluxes vary by 10% or less (i.e., assumption of a constant flux layer). NAVSLaM is chosen for the estimation of C_n^2 due to the dynamic employment of MO similarity theory stability functions for differing stability regimes. NAVSLaM requires the following parameters to estimate C_n^2: skin sea surface temperature and wind speed, specific humidity, and temperature at a reference height. SST and wind speed were obtained from measurements aboard the R/V Sharp since these were not measured by MAPS; specific humidity and temperature were obtained from mean meteorological measurements of MAPS at $z = 12$ m matching the altitude of wind speed measurements from the R/V Sharp. R/V Sharp measurements were conducted synchronously with MAPS measurements and were located at a distance, on average, of 0.6 km away from the location of MAPS deployments [16].

The estimation of the refractive index structure constant (at z = 12 m) was performed via NAVSLaM for the 36 MAPS deployment times as

$$C_n^2 = z^{-\frac{2}{3}} f(z/L)\left(A^2 T_*^2 + 2AB\gamma_{Tq} T_* q_* + B^2 q_*^2\right), \tag{8}$$

where A and B are constants for radio frequencies [28]. Subscript * denotes a MOST scaling parameter [1,28], and $f(z/L)$ represents the MO theory stability functions employed in NAVSLaM [6]. γ_{Tq} is the temperature-specific humidity correlation coefficient, commonly 0.8 [29,30].

4. Particle Swarm Optimization

The TRIF model was optimized to the (instantaneous) MAPS refractivity datasets using particle swarm optimization (PSO) [31,32], an inverse technique. PSO was implemented to investigate the physical significance of MAPS-estimated refractivity fluctuations because a direct estimate of any vertical length scale is not possible with the MAPS data directly. PSO was used to optimize the TRIF model to yield the best match to the statistical properties of the measured refractive index fluctuations by evaluating a fitness or objective function. Because NAVSLaM was used to estimate C_n^2, PSO optimizes the TRIF model for L_z. PSO iteratively optimizes L_z from within a search space that ranges from 0.1 m to 50 m; such a large range is considered for L_z to incorporate the majority of possible outer length scales within the surface layer [33,34]. If the PSO-optimized length scales are reasonable given the atmospheric stability regime, then that is an indicator that the majority of the observed variance in the MAPS measurements can be attributed to turbulence.

PSO is a stochastic technique utilizing a population-based dynamic system where a potential solution (or particle) is introduced into a solution space, with dimensions corresponding to the number of solution parameters, with a multitude of potential solutions (or swarms of particles). Each particle in the swarm moves through the solution space at a unique velocity, which is determined by the unique particle's "best" solution from previous exploration of the solution spaces and the global "best" solution from the swarm over all

previous solution spaces. In this study, the solution parameter, or particle, was L_z from the TRIF model, which corresponds to a one-dimensional solution space. The swarm size for the optimization was set to 30, and optimization was considered complete once the relative change in the objective function between consecutive swarms, after a minimum of 20 swarm iterations, was less than 10^{-6} M-units^2 (see objective function below). More information on PSO can be found in [31,32].

The fitness or objective function determines how "good" a particular particle is within the PSO and therefore should focus on the properties that the optimization is targeting—in this case, the MAPS dataset variability. To match the variability as well as possible, the fitness function compares quantiles of the cumulative probabilities of refractivity fluctuations between TRIF model refractivity and MAPS refractivity measurements. One hundred evenly spaced quantiles (or percentiles) are delineated for modified refractivity fluctuations for both the TRIF model and MAPS measurements. Quantiles (Q_P) are found via ordinal ranking (R_P) as

$$R_P = \left(\frac{P}{100}\right) N_s, \tag{9}$$

where P is the percentile ($P = 1, 2, 3, 4, \ldots 100$), and N_s is the number of samples in the dataset. Modified refractivity fluctuations are sorted from smallest to largest, and R_P identifies which value within the sorted dataset corresponds to each Q_P; thus, each quantile is associated with an M' value. For example, in MAPS dataset 2 (Figure 2A), N_s = 1264, if $P = 2$, then $R_2 = 25.3$, and Q_2 is sample 26 in the sorted dataset, −2.03 M-units (Figure 4A). This M' accounts for 2% or less of all M' in the dataset.

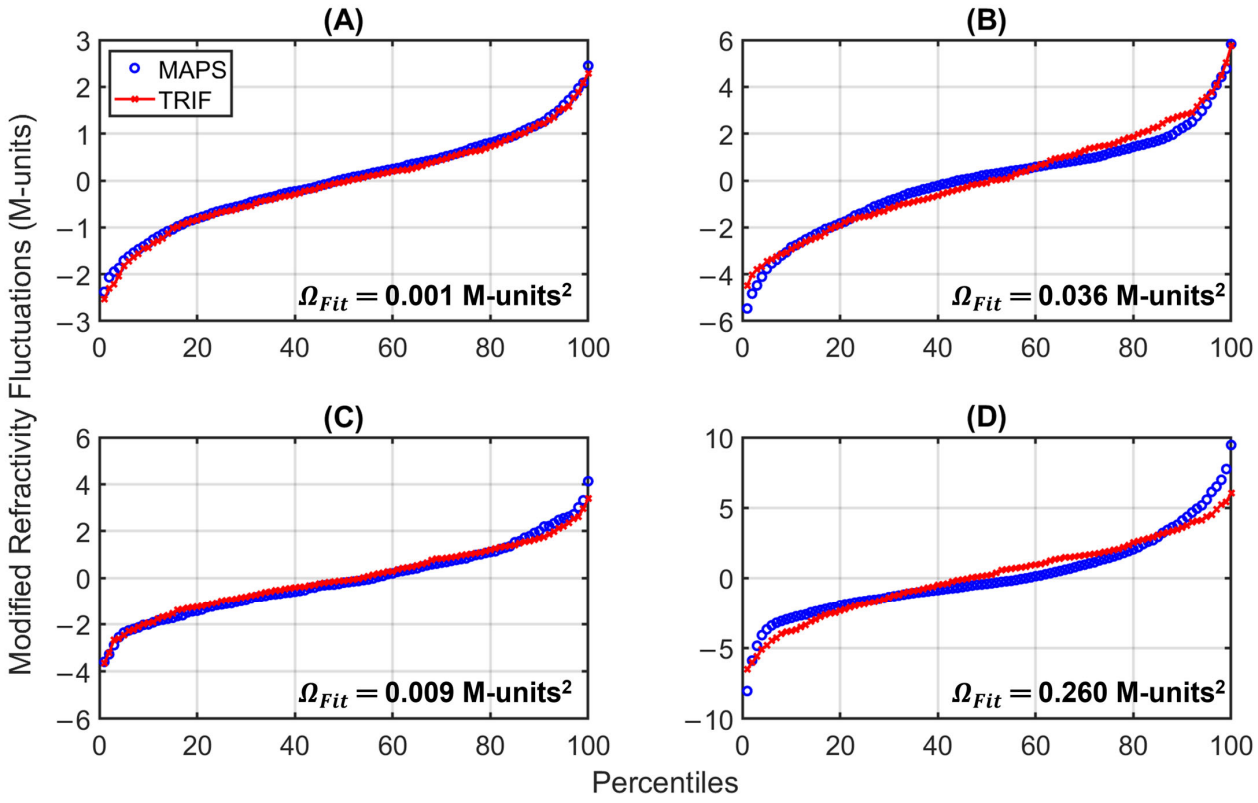


Figure 4. Quantiles for the example MAPS fluctuations illustrated in Figure 3, and quantiles for the associated TRIF model fluctuation predictions realized via particle swarm optimization of L_z. An array of optimization results are displayed in this figure: the dataset with (**A**) the lowest fitness score (dataset 2), (**B**) the fitness score nearest to the mean over all optimizations (dataset 11), (**C**) the MAPS dataset with the fewest measurements (dataset 9), and (**D**) the largest fitness score (dataset 33). Fitness scores (Ω_{Fit}) for each example are included in each panel.

The quantile-based approach allows for the comparison of the cumulative probability distributions between MAPS and TRIF refractive fluctuations. A probability-distribution-based approach is logical due to the differing sample sizes between MAPS measurements and TRIF realizations of refractive fluctuations. A comparison of the quantiles between the two datasets was performed using a mean square error fitness score:

$$\Omega_{Fit} = \frac{1}{N_Q} \sum_{P=1}^{N_Q} \left(Q_P^M - Q_P^T \right)^2, \tag{10}$$

where Q_P is the M' for the Pth percentile computed for either the MAPS dataset,Q^M, or the TRIF model dataset, Q^T. N_Q= 100, corresponding to the hundred quantiles delineated for each dataset. Minimization of (10) ensures that the statistical characteristics (i.e., mean, median, and variance) of M', for both TRIF and MAPS, are similar. Thus, relatively small Ω_{Fit} would indicate that the TRIF model appropriately estimates the distribution of MAPS refractive index fluctuations. Example MAPS and TRIF quantiles for MAPS datasets illustrated in Figures 2 and 3 are displayed in Figure 4.

5. Results and Discussion

TRIF model optimization of the vertical length scale, L_z, was compared with previously reported ranges of L_z within the atmospheric surface layer. Further, the TRIF model was used to simulate the MAPS data cloud, which were also compared directly. These results are exemplified by the four MAPS datasets illustrated in Figures 2–4. These examples were chosen because they represent the best (Figure 3A), average (Figure 3B), and worst (Figure 3D) comparisons between the TRIF model and MAPS data. The last example was chosen because it had the least MAPS measurements (Figure 3C) used for the optimization. These results enable insight into the source of the scatter in the MAPS measurements.

5.1. Vertical Length Scale—L_z

Vertical outer length scales from the PSO experiments range from 2.96 m to 17.02 m, with an average of 5.80 m over the MAPS datasets (Table 1). Bulk C_n^2 and corresponding L_z for the 36 optimizations are illustrated in Figure 5. L_z are visually compared with vertical outer length scales from [26,35] in Figure 5B. The authors of [26] estimate L_z over multiple stability regimes (i.e., unstable, neutral, and stable), yielding a range of values shown as the grey shaded region in Figure 5B. These vertical length scales included from [26] are approximated at 12 m, chosen to be consistent with the TRIF model utilizing C_n^2 estimated from meteorological data at this altitude. Generally, L_z fall close to the values reported by [26] apart from 2 MAPS datasets (24 and 27) associated with near-thermal neutrality. Because the optimized L_z are generally consistent with the ranges in the literature, one can conclude that the MAPS data cloud could be largely driven by turbulence. If the optimization revealed an unrealistic/non-physical L_z (e.g., at maximum/minimum value in the search space) to match the MAPS data, then that would have indicated that uncertainty could be a significant factor. Thus, MAPS-measured refractivity variance is potentially representative of physically relevant fluctuations of the refractive index.

To further confirm the physical nature of the optimized L_z, the correlation between C_n^2 and L_z was examined. L_z reveals a significant inverse relationship with C_n^2 shown by a correlation coefficient (R) of -0.53 with a p-value of <0.05. This result is contrary to expectations as it suggests decreasing vertical outer length scales as C_n^2 increases. Presumably, in thermally unstable conditions, the increase in buoyant effects generating convective plumes would increase both the magnitude of turbulence (C_n^2) and L_z, leading to a direct relationship. While in stable conditions, one would assume that the stable stratification would inhibit development of large-scale fluctuations.

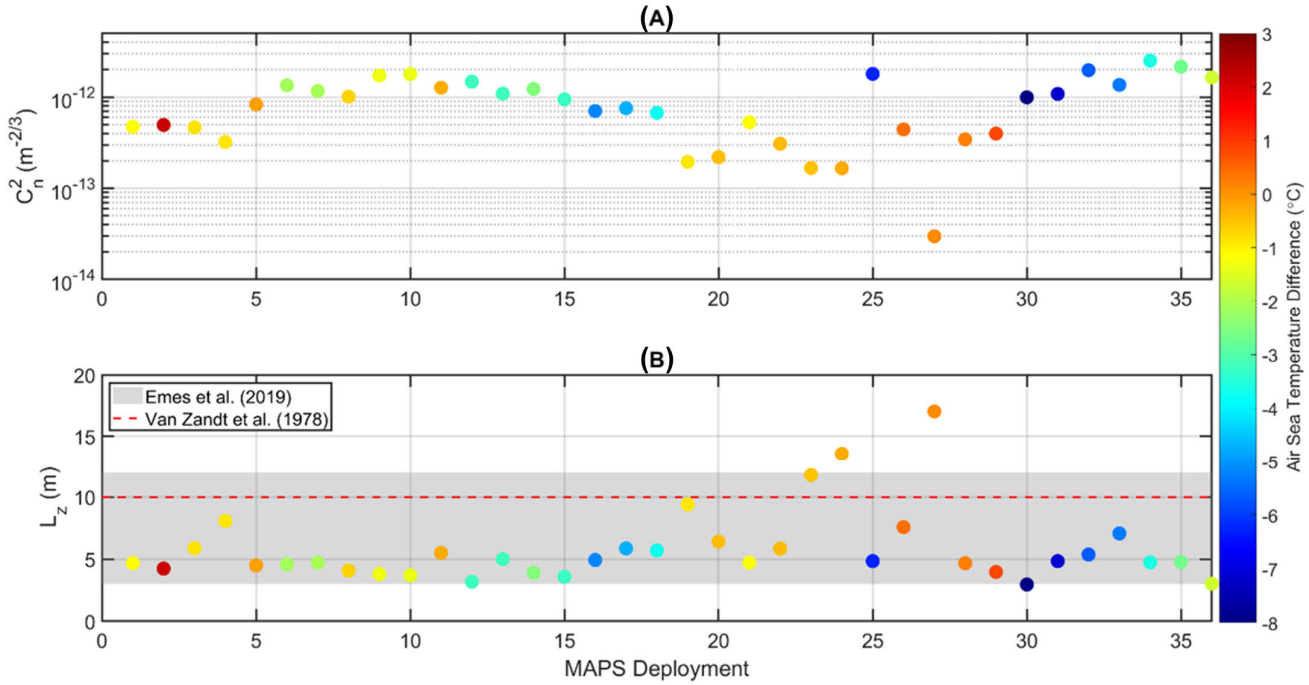


Figure 5. (**A**) Refractive index structure constant (C_n^2) estimated via NAVSLaM from the environmental variables displayed in Figure 1 for each MAPS deployment. (**B**) L_z solutions from the particle swarm optimization corresponding to each MAPS dataset. Included in (**B**) are previously reported ranges of L_z in the atmospheric surface layer (at ~12 m above the boundary) from [26] for differing atmospheric stability regimes (gray shaded region) and L_z reported in [35] for the free atmosphere (10 m) (red dashed line). Marker colors denote the air–sea temperature difference in both panels.

To further investigate the indirect relationship between C_n^2 and L_z, we explored the possible sources of error in the comparisons. One source of uncertainty is due to the C_n^2 estimate being based on an average condition (i.e., based on bulk meteorological measurements), while the MAPS measurements used for the optimization are individually instantaneous (to order 1 s). Secondly, the assumption of a constant C_n^2 with altitude can also result in uncertainty. Finally, Ref. [28] reported that for ASTD > −1 °C, bulk C_n^2 estimates deviate from scintillation-derived (SD) C_n^2. For cases of near-thermal neutrality (−0.5 °C < ASTD < 0.5 °C), bulk C_n^2 can underestimate SD C_n^2 by more than 1 order of magnitude for certain wind and humidity conditions. This underestimation can presumably explain MAPS deployment 27, where near-neutral conditions were observed (ASTD = 0.11 °C) corresponding to an abnormally low C_n^2 (2.97×10^{-14} $m^{-2/3}$) and the largest L_z (17.02 m). This underestimation of C_n^2 effectively leads to overestimation of L_z to match the observed fluctuations; MAPS dataset 24 is similar, where a near-neutral environment was also observed (ASTD = −0.26 °C). For these cases, the relatively small C_n^2 does not correspond with relatively small RMS MAPS refractive fluctuations, and thus a large L_z is derived by the optimization compensating for the small C_n^2. Further, Ref. [28] also reported that during periods of thermal stability (ASTD > 1 °C), bulk C_n^2 estimates can be overestimated by up to 1 order of magnitude. For this study, the overestimation of C_n^2 would lead to derived L_z that are smaller than expected. These uncertainties in NAVSLaM bulk C_n^2 estimates could cause the indirect relationship between C_n^2 and L_z. Thus, since L_z fall within the previously reported ranges of vertical outer length scales and considering some stability-dependent error in the bulk estimation of C_n^2, it is plausible that the majority of the refractive fluctuations in the MAPS measurements are indicative of inertial to large-scale turbulent physical processes.

5.2. Refractive Fluctuations

TRIF-modeled refractivity fluctuations using L_z derived via PSO for the example MAPS datasets (2, 11, 9, and 33) are illustrated in Figure 6, and the associated instantaneous distributions of refractivity are displayed in Figure 7. For these examples, TRIF model fluctuations optimized to corresponding MAPS refractivity have a Ω_{Fit} of 0.001 M-units^2 (Figure 6A), 0.036 M-units^2 (Figure 6B), 0.009 M-units^2 (Figure 6C), and 0.260 M-units^2 (Figure 6D), for MAPS datasets 2, 11, 9, and 33, respectively. The discrepancies between the Ω_{Fit} for the examples displayed in Figure 6 are visually apparent. TRIF fluctuations mostly occur within the bounds of MAPS refractivity in Figure 6A–C, corresponding to relatively low Ω_{Fit}; this is not the case for Figure 6D. Most datasets (32 of 36) are on the order of the mean Ω_{Fit} (0.047 M-units^2) and are visually akin to Figure 6B. In Figure 6D, TRIF fluctuations tend to have a greater magnitude than MAPS refractivity at altitudes greater than ~8 m and fail to span MAPS fluctuations below this 8 m altitude. Consequently, MAPS dataset 33 corresponds to the largest (worst) Ω_{Fit} relative to all MAPS deployments. This vertical inhomogeniety is not accounted for in the TRIF model as turbulence is assumed homogenous with altitude—i.e., C_n^2 and L_z are estimated as one value for the entire profile.

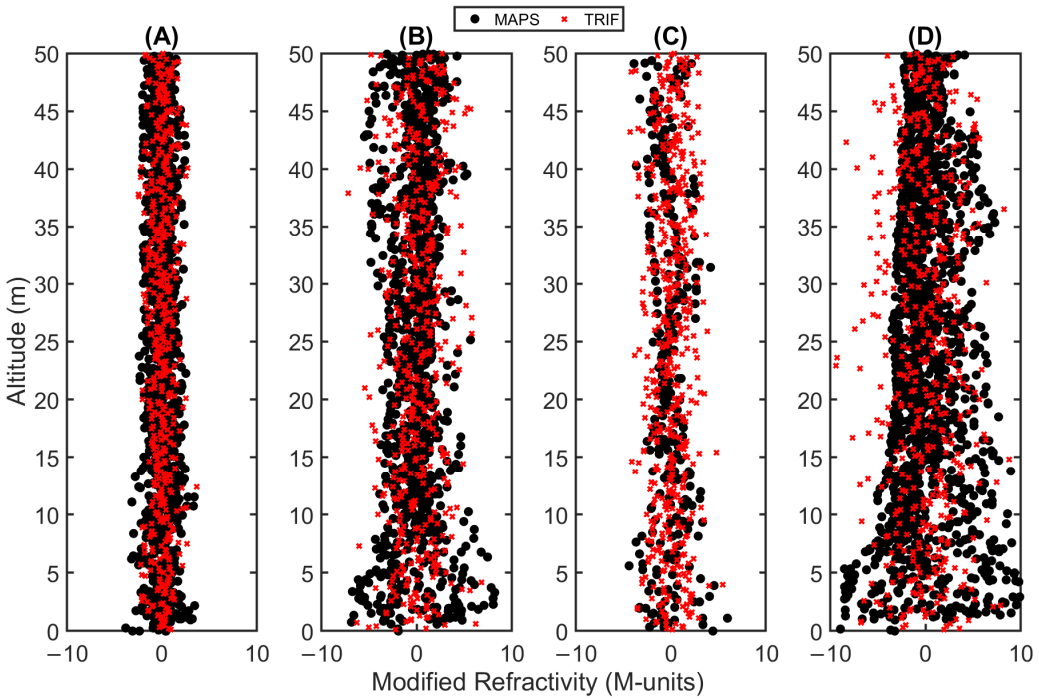


Figure 6. Refractive index fluctuations corresponding to example MAPS datasets in Figures 1–4 along with TRIF model fluctuations using the particle swarm optimization-based vertical outer turbulent length scale. ((**A**) (dataset) 2, (**B**) 11, (**C**) 9, (**D**) 33).

The assumption of homogenous turbulence within TRIF is questionable for C_n^2 in the surface layer [18,21,36,37] but is a reasonable assumption for L_z [18]. Thus, the assumption of C_n^2 homogeneity is presumably a main driver of variation in fitness scores over the 36 datasets. The altitudinal inhomogeneity is illustrated in Figure 8, where fitness score is shown relative to altitudinal variance in the MAPS data. M' variance was computed over 2 altitudinal bins, 0–10 m (δ_A) and 10–20 m (δ_B), exploring the vertical heterogeneity of the refractivity. δ_A is larger than δ_B for 28 of the 36 datasets, showing that the assumption of vertical homogeneity is not ideal (Figure 8A). Additionally, this result gives physical context to variations in the MAPS measurements, further supporting the physical nature of the MAPS-measured fluctuations, as one would expect turbulent fluctuation magnitudes to be largest near the surface.

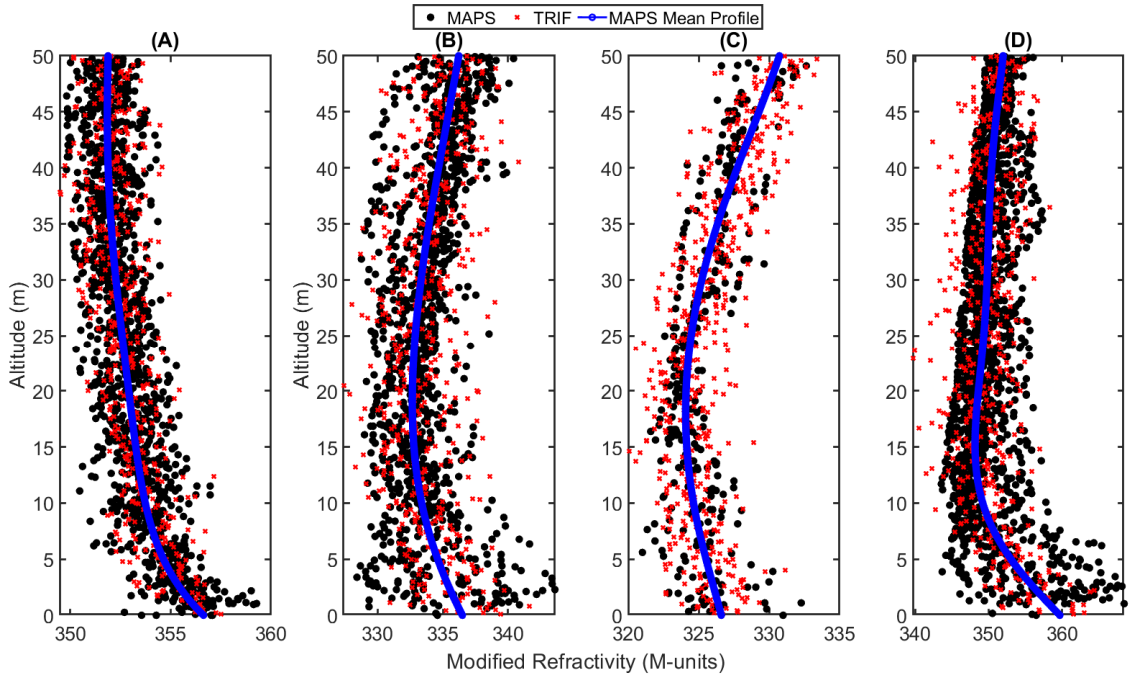


Figure 7. MAPS and TRIF instantaneous refractivity and the corresponding MAPS 7th-order polynomial fit for the MAPS datasets previously described in Figures 2–4 and 6 ((**A**) (dataset) 2, (**B**) 11, (**C**) 9, (**D**) 33).

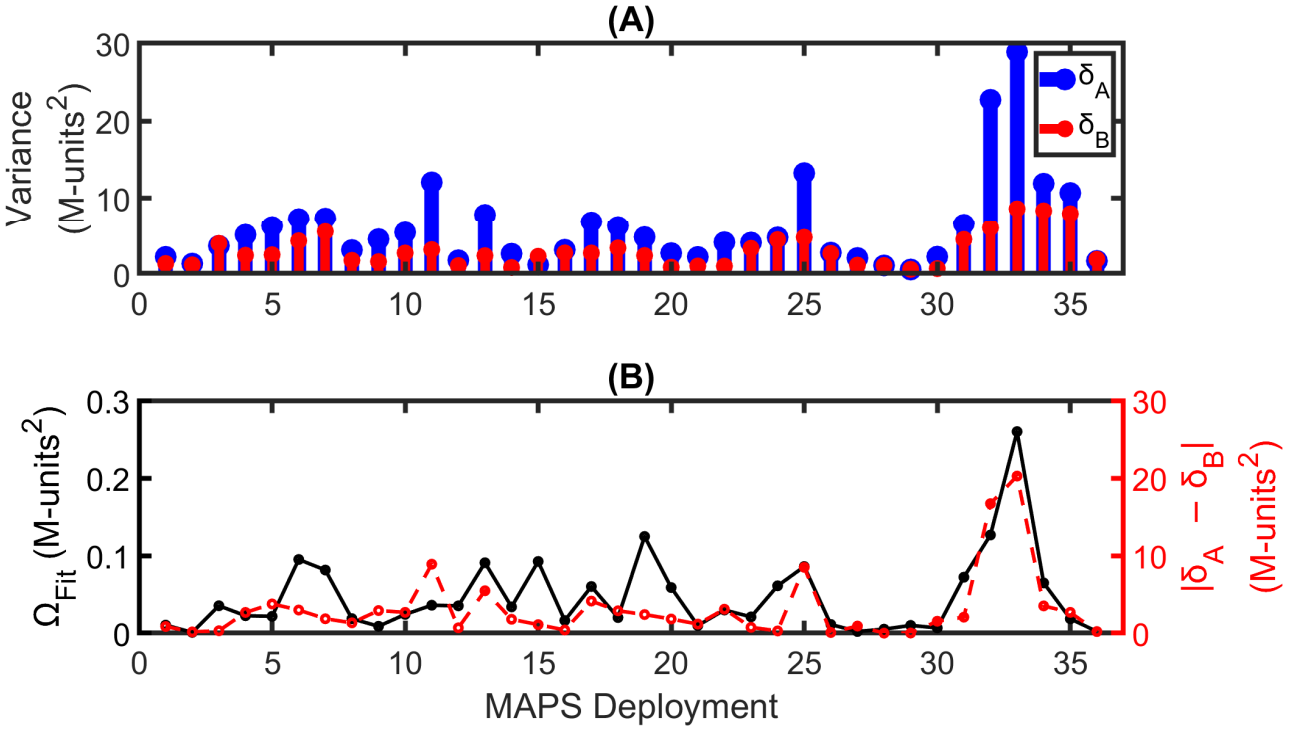


Figure 8. (**A**) Altitudinal variance in MAPS refractive fluctuations (M'). M' variance displayed for altitudes spanning 0–10 m and 10–20 m, δ_A and δ_B, respectively. (**B**) The left axis illustrates fitness scores (Equation (10)) corresponding to the MAPS/TRIF optimizations for each dataset in black, shown in Table 1. The magnitude of difference in MAPS refractive fluctuation variance between the 0–10 m and 10–20 m altitudinal bins ($|\delta_A - \delta_B|$) is illustrated in red on the right-hand axis.

Generally, the datasets shown to have the largest differences between δ_A and δ_B correspond to the largest fitness scores (poorest fit between MAPS and TRIF refractive fluctuations). This result (Figure 8B) was verified through linear correlation between Ω_{Fit} and $|\delta_A - \delta_B|$, yielding $R = 0.75$ ($p < 0.05$), a significant direct relationship. Thus, as the assumption of vertically homogenous turbulence degrades, so follows the TRIF model accuracy; however, even the largest $\sqrt{\Omega_{Fit}}$ are small relative to the RMS M' (Table 1), suggesting that TRIF can adequately model fluctuations in the cases presented. This result further suggests that PSO-estimated L_z falling within the ranges presented in Figure 5 are plausible and support the notion that MAPS variances are primarily related to physical processes.

6. Summary and Conclusions

This study incorporated unique meteorological data acquired with MAPS, deployed during the CASPER-East field campaign [11]. These data were used to examine the physical significance of variability within those measurements, performed within the MASL. MAPS [9] is a cutting edge MASL measurement technique able to obtain vertical distributions of pressure, temperature, humidity, and, thus, refractivity at relatively high temporal resolution. The goal of this study was to investigate the variance captured by these MAPS measurements and determine whether it can be explained by turbulent physical processes. To do this, the turbulence refractive index fluctuation (TRIF) model was implemented. TRIF is a spectral turbulence model based on a 1-D vertically homogenous anisotropic Kolmogorov spectrum that includes parameters describing the magnitude of the refractive index fluctuations (C_n^2) and vertical turbulent outer length scale (L_z). C_n^2 was estimated via bulk methods from MAPS and R/V Sharp meteorological measurements including SST, implemented via NAVSLaM. L_z was derived via PSO utilizing TRIF for 36 MAPS datasets of modified refractivity, which were decomposed into fluctuations. The derived L_z were compared with previously reported values in the MASL, and the accuracy of TRIF to properly emulate MAPS fluctuations was evaluated.

Optimized solutions of L_z are generally in good agreement with previously reported values in the MASL [26], where 94% of L_z solutions fall within a range observed in [26] over a wide range of atmsopheric stability conditions. Two L_z are greater than the reported range, where these L_z occur during near-thermally neutral conditions, likely causing underestimation of bulk C_n^2 (resulting in the large L_z), as previously reported [28]. Furthermore, for periods of thermal stability, NAVSLaM has been shown to overestimate bulk C_n^2, contributing to possible underestimation in the derived L_z. These uncertainties in C_n^2 can at least partly explain why the L_z estimates are within the correct order of magnitude but may not follow expected trends with air–sea temperature difference (ASTD).

Fluctuations from the TRIF model, based on optimization to MAPS measurements, were further examined by highlighting the relationship between fitness scores (Ω_{Fit}) and variations in MAPS fluctuations as a function of altitude. Specifically, when the assumption of C_n^2 homogeneity degrades, Ω_{Fit} increase. Vertical heterogeneity was observed, to some degree, for all MAPS datasets, further suggesting the physical nature of the MAPS measurements' variability. Even in cases where vertical heterogeneity is more prominent, and Ω_{Fit} are relatively large, TRIF refractive fluctuations are generally in good agreement with the MAPS refractivity fluctuations. This result illuminates the effectiveness of the TRIF model to emulate refractive fluctuations over a variety of conditions. Thus, the authors suggest that the variability observed in MAPS-measured instantaneous refractivity is physically significant and not primarily influenced by measurement uncertainty. Future research should incorporate turbulent refractive index fluctuation models that account for vertically heterogenous C_n^2.

Author Contributions: Conceptualization, D.M.P. and E.E.H.; methodology, D.M.P. and E.E.H.; formal analysis, D.M.P.; investigation, D.M.P. and E.E.H.; data curation, D.M.P., R.T.Y. and Q.W.; writing—original draft preparation, D.M.P.; writing—review and editing, D.M.P., R.T.Y., Q.W. and E.E.H.; visualization, D.M.P.; supervision, E.E.H.; project administration, E.E.H.; funding acquisition, E.E.H. All authors have read and agreed to the published version of the manuscript.

Funding: This research was funded by the Office of Naval Research, grant N00014-19-1-2350.

Institutional Review Board Statement: Not applicable.

Informed Consent Statement: Not applicable.

Data Availability Statement: No new data were created in this study.

Acknowledgments: The authors would like to thank Program Officer Steven Russell for his support of this research.

Conflicts of Interest: The authors declare no conflict of interest. The funders had no role in the design of the study; in the collection, analyses, or interpretation of data; in the writing of the manuscript; or in the decision to publish the results.

References

1. Businger, J.A.; Wyngaard, J.C.; Izumi, Y.; Bradley, E.F. Flux-profile relationships in the atmospheric surface layer. *J. Atmos. Sci.* **1971**, *28*, 181–189. [CrossRef]
2. Dyer, A.J. A review of flux-profile relationships. *Bound.-Layer Meteorol.* **1974**, *7*, 363–372. [CrossRef]
3. Webster, P.J.; Lukas, R. TOGA COARE: The coupled ocean–atmosphere response experiment. *Bull. Am. Meteorol. Soc.* **1992**, *73*, 1377–1416. [CrossRef]
4. Fairall, C.W.; Bradley, E.F.; Rogers, D.P.; Edson, J.B.; Young, G.S. Bulk parameterization of air-sea fluxes for tropical ocean-global atmosphere coupled-ocean atmosphere response experiment. *J. Geophys. Res. Ocean.* **1996**, *101*, 3747–3764. [CrossRef]
5. Fairall, C.W.; Bradley, E.F.; Hare, J.E.; Grachev, A.A.; Edson, J.B. Bulk parameterization of air–sea fluxes: Updates and verification for the COARE algorithm. *J. Clim.* **2003**, *16*, 571–591. [CrossRef]
6. Frederickson, P. Navy Atmospheric Measurements for EM Propagation Modeling. Executive Summary, Calhoun.nps.edu. 2016. Available online: https://www.nps.edu/en/web/research/summaries (accessed on 27 April 2023).
7. Hogan, T.; Liu, M.; Ridout, J.; Peng, M.; Whitcomb, T.; Ruston, B.; Reynolds, C.; Eckermann, S.; Moskaitis, J.; Baker, N.; et al. The navy global environmental model. *Oceanography* **2014**, *27*, 116–125. [CrossRef]
8. Grachev, A.A.; Andreas, E.L.; Fairall, C.W.; Guest, P.S.; Persson, P.O.G. SHEBA flux–profile relationships in the stable atmospheric boundary layer. *Bound.-Layer Meteorol.* **2007**, *124*, 315–333. [CrossRef]
9. Yang, Z.; Calderer, A.; He, S.; Sotiropoulos, F.; Doyle, J.D.; Flagg, D.D.; MacMahan, J.; Wang, Q.; Haus, B.K.; Graber, H.C.; et al. Numerical Study on the Effect of Air–Sea–Land Interaction on the Atmospheric Boundary Layer in Coastal Area. *Atmosphere* **2018**, *9*, 51. [CrossRef]
10. Doreene, K.; Wang, Q. Optimized estimation of surface layer characteristics from profiling measurements. *Atmosphere* **2016**, *7*, 14.
11. Wang, Q.; Alappattu, D.P.; Billingsley, S.; Blomquist, B.; Burkholder, R.J.; Christman, A.J.; Creegan, E.D.; De Paolo, T.; Eleuterio, D.P.; Fernando, H.J.S.; et al. CASPER: Coupled air–sea processes and electromagnetic ducting research. *Bull. Am. Meteorol. Soc.* **2018**, *99*, 1449–1471. [CrossRef]
12. Wang, Q.; Franklin, K.; Yamaguchi, R.; Ortiz-Suslow, D.G.; Alappattu, D.P.; Yardim, C.; Burkholder, R. Ducting conditions during casper-west field campaign. In Proceedings of the 2018 IEEE International Symposium on Antennas and Propagation & USNC/URSI National Radio Science Meeting, Boston, MA, USA, 8–13 July 2018; pp. 877–878.
13. Rainer, R.B. *In-Situ Observation of Undisturbed Surface Layer Scaler Profiles for Characterizing Evaporative Duct Properties*; Naval Postgraduate School Monterey United States: Monterey, CA, USA, 2016.
14. Alappattu, D.P.; Wang, Q.; Rainer, R.; Yamaguchi, R.; Lind, R.J. 4.4 Characteristics of surface layer scalar profiles using the in-situ measurements from an undisturbed marine environment. In Proceedings of the 20th Conference on Air–Sea Interaction, Madison, WI, USA, 15–19 August 2016; American Meteorological Society: Boston, UK, 2016.
15. Ulate, M.; Wang, Q.; Haack, T.; Holt, T.; Alappattu, D.P. Mean offshore refractive conditions during the CASPER East field campaign. *J. Appl. Meteorol. Climatol.* **2019**, *58*, 853–874. [CrossRef]
16. Pastore, D.M.; Greenway, D.P.; Stanek, M.J.; Wessinger, S.E.; Haack, T.; Wang, Q.; Hackett, E.E. Comparison of atmospheric refractivity estimation methods and their influence on radar propagation predictions. *Radio Sci.* **2021**, *56*, 1–17. [CrossRef]
17. Pastore, D.M.; Wessinger, S.E.; Greenway, D.P.; Stanek, M.J.; Burkholder, R.J.; Haack, T.; Wang, Q.; Hackett, E.E. Refractivity inversions from point-to-point X-band radar propagation measurements. *Radio Sci.* **2022**, *57*, 1–16. [CrossRef]
18. Rouseff, D. Simulated microwave propagation through tropospheric turbulence. *IEEE Trans. Antennas Propag.* **1992**, *40*, 1076–1083. [CrossRef]
19. Ivanov, V.K.; VShalyapin, N.; Levadny, Y.V. Microwave scattering by tropospheric fluctuations in an evaporation duct. *Radiophys. Quantum Electron.* **2009**, *52*, 277–286. [CrossRef]

20. Levadnyi, I.; Ivanov, V.; Shalyapin, V. Simulation of microwave propagation in turbulent evaporation duct. In Proceedings of the 2012 6th European Conference on Antennas and Propagation (EUCAP), Prague, Czech Republic, 26–30 March 2012; IEEE: Piscataway, NJ, USA, 2012; pp. 1–3.
21. Chou, Y.-H.; Kiang, J.-F. Effect of turbulence on wave propagation in evaporation ducts above a rough sea surface. In *Forum for Electromagnetic Research Methods and Application Technologies*; University of Limoges: Limoges, France, 2014; Volume 12.
22. Wagner, M.; Gerstoft, P.; Rogers, T. Estimating refractivity from propagation loss in turbulent media. *Radio Sci.* **2016**, *51*, 1876–1894. [CrossRef]
23. Bean, B.R.; Dutton, E.J. *Radio Meteorology*; Superintendentof Documents; U.S. Government Publishing Office: Washington, DC, USA, 1966; Volume 92.
24. Buck, A.L. New equations for computing vapor pressure and enhancement factor. *J. Appl. Meteorol. Climatol.* **1981**, *20*, 1527–1532. [CrossRef]
25. Ishimaru, A. *Wave Propagation and Scattering in Random Media*; Academic Press: New York, NY, USA, 1978; Volume 2.
26. Emes, M.J.; Arjomandi, M.; Kelso, R.M.; Ghanadi, F. Turbulence length scales in a low-roughness near-neutral atmospheric surface layer. *J. Turbul.* **2019**, *20*, 545–562. [CrossRef]
27. Percival, D.B. Simulating Gaussian random processes with specified spectra. *Comput. Sci. Stat.* **1993**, *24*, 534.
28. Frederickson, P.A.; Davidson, K.L.; Zeisse, C.R.; Bendall, C.S. Estimating the refractive index structure parameter () over the ocean using bulk methods. *J. Appl. Meteorol.* **2000**, *39*, 1770–1783. [CrossRef]
29. Frederickson, P.A.; Hammel, S.; Tsintikidis, D. Improving bulk Cn2 models for over-ocean applications through new determinations of the dimensionless temperature structure parameter. In *Atmospheric Optics: Models, Measurements, and Target-in-the-Loop Propagation*; SPIE: Bellingham, WA, USA, 2007; Volume 6708, pp. 45–54.
30. Qing, C.; Wu, X.; Li, X.; Tian, Q.; Liu, D.; Rao, R.; Zhu, W. Simulating the refractive index structure constant in the surface layer at Antarctica with a mesoscale model. *Astron. J.* **2017**, *155*, 37. [CrossRef]
31. Kennedy, J.; Eberhart, R. Particle swarm optimization. In Proceedings of the ICNN'95-International Conference on Neural Networks, Perth, WA, Australia, 27 November–1 December 1995; IEEE: Piscataway, NJ, USA, 1995; Volume 4, pp. 1942–1948.
32. Poli, R.; Kennedy, J.; Blackwell, T. Particle swarm optimization. *Swarm Intell.* **2007**, *1*, 33–57. [CrossRef]
33. Tatarskii, V.I. *The Effects of the Turbulent Atmosphere on Wave Propagation*; Israel Program for Scientific Translations: Jerusalem, Israel, 1971.
34. Wheelon, A.D. *Electromagnetic Scintillation: Volume 1, Geometrical Optics*; Cambridge University Press: Cambridge, UK, 2001.
35. VanZandt, T.E.; Green, J.L.; Gage, K.S.; Clark, W.L. Vertical profiles of refractivity turbulence structure constant: Comparison of observations by the Sunset radar with a new theoretical model. *Radio Sci.* **1978**, *13*, 819–829. [CrossRef]
36. Panofsky, H.A. Atmospheric turbulence. In *Models and Methods for Engineering Applications*; Wiley: New York, NY, USA, 1984; Volume 397.
37. Geernaert, G.L. Surface layer. In *Encyclopedia of Atmospheric Sciences*; Elsevier: Amsterdam, The Netherlands, 2003; pp. 305–311.

Disclaimer/Publisher's Note: The statements, opinions and data contained in all publications are solely those of the individual author(s) and contributor(s) and not of MDPI and/or the editor(s). MDPI and/or the editor(s) disclaim responsibility for any injury to people or property resulting from any ideas, methods, instructions or products referred to in the content.

Appendix E: Prepared Manuscript

Pastore, D.M., and E.E. Hackett (2024). Relative influence of sea state and mean, turbulent, and heterogenous refractivity on X-band propagation, *in-preparation*.

Relative Influence of Sea State and Mean, Turbulent, and Heterogenous Refractivity on X-Band Propagation

Douglas M. Pastore and Erin E. Hackett

***Abstract*— In predicting electromagnetic wave propagation within the marine atmospheric surface layer, it is common to assume steady homogenous conditions. However, discrepancies between predicted and measured propagation remain, which could be due in-part to turbulent fluctuations of the refractive index, spatially heterogenous evaporative ducting environments, and mischaracterization of the rough ocean bottom boundary. To better understand the relative importance of these contributors, this study explores the sensitivity of X-band propagation to parameters describing sea-state conditions and refractive environments, including turbulent fluctuations and spatially heterogenous conditions. This study employs the extended Fourier Amplitude Sensitivity Test to compute sensitivity indices that evaluate the leading-order effects and effects due to non-linear interactions between these refractive and sea state parameters on a parabolic wave equation electromagnetic wave propagation simulation. The parameters are delineated and evaluated in three atmospheric stability regime experiments: stable, neutral, and unstable, and consider both trapping and non-trapping propagation conditions. Parameter sensitivity indices are ranked for each experiment to examine the relative effects of the parameters on X-band propagation prediction. The results show that in neutral and stable regimes, mean evaporation duct characteristics have the greatest impact on propagation beyond the geometric horizon, while in unstable conditions, turbulence also plays a significant role. Additionally, in the lowest 10 m of the atmosphere, forward scattering from the rough sea-surface has the greatest effect on propagation predictions regardless of atmospheric stability.**

***Index Terms*— global sensitivity analysis, X-band, electromagnetic wave propagation, refractive turbulence, evaporation ducts, forward scattering, propagation in complex media, heterogenous evaporation ducts, rough ocean surface, marine atmospheric surface layer**

I. Introduction

ELECTROMAGNETIC wave (EM) propagation prediction within the first ~100 m of altitude over the ocean, a region known as the marine atmospheric surface layer (MASL), is a focal point of EM propagation research due to the frequent application of radar and communication systems in this region. EM propagation predictions are commonly estimated via parabolic wave equation (PWE) methods, a physics-based technique that accounts for EM wave refraction, forward scattering, and attenuation due to atmospheric and surface boundary conditions [1]. PWE is widely employed as an EM propagation prediction method within the MASL (e.g., [2]–[9]). Fidelity of PWE propagation predictions is directly related to the accuracy of the estimated propagation environment, specifically the atmosphere and sea-surface conditions [1], [3], [10]–[12].

Description of the atmosphere within PWEs is commonly prescribed as modified refractivity (M) distributions, which are a function of the prevailing meteorological conditions [13]. Commonly, parametric refractivity models are implemented to model refractivity profiles [2], [6], [9], [12], [14], where model parameters generally include refractive characteristics that are known to affect propagation – such as evaporation duct height (EDH), duct curvature, and mixed layer slope [3], [9], [11], [14]–[16]. Parametric models such as these typically neglect turbulent fluctuations and spatial heterogeneity in the refractive environment, which can lead to discrepancies between measured and modeled EM propagation [4], [5], [17], [18].

Inclusion of sea-surface roughness effects on EM propagation are included in PWE via: (i) the computation of a roughness reduction factor augmenting propagation relative to a flat surface [10], [19] or (ii) PWE solution of the EM wave over a 2-D realization of sea-surface displacement at the bottom boundary. While the former is more common in literature, this work focuses on the latter, as it continues to be applied more frequently in recent years as computational power and complex PWE frameworks have become more accessible. Inclusion of sea-surface roughness in PWEs requires ocean wave field information down to the order of the propagating EM wave (~0.03 m for X-band). Spectral wave models are implemented within PWE models and transformed into sea surface realizations to accurately resolve forward scattering at the rough ocean surface. An example of such a model is the modified Pierson-Donelan-Banner wave model ([20]–[22] employed in the Variable Terrain Radio wave Parabolic Equation (VTRPE) [22] model. Waves are modeled over a large range of wavenumbers from swell down to capillary waves covering all the relevant spatial scales needed for accurate computation of the interaction between propagating EM wave field and the sea-surface (Ryan, 1991).

This work was supported by the Office of Naval Research under Grant N00014-19-2350.

D. M. Pastore, was with the Marine Science Department, Coastal Carolina University, Conway, SC 29528 USA. He is now with the Propagation Modeling and Atmospheric Propagation Group, Naval Surface Warfare Center, Dahlgren, VA [ZIP CODE] USA (e-mail: dmpastore@coastal.edu)E. E. Hackett is with the Marine Science Department, Coastal Carolina University, Conway, SC 29588 USA (e-mail: ehackett@coastal.edu).

Previous studies have explored refractive and sea-surface effects on PWEs via sensitivity analysis, where most prior sensitivity studies implement a "one-at-a-time" (OAT) approach [11], [16] where one parameter is varied while others are fixed at a nominal value. Limitations of these OAT sampling schemes, such as their neglect of non-linear parameter interactions, led to the study performed by [3] using a global sensitivity method. [3] employ the extended Fourier Amplitude Sensitivity Test (eFAST) to quantify the effects of refractivity (evaporation and elevated ducts) and sea-surface roughness on propagation for multiple frequencies and polarizations within the marine atmospheric boundary layer (lowest 1 km of altitude). eFAST computes first order sensitivity, similar to what is computed via OAT techniques, and total order sensitivity, which accounts for non-linear parameter interactions making eFAST an excellent method to investigate complex PWE model sensitivities to input parameters.

While the atmospheric and sea-surface estimation methods discussed are widely verified within PWEs [2], [6], [9], [12], [14], [22], differences between measured and modeled propagation persist. These differences can potentially be attributed to three main causes: (i) not accounting for refractive fluctuations due to turbulence, (ii) inaccurate representation of the sea-surface, and (iii) not accounting for spatially heterogenous environments in which evaporation duct height (EDH) and strength can vary with range [5], [17], [18]. Inclusion of sea-surface roughness, turbulence, and spatial heterogeneity is computationally expensive, so few studies have explored their coupled effects on EM propagation predictions [5].

The current study explores the global sensitivity of a PWE to a comprehensive refractivity model (including mean, turbulent, and spatially heterogenous components) and to sea-surface wave model parameters. The eFAST technique is implemented to perform global sensitivity experiments for stable, neutral, and unstable atmospheric regimes because turbulent variations in the refractive index are stability dependent [5]. Furthermore, these stability-based eFAST experiments are broken up into scenarios where the EDH is above and below the transmitter height, i.e., comparing notional trapping and non-trapping effects, giving more insight into the sensitivity of the PWE under certain regimes for comparison. It is anticipated that different regimes (atmospheric stability and trapping conditions) could change the relative importance of refractive and sea state parameters.

The proceeding sections are organized as follows: section II discusses the eFAST technique, the atmospheric refractivity and sea surface models, and the propagation simulation. Section III describes the numerical experiments and section IV presents results and discussion associated with each experiment followed by a concluding section.

II. Methods

A. Extended Fourier Amplitude Sensitivity test

The extended Fourier Amplitude Sensitivity Test (eFAST) is a global sensitivity technique that utilizes variance decomposition to determine the sensitivity of a model to a set of input parameters. eFAST is useful for examining non-linear non-additive models in a computationally efficient manner [23], [24]. The main benefit of eFAST, relative to other sensitivity techniques, is the computation of both first order sensitivity index (S_I) and total sensitivity index (S_{TI}) of the specified model; inclusion of S_{TI} accounts for interactive effects between parameters on model variance. For this study, eFAST is deemed appropriate due to the complexity of the PE simulation and its implementation in a prior propagation study [3]. A brief description of the eFAST technique will be discussed where a more comprehensive description can be found in [3], [24].

For eFAST, model input parameters are varied based on a sampling scheme utilizing an incommensurate frequency (ω_i) unique to each parameter, X_i. As such, using a transformation function, all parameters are varied simultaneously through a single search variable, s [3], [23]:

$$X_i(s) = \mathrm{G}(\sin \omega_i s) = \frac{1}{2} + \frac{1}{\pi}\arcsin(\sin \omega_i s + \varphi_i), \quad -\pi \le s \le \pi \tag{1}$$

where φ_i is a random phase shift accommodating a starting point anywhere within the search curve [23]. The transformation function employed in (1) generates a uniform sampling distribution for each parameter, X_i. This transformation function allows the entire parameter space to be explored by varying one parameter, s, making it computationally efficient. The inclusion of other transformation functions is possible (e.g., Gaussian), but for this study it seems appropriate to explore all parameter search spaces evenly as some variables could be best described by a Gaussian distribution while others a uniform distribution. This transformation function is also the same as that used in [3].

After model simulations are completed for all eFAST model input parameter combinations determined from (1), eFAST method decomposes model output variance into partial variance associated with each parameter (V_i), and partial variance of the complimentary set of each parameter (V_{-i}) computed [3], [24]:

$$V = \frac{1}{N_s}\sum_{r=1}^{N_s} Y_r^2 \tag{2}$$

$$V_i = 2\sum_{j=1}^{M_H} A_{j\omega_i}^2 + B_{j\omega_i}^2 \tag{3}$$

where Y_r is the amplitude of the oscillations of the model output (in this case PE-simulated propagation loss) at each frequency, N_S is the number of samples in s, and M_H is the number of included harmonics (here, M_H=4). A and B are the Fourier coefficients at each harmonic, j, for each incommensurate frequency (ω_i) calculated as [3]:

$$A_j = \frac{1}{N_S}\left\{Y_0 + \sum_{r=1}^{\frac{N_S-1}{2}} (Y_r + Y_{-r}) \cos\frac{\pi jr}{N_S}\right\}, \quad j \text{ even} = 0, j \text{ odd} \tag{4}$$

$$B_j = \frac{1}{N_S}\left\{Y_0 + \sum_{r=1}^{\frac{N_S-1}{2}} (Y_r - Y_{-r}) \sin\frac{\pi jr}{N_S}\right\}, \quad j \text{ odd} = 0, j \text{ even} \tag{5}$$

From the variances computed in (2) and (3) the sensitivity indexes S_{TI} and S_I for each parameter (X_i) can be computed as [3]:

$$S_{I_i} = \frac{V_i}{V} \tag{6}$$

$$S_{TI_i} = 1 - \frac{V_{-i}}{V} \tag{7}$$

where -*i* indicates the complimentary set (all parameters except parameter *i*).

Equation (6) computes the first-order sensitivity, which represents the amount of variance in the model output explained by that one parameter and would be equivalent to what one would obtain using an OAT approach. Further, (7) computes the total order sensitivity, which accounts for the higher-order effects associated with interactions between this parameter and the other parameters, and their combined effect on model output variations.

Aliasing can occur without proper sampling of the search space by the search variable, *s*. Mitigation of this sampling error is achieved through a sampling scheme that accounts for the number of parameters and harmonics used in calculation of the partial variances. This sampling scheme is common practice in eFAST analyses [3], [23], [24] and requires that at least 65 model runs per included parameter are performed (650 total model runs in this case). A dummy parameter is also included in the set of eFAST input parameters, which varies independently of the model output. The dummy's estimated sensitivity indices (S_{TI} and S_I) are assumed to represent random variance within the model and are used to interpret significance level of sensitivity indices of the other parameters. Sensitivity indices less than or equal to the dummy are considered not significantly different than zero (Marino et al., 2008), and therefore, unimportant to the model.

For this study, eFAST will be used to determine the sensitivity of an EM propagation simulation to the propagation environment. The environment is broken into two categories, the sea surface and the refractivity. The following subsections explain the models used to describe the refractivity and sea surface, where specific parameters of each model are the eFAST input parameters (X_i) that are varied to investigate their relative effects on EM propagation predictions.

B. Atmospheric Refractivity Model

The atmospheric refractivity model is comprised of three components: i) a parametric refractivity model describing "mean" atmospheric refractivity, ii) an EDH heterogeneity model accounting for range variation of EDH, and iii) a stochastic refractive index fluctuation model emulating turbulent fluctuations of the refractive index. To the authors' knowledge, this is the first time a refractivity model has included aspects of mean refractivity, turbulence, and spatial heterogeneity to comprehensively describe the atmospheric refractivity within a PE simulation. The individual model components of refractivity are further discussed below.

Mean refractivity is modeled via a parametric refractivity model [2], [6], [9], [12], [14]:

$$\bar{M}(r,z) = M_0 + \begin{cases} c_0\left(z - z_d(r)\ln\left(\frac{z+0.00015}{0.00015}\right)\right) & , z \le z_L \\ m_1 z - M_1 & , z > z_L \end{cases} \tag{8}$$

where $M_0 = 333$ M-units representing surface refractivity, $z_d(r)$ is evaporation duct height as a function of range (r), m_1 is mixed layer slope, and M_1 is a term defined by c_0, z_d, and m_1 ensuring a continuous profile between layers. The potential refractivity gradient [25], c_0, allows modification of the shape of the refractivity profile within the evaporation layer for a specified duct height [9], [12], [14]. The evaporation layer extends from the surface to $z_L \equiv 2z_d$. M_0 is held constant throughout this study because the propagation is influenced by the refractivity gradients and not the absolute values.

Incorporation of EDH heterogeneity over range is included within (8) via a linear variation of z_d:

$$z_d(r) = s_d r + \frac{\overline{z_d}}{2} \tag{9}$$

where, s_d is EDH slope, and $\overline{z_d}$ is the mean EDH over the range transect of duct heights modeled in (9). Application of $z_d(r)$ to (8) makes mean modified refractivity a function of both height and range, $\bar{M}(r,z)$, and creates a set of modified refractivity profiles describing a single transect of a spatially varying mean refractive environment. A linear function to describe variation of z_d in range was chosen for multiple reasons. First, range heterogeneity of refractivity is not yet well understood and can be characterized by a variety of nth degree polynomial functions, where linear functions are dominant in weather model forecasts [26]. And second, few studies account for variation of z_d in range [27] but it is known that range variations can have non-negligible effects on EM propagation [28]. Further, no knowledge exists describing critical refractive gradient and mixed layer slope variation in range, thus, a simplistic linear model, varying only z_d and assuming c_0 and m_1 to be constant over range, is appropriate and practical. Within the eFAST methodology, c_0 and m_1 from (8) as well as $\overline{z_d}$ and s_d from (9) are varied to determine S_I and S_{TI} of the propagation model for each of these parameters.

In addition to mean and spatially heterogenous components

of refractivity, refractivity is assumed to be constantly perturbed by continuous fluctuations due to turbulence within the atmosphere, following the refractive index turbulence model verified in [29]. Modeling of the random fluctuations is achieved by the decomposition of refractivity [4]:

$$M(r,z) = \bar{M}(r,z) + M'(r,z) \tag{10}$$

where $\bar{M}(r,z)$ is a mean refractivity vertical profile and $M'(r,z)$ is the random fluctuations considered to be stochastic. For this formulation, it is assumed perturbations do not change in time while EM waves propagate through the medium, which is a reasonable assumption given EM waves travel at the speed of light (far faster than even the shortest turbulent time scale). The stochastic fluctuating component is described by the 2-D Kolmogorov spectrum [5], [30]:

$$\emptyset(\kappa_r,\kappa_z) = \frac{0.0555C_n^2}{(\kappa_r^2+\kappa_z^2+1/L_0^2)^{4/3}} \tag{11}$$

where κ is the spatial wavenumber (where subscript indicates directional component), C_n^2 is the refractive index structure constant (with units of $m^{-2/3}$), and L_0 is the outer length scale delineating the border between energy containing or "mixing" scales from those in the inertial subrange, with units of meters. To account for anisotropy in the MASL, the 2-D Kolmogorov spectrum from (11) can be modified [5], [30]:

$$\emptyset(\kappa_r,\kappa_z) = \frac{0.0555C_n^2(L_rL_z)^{\frac{4}{3}}}{(\kappa_r^2L_r^2+\kappa_z^2L_z^2+1)^{\frac{4}{3}}} \tag{12}$$

where L_z and L_r are the vertical and horizontal outer length scales, respectively. The relationship between these outer length scales has been previously studied and will be represented in this study as L_z/L_r = 0.27 [31]. Within the eFAST analysis, C_n^2 and L_z from (12) are included to explore the effects of refractive index turbulent fluctuations on EM propagation. They are assumed to be homogenous in both range and altitude.

C. Ocean Wave Model

The bottom boundary for the propagation domain is constructed via an ocean wavenumber spectral model. Specifically, a Donelan-Peirson-Banner model accounts for the wind seas and capillary waves (Pierson and Moskowitz, 1964; Donelan et al., 1985; Banner et al., 1989), which is appended with a narrow band Gaussian swell spectrum (Ryan 1991); for brevity the wave model will be referred to as $\emptyset_W$. $\emptyset_W$ is parameterized by the mean wind speed at z = 10 m (U), the swell height (S_H) and swell wavelength (λ). These sea surface characteristics represent parameters describing the shorter and longer length scales of the rough ocean surface. In this study, the wind wave fields are considered fully developed. Within the eFAST analysis, U, S_H, and λ are varied to explore the sensitivity of X-band propagation to sea state characteristics.

It is important to note, the ocean wave model and the atmospheric refractivity model are not coupled. Thus, certain combinations of the respective model parameters could diverge from physically plausible conditions; this issue is mitigated as much as possible by dividing the sensitivity analysis into several experiments that vary the range of the parameters explored in the eFAST analysis (see section III).

D. Propagation Simulation

EM propagation predictions are performed utilizing the Variable Terrain Radio-Wave Parabolic Equation (VTRPE) simulation (Ryan, 1991). VTRPE is employed in this study because the simulation can model a variety of environmental conditions and it has been used in prior similar studies [3], [6], [7], [9], [12]. A split step rotated Green's function parabolic equation is used to compute the full wave solution of the EM field [1], [22]. For this study, [3], propagation loss (PL), in dB, are used as the simulation output for the eFAST experiments. PL is defined as:

$$P_L = 20\log(2k_0r) - 20\log|F| \tag{13}$$

where k_0 defines wavenumber of the electromagnetic wave, and F is the propagation factor:

$$F = \left|\frac{\boldsymbol{E}}{\boldsymbol{E_0}}\right| \tag{14}$$

where $\boldsymbol{E_0}$ is the electric field in free space and $\boldsymbol{E}$ is the electric field in the modeled environment.

Application of the refractivity model within the propagation simulation is not a trivial process due to the refractive index turbulent fluctuations and range inhomogeneity; associated challenges are described in multiple previous studies [4], [5], [32], [33]. Commonly, stochastic variations in the refractive index are performed via the multiple phase-screen (MPS) method, where the EM field is propagated through successive refractive profile realizations. The MPS method employs the Markov approximation, or the assumption that the phase screens are δ-correlated over propagation space [34], this assumption is valid only when the phase-screen spatial resolution (Δr) is approximately [33], [35]

$$\Delta r \geq 5L_r \tag{15}$$

Consideration of (15) in the implementation of the MPS-method is imperative for the physically practical implementation of stochastic turbulence within the PWE, and thus reducing error in the computation of the EM wave field.

EM wave field solution error for a given frequency, independent of stochastic variation in the refractive index, is a function of the PWE solution range step-size. In this study, Δr = 0.3 m to accurately solve the EM wave field over a rough bottom boundary condition [22] and satisfying the Δr necessary for a propagation frequency of 10.7 GHz and a maximum propagation angle of 6º, an angle shown to be appropriate for propagation through surface ducting conditions [4], [33].

Δr = 0.3 m minimizes error of the PWE solution but violates (15) as horizontal outer length scales are on the order of tens to hundreds of meters [31]. This violation invalidates applicability

of the MPS method in this study. To address this limitation, the correlated phase screen (CPS) technique proposed in [33] is employed. The CPS method relieves the limitations of (15), allowing for closely spaced, and thus, correlated phase screens. These vertical phase screens are computed [33]:

$$S_\phi(\kappa_r\kappa_z) = (\Delta r)^2 \emptyset(\kappa_r, \kappa_z)\left(\frac{\sin\left(\frac{\kappa_r \Delta r}{2}\right)}{\frac{k_r \Delta r}{2}}\right)^2 \quad (16)$$

Realizations of vertical phase screens obeying (16) are performed via convolution of S_ϕ and a zero mean 2-D Gaussian field. This process results in a field of refractive index fluctuations with sampling intervals of Δz = 0.01 m and Δr = 0.3 m that can be added to the duct height heterogeneous mean refractive profiles computed via (8) and (9). The resulting set of profiles, including heterogeneity and turbulence in the refractive index, are implemented within the PWE.

III. eFAST Experiments

For this study, propagation simulations are performed at a frequency of 10.7 GHz transmitted at an altitude of 15 m with vertical polarization and a Gaussian antenna pattern. The dielectric bottom boundary conditions are held constant with a sea surface temperature of 20 °C and a salinity of 35 ppt. Numerical experiments are performed for simulation domains of 0-100 m in altitude and 0 – 60 km in range, fully exploring the MASL including over the horizon propagation.

eFAST sensitivity experiments are performed for the parameters listed in Table 1. Atmospheric refractivity model parameters (§2.2) are varied separately for three different atmospheric stability conditions: stable, neutral, and unstable. Categorization of the atmosphere based on stability is defined via the stability parameter, $\left(\frac{z}{L}\right)$ [36], where L is the Monin Obuhkov length scale [37]. Stable regimes are defined as $0.5 \geq \frac{z}{L} > 0.01$, neutral as $-0.01 < \frac{z}{L} < 0.01$, and unstable regimes as $-5 < \frac{z}{L} \leq -0.01$ [38]. Specifically, C_n^2, L_Z, and C_0 have been shown to be stability dependent [31], [39]–[41] and thus, their respective search spaces will vary between stability experiments, as outlined in Table 1. Search spaces are determined from the literature and are also supported by analysis of CASPER meteorological data [7], [9], [39], [42], [43] (see Table 1). Other parameters included such as, EDH slope over range (s_d), mean EDH ($\overline{z_d}$), and m_1, have search spaces that are the same for each stability experiment due to a lack of consistent findings in the literature on the relationship between these parameters and atmospheric stability.

Table 1. Global sensitivity study atmospheric refractivity and sea-state parameter ranges and related citations for each atmospheric stability regime experiment.

Parameter Nomenclature	Parameter	Stable Regime		Neutral Regime		Unstable Regime		Citations
		Minimun	Maximum	Minimun	Maximum	Minimun	Maximum	
C_n^2	Structure Constant ($m^{-2/3}$)	$5x10^{-16}$	$5x10^{-13}$	$1x10^{-16}$	$1x10^{-12}$	$1x10^{-15}$	$5x10^{-12}$	Junwei et al. (2011); Qing et al. (2016); Wang et al. (2018)
L_z	Outer Length Scale (m)	1	3	3	6	6	8	Van Zandt et al. (1978); Emes et al. (2019)
s_d	Evaporation Duct Height Slope Over Range (m/km)	-5/60	5/60	-5/60	5/60	-5/60	5/60	Zhao et al. (2017); Wang et al. (2018)
$\overline{z_d}$	Mean Duct Height (m)	5	30	5	30	5	30	Skolnik (2001); Wang et al. (2018)
C_0	Duct Curvature (M-units/m)	0.025	0.2	0.115	0.135	0.2	0.45	Paulus (1990); Wang et al. (2018) ; Wessinger (2022)
m_1	Mixed Layer Slope (M-units/m)	0.08	0.12	0.08	0.12	0.08	0.12	Zhang et al. (2011); Wang et al. (2018)
U	Wind Speed (m/s)	0.1	17	0.1	17	0.1	17	Beaufort Scale (0-7)
S_H	Swell Height (m)	0.1	6	0.1	6	0.1	6	Generalized based on Beaufort Scale (0-7)
λ	Swell Wavelength (m)	50	250	50	250	50	250	Coastal swell to open sea swell

Along with experiments delineated by stability, each stability experiment is broken up into two scenarios, trapping and non-trapping. In this study, the trapping and non-trapping nomenclature specifically describes conditions where $\overline{z_d}$ is greater than the transmitter height (Tx; 16 m $\leq \overline{z_d} <$ 30 m) referred to as the trapping condition, and conditions where $\overline{z_d}$ is less than the Tx (5 m $< \overline{z_d} \leq$ 14 m), referred to as the non-trapping condition; application of this nomenclature does not define when trapping occurs, although it is more likely to occur under the respective name of each scenario. The trapping and non-trapping nomenclature is specific to $\overline{z_d}$, where duct height environments varying over range can breach the transmitter height (15 m) due to refractive conditions set by s_d. This breaching occurs in approximately 16% of simulation runs for each of the six experiments.

Wave model (§2.3) parameters, specifically swell height (S_H) and wind speed (U) search spaces are based on the Beaufort scale encompassing force 0 (“calm”) to force 7 (“near gale”). Swell wavelength (λ) search space encompasses a large range of wavelengths from coastal to open ocean swell. While feedback between atmospheric stability and sea state conditions

exists, in this study, sea state parameter search spaces are not varied across the atmospheric stability regime experiments as this interaction is more complex than can be accounted for with the present models.

IV. Results and Discussion

First order (S_I) and total order sensitivity indices (S_{TI}) are presented in subsections for each stability regime (stable, neutral, and unstable) experiment described in §3.0. Recall that the effect of the duct height crossing the transmitter height is largely omitted here due to the division of the experiments into trapping and non-trapping cases. The most significant factor to the propagation is well known to be whether a duct does or does not trap radiated energy [7], [11], [15], [16]; thus, the results presented here are secondary to this mechanism for propagation variation, and sensitivities reported for $\overline{z_d}$ likely correspond primarily to variations in energy leakage by the duct.

Experiment results are presented as the average sensitivity index beyond the geometric horizon (BGH) normalized by the maximum (BGH) average sensitivity index over all parameters, referred to as normalized average sensitivity index (NAS). This metric gives insight into the relative influence of each parameter on long-range propagation and allows for easier comparison between experiments. A NAS of one indicates the most influential parameter at a specific location and values below 1 indicate the relative importance of that parameter with respect to this most influential parameter.

Regionally averaged normalized sensitivity index (NRAS) is also presented for averages taken BGH and over three altitudinal ranges, 2 – 10, 10 – 50, and 50 – 100 m. These results highlight locations of high/low sensitivity of radio-wave propagation within the modeled propagation domain for each of the parameters. The lowest region (2 – 10 m) excludes the lowest altitudes (1 – 2 m) to ensure effects of blockage (by sea surface waves) on averaged sensitivities are minimized [44]. Furthermore, this region is capped at 10 m to capture variations in propagation well below the transmitter. The mid altitude region (10 – 50 m) encompasses a region that generally includes the transition of the refractive environment from super refractive (ducting) to the mixed layer (sub-refractive) and encompasses the altitude of the transmitter. The upper altitudinal region (50 – 100 m) is delineated to capture the portion of the propagation domain explicitly within the mixed layer environment and well above the transmitter.

C_n^2, $\overline{z_d}$, and U are examined further as they tend to have the largest influence on propagation throughout this study, which has also been observed in previous studies of BGH propagation [2], [3], [5], [7], [11], [15], [19]. Specifically, normalized total order sensitivity (NS_{TI}) is computed by normalizing each parameter's S_{TI} at each range and altitude of the propagation domain by the maximum S_{TI} across all parameters at that location. Thus, analogous to NAS, $NS_{TI} = 1$ indicates the most influential parameter at a specific location and values below 1 indicate the relative importance of that parameter with respect to this most influential parameter. Distributions of NS_{TI} for C_n^2, $\overline{z_d}$, and U over the propagation domain enable direct comparison of the relative role of turbulence, mean refractivity, and sea state in various regions of the modeled domain for X-band propagation.

A. Stable Regime

Normalized average S_I (NAS_I) and S_{TI} (NAS_{TI}) for trapping and non-trapping scenarios are illustrated in Fig. 1. In this stable case, generally, mean refractive parameters within the duct (i.e., $\overline{z_d}$ and c_0) are shown to have the largest sensitivities within the atmospheric parameters, for both NAS_I and NAS_{TI} over trapping and non-trapping scenarios. These results are consistent with those reported in the sensitivity study of [3]. This result suggests that while evaporation ducts may not always be present under stable conditions, when they do exist, their mean refractive characteristics tend to be the dominant factors in the propagation. The duct height is, of course, well-known to influence propagation and the c_0 parameter is similar to a measure of duct strength, which is also known to significantly impact propagation [7], [11], [15]–[17]. Recall, the duct height has the effect of the duct height crossing the transmitter removed, thus, the duct strength being more influential than duct height for trapping conditions is logical.

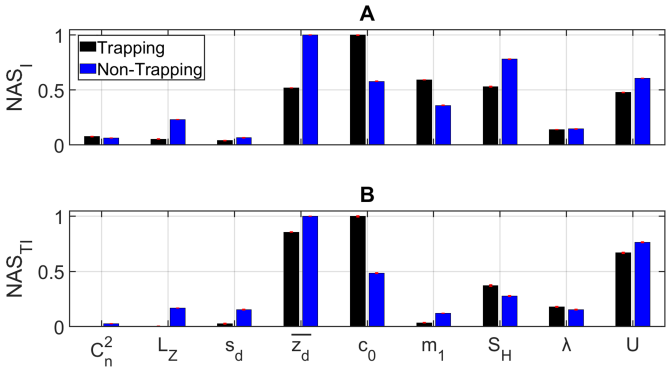


Fig. 1. Stable regime (A) first-order (NAS_I) and (B) total-order (NAS_{TI}) normalized average sensitivity indices. Sensitivity indices for each parameter are averaged over ranges and altitudes beyond-the-geometric horizon and normalized by the maximum average S_I and S_{TI}, respectively, for trapping (16 m $\leq \overline{z_d} <$ 30 m) and non-trapping (5 m $< \overline{z_d} \leq$ 14 m) scenarios. Red error-bars denote 99% confidence intervals.

In both the trapping and non-trapping cases, the sea surface is shown to be significantly influential relative to the mean refractivity characteristics. This result is expected as variations in ocean waves change multipath null locations and thus cause significant variations in the propagation loss at locations near the multipath nulls as sea state is varied ([12]). NAS_{TI} for U is larger than that of swell wave height (S_H), while for NAS_I the opposite is true. This difference indicates that parameter interactions cause the influence of S_H to diminish relative to the influence of U. The larger influence of U is consistent with the concept that EM propagation variations due to forward scattering are primarily driven by smaller-scale wind waves (less than ~50 m wavelength) rather than swell (wavelengths much larger than 50 m).

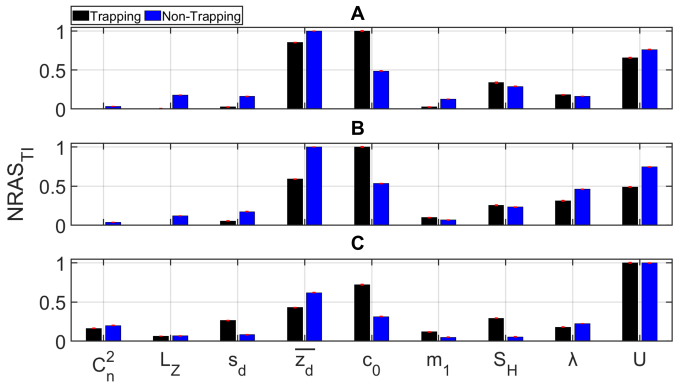


Fig. 2. Stable regime regionally averaged total-order sensitivity ($NRAS_{TI}$), averaged over ranges beyond-the-geometric horizon and altitudes and of (A) 50 – 100 m, (B) 10 – 50 m, and (C) 2 – 10 m, normalized by the maximum regionally averaged S_{TI} over all parameters for trapping and non-trapping scenarios. Red error-bars denote 99% confidence intervals.

Relative to the mean refractive and sea-surface conditions, turbulent fluctuations in the refractive index and duct height heterogeneity are shown to have a relatively negligible effect on propagation. During stable conditions, thermal stratification of the atmosphere is expected to dampen (mechanical and convective) turbulence in the MASL and thus fluctuations within the surface layer are small (Table 1) reducing their influence on EM wave propagation. This result is reflected in Fig. 1 by the small sensitivities for C_n^2 and L_Z. Like the turbulence, propagation sensitivity to evaporation duct height slope (s_d) is minimal relative to the other parameters.

Fig. 2 shows $NRAS_{TI}$. For all altitudes, and consistent with the results shown in Fig. 1, the mean refractivity parameters within the duct ($\overline{z_d}$ and c_0) and the wind speed are shown to be the most influential on propagation for both trapping scenarios; however, near the sea surface (2-10 m altitude range), the wind speed parameter emerges as the most influential parameter while at the other altitudes the mean refractivity parameters are most dominant. It is also notable that swell plays a larger role at higher altitudes (>10 m), especially in non-trapping conditions, suggesting swell primarily influences multipath null locations.

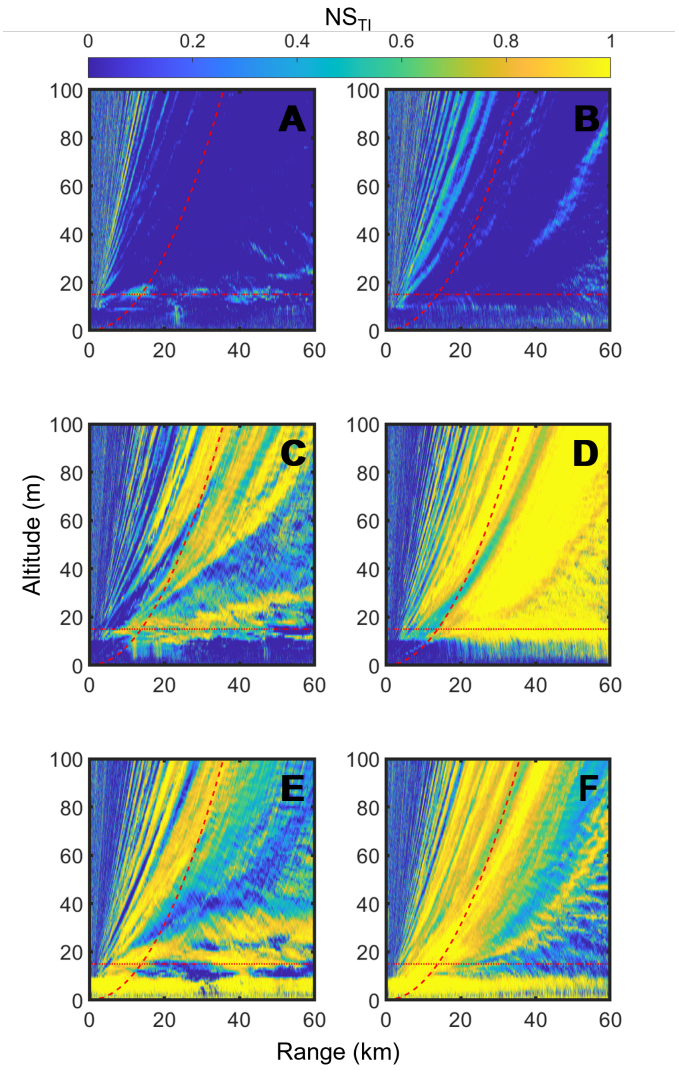


Fig. 3. Stable regime total-order sensitivity (S_{TI}) normalized by the largest magnitude S_{TI} across all parameters, for each range and altitude. Normalized sensitivities (NS_{TI}) are shown for trapping (A, C, and E) and non-trapping (B, D, and F) scenarios; parameters illustrated are (A & B) C_n^2, (C & D) $\overline{z_d}$, and (E & F) U. These parameters are representative of the turbulence, mean atmospheric refractivity, and sea-state components, respectively. The dashed red line represents the geometric horizon, and the dotted horizontal red line represents the RF transmitter height (15 m).

To visualize the regions of the domain where the relative roles of turbulence, mean refractivity, and sea state can be ranked, Fig. 3 shows normalized S_{TI} (NS_{TI}) for C_n^2, $\overline{z_d}$, and U (from top to bottom) in trapping (left column) and non-trapping (right column) scenarios; the dashed red line denotes the range of the geometric horizon for all altitudes. Visual differences between NS_{TI} for the trapping (Fig. 3A, C, ad E) and non-trapping (Fig. 3B, D, and F) scenarios are noticeable.

The overall importance of $\overline{z_d}$ (Fig. 3C and D) over the influence of C_n^2 (Fig. 3A and B) and U (Fig. 3E and F) is apparent when comparing along the columns of subfigures in Fig. 3 for the trapping and, especially, the non-trapping scenario. In the trapping scenario, the sea state (U) plays a comparable role to that of the duct height.

In the trapping scenario, the low sensitivities of the duct height below the transmitter are due to the experiments being divided into the trapping and non-trapping scenarios. Variations in propagation due to the duct height crossing the transmitter height are not captured here intentionally so not to dominate the sensitivity results as this effect on propagation is well understood. Because all the propagation loss simulations have a "trapping" influence on the propagation for the trapping scenario, the duct height sensitivity is small there. The region just above the transmitter is influenced due to differences in leakage from the duct due to the proximity of the duct height to the transmitter height changing. In non-trapping scenarios, the duct height is the most influential parameter in nearly the entire domain BGH and above the transmitter. Again, this region's sensitivity is presumably due to variations in propagation loss due to the duct height's proximity to the transmitter influencing this entire region for non-trapping scenarios. Similar results are discussed anecdotally in [7], but for unstable environments.

The sea state, through the wind speed, shows the low altitude propagation to be most significantly influenced by sea surface forward scatter that diminishes in importance with range in non-trapping scenarios but does not diminish in trapping scenarios. For trapping scenarios, the sea state is also observed to have an influence in the same region as the duct height, just above the transmitter, indicating a possible interaction between these parameters potentially involving duct leakage in trapping conditions. Large NS_{TI} is also observed for U near locations of multipath nulls, as expected. Turbulence (C_n^2) plays an insignificant role relative to mean refractivity and sea state evidenced by the low NS_{TI} for both trapping and non-trapping scenarios.

B. Neutral Regime

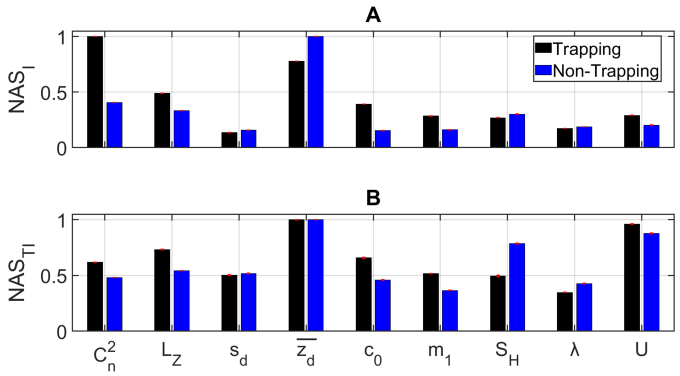


Fig. 4. Neutral regime (A) first order (NAS_I) and (B) total-order (NAS_{TI}) sensitivity averaged over ranges and altitudes beyond-the-geometric horizon and normalized by the maximum average S_I and S_{TI}, respectively, for trapping (16 m ≤ $\overline{z_d}$ < 30 m) and non-trapping (5 m < $\overline{z_d}$ ≤ 14 m) scenarios. Red error-bars denote 99% confidence intervals.

Neutral regime NAS_I and NAS_{TI} are illustrated in Fig. 4, where similarly to the stable case, mean duct height and sea-surface parameters show the largest NAS_{TI}. A strong influence of duct height and sea surface characteristics in neutral regimes is supported in many prior studies [3], [11], [16], [44]. However, contrary to the stable case, there is more relative influence of turbulence and duct height heterogeneity on propagation, where the contributions to PL variations from these phenomena are roughly equal, especially for the non-trapping scenario (Fig. 4B). The relative role of duct strength (c_0) is also significantly smaller for the neutral case, even in trapping conditions, relative to the stable case.

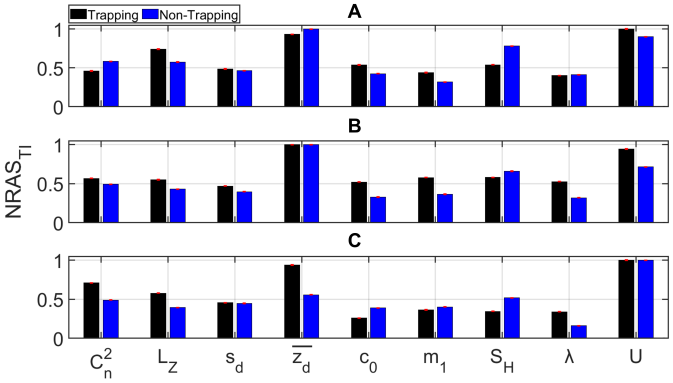


Fig. 5. Neutral regime regionally averaged total-order sensitivity ($NRAS_{TI}$) averaged over ranges beyond-the-geometric horizon and altitudes of (A) 50 – 100 m, (B) 10 – 50 m, and (C) 2 – 10 m, normalized by the maximum regionally averaged S_{TI} over all parameters for trapping and non-trapping scenarios. Red error-bars denote 99% confidence intervals.

In a neutral environment, the magnitude of C_n^2 is larger than in a stable atmosphere (see Table 1), due to mechanical mixing no longer being inhibited by stable stratification, and consequently turbulent fluctuations of the refractive index are larger, causing more variation of the EM signal BGH. In fact, without parameter interactions, EM variations due to turbulence can cause large effects on propagation as evidenced by the highest NAS_I for C_n^2 in the trapping scenario.

The more constrained parameter range for duct curvature (see Table 1 – c_0) observed in neutral atmospheres likely diminishes the role of duct strength on the propagation in favor of duct height variations in range causing more significant changes in propagation. Thus, while duct height proximity to the transmitter and forward scatter of EM energy remain the primary mechanisms for variation in BGH propagation, turbulence and duct height heterogeneity start to become relevant to second-order variations in propagation for the neutral regime, and duct shape effects are less significant.

The regional analysis presented in Fig. 5 (analogous to Fig. 2), reveals similar results relative to the larger spatial averages shown in Fig. 4. For all altitudes BGH, duct height ($\overline{z_d}$) and wind speed (U) primarily vary EM propagation. At the lowest altitude bin (2-10 m) for both trapping conditions, wind speed is the dominate source of propagation variation, while duct height dominates at altitudes between 10-50 m. For the trapping case, wind speed and duct height play nearly equal roles in propagation variability at all altitudes. Similar to Fig. 4, turbulence and duct height heterogeneity play a more significant role, relative to the stable case at all altitudes.

Fig. 6 shows distributions of NS_{TI} for C_n^2, $\overline{z_d}$, and U for the two trapping scenarios for the neutral experiment. Again, similar to the stable case and regionally averaged results, the mean duct height is the most significant factor in most regions BGH for both trapping and non-trapping scenarios. The

influence of the duct height for trapping scenarios is more significant (larger NS_{TI} BGH) than it was for the stable experiment. For both trapping and non-trapping scenarios, the influence of mean wind speed is largest below 10 m at all ranges.

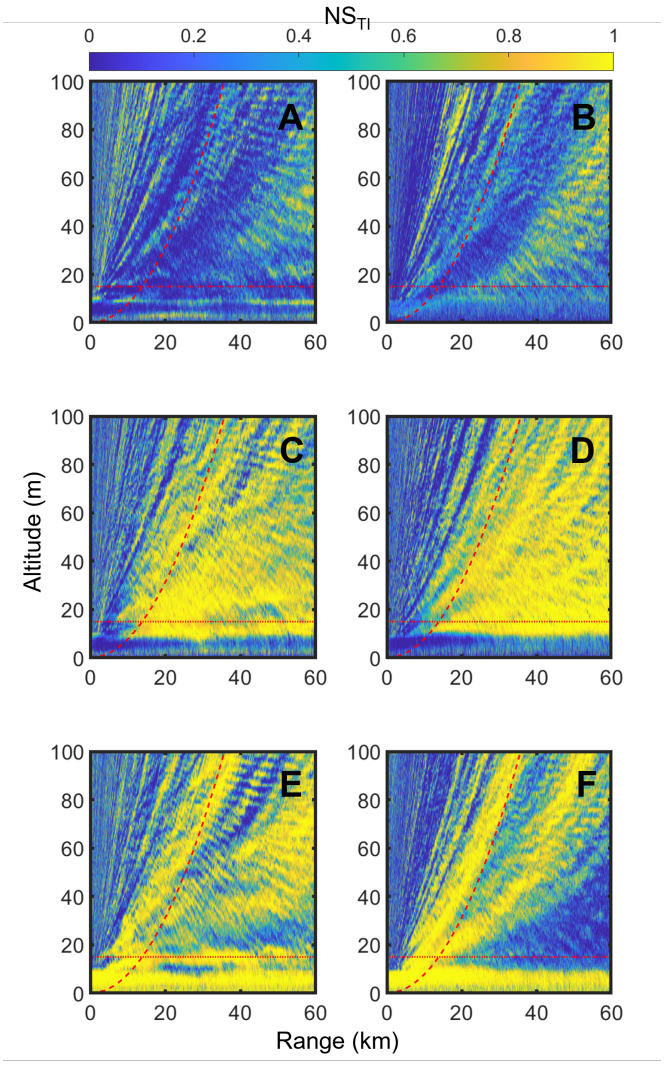


Fig. 6. Neutral regime total-order sensitivity (S_{TI}) normalized by the largest magnitude S_{TI} over all parameters, at each range and altitude. Normalized sensitivities (NS_{TI}) are shown for trapping (A, C, and E) and non-trapping (B, D, and F) scenarios; parameters illustrated are (A & B) C_n^2, (C & D) $\overline{z_d}$, and (E & F) U. These parameters are representative of the turbulence, mean atmospheric refractivity, and sea-state components, respectively. The dashed red line represents the geometric horizon, and the dotted horizontal red line represents the RF transmitter height (15 m).

Above 10 m, in the trapping scenario, the sea state and duct height contribute nearly equal roles to the propagation variability BGH; in contrast, above 10 m, for the non-trapping scenario the duct height is most influential outside of areas near multipath nulls. Compared to the influence of sea state (wind speed) and mean duct height in propagation variability, the turbulence (C_n^2) is a relatively insignificant factor. Its most significant effects on propagation variability occur at around mid-altitudes (~25-75 m) at long range (> 50 km) – far from the transmitter, similar to results illustrated in [5]. This sensitivity is likely due to interactions with other, more significant factors like the duct height, and propagation variations due to cumulative effects of the turbulence over the long path length.

C. *Unstable Regime*

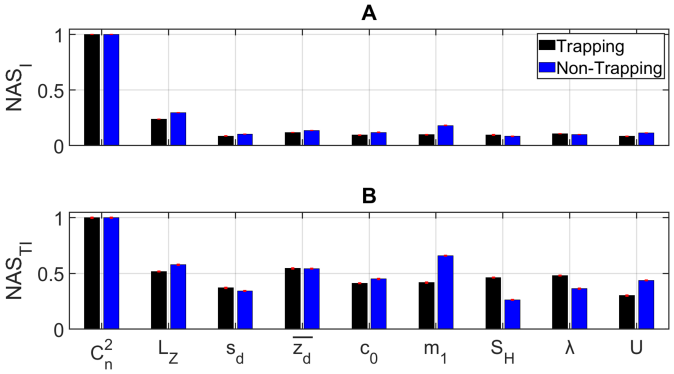


Fig. 7. Unstable regime (A) first order (NAS_I) and (B) total-order (NAS_{TI}) sensitivity averaged over ranges and altitudes beyond-the-geometric horizon and normalized by the maximum average S_I and S_{TI}, respectively, for trapping (16 m ≤ $\overline{z_d}$ < 30 m) and non-trapping (5 m < $\overline{z_d}$ ≤ 14 m) scenarios. Red error-bars denote 99% confidence intervals.

Unstable regime NAS_I and NAS_{TI} are presented in Fig. 7. Unlike the neutral and stable experiments, for the unstable condition, turbulence, C_n^2 (Fig. 7), dominates propagation variability BGH. Larger C_n^2 is associated with unstable atmospheric conditions (see Table 1) due to convective processes combining with mechanical turbulence. The larger C_n^2 translates to increases in the fluctuation of the refractive index causing increased variations of EM energy throughout the propagation domain.

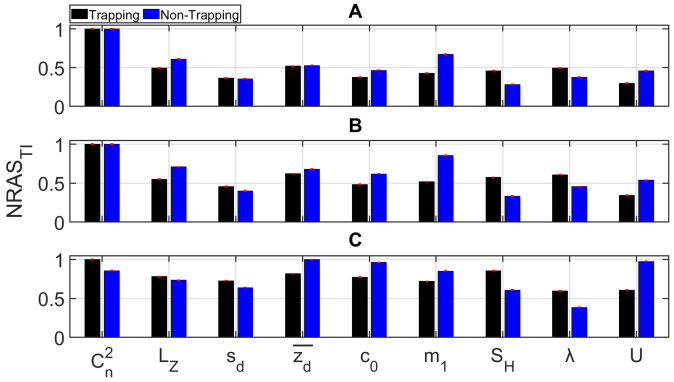


Fig. 8. Unstable regime regionally averaged total-order sensitivity ($NRAS_{TI}$) averaged over ranges beyond-the-geometric horizon and altitudes of (A) 50 – 100 m, (B) 10 – 50 m, and (C) 2 – 10 m, normalized by the maximum regionally averaged S_{TI} over all parameters for trapping and non-trapping scenarios. Red error-bars denote 99% confidence intervals.

The mean duct height remains a significant factor as with the other two experiments, but its role is now comparable to many other parameters in contrast with the stable and neutral experiments. One may find it surprising that the duct height is not the most significant factor in this experiment as well but, recall the omission of the primary trapping effects of EDH in this study; thus, these results indicate that the duct height remains important, even after removing this aspect, but is not as influential as the turbulence in its secondary effects (e.g.,

changes in duct leakage as the distance between the duct height and transmitter changes).

The regional delineation of $NRAS_{TI}$ is presented in Fig. 8. At the higher altitudes (10 – 100 m), for both trapping conditions, C_n^2 is shown to be the dominant parameter in varying propagation, with all the remaining parameters having similarly important secondary effects. At the lowest altitudes (2-10 m), nearly all parameters contribute in an approximately equal manner to propagation variability. The sea state plays a smaller relative role even at the lowest altitudes compared to the neutral and stable experiments. Duct height variability in range shows slightly lower $NRAS_{TI}$ at all altitudes relative to most of the other parameters, suggesting that spatial inhomogeneity is the least significant factor relative to the other phenomena examined (mean refractivity, sea state, and turbulence).

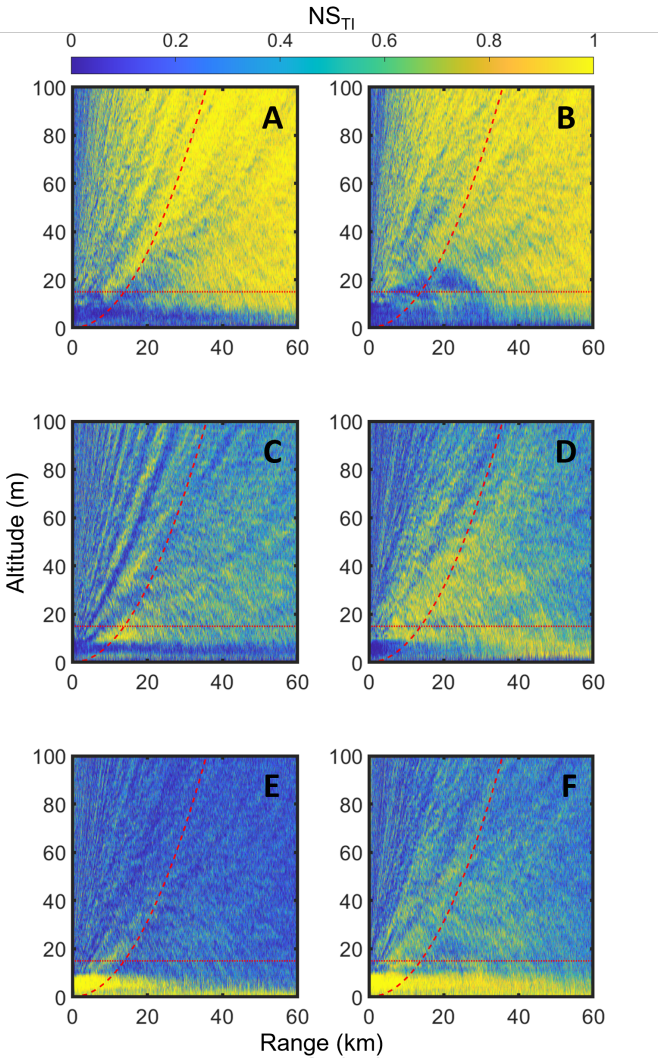


Fig. 9. Unstable regime total-order sensitivity (S_{TI}) normalized by the largest magnitude S_{TI} over all parameters, at each range and altitude. Normalized sensitivities (NS_{TI}) are shown for trapping (A, C, and E) and non-trapping (B, D, and F) scenarios; parameters illustrated are (A & B) C_n^2, (C & D) $\overline{z_d}$, and (E & F) U. These parameters are representative of the turbulence, mean atmospheric refractivity, and sea-state components, respectively. The dashed red line represents the geometric horizon, and the dotted horizontal red line represents the RF transmitter height (15 m).

The mean mixed layer slope being important to propagation variability was also shown in the sensitivity study of [3]. This (often) sub-refractive mixed layer likely increases propagation loss in the mid-altitudinal region as EM waves are deflected upward away from the duct.

These results are further delineated in Fig. 9, where NS_{TI} is displayed for the entire propagation domain for C_n^2, $\overline{z_d}$, and U. The dominance of the turbulence (C_n^2) over the other two parameters in most of the domain is apparent and in stark contrast to the stable and neutral cases. However, at the lowest altitudes, C_n^2 is not as influential as the sea state, or EDH at long range for non-trapping conditions.

The sea state still dominates at the lowest altitudes but presumably due to the increased scatter from the turbulence, the multipath nulls are so washed out that the influence of the sea state even surrounding null positions is not present in the unstable experiment. The mean duct height secondary effects (i.e., after removing effects of trapping vs. non-trapping) are much less significant than in the stable and neutral cases with the duct height being of least consequence in the trapping scenario. This result indicates that if it is known that the duct height is above the transmitter, then the precision to which the duct height is known becomes less consequential for unstable atmospheres relative to the importance of characterizing the turbulence.

V. Summary and Conclusions

This study investigates and quantifies the relative importance of atmospheric and sea-surface conditions on EM propagation within the marine atmospheric surface layer. The extended Fourier Amplitude Sensitivity test is employed to quantify the global sensitivity of a set of parameters describing mean, turbulent fluctuations, and spatial heterogeneity of refractivity as well as swell and wind-wave characteristics of the sea-surface to X-band propagation. Parameter distributions are delineated over atmospheric stability regimes via the stability parameter [36] for stable, neutral, and unstable atmospheric stabilities. Furthermore, experiments for each regime are performed for trapping and non-trapping scenarios to more thoroughly explore how parameters, outside of EDH, vary propagation predictions. This division largely removes the effect of the duct resulting in either trapping or non-trapping propagation so that this effect does not dominate the sensitivities as it is well known. Thus, here, sensitivities to the duct height are beyond this fundamental effect and explore the effects of the finer details of mean duct height variation on propagation (e.g., duct leakage) relative to other secondary effects. Normalized first and total order sensitivity averaged beyond-the-geometric horizon are presented to understand variations in long range propagation, where normalized average total order sensitivity is further explored for three altitudinal regions. To illustrate the relative influence of turbulence, mean refractivity, and sea state as well as explore how the influence of these phenomena vary over the domain, especially BGH, normalized sensitivity over the simulation domain is presented for C_n^2, $\overline{z_d}$, and U – as representative of these components, respectively.

Main results and conclusions are summarized in the following:

In stable regimes, mean duct height and curvature as well as the sea state are important drivers of propagation variability. The sea state plays a significant role near the surface (< 10m) and near locations of multipath nulls. The secondary effects of the duct are significant and primarily influence the region just above the transmitter where effects of duct leakage will vary as the proximity between the duct height and transmitter vary.

In neutral regimes, similar trends as the stable regime are observed except that turbulence and spatial inhomogeneity also tend to take on important secondary roles. Notably, spatially heterogenous EDH causes the most influence on propagation in this regime relative to other stability regimes.

In unstable regimes, variability of propagation becomes significantly influenced by turbulence, which becomes the leading order effect outside of trapping vs. non-trapping conditions. The secondary effects from the duct height are much more limited in this experiment and the influence of the sea state is constrained to just the lowest 10 m, presumably due to the wash out of multipath nulls from the turbulence.

ACKNOWLEDGMENT

The authors would like to acknowledge Professor Denise Kirschner for making their eFAST algorithms publicly available at (malthus.micro.med.umich.edu/lab/usadata/). These provided an initial framework for the eFAST algorithm presented in this study.

REFERENCES

[1] I. Sirkova, ""Brief review on PE method application to propagation channel modeling in sea environment," *" Open Engineering*, vol. 2, no. 1, pp. 19–38, 2012.

[2] P. Gerstoft, D. F. Gingras, L. T. Rogers, and W. S. Hodgkiss, "Estimation of radio refractivity structure using matched-field array processing," *IEEE Trans Antennas Propag*, vol. 48, no. 3, pp. 345–356, 2000.

[3] N. E. Lentini and E. E. Hackett, "Global sensitivity of parabolic equation radar wave propagation simulation to sea state and atmospheric refractivity structure," *Radio Sci*, vol. 50, no. 10, pp. 1027–1049, Oct. 2015, doi: 10.1002/2015RS005742.

[4] M. Wagner, P. Gerstoft, and T. Rogers, "'Estimating refractivity from propagation loss in turbulent media, ' Radio Science," vol. 51, no. 12, pp. 1876–1894, 2016.

[5] Y. H. Chou and J. F. Kiang, "'Effect of turbulence on wave propagation in evaporation ducts above a rough sea surface, ' Forum for Electromagnetic Research Methods and Application Technologies," vol. 12, 2014.

[6] I. J. Matsko and E. E. Hackett, "'Impact of radar data sampling on the accuracy of atmospheric refractivity inversions over marine surfaces, ' Radio Science," vol. 54, no. 7, pp. 704–714, 2019.

[7] D. M. Pastore and others, "'Comparison of atmospheric refractivity estimation methods and their influence on radar propagation predictions, ' Radio Science," vol. 56, no. 9, p. e2020RS007194, 2021.

[8] L. Xu, C. Yardim, and T. Haack, "'Evaluation of COAMPS boundary layer refractivity forecast accuracy for 2–40 GHz electromagnetic wave propagation, ' Radio Science," vol. 57, no. 6, p. e2021RS007404, 2022.

[9] D. M. Pastore and others, "'Refractivity inversions from point-to-point X-band radar propagation measurements, ' Radio Science," vol. 57, no. 2, p. e2021RS007624, 2022.

[10] I. Sirkova, ""Propagation factor and path loss simulation results for two rough surface reflection coefficients applied to the microwave ducting propagation over the sea," *" Progress In Electromagnetics Research M*, vol. 17, pp. 151–166, 2011.

[11] J. D. Turton, D. A. Bennetts, and S. G. Farmer, "'An introduction to radio ducting, ' Meteorological Magazine," vol. 117, no. 1393, pp. 245–254, 1988.

[12] S. E. Penton and E. E. Hackett, "Rough ocean surface effects on evaporative duct atmospheric refractivity inversions using genetic algorithms," *Radio Sci*, vol. 53, no. 6, pp. 804–819, 2018.

[13] B. R. Bean and E. J. Dutton, *Radio Meteorology (1st ed.)*. Dover, 1968.

[14] J. T. Saeger, N. G. Grimes, H. E. Rickard, and E. E. Hackett, "Evaluation of simplified evaporation duct refractivity models for inversion problems," *Radio Sci*, vol. 50, no. 10, pp. 1110–1130, 2015.

[15] K. H. Craig and M. F. Levy, "Parabolic equation modelling of the effects of multipath and ducting on radar systems."

[16] R. C. Cherrett, *Capturing characteristics of atmospheric refractivity using observations and modeling approaches [Doctoral dissertation*. Naval Postgraduate School], 2015.

[17] H. V Hitney, "Evaporation duct propagation and near-grazing angle scattering from a rough sea," in *IEEE 1999 International Geoscience and Remote Sensing Symposium*, 1999, pp. 2631–2633.

[18] V. K. Ivanov, V. N. Shalyapin, and Y. V Levadny, "Microwave scattering by tropospheric fluctuations in an evaporation duct," *Radiophysics and Quantum Electronics*, vol. 52, no. 4, pp. 277–286, 2009.

[19] D. E. Freund, N. E. Woods, H. C. Ku, and R. I. S. Awadallah, "Forward radar propagation

over a rough sea surface: A numerical assessment of the Miller-Brown approximation using a horizontally polarized 3-GHz line source," *IEEE Trans Antennas Propag*, vol. 54, no. 4, pp. 1292–1304, 2006.

[20] M. A. Donelan, J. Hamilton, and W. Hui, "Directional spectra of wind-generated ocean waves," *Philosophical Transactions of the Royal Society of London. Series A, Mathematical and Physical Sciences*, vol. 315, no. 1534, pp. 509–562, 1985.

[21] M. L. Banner, I. S. Jones, and J. C. Trinder, "Wavenumber spectra of short gravity waves," *J Fluid Mech*, vol. 198, pp. 321–344, 1989.

[22] F. J. Ryan, *Analysis of electromagnetic propagation over variable terrain using the parabolic wave equation (No*. NOSC/TR-1453), 1991.

[23] A. Saltelli, S. Tarantola, and K. S. Chan, "A quantitative model-independent method for global sensitivity analysis of model output," *Technometrics*, vol. 41, no. 1, pp. 39–56, 1999.

[24] S. Marino, I. B. Hogue, C. J. Ray, and D. E. Kirschner, "A methodology for performing global uncertainty and sensitivity analysis in systems biology," *J Theor Biol*, vol. 254, no. 1, pp. 178–196, 2008.

[25] R. A. Paulus, "Evaporation duct effects on sea clutter," *IEEE Trans Antennas Propag*, vol. 38, no. 11, pp. 1765–1771, Nov. 1990.

[26] D. P. Greenway, *Parametric Model Development For Heterogeneous Atmospheric Conditions*. PhD dissertation, Coastal Carolina University, 2020.

[27] X. Zhao, C. Yardim, D. Wang, and B. M. Howe, "Estimating range-dependent evaporation duct height," *J Atmos Ocean Technol*, vol. 34, no. 5, pp. 1113–1123, 2017.

[28] J. Goldhirsh and D. Dockery, "Propagation factor errors due to the assumption of lateral homogeneity," *Radio Sci*, vol. 33, no. 2, pp. 239–249, 1998.

[29] D. M. Pastore, R. T. Yamaguchi, Q. Wang, and E. E. Hackett, "On the Variability of In Situ Surface Layer Refractivity Measurements," *Atmosphere (Basel)*, vol. 14, no. 7, p. 1085, Jun. 2023, doi: 10.3390/atmos14071085.

[30] A. Ishimaru, "Wave Propagation and Scattering in Random Media," vol. 2, 1978.

[31] M. J. Emes, M. Arjomandi, R. M. Kelso, and F. Ghanadi, "Turbulence length scales in a low-roughness near-neutral atmospheric surface layer," *Journal of Turbulence*, vol. 20, no. 9, pp. 545–562, 2019.

[32] D. Rouseff, "Simulated microwave propagation through tropospheric turbulence," *IEEE Trans Antennas Propag*, vol. 40, no. 9, pp. 1076–1083, Sep. 1992.

[33] S. Mukherjee and C. Yardim, "Accurate computation of scintillation in tropospheric turbulence with parabolic wave equation," *IEEE Trans Antennas Propag*, vol. 69, no. 8, pp. 4748–4757, 2021.

[34] M. Charnotskii, "Wave propagation modeling with non-Markov phase screens," *Journal of the Optical Society of America A*, vol. 33, no. 4, p. 561, 2016.

[35] D. L. Knepp, "Multiple phase-screen calculation of the temporal behavior of stochastic waves," *Proceedings of the IEEE*, vol. 71, no. 6, pp. 722–737, 1983.

[36] A. Panofsky and J. A. Dutton, "Atmospheric turbulence: models and methods for engineering applications," *QC880*, vol. 4., 1984.

[37] T. Foken, "50 years of the Monin-Obukhov similarity theory," *Boundary Layer Meteorol*, vol. 119, pp. 431–447, 2006.

[38] J. R. Garratt, "The atmospheric boundary layer," *Earth Sci Rev*, vol. 37, pp. 89–134, 1994.

[39] S. E. Wessinger, *Improving near Surface Refractivity Estimates in Marine Environments*. Coastal Carolina University, 2022.

[40] P. A. Frederickson, K. L. Davidson, C. R. Zeisse, and C. S. Bendall, "Estimating the refractive index structure parameter (Cn2) over the ocean using bulk methods," *Journal of Applied Meteorology*, vol. 39, no. 10, pp. 1770–1783, 2000.

[41] P. A. Frederickson, S. Hammel, and D. Tsintikidis, " Improving bulk C n 2 models for over-ocean applications through new determinations of the dimensionless temperature structure parameter ," in *Atmospheric Optics: Models, Measurements, and Target-in-the-Loop Propagation*, SPIE, Sep. 2007, p. 670807. doi: 10.1117/12.739617.

[42] P. Frederickson, *Navy Atmospheric Measurements for EM Propagation Modeling*. [Executive Summary], Naval Postgraduate School, 2016.

[43] Q. Wang *et al.*, "CASPER: Coupled air-sea processes and electromagnetic ducting research," *Bull Am Meteorol Soc*, vol. 99, no. 7, pp. 1449–1471, 2018.

[44] O. Benhmammouch, N. Caouren, and A. Khenchaf, "Influence of sea surface roughness on electromagnetic waves propagation in presence of evaporation duct," *International Radar Conference* , 2009.



Douglas M. Pastore received the B.S. degree in marine science from Stockton University, New Jersey, USA, in 2015, the M.S. degree in coastal marine and wetlands studies from Coastal Carolina University, South Carolina, USA, in 2018. He is currently a Ph.D. candidate and member of the Environmental Fluids Laboratory at Coastal Carolina University, South Carolina, USA. His research interests are in atmospheric surface layer turbulence, propagation in the marine environment, and remote sensing.



Erin E. Hackett received the B.S. degree in physics from Roanoke College, Salem, VA, USA, and the Master's degree in civil engineering and the Ph.D. degree in earth and planetary sciences from The Johns Hopkins University, Baltimore, MD, USA. She is currently a Professor at the Department of Marine Science, and co-director of the Environmental Fluids Laboratory, at Coastal Carolina University, Conway, SC, USA. Previously, she held positions as a Research Scientist with the Carderock Division, Naval Surface Warfare Center, Bethesda, MD, and as a Systems Engineer with The Johns Hopkins University Applied Physics Laboratory, Columbia, MD. Her research focuses on experimental fluid mechanics as applied to coastal ocean and atmospheric dynamics, including boundary layers, surface waves, and turbulence, as well as electromagnetic wave propagation in the marine environment and radar remote sensing.

REPORT DOCUMENTATION PAGE

Form Approved
OMB No. 0704-0188

The public reporting burden for this collection of information is estimated to average 1 hour per response, including the time for reviewing instructions, searching existing data sources, gathering and maintaining the data needed, and completing and reviewing the collection of information. Send comments regarding this burden estimate or any other aspect of this collection of information, including suggestions for reducing the burden, to Department of Defense, Washington Headquarters Services, Directorate for Information Operations and Reports (0704-0188), 1215 Jefferson Davis Highway, Suite 1204, Arlington, VA 22202-4302. Respondents should be aware that notwithstanding any other provision of law, no person shall be subject to any penalty for failing to comply with a collection of information if it does not display a currently valid OMB control number.
PLEASE DO NOT RETURN YOUR FORM TO THE ABOVE ADDRESS.

1. REPORT DATE *(DD-MM-YYYY)*	2. REPORT TYPE	3. DATES COVERED *(From - To)*
07/27/2023	Final Technical	5/1/19-7/27/23

4. TITLE AND SUBTITLE
Influence of Horizontal Inhomogeneity of Refractivity Vertical Profiles on Electromagnetic Measurements in Application to Refractivity Inversions

5a. CONTRACT NUMBER

5b. GRANT NUMBER
N00014-19-1-2350

5c. PROGRAM ELEMENT NUMBER

6. AUTHOR(S)
Hackett, Erin, E., Ph.D.

5d. PROJECT NUMBER

5e. TASK NUMBER

5f. WORK UNIT NUMBER

7. PERFORMING ORGANIZATION NAME(S) AND ADDRESS(ES)
Coastal Carolina University
P.O. Box 261954
Conway, SC 29528-0654

8. PERFORMING ORGANIZATION REPORT NUMBER

9. SPONSORING/MONITORING AGENCY NAME(S) AND ADDRESS(ES)
Office of Naval Research
Ship Systems and Engineering Division
875 N. Randolph Street
Arlington, VA 22203-1995

10. SPONSOR/MONITOR'S ACRONYM(S)
ONR

11. SPONSOR/MONITOR'S REPORT NUMBER(S)

12. DISTRIBUTION/AVAILABILITY STATEMENT
Approved for Public Release; Distribution is Unlimited

13. SUPPLEMENTARY NOTES

14. ABSTRACT
This report describes results of research studying horizontal inhomogeneity of vertical refractivity profiles in evaporation ducting conditions. Horizontal inhomogeneity is characterized by examining range distributions of important ducting parameters, such as the duct height, and classifying them as well as linking them with atmospheric conditions. These inhomogeneities are evaluated in terms of their effect on X-band electromagnetic wave propagation through application of a global sensitivity analysis investigating the relative importance of sea state and mean, turbulent, and horizontally inhomogeneous refractivity for varying atmospheric stability regimes.

15. SUBJECT TERMS
Atmospheric refractivity, electromagnetic wave propagation, evaporation ducts, sensitivity analysis, inverse problems, rough sea surfaces, propagation loss measurements, refractive index turbulence, X-band, numerical weather prediction, atmospheric measurements, boundary layer theory

16. SECURITY CLASSIFICATION OF:			17. LIMITATION OF ABSTRACT	18. NUMBER OF PAGES	19a. NAME OF RESPONSIBLE PERSON
a. REPORT	b. ABSTRACT	c. THIS PAGE			Erin E. Hackett
U	U	U	UU	95	19b. TELEPHONE NUMBER *(Include area code)* 843-349-4087